

# **Binospec Design Summary** 11/04/08

<b>1</b>	<b>Binospec Scientific Overview .....</b>	<b>5</b>
1.1	Scientific Goals .....	5
1.2	Binospec Configuration .....	6
1.3	Operating Modes .....	6
1.4	Binospec Slit Mask and Guider Layout .....	7
1.5	Optical Layout .....	7
1.6	Optical Performance .....	9
1.7	Project Team .....	15
1.8	Binospec Status as of December 2007 Review .....	15
<b>2</b>	<b>Scientific Requirements.....</b>	<b>17</b>
2.1	Operating Environment.....	17
2.2	Telescope Envelope and Instrument Mass Constraints .....	18
2.3	Interface Connections .....	20
2.4	Science and Flexure Control CCDs .....	20
2.5	Flexure Control .....	22
2.6	Filters .....	26
2.7	Slit Masks.....	26
2.8	Gratings.....	26
2.9	Calibration System.....	27
2.10	Guiders and Wavefront Sensing .....	28
2.11	Access and Service Issues.....	29
2.12	Reconfiguration Times.....	29
2.13	Thermal Requirements.....	31
2.14	Optics Sensitivity Summary and Image Quality Goals .....	35
2.15	Optics Fabrication Errors.....	36
2.16	Clear Apertures and System Geometry Documents .....	37
2.17	Software Requirements.....	37
<b>3</b>	<b>Instrument Overview.....</b>	<b>43</b>
3.1	Optical Layout .....	43
3.2	Support Structure Overview .....	43
3.3	Mechanism Overview .....	44
3.4	Thermal Environment and Thermal Design .....	45
3.5	Lens Mount Overview .....	47
3.6	System Electronics.....	50
3.7	Science and Flexure CCDs .....	52
3.8	Calibration System.....	52
3.9	Service and Maintenance .....	54
<b>4</b>	<b>Binospec Mechanical Section.....</b>	<b>56</b>
4.1	Introduction.....	56
4.2	Slit Mask Assembly .....	56
4.3	Single Object Guider/Acquisition Camera Assembly .....	64
4.4	Wave Front Sensor Assembly.....	66
4.5	Guider Assemblies.....	68
4.6	Guide Camera Vacuum Manifold.....	72
4.7	Periscope Fold Mirror Assembly .....	73

4.8	Filter Changer Assembly .....	74
4.9	Grating Stage .....	76
4.10	Science Camera and High Speed Shutter Assembly.....	88
4.11	Collimator and Camera Lens Assemblies.....	93
4.12	Flexure Control System .....	95
4.13	Calibration/Derotator Assembly .....	96
4.14	Thermal Covers.....	103
4.15	Servo-Driven Stage Summary .....	109
<b>5</b>	<b>Structural Analysis .....</b>	<b>110</b>
5.1	Introduction.....	110
5.2	Main Structure .....	113
5.3	Optical Mounts.....	117
5.4	System Level Finite Element Model and System Performance.....	136
5.5	Predicted Image Motion and Image Quality from Zemax .....	141
5.6	Subassembly Finite Element Analysis.....	145
5.7	Shipping and Handling .....	147
<b>6</b>	<b>Optics Assembly .....</b>	<b>151</b>
6.1	Lens Fluid Seals.....	151
6.2	Optical Assembly with the Opticentric Lens Alignment Machine.....	156
6.3	Collimator and Camera Assembly Tolerances .....	160
<b>7</b>	<b>Summary Image Quality Error Budget.....</b>	<b>172</b>
<b>8</b>	<b>Electronics .....</b>	<b>173</b>
8.1	Introduction.....	173
8.2	Electronics Functional Requirements and Subsystems Layout .....	175
8.3	Power Control and Communication Assembly.....	177
8.4	Motion Control Electronics Assembly.....	179
8.5	Piezoelectric Motion Control Assembly.....	183
8.6	Calibration Electronics.....	185
8.7	Science/Flexure Detector Electronics Assembly .....	188
8.8	Guider Detector Electronics Assembly.....	190
8.9	Thermal Impact of Electronics.....	192
<b>9</b>	<b>Software .....</b>	<b>195</b>
9.1	Introduction and Heritage .....	195
9.2	Software Architecture .....	195
9.3	Software Block Diagram.....	197
9.4	Observation Planning and Mask Design Program .....	197
9.5	Graphical User Interfaces .....	198
9.6	Servers.....	205
<b>10</b>	<b>Project Management, Budget, and Schedule.....</b>	<b>208</b>
10.1	Overview.....	208
10.2	Management and Cost Estimating .....	208
10.3	Major Schedule Milestones for FY2011 delivery.....	209
10.4	Costs to Complete with FY11 Delivery.....	210
10.5	Table 65. Major Schedule Milestones for FY2013 delivery.....	214
10.6	Costs to Complete with FY13 Delivery.....	215
10.7	Costs Through FY07.....	215

<b>11</b>	<b>Appendices.....</b>	<b>216</b>
11.1	Description of Slit Mask Geometry .....	216
11.2	Image Spot Diagrams from Raytracing .....	222
11.3	Image Motion Sensitivity Matrix.....	235
11.4	Published Papers Concerning Binospec Thermal Design.....	245

# 1 Binospec Scientific Overview

## 1.1 Scientific Goals

Binospec has been designed to aggressively pursue wide-field surveys using moderate dispersion optical spectroscopy. Our original goal was to make an efficient spectrograph to survey the intermediate and high redshift Universe. At the moment, the premier instrument for surveys of this kind is DEIMOS on Keck. Our ambition for Binospec is to provide the MMT with an instrument of comparable power measured in étendue. The MMT concedes a factor of 2.4 in mirror area to the Keck, but with its twin 8' by 15' fields of view, Binospec offers very nearly three times the field of view of DEIMOS.

With a wavelength coverage of 3900 to 10,000 Å, Binospec accesses two redshift windows:  $z=0.05$  to 1.4 observing the rest frame spectrum around [OII] 3727 and  $z=2.2$  to 7 using the rest-frame spectrum around Ly  $\alpha$ . Binospec will enable CfA scientists to efficiently gather the spectra of large samples of faint galaxies and to measure their masses, chemical evolution, star formation rates, and distances. CfA scientists have used spectroscopy to lead the way in uncovering the nature of the large scale structure at low redshifts, and are currently using Hectospec at the MMT to determine the distribution of the dark matter and the nature of the large scale structure at intermediate redshifts. Binospec will carry forward this tradition of using spectroscopy to answer fundamental questions in cosmology by enabling CfA scientists to observe the faintest objects accessible with the current generation of ground-based telescopes.

Binospec will also be a powerful tool for “near-field cosmology”. Examples of this low-redshift science are using planetary nebulae and globular clusters to survey galaxy kinematics, as well as globular clusters to measure the formation epochs and subsequent chemical evolution of disks, bulges, and halos. Stellar surveys in M31 to measure its detailed kinematics and chemical abundance distribution will become of increasing interest in the next few years when deep photometric surveys like PanSTARRS are underway.

Binospec is a versatile optical spectrograph that will become the MMT’s general-purpose high-throughput optical spectrograph for a very wide variety of programs. It will be used to study the nature of the dark energy using distant supernovae as standard candles to measure the geometry of the Universe, to identify the faint counterparts of X-ray and infrared sources detected with NASA’s Chandra and Spitzer Observatories, to track the evolution of massive black holes at the centers of galaxies through cosmic time, and to study faint icy planetesimals in the outer solar system.

Binospec directly images faint objects at the focus of the MMT without the optical fibers that convey light to Hectospec’s spectrograph. Direct imaging cannot address Hectospec’s huge field of view, which is critical for Hectospec’s studies of the intermediate redshift Universe, but direct imaging allows more precise rejection of the background light that obscures our view of very faint galaxies. In addition, direct imaging preserves the spatial information that allows us to measure the masses and structure of galaxies.

## 1.2 Binospec Configuration

Wide-field imaging spectrographs are key scientific tools at most large telescopes; aperture masks with slitlets use these wide fields to gain an important multiplex advantage while maintaining the superb sky-subtraction of conventional slits. In addition to DEIMOS at Keck, other recent examples of powerful, wide-field optical spectrographs include VIMOS at VLT, and IMACS at Magellan. Beginning in 1995, Daniel Fabricant and Harland Epps began to explore the possibility of designing such a spectrograph for the converted MMT's  $f/5$  focus. The  $f/5$  focus offers a field of view  $1^\circ$  in diameter with atmospheric dispersion compensation, and this fast focal ratio leads to a compact instrument.

However, the slower final focal ratios of the Keck, VLT, and Magellan telescopes ease the optical design of their collimators; in fact, Magellan's  $f/11$  Gregorian design was chosen to match the requirements of IMACS's collimator. Designing a wide-field  $f/5$  collimator has proven to be the most difficult element in Binospec's optical design, but the remainder of Binospec's optics have presented significant optical design and practical challenges, including athermalization of the optics and obtaining the necessary large calcium fluoride lenses. One significant advantage of the MMT's  $f/5$  focus is that it provides atmospheric dispersion compensation and is highly telecentric, allowing the focal surface to accommodate two adjacent Binospec beams.

## 1.3 Operating Modes

We plan to use Binospec mainly as a spectrograph because Megacam is a more powerful imager, but we expect that Binospec will see some use as an imager to allow flexible scheduling and for cases where the full power of Megacam is overkill. We plan to purchase SDSS  $g$ ,  $r$ ,  $i$ , and  $z$  filters.

Table 1 shows Binospec's performance with 270 gpm and 600 gpm gratings that were ruled for Hectospec, as well as with a 632 gpm 2<sup>nd</sup> order grating. The grating blaze shown is for these existing master gratings. Binospec's camera-collimator angle is  $45^\circ$ .

**Table 1. Spectroscopic Modes**

Grating Ruling	Order	Grating Blaze	Angle of Incidence	Ana. Mag.	Spectral Coverage ( $\text{\AA}$ )	Dispersion $\text{\AA}/\text{pixel}$	Pixels for 1" slit	Resolution for 1" slit
270	1	$5.5^\circ$	$28.0^\circ$	1.08	3900-9240	1.30	3.75	1340
600	1	16.0	$33.2^\circ$	1.17	4500-6960	0.60	3.47	2740
600	1	16.0	$36.1^\circ$	1.22	6000-8480	0.61	3.32	3590
600	1	16.0	$38.5^\circ$	1.27	7255-9750	0.61	3.20	4360
632	2	$22.1^\circ$	$51.1^\circ$	1.58	6405-7590	0.29	2.56	9427

## 1.4 Binospec Slit Mask and Guider Layout

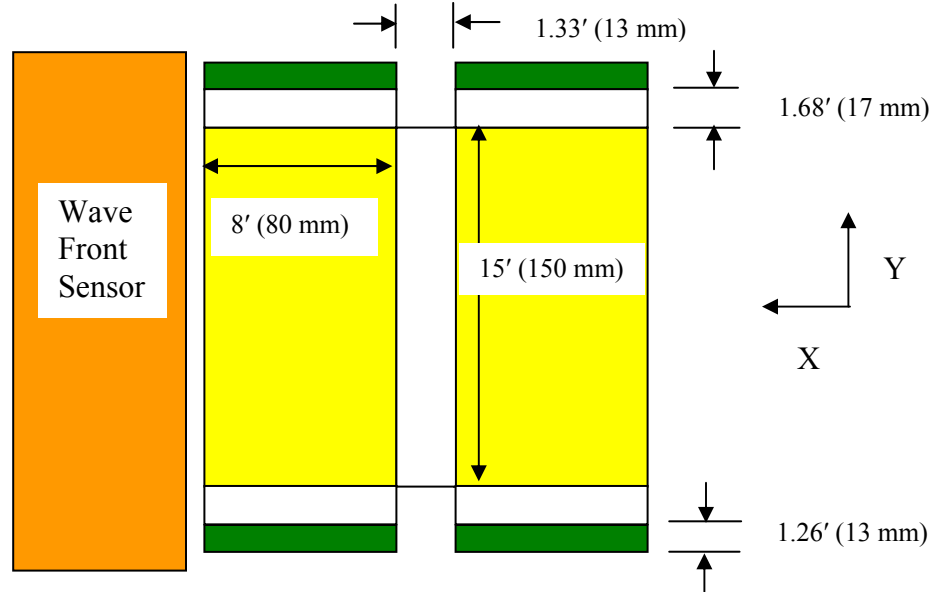


Figure 1. The layout of the two beams at the Binospec focal surface. The slits will be placed in two adjacent 8' by 15' regions (shown in yellow). The slit masks have a total length of ~21' including extra field for guide stars. Two guiders, viewing through the slit masks, will each cover two adjacent guider strips at opposite ends of the slit regions (shown in green). Each guider will access a field of 26.9 sq. arcmin. At the North Galactic Pole, each guider region contains ~4.4 stars with  $17 < g < 19$  and ~6.4 stars with  $17 < r < 19$ . The wave front sensor will patrol a region 7.1' wide and 21.3' long adjacent to the slit mask field for a total area of ~150 sq. arcmin (shown in orange).

## 1.5 Optical Layout

Binospec's collimator and camera optics are shown in Figure 2. Binospec's collimator has a focal length of 1097 mm, producing a collimated beam diameter of ~200 mm. Binospec's camera has a focal length of 404 mm, producing an image scale at the CCD (15  $\mu\text{m}$  pixels) of 0.24" per pixel. The demagnification of the Binospec optics is 2.72. The overall optical path is 2.9 meters from the slit to the detector.

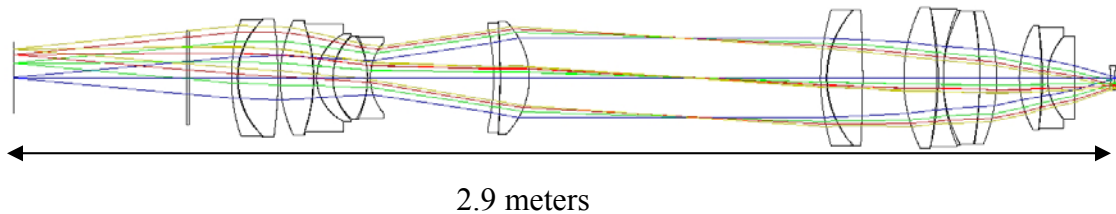
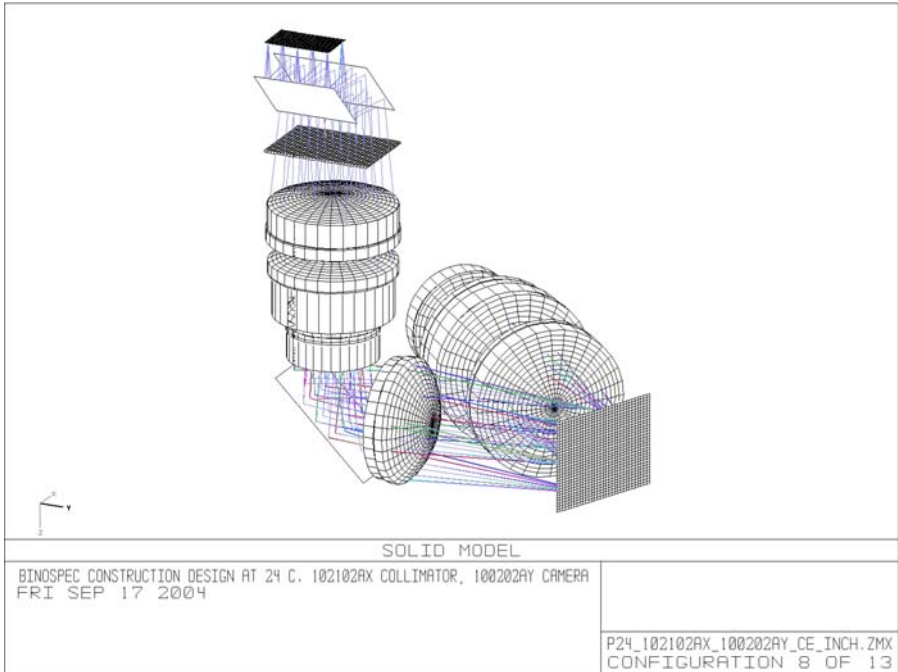


Figure 2. Binospec's optical layout in the imaging mode with all fold mirrors removed. The MMT's focal surface is on the left and the spectrograph focus is on the right. The collimator consists of a doublet, a quintet, and a doublet. The camera consists of a doublet, a quartet, a triplet and a singlet that serves as the dewar window. The fluid lenses are visible on close inspection.

In order to maintain a compact package, Binospec uses three fold mirrors in addition to a reflection grating. The first two mirrors act as a periscope to separate the two beams to

accommodate the collimator optics side by side. The third fold mirror, following the quintet in the collimator, folds the beam so that the subsequent optics can all sit in a plane on an optical bench.



**Figure 3. The overall Binospec layout with fold mirrors and grating. One of two adjacent beams is shown. The rectangular objects at the top left are in order: the slit masks, two fold mirrors arranged as a periscope, and a filter. The third fold mirror is at the lower left and the grating is at the lower right.**

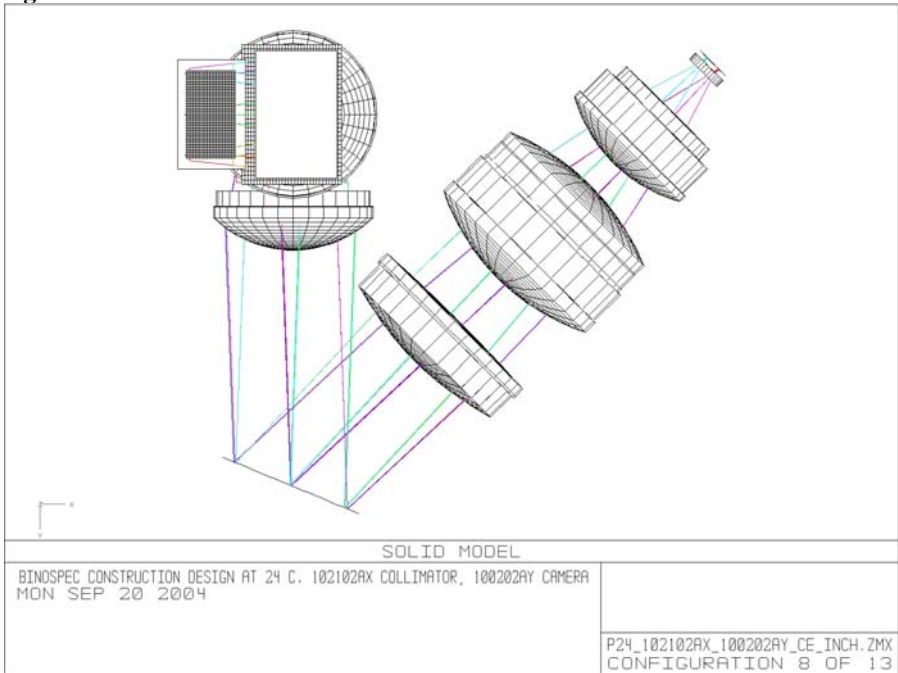


**Figure 4. Looking down at the Binospec optics from the telescope focal plane. The full 8' wide slit mask is illuminated. The clearance between the light leaving the collimator and the first camera lens is tight.**

## 1.6 Optical Performance

### 1.6.1 Estimated Throughput

The estimated throughput of Binospec is shown in Table 2 with the two first-light gratings. The highlighted columns to the right show the estimated combined throughput of Binospec and the converted MMT.

**Table 2. Estimated Binospec throughput. The reflection losses are averaged over wavelength.**

		270	600	Refl	Fold	Telescope	270	600	270	600
		gpm	gpm	Losses	Mirrors	and	gpm	gpm	gpm	gpm
	CCD	Grating	Grating	14 Surf	3 Refl	Corrector	Bino	Bino	Bino	Bino
									+Tel	+Tel
3900	0.78	0.60	0.22	0.87	0.94	0.65	0.38	0.14	0.25	0.09
4000	0.80	0.62	0.25	0.87	0.94	0.66	0.41	0.16	0.27	0.11
4500	0.82	0.70	0.42	0.87	0.94	0.70	0.47	0.28	0.33	0.20
5000	0.81	0.72	0.58	0.87	0.94	0.79	0.48	0.38	0.38	0.30
5500	0.80	0.71	0.68	0.87	0.94	0.79	0.46	0.44	0.37	0.35
6000	0.78	0.67	0.71	0.87	0.94	0.79	0.43	0.45	0.34	0.36
6500	0.76	0.62	0.71	0.87	0.94	0.77	0.39	0.44	0.30	0.34
7000	0.74	0.56	0.69	0.87	0.94	0.75	0.34	0.42	0.25	0.31
7500	0.72	0.50	0.65	0.87	0.94	0.70	0.29	0.38	0.21	0.27
8000	0.70	0.44	0.59	0.87	0.94	0.66	0.25	0.34	0.17	0.22
8500	0.60	0.39	0.55	0.87	0.94	0.66	0.19	0.27	0.13	0.18
9000	0.45	0.36	0.55	0.87	0.94	0.65	0.13	0.20	0.09	0.13
9500	0.25	0.34	0.55	0.87	0.94	0.65	0.07	0.11	0.05	0.07
10000	0.10	0.30	0.52	0.87	0.94	0.65	0.02	0.04	0.02	0.03

### 1.6.2 Description of Analysis Configurations and Vignetting

During the design of the Binospec optics, we tracked the system performance using thirteen configurations. These include seven spectroscopic configurations and six imaging configurations. The spectroscopic configurations using gratings with ruling densities between 270 and 1200 gpm, typically set to sample Binospec's performance in the spectral extremes. Four of the imaging configurations correspond to broad band SDSS filters; the remaining two imaging configurations sample broad bands at the spectral extremes.

The only significant vignetting in Binospec occurs at the grating since the optics were designed for a maximum unvignetted anamorphic magnification of  $\sim 1.3$ . The only configurations with significant vignetting are those with larger anamorphic magnifications as shown in the following table. Because the vignetting is at the pupil, it is independent of wavelength.

**Table 3. Summary of Binospec optical performance evaluation configurations and vignetting.**

Config	Wavelength ( $\mu\text{m}$ )	Notes	Angle of Incidence	Angle of Diffraction	Anamorphic Mag	Vignetting
1	0.39-0.93	270 gpm	28.103°	16.987°	1.08	none
2	0.39-0.62	650 gpm	32.710°	12.290°	1.16	none
3	0.77-1.00	650 gpm	40.585°	4.415°	1.31	none
4	0.57-0.74	900 gpm	41.143°	3.857°	1.33	none
5	0.83-1.00	900 gpm	48.983°	-3.983°	1.52	7%
6	0.39-0.52	1200 gpm	39.615°	5.385°	1.29	none
7	0.88-1.00	1200 gpm	60.084°	-15.084°	1.94	27%
8	0.39-0.50	blue imaging	22.500°	22.500°	1.00	none
9	0.70-1.00	red imaging	22.500°	22.500°	1.00	none
10	0.41-0.54	g'-band	22.500°	22.500°	1.00	none
11	0.56-0.69	r'-band	22.500°	22.500°	1.00	none
12	0.69-0.83	i'-band	22.500°	22.500°	1.00	none
13	0.86-0.99	z'-band	22.500°	22.500°	1.00	none

### 1.6.3 Image Quality Tabular Summary at Three Temperatures

Table 4 through Table 7 summarize the optical performance of the Binospec optics for the optical configurations listed in Table 3. The RMS image diameters averaged over field angle and wavelength are less than one pixel (15  $\mu\text{m}$ ), and the worst RMS image diameters at any field angle or wavelength are always significantly less than two pixels. Spot diagrams are shown in Section 11.2.

**Table 4. RMS Image Diameters (in  $\mu\text{m}$ ) Averaged Over Field Angles and Wavelengths (on-axis Binospec models)**

	Conf 1	Conf 2	Conf 3	Conf 4	Conf 5	Conf 6	Conf 7
$\lambda$ ( $\mu\text{m}$ )	0.39-0.93	0.39-0.62	0.77-1.00	0.57-0.74	0.83-1.00	0.39-0.52	0.88-1.00
Notes	270 gpm	650 gpm	650 gpm	900 gpm	900 gpm	1200 gpm	1200 gpm
-10 °C	11.7	13.0	11.7	9.7	14.4	15.3	12.4
+8 °C	11.5	11.3	11.2	10.4	13.4	12.3	11.7
+25 °C	13.5	10.9	12.5	13.1	14.4	12.1	12.4

	<b>Conf 8</b>	<b>Conf 9</b>	<b>Conf 10</b>	<b>Conf 11</b>	<b>Conf 12</b>	<b>Conf 13</b>
$\lambda$ ( $\mu\text{m}$ )	0.39-0.50	0.70-1.00	0.41-0.54	0.56-0.69	0.69-0.83	0.86-0.99
Notes			g-band	r-band	i-band	z-band
-10 °C	12.7	11.7	9.4	10.1	11.4	13.6
+8 °C	10.8	12.5	9.0	11.0	11.9	13.0
+25 °C	10.8	14.4	10.4	13.1	14.0	13.0

**Table 5. 80% Encircled Image Diameters (in  $\mu\text{m}$ ) Averaged Over Field Angles and Wavelengths (on-axis Binospec models)**

	<b>Conf 1</b>	<b>Conf 2</b>	<b>Conf 3</b>	<b>Conf 4</b>	<b>Conf 5</b>	<b>Conf 6</b>	<b>Conf 7</b>
$\lambda$ ( $\mu\text{m}$ )	0.39-0.93	0.39-0.62	0.77-1.00	0.57-0.74	0.83-1.00	0.39-0.52	0.88-1.00
Notes	270 gpm	650 gpm	650 gpm	900 gpm	900 gpm	1200 gpm	1200 gpm
-10 °C	14.1	15.5	13.8	11.4	16.1	17.9	14.2
+8 °C	13.2	12.9	13.2	12.0	14.8	13.6	13.4
+25 °C	16.0	13.0	14.5	15.2	16.0	14.0	14.2

	<b>Conf 8</b>	<b>Conf 9</b>	<b>Conf 10</b>	<b>Conf 11</b>	<b>Conf 12</b>	<b>Conf 13</b>
$\lambda$ ( $\mu\text{m}$ )	0.39-0.50	0.70-1.00	0.41-0.54	0.56-0.69	0.69-0.83	0.86-0.99
Notes			g-band	r-band	i-band	z-band
-10 °C	15.1	14.5	11.1	12.3	13.9	16.6
+8 °C	12.8	14.9	10.9	13.1	14.1	15.6
+25 °C	12.8	17.2	12.5	15.8	16.8	18.2

**Table 6. 95% Encircled Image Diameters (in  $\mu\text{m}$ ) Averaged Over Field Angles and Wavelengths (on-axis Binospec models)**

	<b>Conf 1</b>	<b>Conf 2</b>	<b>Conf 3</b>	<b>Conf 4</b>	<b>Conf 5</b>	<b>Conf 6</b>	<b>Conf 7</b>
$\lambda$ ( $\mu\text{m}$ )	0.39-0.93	0.39-0.62	0.77-1.00	0.57-0.74	0.83-1.00	0.39-0.52	0.88-1.00
Notes	270 gpm	650 gpm	650 gpm	900 gpm	900 gpm	1200 gpm	1200 gpm
-10 °C	19.3	22.9	18.8	15.5	24.8	28.0	20.4
+8 °C	18.8	19.7	17.7	17.5	24.6	22.5	19.7
+25 °C	22.1	18.3	19.1	22.3	25.2	20.6	20.9

	<b>Conf 8</b>	<b>Conf 9</b>	<b>Conf 10</b>	<b>Conf 11</b>	<b>Conf 12</b>	<b>Conf 13</b>
$\lambda$ ( $\mu\text{m}$ )	0.39-0.50	0.70-1.00	0.41-0.54	0.56-0.69	0.69-0.83	0.86-0.99
Notes			g-band	r-band	i-band	z-band
-10 °C	19.9	16.4	14.1	14.1	15.3	18.6
+8 °C	17.0	17.0	13.7	15.7	15.9	17.7
+25 °C	16.3	20.5	16.2	19.8	20.5	21.6

**Table 7. Worst RMS Image Diameter (in  $\mu\text{m}$ ) at any Field Angle or Wavelength (on-axis Binospec models)**

	<b>Conf 1</b>	<b>Conf 2</b>	<b>Conf 3</b>	<b>Conf 4</b>	<b>Conf 5</b>	<b>Conf 6</b>	<b>Conf 7</b>
$\lambda$ ( $\mu\text{m}$ )	0.39-0.93	0.39-0.62	0.77-1.00	0.57-0.74	0.83-1.00	0.39-0.52	0.88-1.00
Notes	270 gpm	650 gpm	650 gpm	900 gpm	900 gpm	1200 gpm	1200 gpm
-10 °C	20.3	15.8	18.7	16.9	19.9	19.1	18.9
+8 °C	19.3	22.7	21.1	15.0	24.3	22.3	22.4
+25 °C	24.2	18.4	21.0	20.4	22.4	22.0	20.6

	<b>Conf 8</b>	<b>Conf 9</b>	<b>Conf 10</b>	<b>Conf 11</b>	<b>Conf 12</b>	<b>Conf 13</b>
$\lambda$ ( $\mu\text{m}$ )	0.39-0.50	0.70-1.00	0.41-0.54	0.56-0.69	0.69-0.83	0.86-0.99
Notes			g-band	r-band	i-band	z-band
-10 °C	19.5	20.3	15.1	19.3	19.6	20.1
+8 °C	21.5	18.5	19.5	19.9	20.8	21.5
+25 °C	19.0	22.9	15.6	22.5	22.3	23.2

## 1.6.4 Athermal Performance

### 1.6.4.1 Focus Offsets

The goals of the athermal optical design were to maintain excellent image quality (and constant focus) across wavelength and temperature and to maintain constant imaging scale through the spectrograph optics. The tables below give an indication of how well we achieved the design goals. Note that the reference focal position is arbitrary, only the relative offsets have significance. Table 8 lists the focus offsets determined by examining the best focus for each of the thirteen configurations. The results indicate that if the optics are fabricated perfectly, we understand the thermal performance of all the spectrograph materials perfectly, and the optics are isothermal, we would need a total focus range of 71  $\mu\text{m}$ .

**Table 8. Focus Offsets ( $\mu\text{m}$ )**

	<b>Conf 1</b>	<b>Conf 2</b>	<b>Conf 3</b>	<b>Conf 4</b>	<b>Conf 5</b>	<b>Conf 6</b>	<b>Conf 7</b>
$\lambda$ ( $\mu\text{m}$ )	0.39-0.93	0.39-0.62	0.77-1.00	0.57-0.74	0.83-1.00	0.39-0.52	0.88-1.00
Notes	270 gpm	650 gpm	650 gpm	900 gpm	900 gpm	1200 gpm	1200 gpm
-10 °C	-48	-56	-51	-64	-56	-51	-51
+8 °C	-58	-64	-38	-64	-41	-66	-66
+25 °C	-36	-51	-13	-38	-13	-51	-18

	Conf 8	Conf 9	Conf 10	Conf 11	Conf 12	Conf 13
$\lambda$ ( $\mu\text{m}$ )	0.39-0.50	0.70-1.00	0.41-0.54	0.56-0.69	0.69-0.83	0.86-0.99
Notes			g-band	r-band	i-band	z-band
-10 °C	-48	-38	-74	-71	-48	-46
+8 °C	-66	-36	-81	-64	-36	-33
+25 °C	-56	-8	-66	-38	-10	-10

### 1.6.5 Thermally Induced Image Shifts

One of the key optical design goals was to maintain a constant magnification with temperature. Prior to the athermal redesign of Binospec, the scale change was ~one pixel per degree C. Table 9 indicates that the current athermal design maintains a constant scale.

**Table 9. Worst Thermal Image Shifts in the field corners by configuration (in  $\mu\text{m}$ )**

	Wavelength ( $\mu\text{m}$ )	Notes	+25 °C to +8 °C	-10 °C to +8 °C
Configuration 1	0.39-0.93	270 gpm	2.0	3.9
Configuration 2	0.39-0.62	650 gpm	1.4	3.8
Configuration 3	0.77-1.00	650 gpm	2.5	1.6
Configuration 4	0.57-0.74	900 gpm	2.4	1.3
Configuration 5	0.83-1.00	900 gpm	3.0	1.9
Configuration 6	0.39-0.52	1200 gpm	1.5	4.5
Configuration 7	0.88-1.00	1200 gpm	2.3	1.8
Configuration 8	0.39-0.50	blue imaging	0.4	0.7
Configuration 9	0.70-1.00	red imaging	1.6	1.4
Configuration 10	0.41-0.54	g'-band	0.6	0.6
Configuration 11	0.56-0.69	r'-band	1.3	1.3
Configuration 12	0.69-0.83	i'-band	1.4	1.6
Configuration 13	0.86-0.99	z'-band	1.3	2.1

### 1.6.6 Ghost Image Studies

The Binospec design has been checked for ghost images. The worst ghost images are from the two sides of the filter. The filter is 5 mm thick, so the filter ghost is out of focus by 10 mm. At f/5, this image is ~2 mm in diameter, and is about 10 magnitudes fainter than the original image. The remaining ghosts are larger in diameter. A summary of the ghost image analysis is given in an October 30, 2002 memo entitled [Binospec\\_Construction\\_Design\\_Ghost\\_Images.pdf](#).

## 1.7 Project Team

Principal Investigator	Daniel Fabricant
Project Engineer	Robert Fata
Project Manager	Leslie Feldman
Electronic Lead Engineer	Tom Gauron
Mechanical Lead Engineer	Mark Mueller
Structural Lead Engineer	Robert Fata
Software Lead Engineer	John Roll
Lead Designer	Jack Barberis
Structural Engineers	Vladimir Kradinov, Henry Bergner
Optical Materials Testing and Optics Assembly	Joe Zajac
CCD Electronics and CCD Procurement	John Geary
Thermal Analysis	Warren Brown
Optical Analysis, Flexure Control, Calibration	Deborah Freedman Woods

## 1.8 Binospec Status as of December 2007 Review

### 1.8.1 Overview

In writing this document over more than a year, we have reviewed our solutions to key technical challenges and attempted to address any open issues in the instrument design. Such a process is never 100% complete until the instrument is delivered and commissioned, but we have attempted a fairly rigorous approach to the internal design review process. We are now ready to hear from reviewers with fresh eyes from outside the project.

### 1.8.2 Optics Status

The six aspheric lenses and the twelve calcium fluoride lens have been completed and their glass-air surfaces have been antireflection coated. The optical designs for both of Binospec's beams have been reoptimized to account for the deviations of the as-built surfaces from the construction optical design. All of the lens blanks have been procured and the optical designs reflect the melt sheet data for the delivered blanks.

### 1.8.3 Mechanical Design

The complete Binospec mechanical design is captured on a detailed 3D CAD model that is ~95% complete. We will machine all parts from conventional 2D drawings. Currently, ~50% of the 2D drawings for the mechanisms and 20% of the 2D drawings for the optical mounts have been completed.

#### **1.8.4 Electrical Design**

The system level electrical design and the system architecture are ~90% complete, and prototypes of critical circuits that require new design have been tested. The board level design is incomplete, and no cable drawings or board layouts have been produced.

#### **1.8.5 Software Design**

Almost all of the low level software to control hardware and communicate with the PMAC motion controller has been developed and extensively tested on earlier instruments. We have begun to design high level GUIs that would be used to control the instrument at the telescope, based on our experience with earlier instruments. Most of the mid-level code and scripts remain to be written.

## 2 Scientific Requirements

### 2.1 Operating Environment

#### 2.1.1 Seasonal Temperature Range

Figure 5 is a plot of end of the night temperatures at the MMT for a period of six years in the 90's. Data was obtained most nights when the telescope was active.

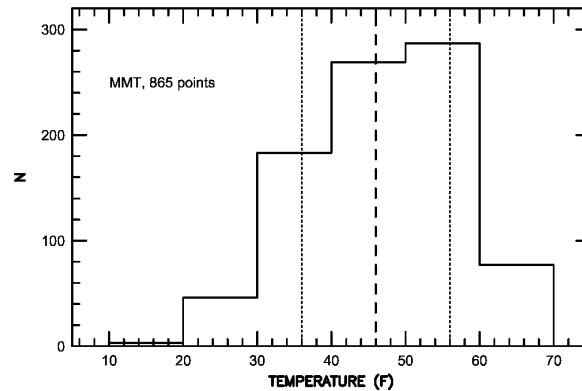


**Figure 5. MMT night time temperature obtained at the end of the night on those nights when the telescope was open for observing during six years in the 1990s. The mean temperature is 46 °F (8 °C) with a standard deviation of 10 °F (5.6 °C).**

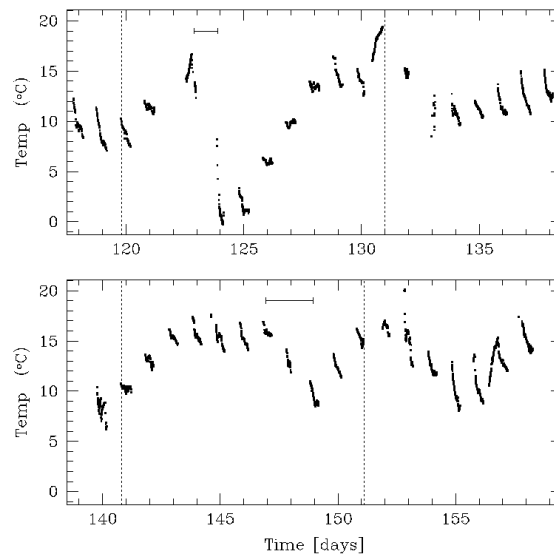


**Figure 6. MMT dome temperatures between 27 April and 6 June 2001. The dotted lines show the time intervals we used for the extreme (upper panel) and moderate (lower panel) boundary conditions. The temperature gradients are a factor of two worse for the extreme conditions.**

### 2.1.2 Short Term Temperature Changes

The short term MMT thermal environment has been less well analyzed, although a several year data record from the converted MMT now exists. Early on, we examined plots of temperatures recorded between 27 April and 6 June 2001 to identify periods of “moderate” and “extreme” temperature changes as input for our thermal models (see Figure 6).

Both of these periods show temperature changes noticeably larger than the typical diurnal cycle of  $\sim 4$  °C. The “moderate” thermal environment has ambient temperature changes as large as 14 °F (8 °C) over 48 hours. The “extreme” thermal environment has ambient temperature changes as large as 31 °F (17 °C) in 24 hours. Examination of the temperature histogram (Figure 5) and our experience observing at the MMT suggest that the extreme environment must be unusual.

### 2.2 Telescope Envelope and Instrument Mass Constraints

The MMT accepts only Cassegrain instruments mounted to a 72 inch rotator bearing. Critical clearances are shown in Figure 7 and Figure 8. The horizontal span between the two telescope drive arcs on either side of the instrument volume is 175 inches.

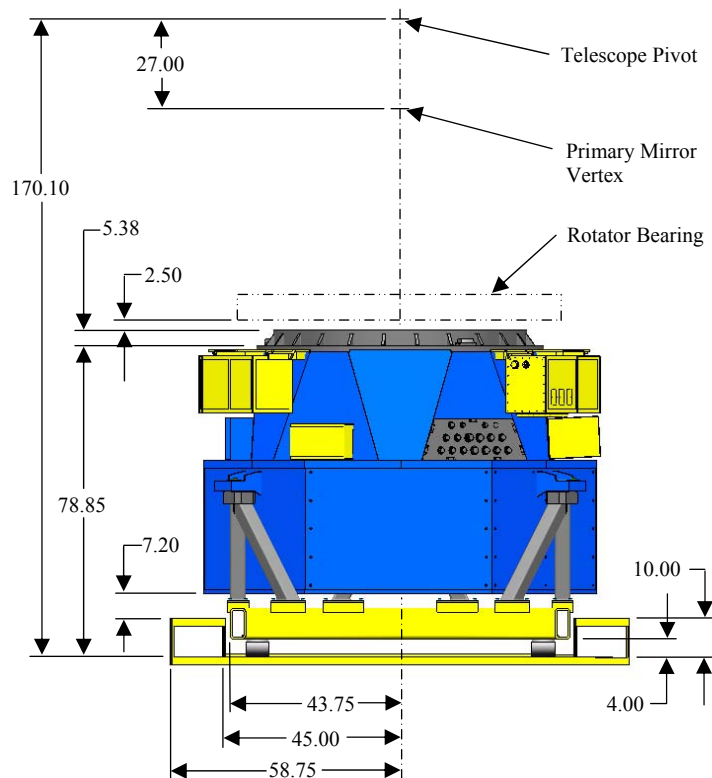
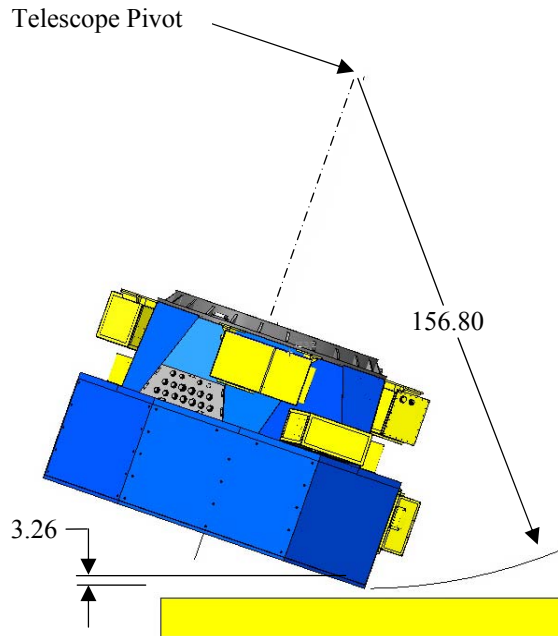


Figure 7. Critical dimensions for mounting Binospec



**Figure 8. Side view of Binospec on the MMT showing allowed swing clearance.**

Binospec weighs ~6000 lbs with a center of gravity 30.0 inches below the instrument mounting flange, yielding a maximum overturning moment of 15000 ft-lbs. Reducing the Binospec weight would require accepting larger gravitational flexure. We contracted Simpson Gumpertz and Heger (SG&H) to analyze the MMT telescope for the Binospec loads, which are larger than with current instruments. Their results show that there is no significant optical or structural degradation of the MMT optical support structure or instrument rotator resulting from the increased Binospec weight. The full SG&H report is in a memo by Frank Kan dated April 12, 2006. We summarize the SG&H results in Table 10.

**Table 10 Displacements and rotations relative to the optical axis (Z= -70.67 in.)**

Load Case	$\Delta Z$ shift	$\Delta Y$ shift	$\Theta X$ Rotation
Gravity Zenith Pointing	-.0049 in.		13.9 $\mu\text{rad}^1$
Gravity Horizon Pointing		-.0029 in.	-49.0 $\mu\text{rad}^2$

<sup>1</sup> This tilt results in a  $\pm 0.0002$  in. defocus at the edge of the full 24 in. dia. focal surface.

<sup>2</sup> This tilt results in a  $\pm 0.0006$  in. defocus at the edge of the full 24 in. dia. focal surface.

The maximum stress levels in the instrument rotator and OSS near the rotator are low: 1.3 ksi and 2.5 ksi respectively. SG&H consulted with Avon Bearing to evaluate the rotator bearing with the Binospec loads. Avon Bearing show the increased weight is not a problem for the rotator bearing. The minimum safety factor on the static loading is 6.5 and the minimum safety factor on theoretical stress limit is 12.4. The theoretical life of

the rotator bearing run at 4 rpm continuously with the Binospec loads applied is 235,700 hours. There appears to be no significant optical or structural degradation of the MMT OSS or the instrument rotator resulting from the increased Binospec loads. However, additional counterweights must be added to balance the MMT with Binospec mounted.

### 2.3 Interface Connections

In order to simplify the mounting and dismounting of Binospec on the MMT, we are adopting the strategy that the only wiring and plumbing connections between the instrument and the outside world are power, ethernet, compressed air and coolant.

### 2.4 Science and Flexure Control CCDs

#### 2.4.1 Science CCD

The package dimensions for the 4096 by 4096 E2V CCD231-84 devices are shown in Figure 9. These devices have 15  $\mu\text{m}$  square pixels. We use one science CCD per beam.

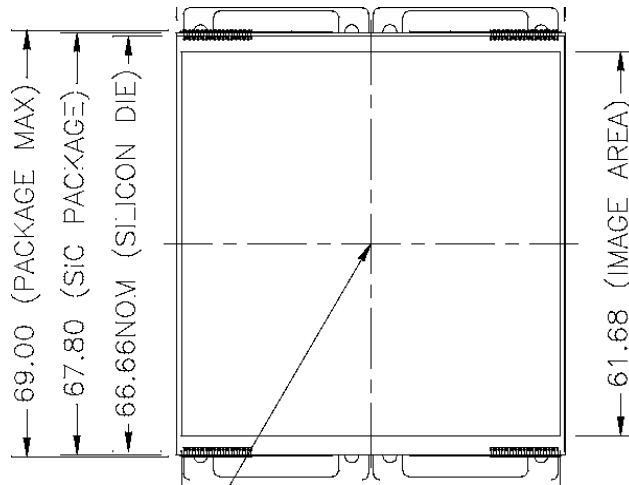


Figure 9. E2V CCD 231-84. 4096 x 4096 pixels 15 $\mu\text{m}$  square.

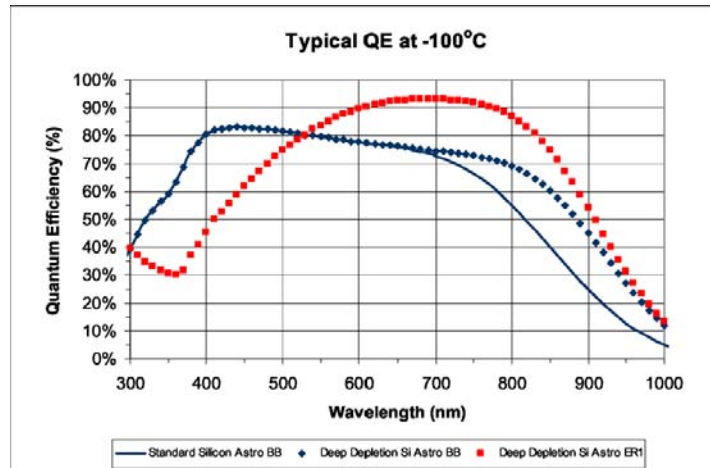


Figure 10. Available quantum efficiency curves for CCD 231-84. We intend to use deep depletion devices with QE plotted as blue diamonds.

Available quantum efficiency curves for the CCD231-84 are shown in Figure 10 for standard silicon and for deep depletion silicon with two different antireflection coatings. We intend to use deep depletion devices with a broad band antireflection coating.

### 2.4.2 Flexure Control CCDs

The 512 by 2048 flexure control CCDs are type E2V CCD42-10 devices in a custom package as shown in Figure 11 to allow close butting to the science CCD. These devices have 15  $\mu\text{m}$  square pixels and have a quantum efficiency curve as shown in Figure 10 for the standard depletion devices.

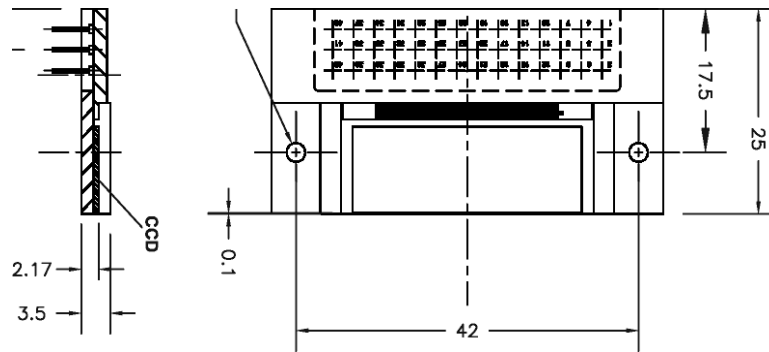


Figure 11. Custom packaged E2V CCD41-10 devices for flexure control.

### 2.4.3 CCD Controller Electronics

Control electronics systems for both the two 4096 x 4096 science CCDs and the four 512 x 2048 flexure-control CCDs are based on a proven design that has extensive heritage at SAO, from single CCD imagers such as Keplercam up to the very large 72-channel Megacam. These controllers interface to the data acquisition computer(s) via a duplex fiber-optic cable for both control commands and streaming serial data. The bandwidth of the data link is much greater than any Binospec requirement. Separate, asynchronous controllers will be provided, one dedicated to the science imagers and the other dedicated to the flexure-control imagers. All video channels for both science and flexure-control imagers will feature low-noise preamplifiers mounted on the hermetic connectors of the dewars, providing a fully-differential output to the video processors that can be located 2-3 meters away.

### 2.4.4 Science CCD Controller

Each of the two 4K X 4K science imagers has four output ports, so this controller will be configured with a total of eight video channels. The controller will allow either CCD to be read out separately, or both simultaneously. For best noise performance, the imagers will be read out at approximately 100 kHz pixel rate, giving a readout time (unbinned) of about 42 seconds, and about half this time if binning X 2 in the parallel register can be used. During integration, charge may be dithered in position in the column direction in order to smooth out interpixel response variations and thus increase photometric accuracy.



may be more difficult. We have elected to provide active flexure compensation in Binospec, implemented much like the DEIMOS system.

### 2.5.2 Flexure Control Implementation

Flexure corrections, including focus and tip/tilt, are to be provided by five axis positioning of the science detector. The selected PI piezo stage provides a travel range of 0.020 inches (500  $\mu\text{m}$ ) in each of the two in-plane axes, and 0.059 inches (1.5 mm) for focus. Zemax modeling predicts that between -10  $^{\circ}\text{C}$  and +25  $^{\circ}\text{C}$  (14  $^{\circ}\text{F}$  and 77 $^{\circ}\text{F}$ ) and over a wide range of grating and filter choices, we will need 0.0028 inches (70  $\mu\text{m}$ ) of focus travel. We expect a focus range of 0.0042 inches (110  $\mu\text{m}$ ) due to flexure, giving a total focus travel requirement of 0.007 inches (180  $\mu\text{m}$ ). The flexure in each of the other two orthogonal axes (image motion) is expected to be  $\sim$ 0.005 inches (130  $\mu\text{m}$ ). The flexure control CCDs are mounted on the same frame as the 4096 by 4096 science CCDs for each channel to eliminate relative flexure. Because the flexure control system must operate with dispersed light, the flexure control CCDs are placed so that their long axis is in the direction of dispersion, as close as practical to the science CCDs as shown in Figure 11.

We will inject light into Binospec's collimator behind the slit mask with 100  $\mu\text{m}$  core diameter optical fibers to track all sources of flexure following the slit mask. It is not practical to inject the flexure control light through the slit mask, because the through-the-slit guiders block the focal surface for a considerable distance at the ends of the slit mask. We inject the light 5.616' off axis in X (centered on the Binospec slit masks in their narrow, spectral direction, and 9.6' off-axis in Y. At the focus of the MMT, this corresponds to an off axis position (X,Y) = (2.214, 3.788) inches. The fiber should be aimed to match the angle of the chief ray from the MMT with the spectroscopic wide field corrector at this point: tipped 0.466 $^{\circ}$  about the Y-axis and 0.796 $^{\circ}$  about the X-axis. These angles only need to be held to  $\sim\pm 0.3^{\circ}$ , and it is better to err in the direction of less tilt rather than more. It would probably be prudent to machine the assembly flat and put the angle in with shims. The chief ray from the telescope is normal to a concave surface facing upwards. The flexure control fiber will be imaged 1.398 inches (35.51 mm) off axis in the spatial direction and on axis in the dispersion direction in the imaging mode. This point will be  $\sim$ 0.76 mm from the edge of the flexure control CCD in its short direction.

The flexure control light box includes a set of three pen-ray spectral lamps chosen to provide a set of spectral lines appropriate for a wide variety of grating central wavelengths (see Table 11 and Table 12). The pen-ray lamps are fed into a 6 inch diameter integrating sphere. The output of the integrating sphere is placed at the entrance pupil of an achromatic doublet lens to produce a uniformly illuminated f/8 beam. The optical fibers carry the light to the focal surface. We choose a beam slower than that produced by the telescope to minimize the impact of the flexure control system on the size of the periscope fold mirrors in the collimator as well as the filters.

Two filter wheels hold band pass filters to select only the desired spectral line(s), and neutral density filters to reduce the light level to the minimum required for accurate

measurement of the calibration spot position. A shutter is provided to pass light only when the FCS detector is integrating without cycling power to the lamps constantly. The band pass filters and shutter minimize the stray light reaching the science detector.

**Table 11. Potential Binospec grating configurations and available spectral lines. Three Oriel pen-ray lamps (Hg(Ar), Kr, Ne) are sufficient. Bright lines well separated from adjacent lines are chosen.**

Configuration	Blue Limit (nm)	Red Limit (nm)	Line (nm)
1	390.0	931.2	Ar 696.54
2	390.0	619.7	Hg 546.07
3	765.6	1000.0	Kr 877.87
4	571.8	741.2	Ar 696.54
5	830.6	1000.0	Ar 912.30
6	390.0	516.1	Hg 435.84
7	877.1	1000.0	Ar 912.30
8	390.0	500.0	Hg 435.84
9	700.0	1000.0	Kr 877.87

**Table 12. Pen-ray spectral lines sorted by wavelength with the appropriate band-pass filters.**

Target wavelength (nm)	Line (nm)	Filter Source	Filter model	Filter center (nm)	Filter FWHM (nm)
400	Hg 435.84	Asahi	YBPA436	436	10
450	Hg 435.84	Asahi	YBPA436	436	10
500	none	none	none	none	none
550	Hg 546.07	Asahi	YBPA546	546	10
600	Ne 594	Asahi	ZBPB082	590	40
650	Ne 650.65	Asahi	YBPA650	650	12
700	Ar 696.54	Asahi	ZBPB142	690	40
750	Ar 763.51	CVI Laser	F10-765.0-4	765	10
800	Ar 794.82	CVI Laser	F10-794.7-4	795	10
850	Ar 842.4	CVI Laser Newport	F40-850.0-4 S10-840-R	850 840	40 13
900	Ar 912.3	CVI Laser Newport	F40-900.0-4 S10-910-S	900 910	40 10
950	Ar 965.79	CVI Laser	F40-950.0-4	950	40

The spectral lines from the same type of Oriel pen-ray lamps in consideration for the calibration source have been examined with Hectospec. The Hectospec data verify that the chosen lines have adequate intensity and are not blended.

### 2.5.3 Required Flexure Control Spot Intensity

Correction for image motion at the focal plane depends on deriving an accurate centroid from the calibration spot. The lowest intensity light source that achieves accurate centroiding goal should be used in order to minimize stray light in the system. We have modeled the accuracy of spot centroid determination taking into account a realistic fiber image profile (scaled from Hectospec), readout noise, and counting statistics.

We use the IRAF task **center** to find the coordinates of the fiber image. The task **center** determines the position by solving the equation,

$$\int (I - I_0) f(x - x_c) dx = 0$$

Where  $I$  = intensity at position  $x$ ,  $I_0$  = continuum intensity ( $I_0 = 0$  in the case of an emission feature), and  $x_c$  = the feature position. The function convolution function  $f(x)$  is a sawtooth. The equation is solved iteratively, starting from the initial guess. The center position,  $x_c$ , is determined when successive guesses agree within 0.1% of a pixel.



**Figure 13. Model calibration spots with 2.8 electrons RMS read noise and Poisson noise added to the image. The spots here have about 650 integrated counts.**

Table 13 shows the integrated counts required to achieve centroid accuracies between 0.03 and 0.1 pixels. For large numbers of counts, the effects of read noise become negligible, and the centroid accuracy should increase as the square root of the number of counts.

**Table 13. Centroid Accuracy in each of two orthogonal dimensions. The modeled profiles assumed 13.5  $\mu\text{m}$  pixels rather than the current 15  $\mu\text{m}$  pixels, but the differences should be minor.**

Accuracy (pixels)	Integrated Counts
0.1	565
0.05	1550
0.04	2300
0.033	3000

### 2.5.4 Flexure Control Performance

We plan to correct flexure by moving the smallest and lightest optical element in the spectrograph, namely the CCD detector. However, this will not perfectly correct flexure at all wavelengths and field angles due to distortion in the optics, index of refraction dependence on wavelength, etc. Our goal in implementing flexure control is to correct image motion to the subpixel level. Our early finite element models for the Binospec optics and structure suggested that we should expect about six pixels of flexure so that a

correction good to ~10% across field angles and wavelengths would be adequate. In fact, detailed modeling with ZEMAX show that this is the approximate level of correction that we can expect. This is discussed in section 5.5.

## **2.6 Filters**

Binospec needs to accommodate at least six filters: g, r, i, and z, a clear filter (to maintain focus) and a spare slot for a user-selected filter such as an order-blocking filter. Seven or eight slots are desirable if space and weight constraints allow. The filters for Binospec's two beams may be deployed in pairs to save weight, space, and complexity. The position repeatability requirement for the filters is not particularly stringent since the pupil size on the grating is 82 mm. However, it should be possible to achieve 100  $\mu\text{m}$  or better repeatability without much difficulty.

## **2.7 Slit Masks**

A minimum of ten slit masks (each covering both Binospec beams) should be loaded at one time. The space and weight implications of a larger number of masks should be investigated. Repeatability of slit mask placement is more important than absolute placement accuracy. To allow the possibility of advance calibration during the daytime, the slit mask placement should repeat to 4  $\mu\text{m}$  (0.025", equivalent to 0.1 pixel at the detector) or better.

The f/5 spectroscopic focal surface of the MMT is a hyperboloid of revolution. It would be inconvenient to manufacture slit masks in this geometry, so we approximate this shape with two tipped, cylindrical surfaces for the two Binospec channels. The slit masks are curved about their short axis ( $R=-177.0$  inches) and tipped  $0.841^\circ$  about their long axis as documented in Section 11.1.

## **2.8 Gratings**

Binospec should accommodate three gratings and a fold mirror for imaging in each of its two beams. The grating mount and rotary stage are potentially the biggest contributors to instrument motion due to flexure, with a sensitivity of 4 microns of image motion at the detector per arcsecond of unwanted tip or tilt.

The commanded grating motion raises interlocking issues of accuracy, precision, and repeatability. If the grating stage is continuously powered, the control dead band and repeatability threshold is at least as large as the encoder resolution, and the positioning jitter will directly affect the image quality. If the servo motor is turned off, a very low backlash brake is required at the minimum, and if advance calibration is to be possible, a very repeatable brake is required.

The encoder resolution for the grating rotation should be at least 0.1", better is desirable. If at all possible repeatability of the grating positioning should be 0.3" (corresponding to 0.1 pixel of image motion) or better.

## 2.9 Calibration System

The spectrograph should be light tight to allow calibration during the daytime. A dark hatch near the mounting flange will be necessary. We will include internal HeNeAr hollow cathode lamps and continuum lamps to illuminate a screen on the back of the dark hatch. Pupil masking at the grating will reject most of the unwanted light falling outside the natural illumination of the  $f/5$  telescope beam to allow reasonably accurate flatfielding and wavelength calibration. The MMT is already equipped with a dome screen for external wavelength calibration and flat fields.

The calibration system is a separate set of lamps mounted in an integrating sphere that is used to perform wavelength and flat calibration of the science detectors. The integrating sphere produces a uniformly illuminated output beam that is baffled and folded to illuminate a rear projection screen. The system is shown in Figure 14. With uniform illumination of the pupil, Binospec will be able to take calibration images without relying on the telescope dome screens and light sources, enabling more efficient calibration measurements throughout the night of observing.

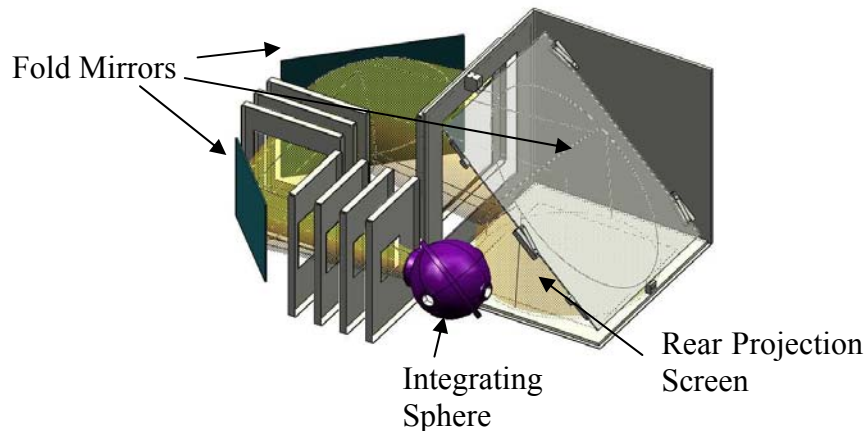


**Figure 14. Calibration system fed with light emanating from an integrating sphere (purple, at center). The light is baffled and folded three times before striking a rear projection screen.**

Using lab measurements and Zemax modeling of the calibration system, we estimate the integration time that will be required for obtaining wavelength calibration data. Our goal is to have at least 500 counts in the blue spectral lines that are generally the faintest lines. Lab measurements of a Helium-Neon-Argon (HeNeAr) hollow cathode lamp with a calibrated spectrograph allow us to measure the relative strengths of the spectral lines; measurements of the HeNeAr lamp with a calibrated diode and bandpass filters provide a measure of the absolute intensity of the spectral lines. We created a Zemax model of the calibration system, including the integrating sphere, fold mirrors, scattering screen, and baffles to determine what fraction of the lamp's initial light output is incident on the slitmask within angles corresponding to an  $f/5$  light beam. We assume that a 1" square region is used for acquiring the calibration data, and account for the spectrograph efficiency, CCD efficiency, and reflectivity of the fold mirrors, and transmission of the rear projection screen. We estimate that the integration time required to obtain 500 counts in a representative spectral line is 5.5 sec, quite acceptable.

## 2.10 Guiders and Wavefront Sensing

Normal guiding with slit masks will be accomplished by viewing guide stars with two cooled CCD guide cameras through 10-20" holes drilled at opposite ends of the slit masks. Field acquisition over a larger field is accomplished with the slit mask removed. A third guide camera does double duty: a movable mirror allows the camera to view a small pickoff mirror positioned on the optical axis of the telescope, or a similar small mirror mounted on the long slits used for single or extended object work. All three guide cameras have fields of view of 80" by 80".

Continuous wavefront sensing is carried with a dedicated Shack-Hartmann instrument that can view a strip of 7.1' by 21.3' at the edge of the slit mask. The "CfA" guide cameras that we intend to use for Binospec are based on the Carnegie/Magellan guiders but with different packaging. The overall dimensions of the camera housing, exclusive of connectors and coolant loop, are 3.2 inches (wide) by 1.82 inches (thick) by 4.7 inches (long). Steward Observatory has developed a similar design. The CfA guider uses an updated version of the Carnegie electronics boards modified with an optical fiber data interface.

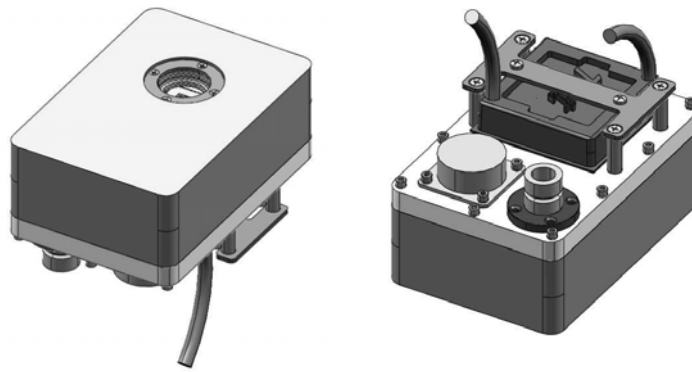


**Figure 15. Guider package in front and back views. The back of the device has an electrical connector (lower left), a pumping port (lower right), and a heat exchanger (upper center). We will not use the liquid heat exchanger with Binospec, but will couple the camera's heat to the internal structure.**

The CCD that we intend to use in the guiders is the same as that used in the Carnegie/Magellan guiders, the E2V CCD47-20, a 2048 by 1024 CCD with 13  $\mu\text{m}$  pixels, arranged in a 1024 by 1024 frame transfer geometry. The active area of the device is 13.3 by 13.3 mm. At the focal plane scale of the MMT,  $0.167 \text{ mm arcsec}^{-1}$ , this format corresponds to 80" by 80".

### 2.10.1 Wave Front Sensing

Due to instrument weight constraints and space conflicts with Binospec's calibration system, we are not planning to mount the existing 300 kg general-purpose wave front sensor with Binospec. We provide an internal wave front sensor to allow continuous off-axis wave front sensing. (The existing wave front sensor can only be used in interrupt mode.) The wave front sensing optics already used in the general-purpose f/5 wave front

sensor are adaptable to Binospec. We need to form a pupil that is smaller than the format of the guide camera; a pupil in the 8 to 10 mm diameter range is near optimal.

A lenslet pitch of 0.6 mm gives a pattern of 13 by 13 spots (8 mm pupil) to 16 by 16 spots (10 mm pupil). The Adaptive Optics Associates catalog of standard lenslet arrays does not have a large selection, so the 0600-40-S array used in the existing f/5 wave front sensor seems to be a good choice. It is a square format array and can be supplied on 25 by 25 mm, 1 mm thick glass substrate. When coupled with a 40 to 50 mm focal length collimator, this lenslet array performs well.

### 2.10.2 Guider Optics Dimensions (calculated 5.62' off-axis)

Table 14. Guider optics dimensions

Distance from focus	Beam Diameter to image 13.3 by 13.3 mm patch
10 mm	20.9 mm
20 mm	22.8 mm
50 mm	28.6 mm
75 mm	33.4 mm
100 mm	38.3 mm
150 mm	48.0 mm
200 mm	57.7 mm
250 mm	67.5 mm
300 mm	77.3 mm

### 2.11 Access and Service Issues

Good access to as many mechanical and electronic parts of the instrument while it is mounted to the telescope is a design priority. However, we know that we need convenient access for changing the slit mask cassette, the filters, and gratings. The slit mask cassette will normally be changed each day for the following night's observing. Filter and grating changes will be less frequent, but require care design to avoid endangering these expensive parts.

### 2.12 Reconfiguration Times

Table 15. Maximum reconfiguration times.

Operation	Maximum reconfiguration time (seconds)

Exchange grating and rotate to commanded position	30
Rotate grating to new setting	10
Exchange slit mask	15
Exchange filter	15
Configure guide stages	15
Open or close dark hatch	15
Focus or offset CCDs in plane	0.1

## 2.13 Thermal Requirements

### 2.13.1 Introduction

At the 1998 SPIE meeting on astronomical instrumentation we presented an optical design for Binospec that met almost all of our design goals, with one important exception: athermalization. Careful consideration of how temperature changes affect optical performance is good practice in general, but is particularly important for Binospec because the MMT's thermal environment is relatively demanding: the mean temperature is 8 °C with an RMS dispersion of  $\pm 6$  °C and extremum night time temperatures of -10 °C and +20 °C are encountered (see Figure 6). Refractive optics are thermally sensitive: the optical powers of the lenses are affected by their thermal expansion and thermally-dependent refractive indices, and lens spacings vary due to the thermal expansion of the lens and cell materials.

We discovered that the 1998 optical design was unacceptably thermally sensitive, with a temperature-dependent lateral magnification that resulted in image shifts of one pixel ( $\sim 15$   $\mu\text{m}$ ) per °C at the edges of the field, and unacceptable image quality at the extremum temperatures. In order to athermalize the Binospec optics, Epps and Fabricant developed a new technique using weak coupling fluid lenses formed in the existing coupling fluid-filled gaps within multiplets. The large variation of the coupling fluid's refractive index with temperature is used to compensate the thermal changes in the lenses and cell. This technique is described in detail in the attached PASP paper by Epps and Fabricant.

The coupling-fluid athermalization technique of Epps and Fabricant assumes that temperature changes are slow enough so that at any given time the optics are isothermal. To investigate the expected thermal gradients within Binospec, Brown, Fabricant, and Boyd constructed thermal models of Binospec. (See PASP and SPIE papers attached). Fortunately, the expected thermal gradients are quite small; under typical conditions the axial and radial gradients within the lenses will be less than 0.15 °C and lens group-to-group temperature differences will be less than 0.5 °C. Epps and Fabricant have checked that these gradients and temperature differences have little effect on the optical performance of Binospec.

We have undertaken a detailed thermal analysis of Binospec to guide its design and to assess its expected level of thermal response to environmental changes. Our goal is to minimize temperature gradients and transients by using passive techniques to increase the thermal time constant of the system. We did not adopt active thermal control because we believe that it is difficult to apply heat without creating temperature gradients.

### 2.13.2 Thermal Analysis Techniques

Our approach to the thermal analysis relies on a mixture of coarse and detailed models. In brief, we begin our analysis by calculating thermal time constants to understand the scale of temperature variations in the instrument and to determine what areas of the instrument require detailed modeling. We generate a low-resolution finite difference thermal model

of the entire spectrograph, and high-resolution models of thermally sensitive sub-assemblies. We use temperature data recorded at the MMT to set the boundary conditions for the models. While some details of Binospec have changed since the thermal models were made, the large-scale structure and mass distribution remain the same. Refer to the Binospec thermal Analysis memos for the details of models.

### 2.13.3 Thermal Requirement: Insulate the Spectrograph

Temperature gradients in Binospec can be minimized if all the internal parts are designed to have short time constants, but this is difficult in practice because the internal parts (especially large refractive optics) have significant mass. Instead, *we recommend that Binospec be heavily insulated* to reduce the amplitude and time scale of temperature gradients. Image quality is maintained if thermally induced de-focus and image drift are insignificant over the ~1 hr time scale of a single observation.

Binospec should be insulated with continuous panels, sealed to prevent air infiltration. Binospec has a large surface area (>20 m<sup>2</sup>) like many modern astronomical instruments. To help us select the appropriate quantity of insulation, Table 16 displays the time constant of the optical bench and the maximum temperature gradients in the lens groups for different thicknesses of Owens Corning Foamular 150 foam insulation. To minimize temperature gradients in the optics to the level of ~0.1°C, foam insulation with an R-value per inch of 5 and at least 2 inches thick is required.

Owens Corning Foamular 150 is an extruded polystyrene foam with an R-value per inch of 5.0 (Hr ft<sup>2</sup> °F BTU<sup>-1</sup>). Polyisocyanurate foams have better thermal conductivities (Elfoam P200 foam insulation has an R-value per inch of 5.4), but polyisocyanurates absorb an order of magnitude more water vapor by volume and their thermal properties degrade by ~20% over 5 years, unlike extruded polystyrene foam. Polyisocyanurates are also brittle, dusty, and denser than extruded polystyrene, all of which are undesirable physical properties for Binospec. Thus we recommend insulating with an extruded polystyrene foam such as Foamular 150 ( $\rho = 1.5 \text{ lb ft}^{-3}$ ).

**Table 16. Insulation thickness sets the time constant of Binospec’s optical bench and the maximum radial and axial temperature gradients in its lens groups. Foamular 150 insulation has an R value per inch of 5.0.**

<b>Insulation Thickness</b> (inches)	<b>Optical Bench Time Constant</b> (hrs)	<b>max <math>\Delta T_{\text{radial}}</math></b> (°C)	<b>max <math>\Delta T_{\text{axial}}</math></b> (°C)
0.5	12	0.22	0.21
1.0	20	0.17	0.17
2.0	33	0.13	0.14
3.0	44	0.11	0.12

Binospec's optical bench should be thermally isolated from the MMT mounting flange. In our baseline thermal model, 30% of the peak heat flux between the environment and the spectrograph flowed through the graphite-epoxy A-frame struts connecting the optical bench to the mounting flange. The current Binospec design solves this problem by using stainless steel struts with lower conductivity and four times smaller cross-sectional area than the earlier graphite epoxy struts. We recommend that the struts and strut interface blocks be lightly insulated to mitigate convective and radiative heat flux.

Binospec should have an entrance window. The entrance window insulates the instrument from the environment and protects the instrument from dust. If the entrance window is removed from our baseline thermal model, the temperature gradients in the optics are increased by a factor of 1.7 (from  $\sim 0.1$  °C to  $\sim 0.17$  °C).

#### 2.13.4 Thermal Design Requirement: Minimize Internal Heat Sources

We want to minimize heat sources inside the spectrograph, because the greatest source of heat flow will dominate the thermal effects in Binospec. Motors are not a major issue because their duty cycle is at most 3% for all plausible modes of operation, and it is impractical to move them outside the insulated volume in any case. We should minimize all internal heat sources that we can control, by choosing low power dissipation components and, wherever possible, turning off components when not in use.

We recommend that stepper motors cycled on/off near sensitive optical elements (like the gratings) be attached with thermal stands-offs. When on, stepper motors are very large ( $\sim 20$  W) transient heat sources that will cause localized mechanical deflections. This can be mitigated with a 0.25 inch thick Delrin pad as shown in Figure 16. The Delrin pad reduces heat conduction by a factor of  $\sim 3$ , allowing radiation and convection to distribute the heat more evenly around the spectrograph. Any hot motor with a direct line-of-sight to an optical element should also have a radiation shield (see Figure 16).

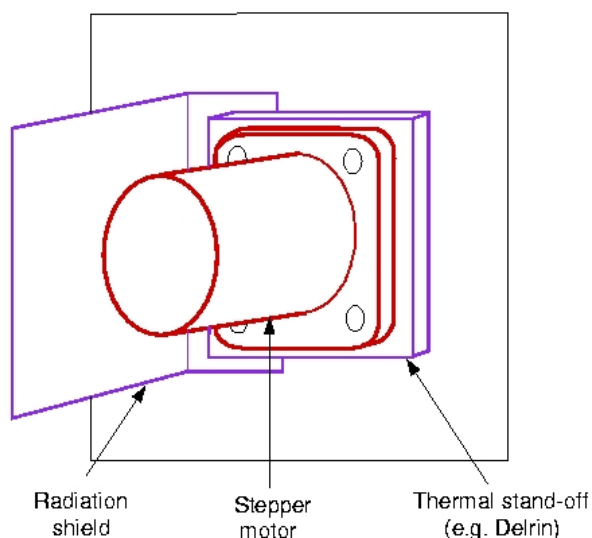


Figure 16. An example motor mounted with a thermal stand-off and radiation shield.

### **2.13.5 Thermal Requirement: Electronic Box Heat Exchangers**

To preserve the local seeing in the telescope dome it is important to minimize heat losses into the dome. Binospec's electronics boxes dissipate ~800 W, and must be liquid cooled. All electronics boxes should contain a liquid-to-air heat exchanger plus fan. Cold plates are more efficient and should be used where practical. However, most components like circuit boards must be air-cooled. Designing an effective air circulation path is therefore very important. Internal components must run below their maximum rated temperatures 45 – 50 °C for an ambient temperature of 20 °C, and the components equilibrate 10 – 20 °C above the interior air temperature. Thus we recommend heat exchangers rated to keep air internal temperature no more than 5 - 10 °C above ambient.

We also recommend that all electronics boxes have 0.5–1 inch thick Foamular 150 insulation or equivalent. The boxes must be sealed against air infiltration; otherwise, heat will escape into the environment and defeat the heat exchangers and cold plates. Our goal is to allow less than 100 watts of heat dissipation from all sources into the dome.

### **2.13.6 Thermal Requirement: Increasing Convection**

Increasing the efficacy of convection inside Binospec can help equilibrate its components, reducing temperature gradients. For example, the thermal deflection of the Binospec optical bench is largely caused by the difference in temperature above and below the optical bench. The optical bench would have 50% smaller (~0.05 °C) temperature gradients in our baseline model if the air temperatures above and below the optical bench are identical.

Thus we recommend that allowance be made for air pathways through, or around, the optical bench to connect the upper and lower compartments. We do not believe that fans are a good tool to increase convection because fans may be a significant internal heat source and thus drive larger temperature gradients than they alleviate. Instead, we are interested in passive means to equilibrate temperatures inside the instrument.

We recommend placing ventilation holes in the lens barrel covers. The Binospec lens groups tend to have large ~0.5 °C temperature differences, in part because the middle lens groups are protected from convective and radiative heat flow with the rest of the instrument by the lens barrel covers. Our thermal model suggests that ventilation holes in the lens barrels may reduce the lens group temperature differences by 20% (from ~0.5 °C to ~0.4 °C).

### **2.13.7 Thermal Requirement: Minimize Coupling Fluid Thickness**

We also investigate how the coupling fluid will affect the thermal characteristics of a lens group. The coupling fluid used in Binospec, Cargille Laser Liquid 5610, is an excellent insulator ( $k=0.147 \text{ W m}^{-1} \text{ K}^{-1}$ ) and will tend to thermally isolate the lenses in a lens group. If we double the thickness of the coupling fluid layers in the camera, which contains the majority of the “thick” ~4 mm fluid layers, our model predict that temperature gradients increase by 10% to 20%. We conclude that the coupling fluid

layers should be kept smaller than  $\sim 5$  mm in the Binospec optics to keep temperature gradients at a minimum.

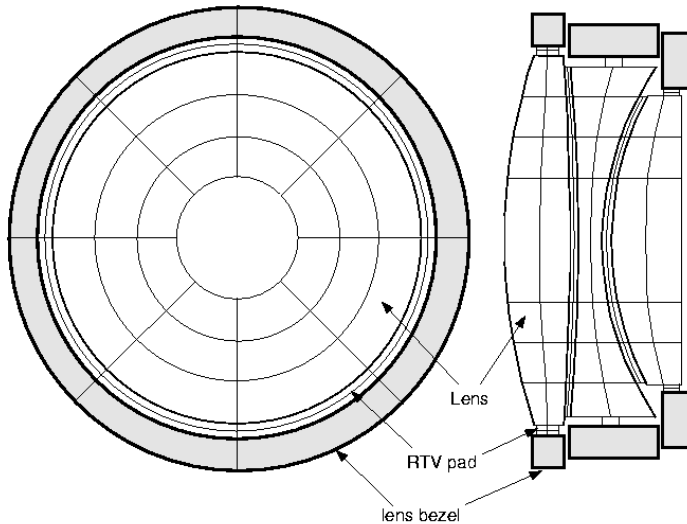


**Figure 17.** Our thermal model of Binospec camera lens group 3. Each optical element is divided into multiple axial, radial, and angular slices. Spaces between the lenses and the lens bezels are exaggerated to show the coupling fluid layers and the RTV bonds.

## 2.14 Optics Sensitivity Summary and Image Quality Goals

One of the key mechanical design goals for Binospec is to minimize image motion at the detector due to gravitational flexure of Binospec's optics. We can make a few general comments about the image motion arising from optical elements: (1) centration and tilts of glass-air surfaces are considerably more critical than glass-fluid surfaces, (2) decenters of steeply curved elements close to collimated light are the most harmful, and (3) grating stability is crucial. A complete element by element sensitivity summary is given in Section 11.3.

We set our overall goals for image blur from optics fabrication, instrument flexure, misalignment, and mount induced deformations in reference to the image of a 0.75" slit at the detector. With an anamorphic demagnification of 1.3, and a pixel scale of 0.24" per pixel, this slit is imaged onto 2.4 pixels, corresponding to 36  $\mu\text{m}$ . The intrinsic RMS image diameter produced by perfect optics, exactly as described in the optical prescription, is typically one pixel, or 15  $\mu\text{m}$ . Adding 36  $\mu\text{m}$  and 15  $\mu\text{m}$  in quadrature, we get 39  $\mu\text{m}$ , or an additional blur of  $\sim 8\%$  due to "perfect" optics. If we allow an error budget for all additional sources of blur of 10  $\mu\text{m}$ , and add this term in quadrature to the slit width and "perfect" optics blur, we get a final image width of 40.3  $\mu\text{m}$ , 12% larger than the original 36  $\mu\text{m}$ . We adopt 10  $\mu\text{m}$  as our goal for the added blur diameter due to all causes.

## 2.15 Optics Fabrication Errors

There are a variety of optics fabrication errors that can degrade the image quality of the perfect system on the computer. Our goal is to control these errors so that they are negligible in the final system. Potential error sources include errors in the radii of curvature of the spherical lenses, errors in the aspheric shapes for the three aspheric lenses in each beam, surface irregularities, and inhomogeneous substrates. Since we are aligning the lens to each other using the optical surfaces, geometrical tolerances of the lenses don't contribute. The aspheric lenses are a potential exception except that they were manufactured accurately, and the opposite face is quite insensitive because it is fluid-coupled. We expect that the only sizable contribution to image blur will arise from slope errors on the aspheric lenses.

**Table 17. Summary of Lens Manufacturing Contributions to Image Blur.**

<b>Error Source</b>	<b>Specification or Comments</b>	<b>Expected Contribution to Image Blur Diameter (<math>\mu\text{m}</math>)</b>
Spherical Radii of Curvature	Errors accurately quantified and image blur essentially eliminated by reoptimization of optical design	negligible
Aspheric Prescription	Errors accurately quantified and image blur essentially eliminated by reoptimization of optical design	negligible
Spherical Surface Irregularity	Essentially diffraction limited. Spec is $1/6 \lambda$ surface over test place, comparable to pupil size.	negligible
Aspheric Surface Slope Errors	$5 \times 10^{-6}$ radians in transmitted wavefront. Negligible for collimator lens 1; Collimator lens 8 and Camera lens 1 contribute.	4.7
Surface Roughness	$< 30 \text{ \AA}$ RMS	Very small amount of wide angle scatter
Inhomogeneous Substrates	Essentially diffraction limited. Glass blanks have homogeneity of $\pm 2 \times 10^{-6}$ , $\text{CaF}_2$ blanks have homogeneity of $\pm 3 \times 10^{-6}$	negligible

## 2.16 Clear Apertures and System Geometry Documents

The system geometry and clear apertures are given in a series of memos listed in Table 18.

**Table 18. System geometry and clear aperture memos.**

<b>File Name</b>	<b>Use For</b>	<b>Date</b>
prescrip_p24_020907av_102506ae.txt	Lenses, System Geometry	03/14/07
prescrip_p24_021107ac_102606aj.txt		03/14/07
Beam_Footprints_Collimator_Fold_Mirror.pdf	Collimator Fold Mirrors	04/18/07
Binospec_Beam_Footprint_Near_Grating.pdf	Grating Area	08/23/06
Slit_Mask_Geometry.pdf	Slit Mask Bkgd	12/01/06
Clear_Ap_Binospec_above_focus.pdf	Slit Mask, WFS	04/04/06
Calibration_Screen_Clear_Apertures.pdf	Calibration System	08/01/07

## 2.17 Software Requirements

### 2.17.1 Introduction

This section outlines the procedures that are required to operate Binospec. Two basic types of procedures are described, high level operating procedures and low level mechanical procedures. Operating procedures are used to obtain scientific data while mechanical procedures are required for instrument setup and maintenance.

### 2.17.2 Target Field Acquisition and Guiding

Field acquisition and guiding are fundamental to the successful operation of a multiobject spectrograph. We have a good deal of experience in operating Hectospec with procedures very similar to those required for Binospec. The steps in this procedure are given in the following list. The telescope pointing is normally good enough that steps 1-4 are unnecessary, but they are required as a back-up.

#### **Check Telescope Pointing**

1. Point to a bright star near the field.
2. Deploy the single object guider to the center of the field.
3. View the star in the single object guider and correct the telescope pointing.
4. Stow the single object guider.

#### **Set-up Guiding**

5. Offset to the target field coordinates and position angle.
6. Move the guide cameras to their expected positions.

7. View the guide stars on the guide cameras. The guide stars should be near previously recorded guide star expected positions.
8. Start guiding on the guide stars to center the masks on the field.
9. Pause guiding
10. Insert the slit mask.
11. Update guide hole reference.
12. Confirm that the guide stars remain visible after the masks are in place
13. Resume guiding.
14. Verify that a star is on the WFS and start the WFS.

If the guide star alignment holes have been elongated to accommodate either the IFU or the nod and shuffle mode, the initial guide star centroid will be obtained from an adjacent guide star alignment hole.

### **2.17.3 Slit Mask Design and Generation**

Slit masks for the instrument will be designed using a modified version of the software that was developed for IMACS.

We require software to design and produce slit masks for several types of observations. The mask design program should allow the user to select and fit a catalog of user targets onto the available mask area. The software should allow the global optimization of multiple masks to most efficiently observe the selected catalog. The slit width, height and unused area above and below each slitlet should be user specified.

The mask design program will identify available guide stars from those provided in the user catalog. The program will choose a guide star and specify a guide alignment hole position for the mask generation program. The user will be able to specify a number of arc seconds that the guide alignment hole is to be elongated in either the spatial or spectral direction to allow special IFU and Nod and Shuffle observing modes. When the guide alignment hole is elongated the mask program will specify a second “offset guide alignment” hole position to allow the guide star centroid to be accurately determined during the field acquisition procedure.

The mask design program will identify a star suitable for use in the wave front sensor from the user catalog. The program will write the coordinates of the candidate WFS star along with the coordinates of the guide stars and the selected targets into an additional data file to be used by the software during observation setup and data reduction.

### **2.17.4 Spectrograph Setup and Calibration**

Each afternoon before observing begins several calibration files must be obtained. Each slit mask that will be used during the night must be inserted into the focal plane for calibration. Wavelength and flat field calibration images will be taken using the calibration lamp system. The guide cameras will be positioned under the guide holes of the slit mask to allow preliminary registration of the guide reference holes.

### **2.17.5 Flexure Control**

The flexure control system for Binospec will correct image shifts and focus changes during an observation, and will allow locking the image position to daytime calibration images. Two flexure control CCDs on either side of the science CCD will obtain images of fiducial fibers that are illuminated by wavelength calibration sources. The light from these fibers travels the entire optical path of the instrument and is dispersed onto the flexure control CCDs. A single line is selected with filters. The positions of these images can be used to directly measure instrument flexure and the science/flexure control CCD assembly will be moved to compensate.

### **2.17.6 Grating Angle Acquisition**

The spectrograph grating angle must be able to be set to bring a desired range of wavelengths into the CCD camera. Using the flexure control system Binospec will be able to preset the desired grating angle and the desired wavelength coverage.

### **2.17.7 Telescope Focus**

The telescope focus is managed by the wave front sensor (WFS) system. Computation and actual correction of the primary deformations and secondary position are handled by the MMT facility. The instrument must provide WFS images to the telescope's analysis system. Additional focus and aberration compensation based on the position of the WFS star will need to be provided since off axis images from Binospec will have some inherent aberration. Focus information will be extracted from the guide star images by the Binospec guiding software and sent to the telescope as guide focus offsets.

### **2.17.8 Spectrograph Focus**

The spectrograph focus will be maintained by the flexure control system. This is accomplished by placing one of the flexure control fibers slightly ahead of focus and one slightly after focus. The FWHM of these images on the flexure control chips will be used to maintain the focus of images on the science chip.

### **2.17.9 Nod and Shuffle**

Nod and shuffle data taking is a form of beam switching adapted for multiple aperture spectroscopy with slitlets. Each aperture must have masked areas of width equal to the object aperture above and below the object aperture in the spatial direction. As originally proposed, an nod and shuffle integration is taken exposing 50% on the object and 50% on the sky. An observing sequence is as follows:

1. Expose on the object for **n** seconds.
2. Close the shutter and shift the charge up into the masked area.
3. Offset the telescope onto a sky region.
4. Expose on sky for **n** seconds.
5. Close the shutter and shift the charge down to the original position.
6. Repeat 1-5 an even number of times and readout.
7. Subtract sky from the object.

A full discussion is given in Glazebrook and Bland-Hawthorn 2001, *PASP*, **113**, 197. Currently, most observers use a modified version of this procedure to avoid losing 50% of the exposure time on the object. If a slitlet  $x$  arcseconds long is used, the telescope mount is used to nod by  $\sim x/3$  to  $x/2$  arcseconds, exposing alternately on two detector regions each  $x$  arcseconds long that are clocked between the physical slit and a blocked region on the slit mask. When the exposure is complete, the two  $x$  arcsecond-long regions are subtracted from each other, leaving a sky subtracted positive and negative spectrum that are then combined.

The software requirements are to coordinate the CCD shutter, offset commands to the telescope, and charge shifting on the CCD.

### **2.17.10 IFU Simulation**

We do not currently plan to build an integral field unit (IFU) for Binospec. However, we will provide software to allow precision stepping of the slit along the dispersion direction to build up a three dimensional data cube analogous to IFU observation. In this mode, the full 15 arcminute long slit is available, much longer than would be available with an IFU. However, unlike with an IFU, the data from all parts of the data cube are not simultaneous. The software requirements are limited to moving the guide box along the guide star track and choosing a guide star that can be tracked for the desired offsets.

The guide star “hole” will be extended along the stepped (spectral) direction to create a guiding slot. An additional guide registration hole will be created at a small offset from the start position of the guide slot. The position of this guide registration hole will be measured when the slit mask registration images are taken. Slit masks will be registered with the normal procedure, taking the small offset of the registration hole into account.

### **2.17.11 Slit Mask Installation**

Slit masks will be individually inserted into the slit mask cassette through an instrument port during the daytime. A switch located near the mask insertion port allows the operator to obtain local control of the slit mask cassette selection mechanism, locking out remote control from other interfaces in the spectrograph software. When this switch is activated, a push button will move the cassette to the next mask location. When the desired set of masks is inserted into the cassette, control is returned to the remote software. The filled slit mask cassette will be scanned with a barcode reader, allowing the masks to be selected by name (bar code).

### **2.17.12 Slit Mask Selection**

The slit mask changer has a mask cassette containing multiple masks and an arm to deploy masks on the focal plane or return them to the mask cassette. The masks are held in the cassette when stowed by spring-loaded pins. The pins are released from the mask by pneumatic actuators before the loader arm moves a mask in or out of the cassette. When masks are initially loaded into the cassette the software will record which masks is in which cassette slot. In addition to the necessary axis limit switches the slit mask

assembly has several in position indicators to allow the motion control software to determine that the axes are at their desired positions before proceeding. An indicator at each end of the loader arm axis indicates that it has successfully reached the focal surface or the cassette load positions. An indicator on the cassette axis detects whether there is a mask in the currently selected slot. The logic of the mask selection procedure is as follows:

1. If there is a mask in the focal surface, move the mask cassette to its storage position. If no mask is in the focal surface, move the mask cassette to the “empty” slot, a cassette position where no mask can actually be stored, but which allows the mask puller arm to be moved to the load position. The mask puller arm is always in the retracted position except when changing masks. Motion of the cassette is locked out except when the mask puller arm is at an extreme of travel.
2. Pull the stow pins in the selected slot to allow the mask to be returned to the cassette. If this is the “empty” slot, there are no pins to pull.
3. Move the arm to the load position.
4. Return the mask stow pin to the lock position to hold the returning mask in place.
5. Move the cassette to the selected mask.
6. Pull the stow pins in the selected slot to allow the mask to be removed from the cassette.
7. Move the arm to the focal surface position.
8. Return the mask stow pin to the lock position.

### **2.17.13 Filter Insertion**

Filters are inserted into the filter holder cassette in a similar manner to that described above for slit masks. The filter changing mechanism is logically identical to the mask changer; the physical dimensions of the changer are different to accommodate the filter holders.

### **2.17.14 Filter Selection**

The filter selection mechanism is identical in its operation to the mask selection mechanism described above. Filters are held in a cassette and are selected one at a time by a loader arm to be deployed above the focal surface. Similar in-position and filter present indicators are available on the filter changer.

### **2.17.15 Grating Installation**

Gratings are inserted into the instrument in a manner which is similar to that used for filters and masks. The grating selection mechanism is slightly different and so the procedure differs in a few details.

### **2.17.16 Grating Selection**

The grating changer has a grating storage roundhouse, a turntable, and an arm to move the grating between the two. Gratings are held in the roundhouse by spring loaded pins. The pins are released by pneumatic actuators before the loader arm moves the grating in

or out of the roundhouse. Pneumatically actuated pins also hold the grating securely when it is deployed on the turntable. When gratings are initially loaded into the instrument the software will record which grating is stored in which roundhouse slot. In addition to the necessary axis limit switches there are switches to indicate which roundhouse slots are currently occupied and whether or not the turntable is occupied.

### 3 Instrument Overview

#### 3.1 Optical Layout

The mechanical design of Binospec is driven by the requirement to accommodate two beams of large optics. The optics are folded to provide maximum compactness. Periscope fold mirrors behind the slit mask spread the two beams to provide clearance between the two collimator housings. A third fold mirror within each collimator group shortens the instrument to allow it to fit underneath the MMT telescope (see Figure 18).

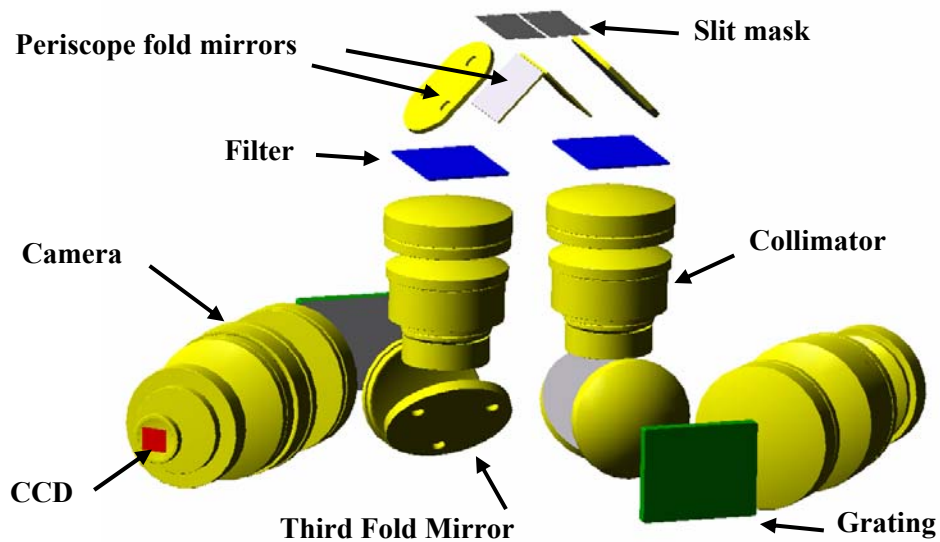
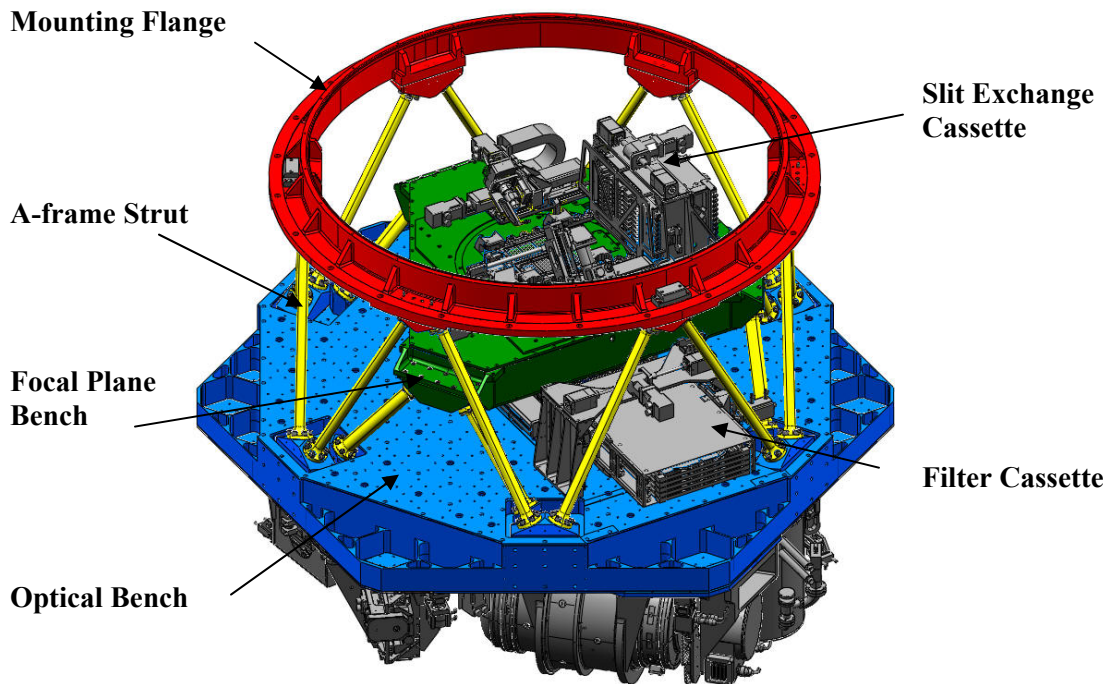


Figure 18. Binospec optical layout.

#### 3.2 Support Structure Overview

Binospec’s structure is comprised of four major components: 1) an instrument mounting flange, 2) an A-frame truss that connects the instrument to the mounting flange, 3) an optical bench that supports most of Binospec’s components, and 4) a focal plane bench that supports the slit mask assembly, the guiders, and the periscope fold mirrors. Figure 19 shows the Binospec structure.

The mounting flange is made from 400 series stainless steel for thermal expansion compatibility with the carbon steel telescope rotator flange, while eliminating the potential for corrosion. The outer A-frame truss members are made from 300 series stainless steel for its low thermal conductivity, to minimize conduction between the mounting flange and the optical bench. The inner truss and support benches are made from aluminum to meet the optical element spacing characteristics assumed in the athermalization of the optical design as well as to minimize the overall weight of the instrument.



**Figure 19. Binospec structure with covers removed.**

The optical bench is a closed-back honeycomb structure, approximately 90 inches in diameter and 8 inches thick. To minimize the relative motion between each optical assembly, all of the lenses, gratings, and science cameras mount directly to the bottom of the optical bench as shown in Figure 20. The focal plane bench is attached to the top of the optical bench with three A-frame truss members. The focal plane bench supports the slit mask mechanism, the guiders, the wave front sensor, the acquisition camera, and the periscope fold mirrors.

### **3.3 Mechanism Overview**

Binospec’s main mechanisms are a slit mask exchanger, a filter exchanger, and a grating exchanger as shown in Figure 19 and Figure 20. Binospec allows the user to exchange ten slit masks, six filters and four gratings. The control electronics are mounted in external boxes carried by the instrument.

The slit mask and filter mechanisms consist of a cassette assembly on a vertical stage to select a slit mask or filter and an actuator assembly that is used to move the selected item between storage and operating positions. The lightweight cassettes provide compact storage for these interchangeable parts. Variants of this design have been used in a number of previous instruments.

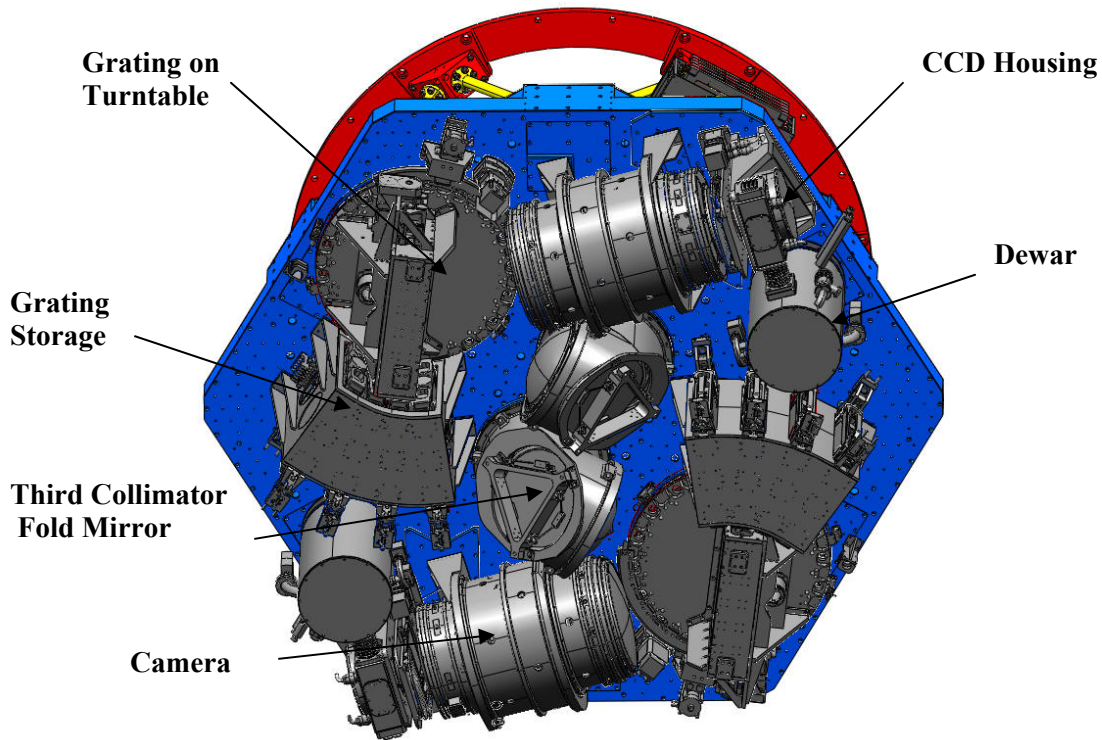


**Figure 20. View below Binospec’s optical bench.**

The grating exchange mechanism differs from the slit and filter mechanisms. We use a rotary turntable with fixed bulkheads for each stored grating (much like a locomotive roundhouse). The turntable provides the motion required to align gratings with the fixed storage positions as well as to set the precision grating tilt during operation, eliminating the need for a separate cassette stage.

Most of Binospec’s subsystems are modular, including the electronic enclosures, lens mounts, the slit mask, filter, and grating mechanisms as well as the science camera and calibration systems. This approach allows each assembly to be tested and debugged prior to integrating the completed unit with the instrument. For extensive repairs, these subsystems can be removed from the instrument, repaired offline and then reinstalled. This approach also gives us the option of assembling spare assemblies that can be readily swapped in the event of a failure to minimize the telescope downtime. We have provided good access to service motors, electronics and CCD cameras. These components are typically mounted near the outside of the instrument so that they can be tested or serviced through access covers.

### **3.4 Thermal Environment and Thermal Design**

We minimize thermal gradients within Binospec by enclosing it in insulated covers as shown in Figure 21. Wherever possible, heat sources are placed outside of the thermal

enclosure. Liquid cooling is used to remove heat from the electronics boxes mounted externally.

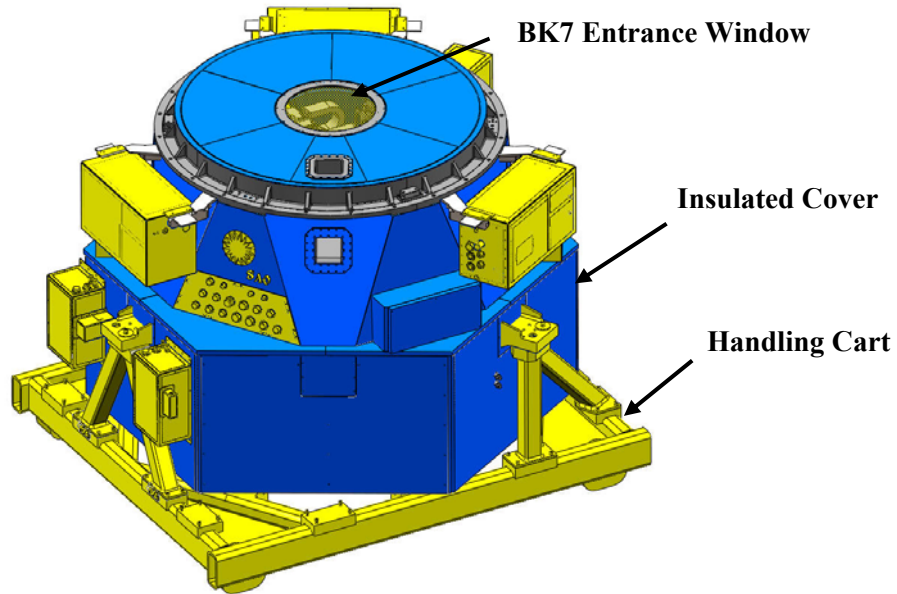


**Figure 21. Binospec on its support cart with insulated covers installed. Access to load slit masks, filters and gratings is gained by removing the appropriate panel or cover. A fused BK7 entrance window completes Binospec's thermal seal.**

The insulated covers contain a 2.0 inch extruded polystyrene foam core with an R value of  $\sim 10$ , providing a  $\sim 30$  hour thermal time constant.

Motors, encoders, limit switches, solenoid valves, temperature sensors, science cameras, and guide cameras must be inside the thermal enclosure. The guide cameras, encoders, dewar electronics, and the flexure control stage will be on continuously, but the motors and most feedback devices will run at a low duty cycle ( $\sim 2\%$ ). During normal operation the total estimated power of all heat sources inside the instrument thermal enclosure is  $\sim 27$  watts.

To promote convection and to help maintain a uniform temperature on both sides of and within the main optical bench, we provide  $\sim 82$  one inch diameter holes through the top and bottom face sheets of the optical bench. The collimator and camera lens housings are perforated for the same reason.

The support electronics, including motor drives, controllers, power supplies, calibration light sources, guider, flexure control, and CCD electronics, are mounted externally of the main insulated volume in separate thermal enclosures. The total heat generated by these components is  $\sim 785$  watts. Each electronics enclosure is insulated with 1 inch of extruded polystyrene foam with an R value of  $\sim 5$ . Heat is extracted using a combination of liquid-cooled cold plates and heat exchangers (with fans) mounted inside the electronics boxes. The coolant is a methanol-water mixture supplied by a NESLAB M75 chiller located about 30 feet above the chamber floor in the MMT loft.

### 3.5 Lens Mount Overview

The lens mounts went through two distinct rounds of development. Early on, we developed mounts that used a continuous ring of RTV to support the lenses. The advantages of this type of mount are well understood: ease of assembly, lower cost, straightforward athermalization and a convenient fluid seal. However, we discovered two serious defects of this design for our application. (1) The siloxane based LL5610 that we use to couple our multiplets interacts with the silicone based RTV, causing a large increase of LL5610's refractive index. The refractive index change would degrade the athermal optical performance. (2) It is difficult to achieve sufficient axial stiffness with the elastomeric mounts to reduce gravity and pressure head induced displacements and tilts of the lenses to acceptable levels. We therefore developed flexure mounts that provide very high axial stiffness while decoupling radial loads due to the differential thermal expansion of the lenses and bezels. The flexure mounts use Teflon fluid seals to contain the LL5610 fluid between the coupled multiplets.

The lens mount flexures have a tangent geometry with a rectangular cross-section. The flexures are an integral part of the bezel and are formed using electrical discharge machining. The integral design eliminates all hardware or entrapped air pockets inside the couplant volume and allows us to minimize the bezel diameter. Figure 22 shows a prototype bezel for collimator lens 8. The bezel (and flexure) material is heat treatable aluminum alloy 7050-T7451, chosen for its high yield strength (57 ksi), ultimate strength (75 ksi), good machinability, and availability in plates up to 6 inches thick.

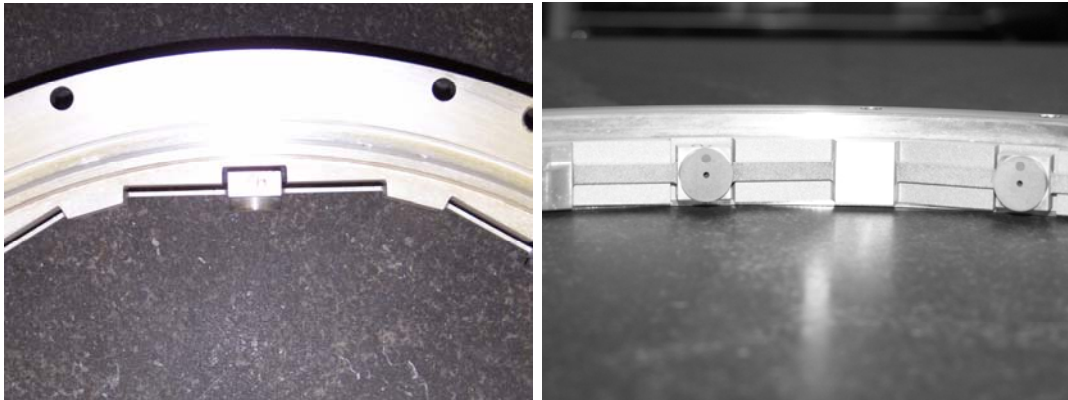


**Figure 22. Machined prototype bezel for collimator lens 8 showing the integral flexures. The nubs are pressed onto the flexure prior to electrical discharge machining.**

A circular nub is pressed in the middle of each flexure. After the lens is aligned to the bezel, Hysol 9313 epoxy, filled 80% by weight with Siltex 44, will be injected to bond the nub to the lens. The nominal bond thickness is 0.010 inches. The Siltex filler reduces the thermal expansion of the 9313 epoxy to about 16.2 ppm/°F without reducing the epoxy's strength. The nub material used for each lens has a thermal expansion closely matching the lens material (to 1 ppm/°F or better) to minimize thermally induced stresses at this bond interface. Figure 23 gives a detailed view of a lens, bezel, and coupling fluid seal.

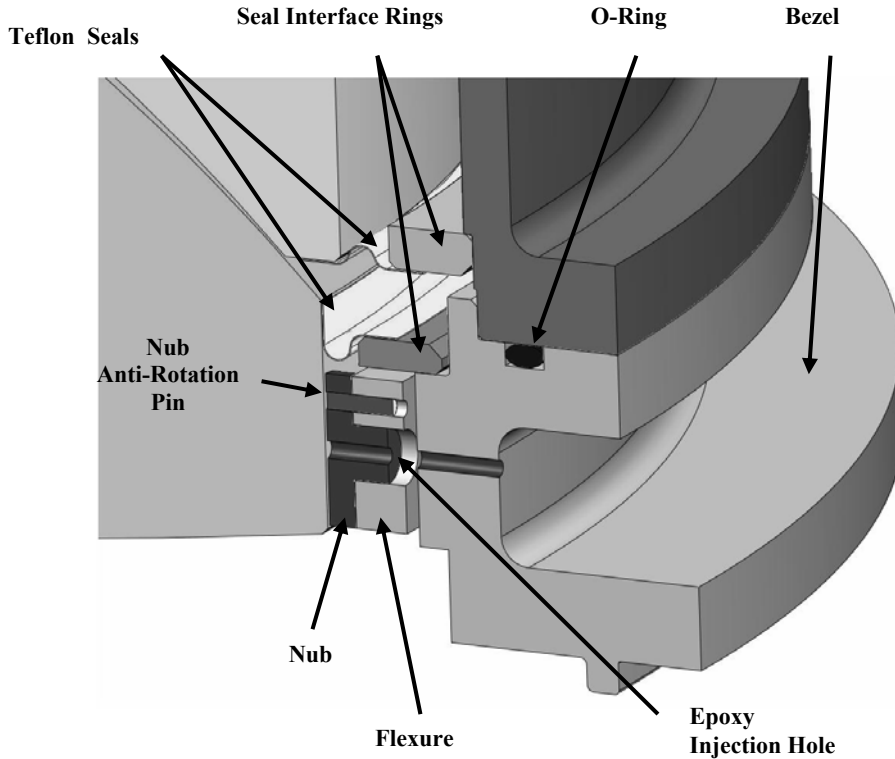


**Figure 23. A detailed view showing the lens, nub, O-ring and Teflon fluid seals.**

The collimator and camera lens assemblies are assembled from individual lens/bezel assemblies that bolt together as shown in Figure 24 and Figure 25. Precision pins are used to align the bezels to each other and O-ring seals retain the Cargille 5610 laser liquid between the coupled lens multipliers. Teflon seals will be bonded around the perimeter of the lens to a seal interface ring to retain the couplant fluid. The seal interface ring is a separate aluminum piece bonded to the bezel. In most cases, the seals will be located as close to the oil coupled surfaces as possible to minimize the required volume of fluid. Bladders to accommodate the thermal expansion of the coupling fluid are not shown. Two of the lenses (and their flexure mounts) in the collimator quintuplet are submerged in couplant because there is insufficient room to bond fluid seals onto these lenses.

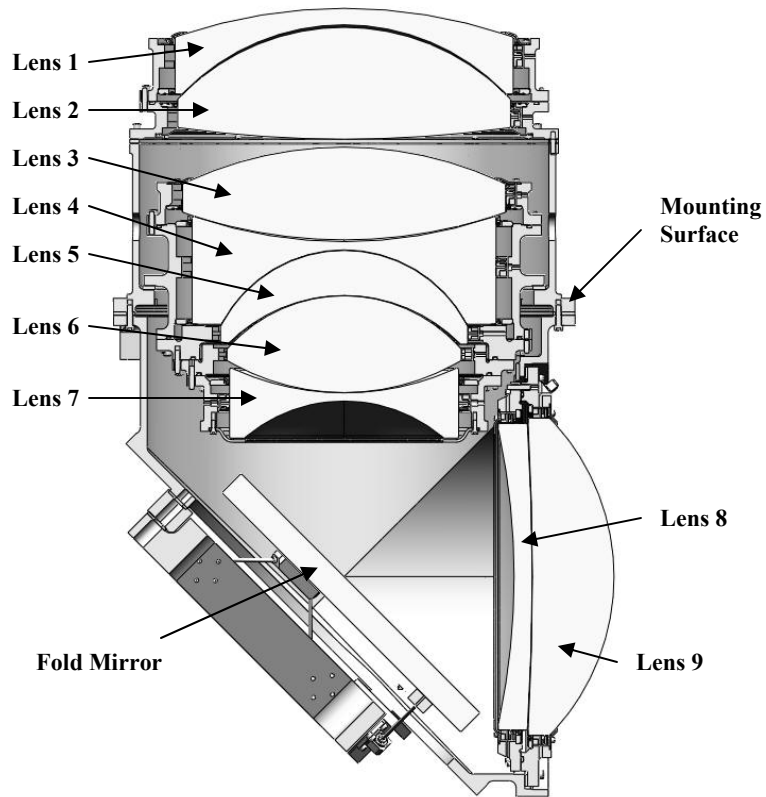


Figure 24. Cross-sectional view of collimator lens assembly.

Each main camera assembly contains nine lenses arranged in three groups as shown in Figure 25. The third group is a triplet with a central NaCl element. The fourth camera lens group is the field flattener/vacuum window for the science camera.

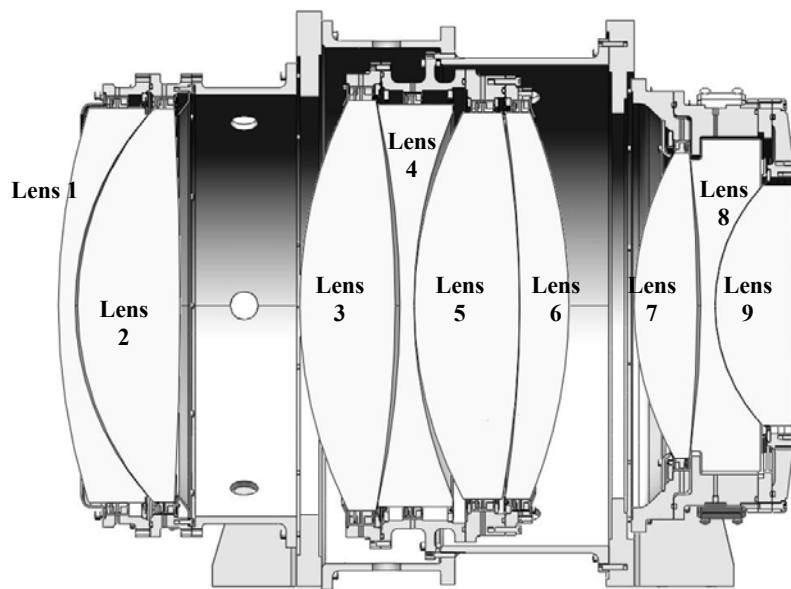
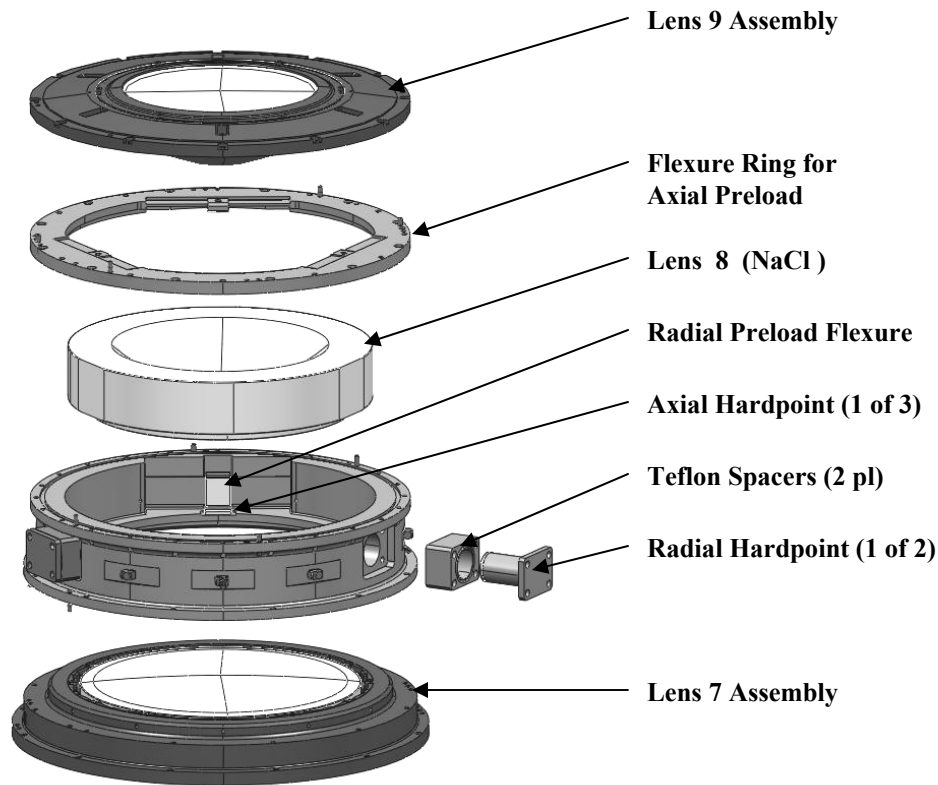


Figure 25. Cross-sectional view of the camera lens assembly



**Figure 26. View showing the camera lens triplet containing the NaCl lens mount. Flexures provide preload forces to the three axial and two radial hard points.**

The single NaCl lens (lens 8 in the camera) could not practically be mounted with bonded flexures while meeting our stress limit of 100 psi. The thermally induced stresses at an epoxy bond interface would likely fracture the lens. Consequently, there are no couplant seals bonded to this lens for the same reason. For the NaCl lens we have designed an alternate mount that uses flexures to apply preload forces against hard points. In the lateral direction, a single radial flexure is applied a 3g preload to the lens that is reacted by two radial hard points. To maintain the centration of the NaCl lens with respect to the bezel, the radial hard points are athermalized using pre-sized Teflon spacers. In the axial direction, a ring with three flexures provides a 3g preload to the lens and is reacted by three axial hard points. The NaCl lens is the center lens in the camera triplet so it is completely submerged in couplant. Figure 26 is a schematic of the camera lens triplet containing the NaCl lens.

### **3.6 System Electronics**

The Binospec systems electronics provide the precision motion control of all optical positioning stages, control of optical calibration sources and associated mechanisms, controlled AC and DC power for all instrument subsystems (including CCD camera electronics), control and data communications channels, and housekeeping telemetry. Figure 27 is a simplified electronics functional block diagram.

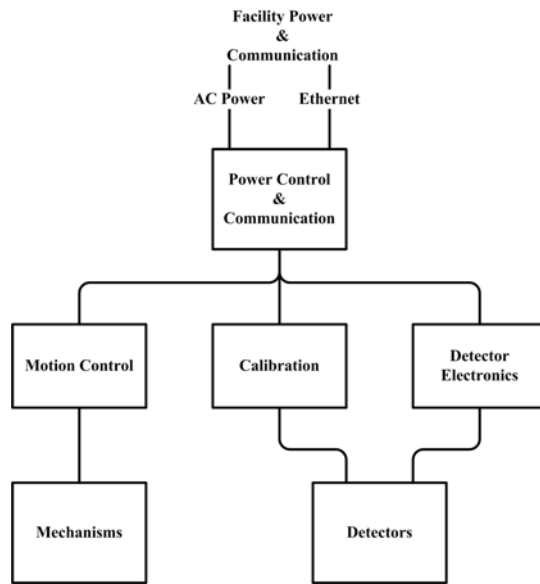


Figure 27. A simplified Binospec electronics block diagram.

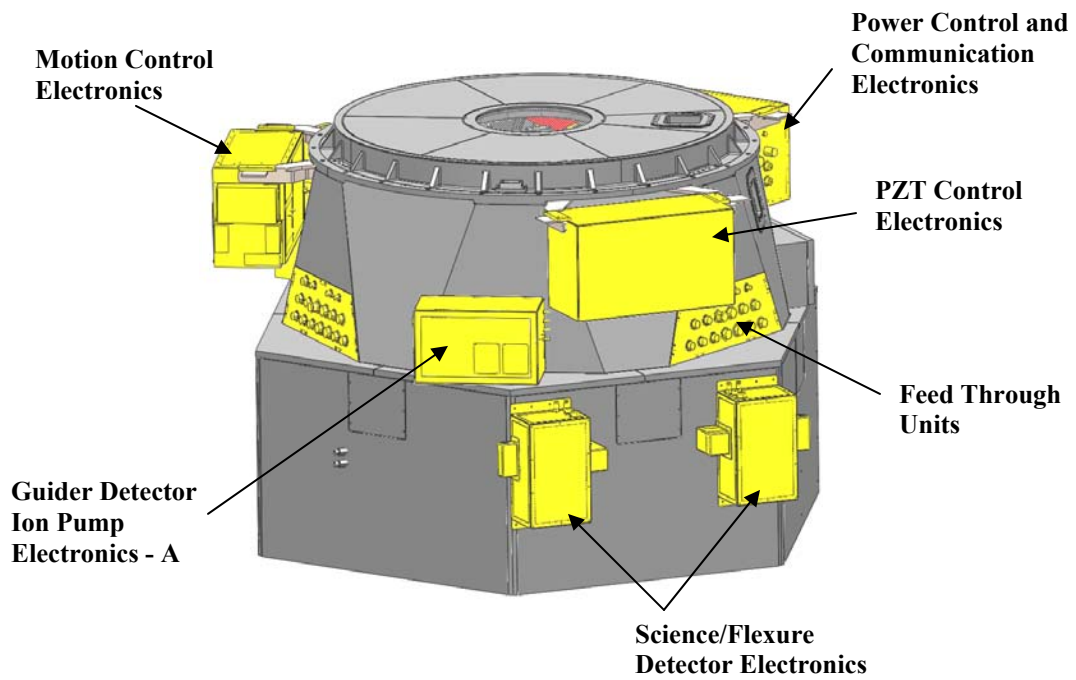
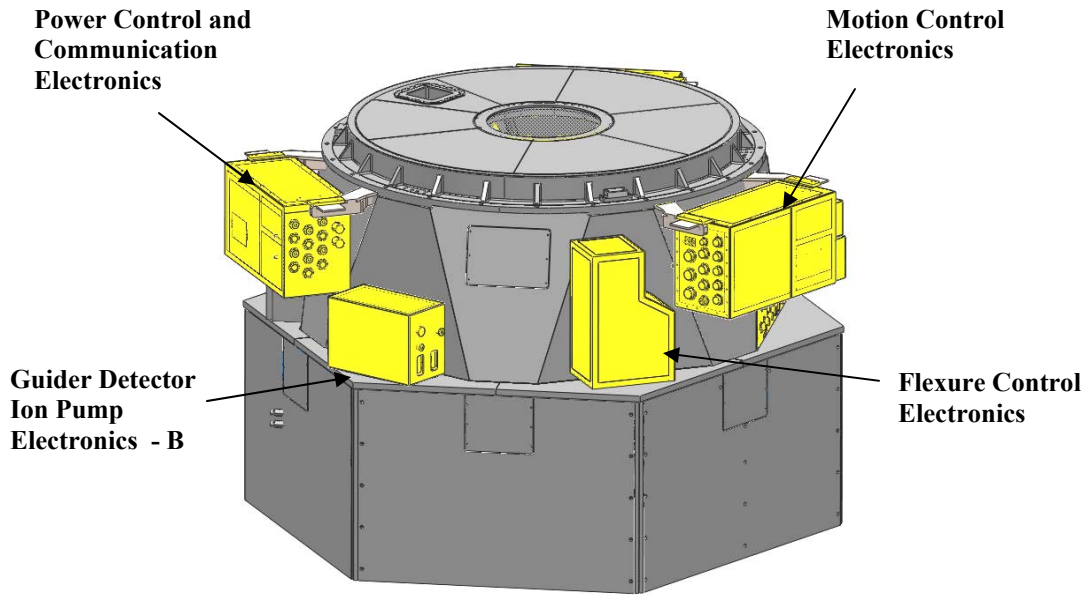


Figure 28. View of Binospec electronic assemblies from side A.



**Figure 29. View of Binospec electronic assemblies from side B**

The system electronics are packaged in subassemblies mounted on the outside structure of Binospec as shown in Figure 28 and Figure 29. Partitioning of these subassemblies was determined by function, size and weight limitations, cable length limitations, and servicing considerations.

### **3.7 Science and Flexure CCDs**

The science and flexure control CCDs are mounted to an Invar cold plate and cooled by LN<sub>2</sub> contained in an expanded Infrared Laboratories ND 10 dewar to allow a minimum hold time of 24 hours. The LN<sub>2</sub> tank as well as the fill and vent lines are outside of the thermal shroud to provide convenient fill access, to prevent spillover into the spectrograph, and to prevent local cooling of the optical bench. The CCD array is mounted on a 5-axis piezo-driven stage supplied by Physik Instrumente that is commanded to actively correct for gravity and thermal induced image motion, tip/tilt, and focus changes. This stage has a travel range of 0.020 inches (500 μm) in the lateral directions and .059 inches (1500 μm) in the focus direction.

### **3.8 Calibration System**

A retractable calibration screen and calibration light source is mounted directly above Binospec on the telescope rotator assembly (see Figure 30) to provide periodic wavelength calibration of the detector before or after an observation without repointing the telescope or closing the dome. The calibration system consists of a set of wavelength standard and continuum lamps in an integrating sphere with fold mirrors that illuminate a Spectralon-coated diffuse reflective screen. This subsystem also derotates the power cables, Ethernet cable, pneumatic air lines and coolant lines. The cables and lines will be routed through the primary mirror cell and enter the flexible e-chain through a hole in the central cone. During installation, the electrical, coolant and air connections will be made at the telescope cone end and where the cables enter through the top of Binospec.

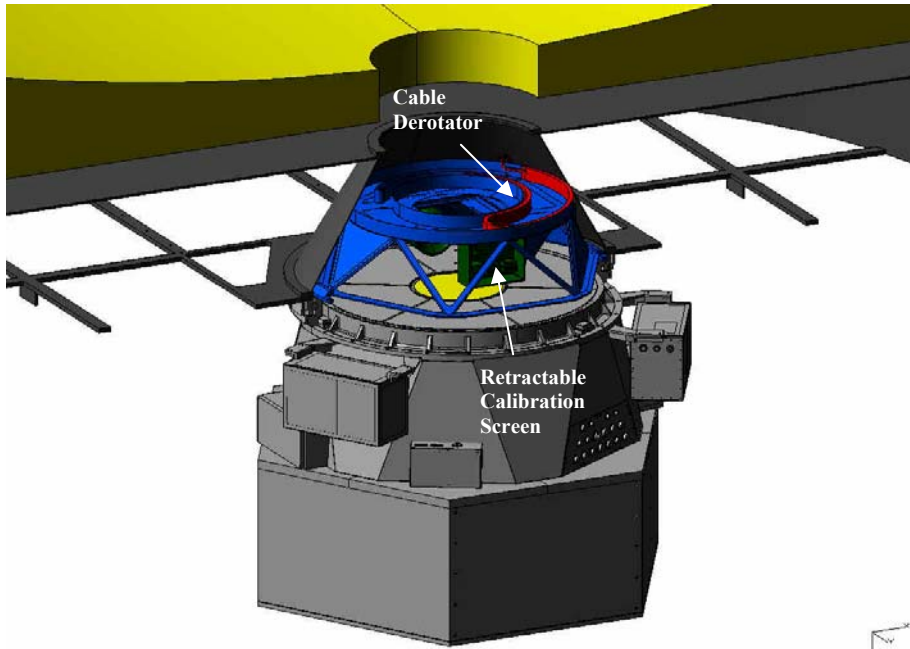


Figure 30. Binospec along with the retractable calibration screen/cable derotator mounted on the MMT rotator bearing.

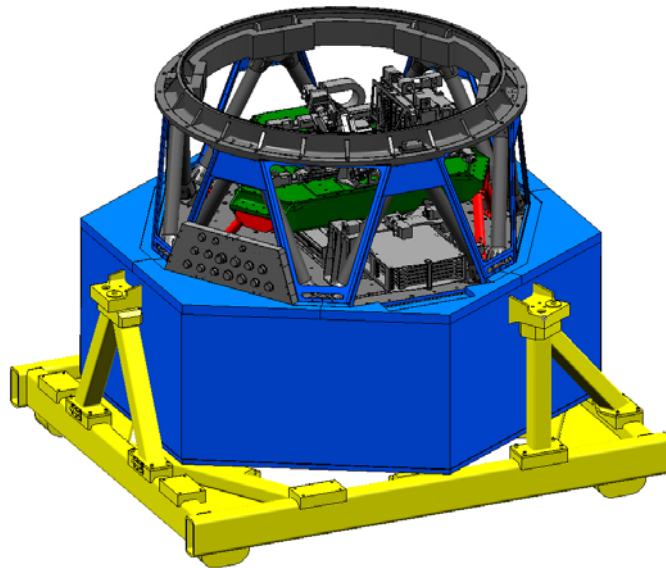


Figure 31. Binospec shown with upper insulation panels removed for inner bench maintenance.

### 3.9 Service and Maintenance

Figure 31 shows Binospec with the upper insulation panels removed for routine maintenance of the slit mask, filters, guider motors, or wave front sensor. Figure 32 shows the inner bench hoisted out of the instrument for major inner bench maintenance. This provides access to the guider stages and the periscope fold mirror assembly. Figure 33 shows the instrument with the lower insulation panels removed to access the science camera and gratings. For extensive maintenance of the camera or collimator lenses as well as the science camera and grating turntable, the entire instrument is lifted off the handling cart and rotated 180 degrees as shown in Figure 34. The instrument is then reattached to the handling cart upside down and then all insulation panels and frames are removed as shown in Figure 35.

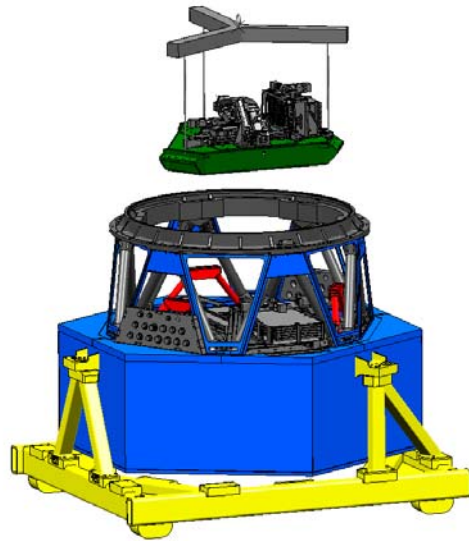


Figure 32. Binospec inner bench hoist for major maintenance.

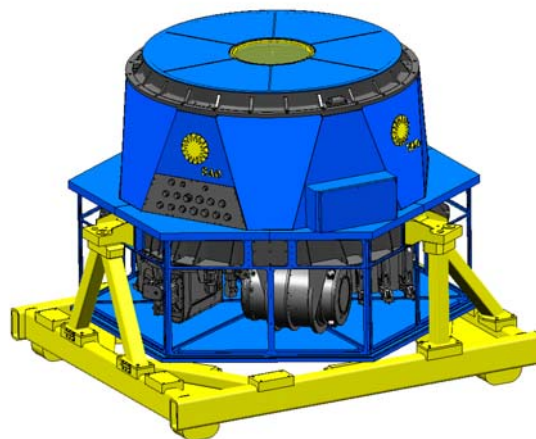


Figure 33. Binospec with lower insulation panels removed for main bench subassembly maintenance.

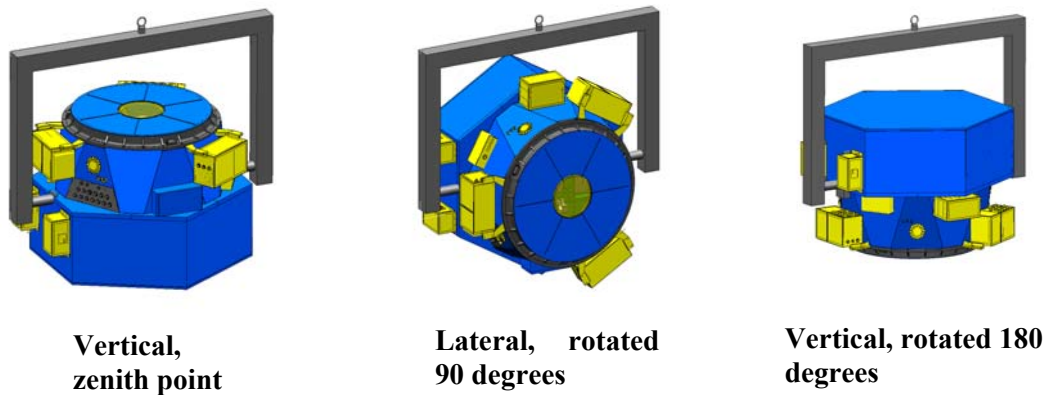


Figure 34. Binospec hoisted and rotated 180 degrees.

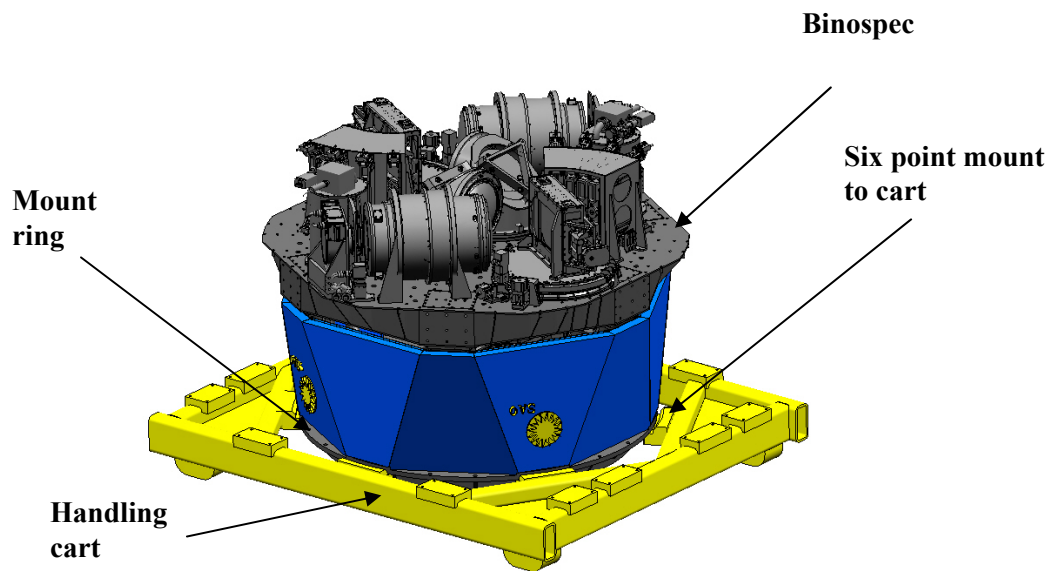


Figure 35. Binospec rotated on handling cart with lower subassemblies exposed for major maintenance.

## 4 Binospec Mechanical Section

### 4.1 Introduction

Here we provide a detailed overview of Binospec's mechanical subsystems, including:

1. Slit mask assembly
2. Single object guider/acquisition camera assembly
3. Wave front sensor assembly
4. Guider assemblies
5. Periscope fold mirror assembly
6. Filter changer assembly
7. Grating changer assembly
8. Collimator and camera lens assemblies
9. Science camera and high speed shutter assemblies
10. Flexure control system
11. Calibration screen/derotator system
12. Thermal shroud

The slit mask, filter changer and grating changer assemblies are the most complex mechanisms. Because these mechanisms are similar, we have maintained common design elements, including:

- The elevator assemblies of the slit mask and filter cassettes
- The exchange or insertion mechanisms and lateral preloader designs of the slit mask, filter and grating mechanisms.
- The normal force preload mechanisms for the slit mask, filter and grating mechanisms.

### 4.2 Slit Mask Assembly

#### 4.2.1 Slit Mask Cassette and Loader Mechanism Overview

The paired slit masks are mounted in a common reusable aluminum frame. Each mask is made from 0.005 inch thick stainless steel. The slits are cut in the masks using a programmable laser cutter. When the (initially flat) masks are mounted into their respective aluminum frame, they are formed into a cylindrical shape, bent about their short axis and tilted by  $0.841^\circ$  about their long axis to approximate the curvature of the focal surface. The center of each slit mask is 2.214 inches off-axis.

The slit mask changer consists of two major assemblies: the slit mask loader assembly and the slit mask cassette elevator assembly (see Figure 36). The slit mask loader assembly consists of a servo-driven, ball screw linear stage, which picks a single slit mask from the cassette elevator. A servo-controlled THK KR3306 X 500mm stroke linear actuator assembly is the active component in the slit mask insertion mechanism. This linear stage draws each slit mask into the focal plane where spring-loaded mechanisms preload each slit mask in six degrees of constraint, approximating a

kinematic mount. The drive torque required to accomplish this is 6.37 oz-in; please refer to Calculation 1. Sample Mechanisms Ballscrew Torque Calculation for the calculation. The available continuous torque from the Compumotor NEMA 23 series servo motor is 53 oz-in.

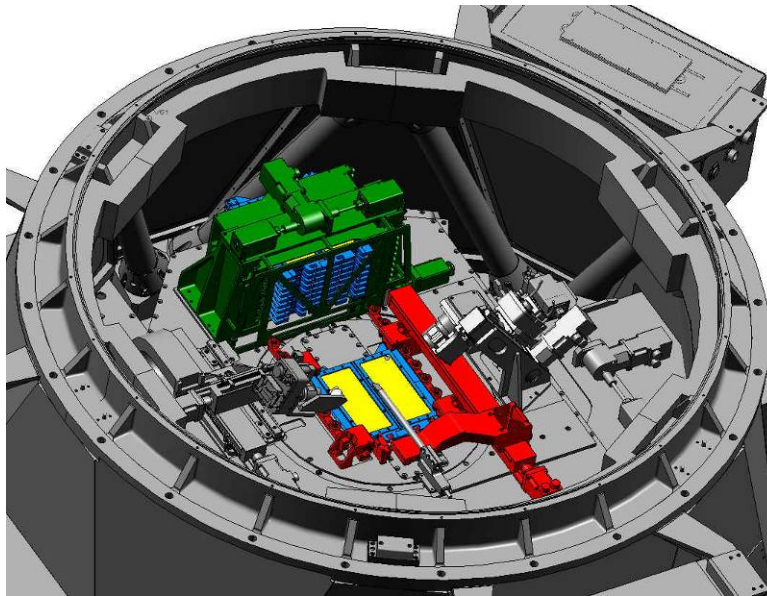


**Figure 36. The slit mask changer assembly. The elevator assembly is green, the slit masks are blue, and the slit mask loader is red.**

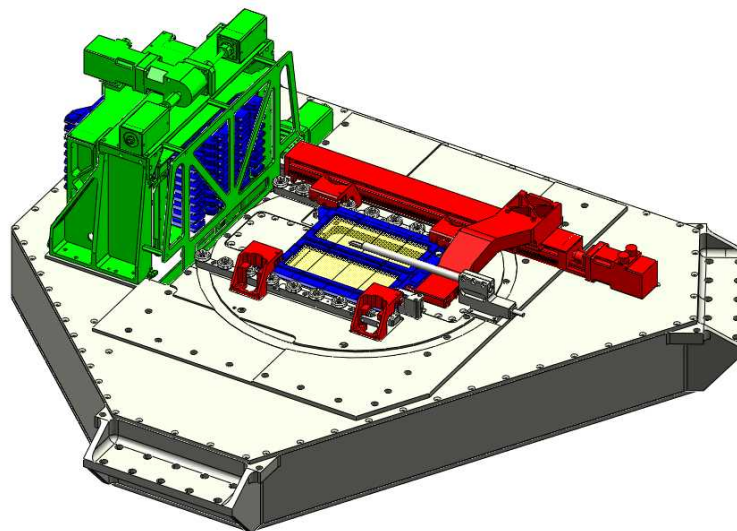


**Figure 37 - Slit mask loader assembly on inner bench. The color codes are the same as in Figure 36.**

Figure 37 shows the slit mask loader assembly on the inner bench. The cassette elevator (Figure 38) holds ten slit masks that are loaded individually into the cassette through a port on the side of Binospec. Each mask is held in the cassette with two spring-loaded retaining pins. The pins provide a lateral preload force three times the weight of each mask/frame assembly; each frame weighs ~2 lbs. The result is zero clearance between the

masks and guide rollers within the cassette. This ensures that the masks will be securely held when the instrument moves.

**Calculation 1. Sample Mechanisms Ballscrew Torque Calculation**

<b>Binospec Ballscrew Torque Calculation:</b>	
Lead := 6·mm	Ballscrew Lead
Load := 9·lbf	Axial Load on Ball Screw
$\eta := .85$	Ball Screw Efficiency
Gear := 1	Gear Reduction (used in cases where a gear reducer is used. For no gearbox, set value to 1.0)
$\eta_{gear} := 1$	Gear Efficiency (for no gearbox, set value to 1.0)
<b>Calculations:</b>	
$\text{Torque}_{\text{shaft}} := \frac{(\text{Load} \cdot \text{Lead})}{2 \cdot \pi \cdot \eta \cdot \text{Gear} \cdot \eta_{\text{gear}}}$	
$\text{Torque}_{\text{shaft}} = 0.398 \text{ in} \cdot \text{lbf}$	Calculated Torque (in-lb)
$\text{Torque}_{\text{shaft}} \cdot \frac{16}{\text{in} \cdot \text{lbf}} = 6.369$	Torque in (oz-in)

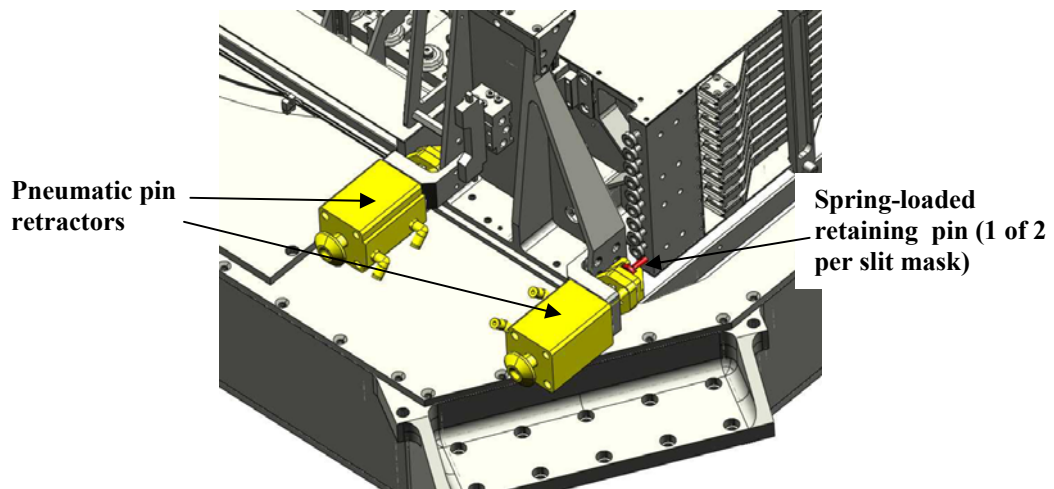


Figure 38. Pneumatic pins on the slit mask cassette assembly.

The preloading pins are normally locked. To remove a slit mask from the cassette, pneumatic mechanisms retract the retaining pins for that mask. The slit mask loader mechanism then pulls the mask from the cassette into the focal plane, guided by V-grooved rollers. The drive torque required to move the 50 lb elevator (loaded with ten slit masks) is 2.31 oz-in. The available continuous torque from the Compumotor NEMA 23 series servo motor is 53 oz-in.

#### 4.2.2 Loading Slit Masks

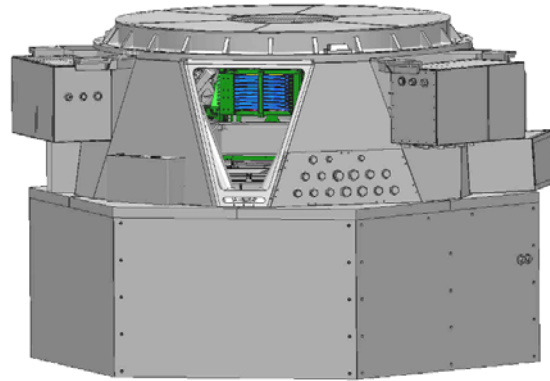


Figure 39. Access port to load slit masks.

The slit masks are loaded individually into the elevator assembly through the load port shown in Figure 39 Figure 40. The slit masks must be loaded with Binospic at zenith pointing. Once the slit mask load port is opened, the user will see a control panel near the slit mask cassette elevator that allows local control of the cassette elevator. The panel has two toggle switches, two momentary contact button switches, and an emergency stop switch (E-stop). Toggle switch #1 (labeled **Local/Remote**) overrides normal remote operation of the slit mask assembly and transfers control to the local control panel. The momentary contact switches (labeled **Index Up** and **Index Down**) move the cassette up or down one position. Toggle switch #2 (labeled **Mask Lock Released/Mask Lock Engaged**) releases and engages the locking pins for the slit mask at the load position.

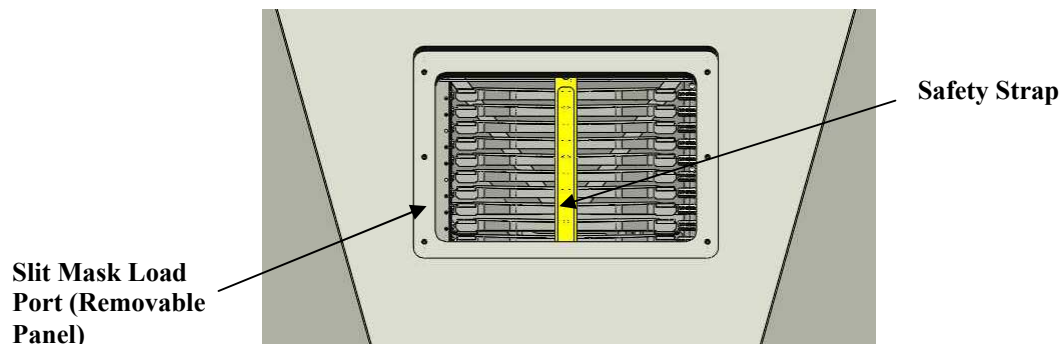


Figure 40. Close up of slit mask load port. A metal safety strap, held in place with two captured thumb screws, is removed to insert or remove slit masks.

#### Procedure to remove or load slit masks:

1. Set switch #1 to “Local”.
2. Index the slit mask to be changed to the “Load Position”.
3. Open the locking pins by setting switch #2 to “Open”.
4. Press the E-stop.
5. Carefully remove the slit mask by hand.
6. Install a new slit mask in the same slot.
7. Reset the E-stop.
8. Close the locking pins by setting switch #2 to “Closed”.
9. Index the next slit mask to be changed to the “Load Position” and repeat 3-8 until all of the desired slit masks are changed.
10. Replace the safety strap.

#### 4.2.3 Slit Mask Loading Arm and Slit Mask Clamping Mechanism

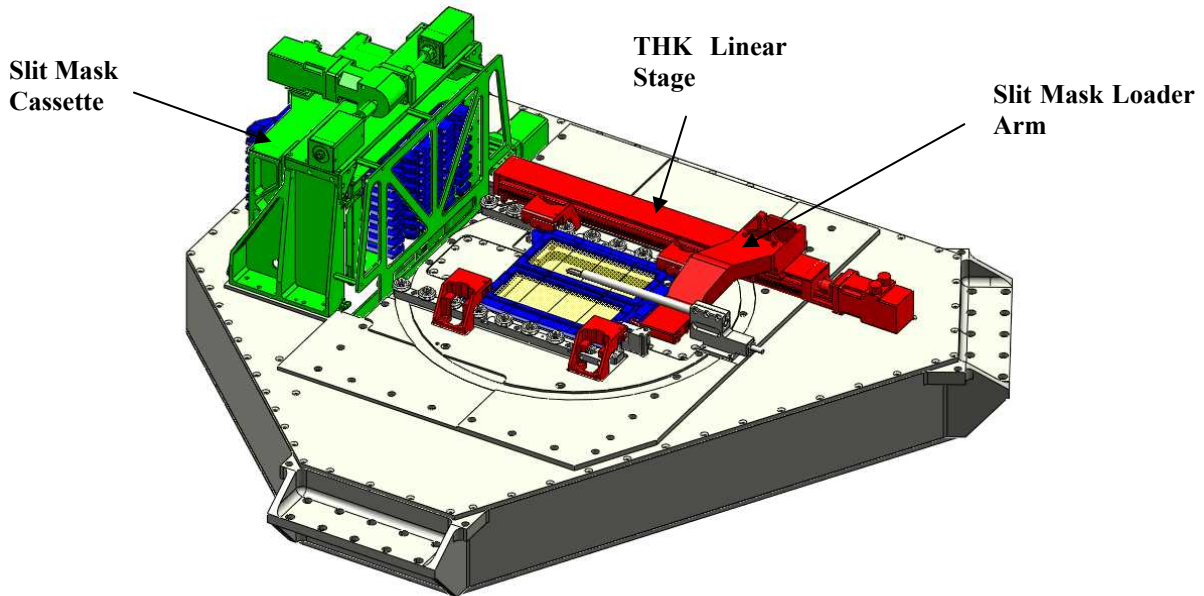
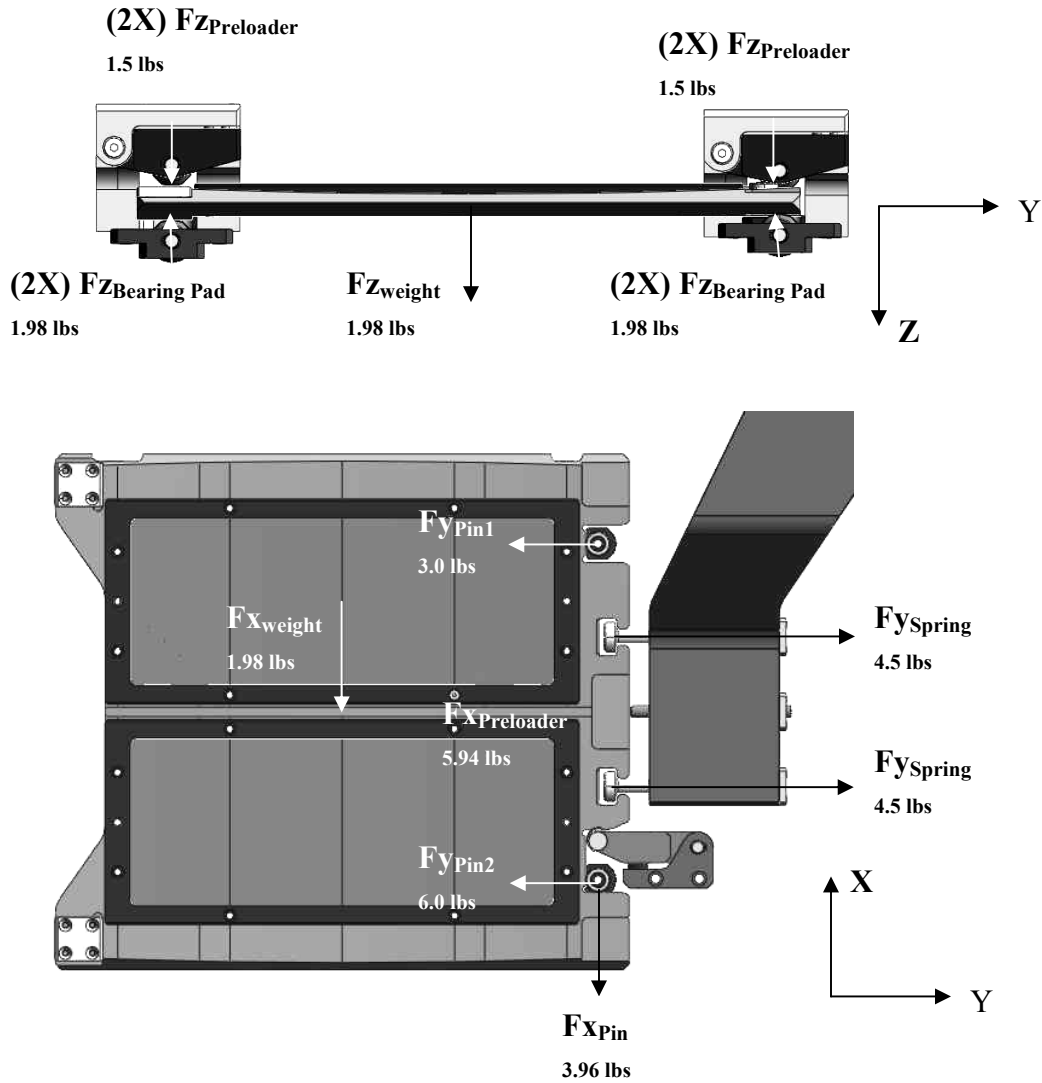


Figure 41. Slit mask loader and cassette assemblies on inner bench.

An aluminum loader arm moves the slit mask from the cassette to the focal plane. The arm is mounted to a THK ball screw linear stage (KR3306C X 530 mm stroke) (Figure 41). This stage features dual bearing blocks and a 10 mm OD X 6 mm pitch ball-screw and a Parker single stack servo motor (part number: BE230FJNMSN with power-off brake) with 53 oz-in of available continuous torque. 6.37 oz-in of torque is required to move this load and provide the required 9 lbs of preload force, providing a 7.3 factor of safety on the motor torque. The required travel is 16.875 inches from the cassette to the focal plane.

A clamping system preloads the slit mask at the focal plane to ensure that the positioning requirements are met. Spring-loaded pins within the loading arm are calibrated to provide 9 lbs of Y-direction preloading force. A single X-direction preloader provides 6 lbs of

preloading force. Four Z-direction preloaders provide a total of 6 lbs of Z direction preloading force (1.5 lbs at each of the 4 corners of the mask). A free body diagram of this clamping mechanism is shown in Figure 42.



**Figure 42. Slit mask focal plane clamping mechanism free body diagram.**

The puller arm provides Y direction preload to the slit mask assembly via two spring loaded puller pins (detail view shown in Figure 43). As the slit mask is drawn from the cassette into its operational position, it contacts two locating pins. The arm over-travels an additional 0.075 inch allowing the two compression springs to apply a precise preload on the slit mask.

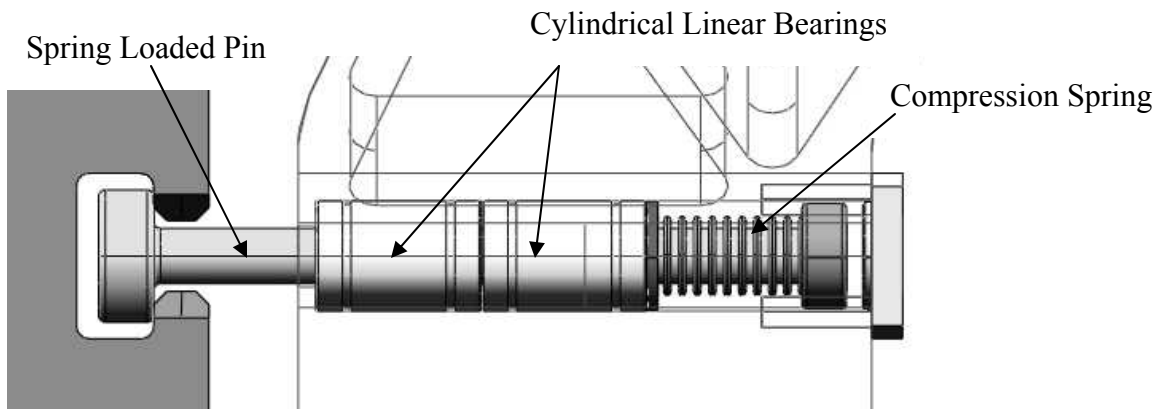


Figure 43 - Detail of slit mask puller pin assembly inside of loader arm.

#### 4.2.4 Parker BE Series Servomotor



Figure 44. Parker BE Series Servomotor

We have standardized on the BE series single stack-motor for use throughout all of the Binospec mechanisms (see Figure 44).

This motor features:

- NEMA 23 mounting interface ( $\text{Ø}3/8$  inch shaft,  $\text{Ø}1.5$  inch pilot)
- 53 oz-in continuous torque
- Integral power-off brake
- 2.2 lb overall weight

The standard optical rotary encoder for this motor is undesirable due to concern about light leaks and its relatively high power consumption. The motor will therefore be built with a special order Netzer rotary encoder, model RE<sup>2</sup>37, a 37 mm capacitive encoder with 32768 counts/revolution resolution. This encoder offers high precision, no light sources, and low power consumption.

The only mechanism that will have a different Parker motor stack will be the grating drive system. This motor will be built without the power-off brake. The grating drive mechanism has its own pneumatically operated brake caliper.

#### 4.2.5 Slit Mask Damping Mechanism

The damping mechanism smoothes the movement of the slit mask as it is pushed away from its clamped position. The damping mechanism is shown in Figure 45. Without the damping mechanism pressing the slit mask against the back flange of the spring loaded pins, the slit mask has a tendency to “squirt” out of the clamp in a brief moment of uncontrolled movement as the spring loaded clamps encounter their lead-ins. The damping mechanism only comes into play during about an inch of movement away from the locating pins. Similar damping mechanisms are incorporated into the filter changer mechanism and grating changer mechanism.

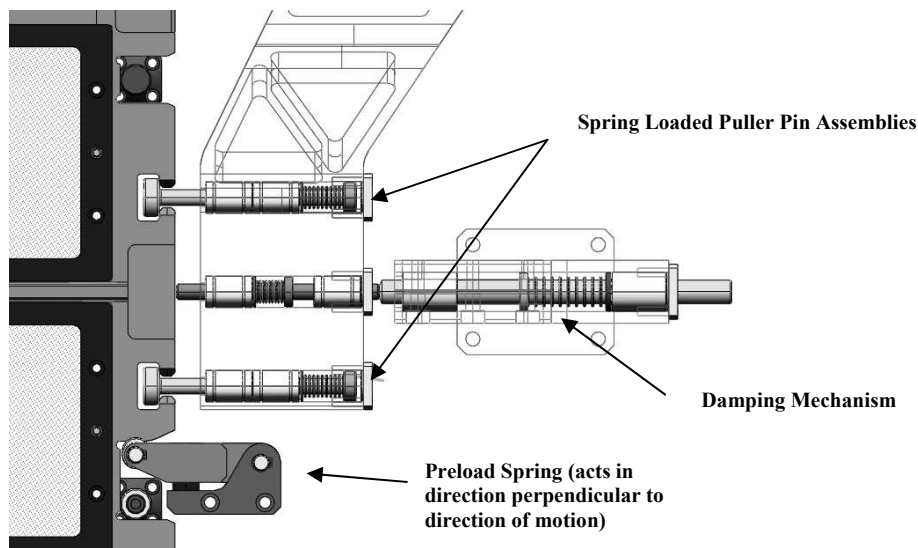


Figure 45. Detail of slit mask loader and the fixed damping mechanism at the focal surface. The damping mechanism keeps the puller pins engaged against the slit mask as the mask is moved from the focal surface and returned to the cassette. Without this mechanism, the puller pins would push the slit mask on their opposing face as the slit mask is removed from the focal surface. There would be an abrupt “snap” to the face shown as the preload springs reach their tapered lead in.

#### 4.2.6 Slit Mask Prototype Testing

A prototype of the Focal Plane assembly (shown in Figure 46) was built to verify the positioning repeatability of this design. Tests with this prototype led to the development of the damping mechanism discussed above. Repeatability measurements are summarized in Table 19.

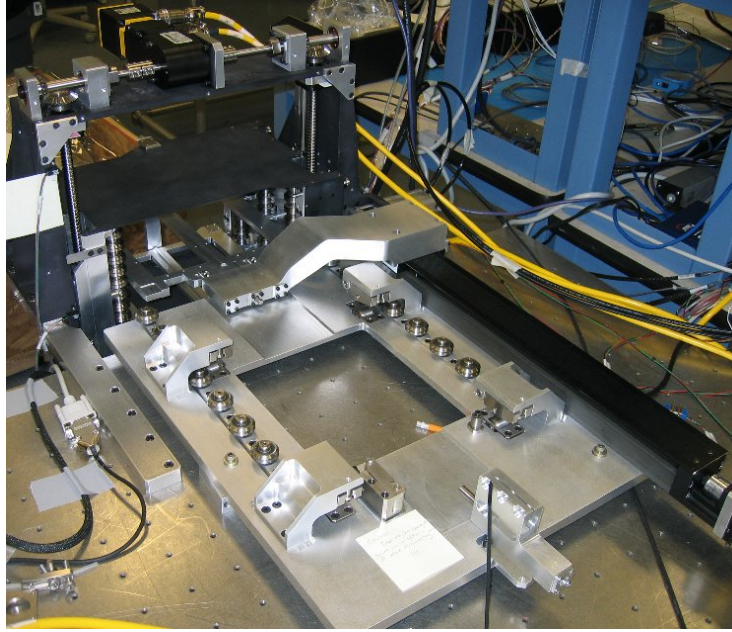


Figure 46 - Slit mask prototype.

Table 19 - Repeatability of slit mask positioning with prototype assembly.

Measurement	Requirement	Measurement Method	Results
Repeatability along slit (Y)	$\pm 20 \mu\text{m}$	Interferometer (1000 cycles)	$\pm 5.6 \mu\text{m}$
Repeatability across slit (X)	$\pm 3.5 \mu\text{m}$	Interferometer (1950 cycles)	$\pm 3.3 \mu\text{m}$
Repeatability focus (Z)	$\pm 50 \mu\text{m}$	Dial Indicator (10 cycles)	$\pm 3.2 \mu\text{m}$

### 4.3 Single Object Guider/Acquisition Camera Assembly

The single object guider/acquisition camera is mounted on the focal plane bench slightly above and to the side of the slit mask as shown in Figure 47. It allows two operational modes: central field target acquisition for pointing checks and blind offsets, and single object slit guiding. In acquisition mode, the relay lens assembly is aimed at the pick-off mirror located between the two slit masks, 1.25 inches above the focal plane. For single object slit guiding, the relay lens assembly is repositioned to aim at the center of a slit mask with a single slit. The relay lens assembly sends the light to the camera head assembly which does not move; the relay lens/focus/fold mirror assembly is mounted on a single-axis linear stage.

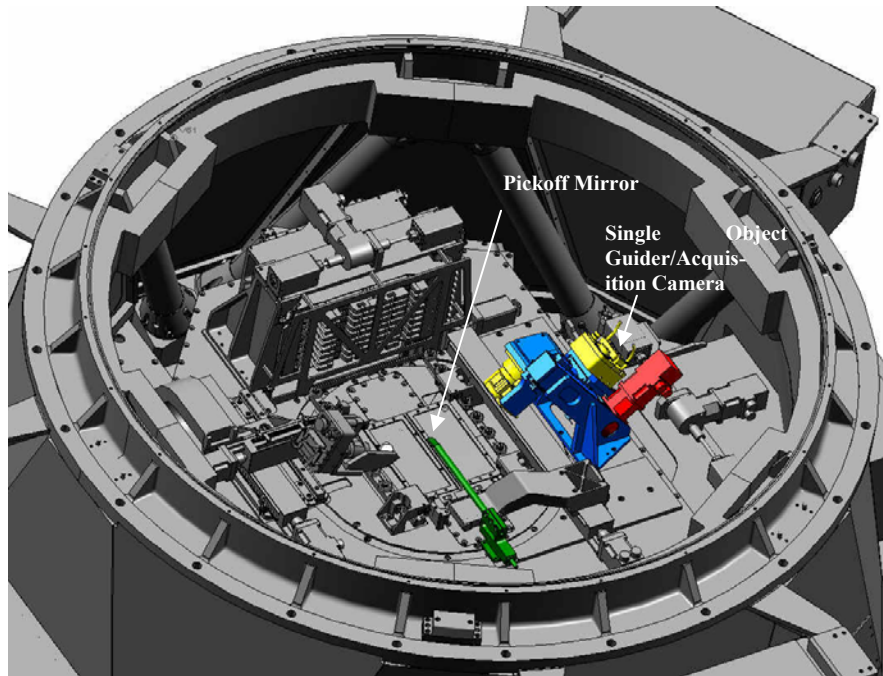


Figure 47. Single object guider/acquisition camera and central pickoff mirror.

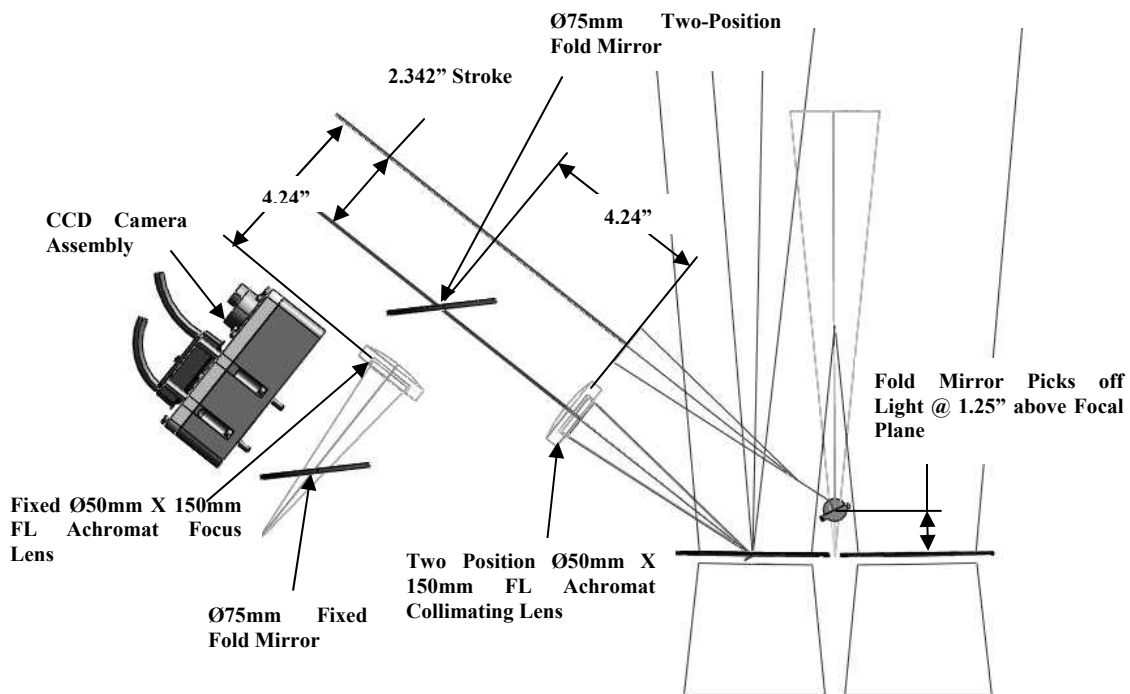


Figure 48. Single object guider optical layout – side view.

Several mechanisms including the single object guider/acquisition camera, use a PI M-111.2DG servo driven microstage. The other mechanisms that use this PI microstage are the wave front sensor and the two guider assemblies. The stages are used to adjust the

position of a collimating (achromatic) lens for focus control of each system. The PI microstage is shown in Figure 49.



**Figure 49. PI M-111.2DG microstage**

The important features of this stage include:

- Compact size (70 mm x 62mm x 20.5 mm)
- DC servo/recirculating ballscrew drive
- 2048 count/revolution magnetic encoder (no light leaks)
- Hall effect limit switches (no light leaks)
- 15 mm travel
- 2.25 lb max thrust capacity

The lack of a power-off brake was initially a concern. However, a ballscrew pitch of 0.5mm combined with a gearbox ration of 28.4:1 between the servo and the ballscrew means that back driving the system is nearly impossible without damaging the drive train. We verified that the PI microstage holds position with a representative load of 0.7 lbs with the power removed.

#### **4.4 Wave Front Sensor Assembly**

The wave front sensor is also mounted above the slit mask opposite the single object guider/acquisition camera as shown in Figure 50. It provides continuous wave front sensing at the edge of the slit mask over a rectangular field of 2 by 6.5 inches, or about 5' by 16', centered 5.49 inches (~14') off-axis. The system includes a 2-axis positioning system with a 30 mm OD pickoff mirror. The fold mirror and focus stage are mounted to two servo-driven THK linear stages arranged in an X-Y configuration. Unlike the through-the-slit guiders and the acquisition camera, the wave front sensor requires a moving camera. For calibration, a 20  $\mu\text{m}$  aperture backlit by an amber LED is mounted in a fixed stalk at a position which can be accessed by the moving head of the wave front sensor. The optical layout of the Wave Front Sensor is shown in Figure 51 with an overhead view in Figure 52.

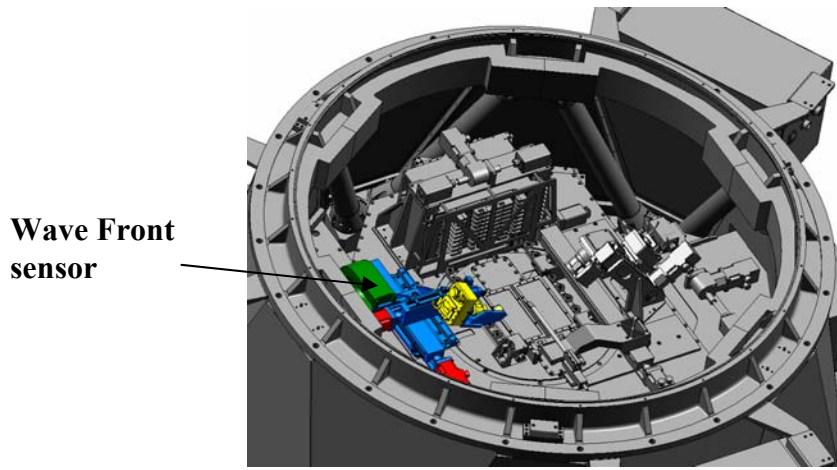


Figure 50. Wave front sensor assembly.

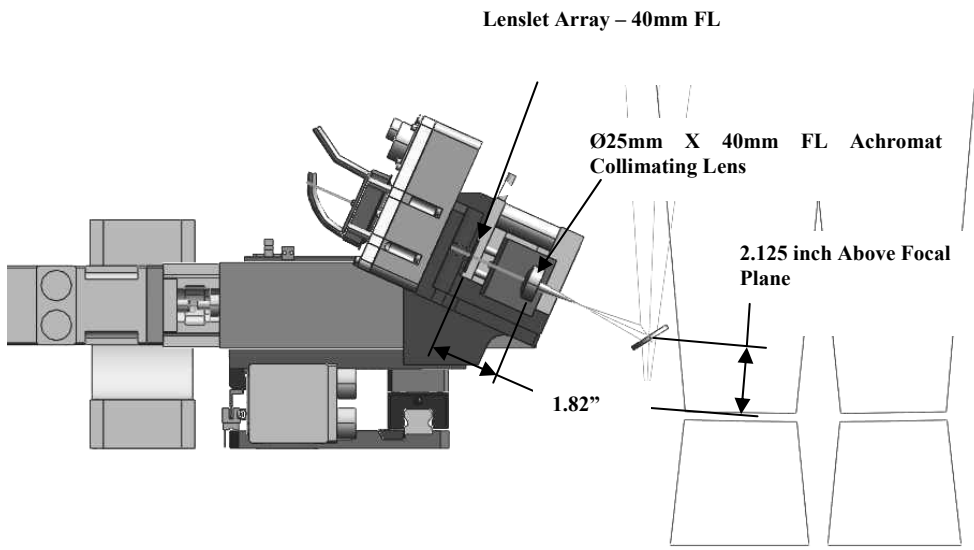


Figure 51. Wave front sensor optical layout (side view).

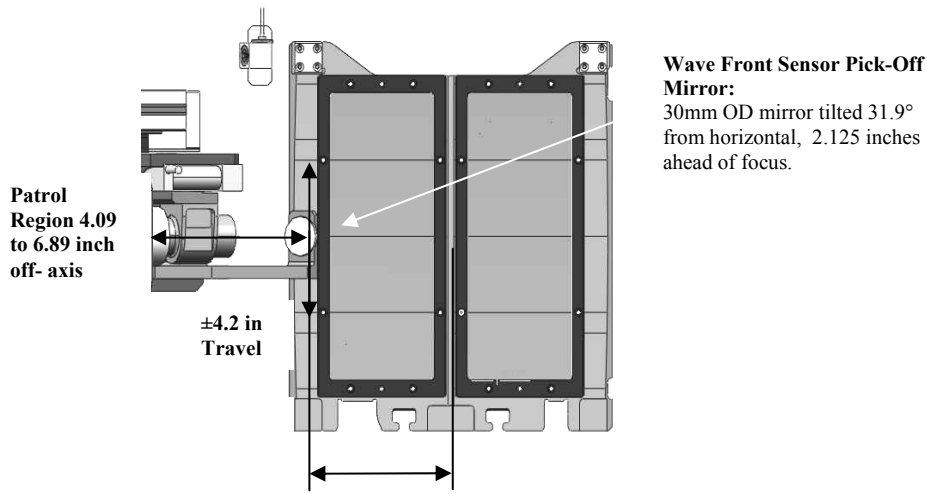


Figure 52. Wave front sensor – view looking down at slit mask.

## 4.5 Guider Assemblies

The identical guiders are located at the ends of the slit mask, and normally guide through holes in the slit masks as shown in Figure 53 , Figure 54, Figure 55 and Figure 56), which look through strips at opposite ends of the slit masks. The guiders scan +/- 3.7 inches at opposite ends of the slit mask.

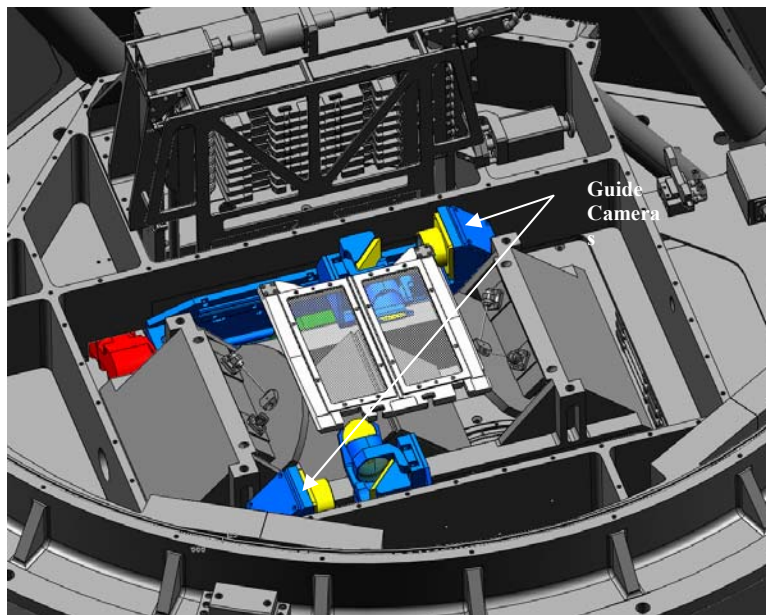


Figure 53 - Location of the guider assemblies. Several focal plane mechanisms as well as the top face sheet of the focal plane bench are removed for clarity.

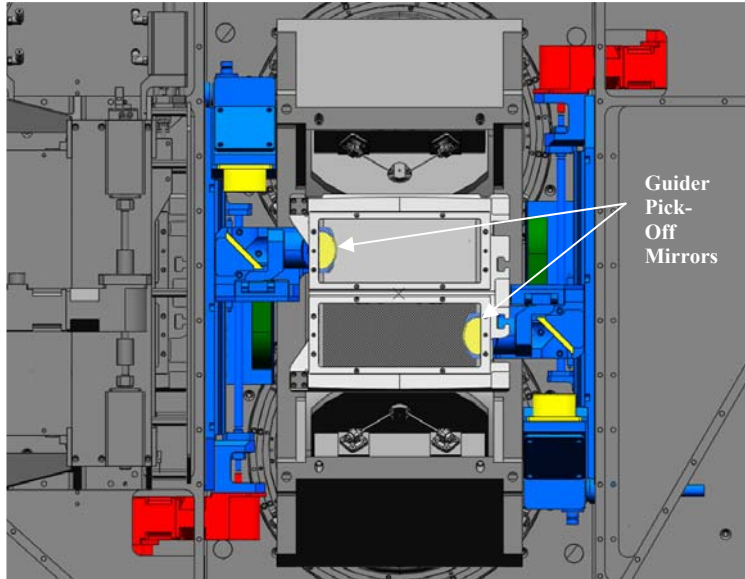


Figure 54 - View looking from above the focal plane that shows the pick-off mirrors located at the edge of the slit mask FOV.

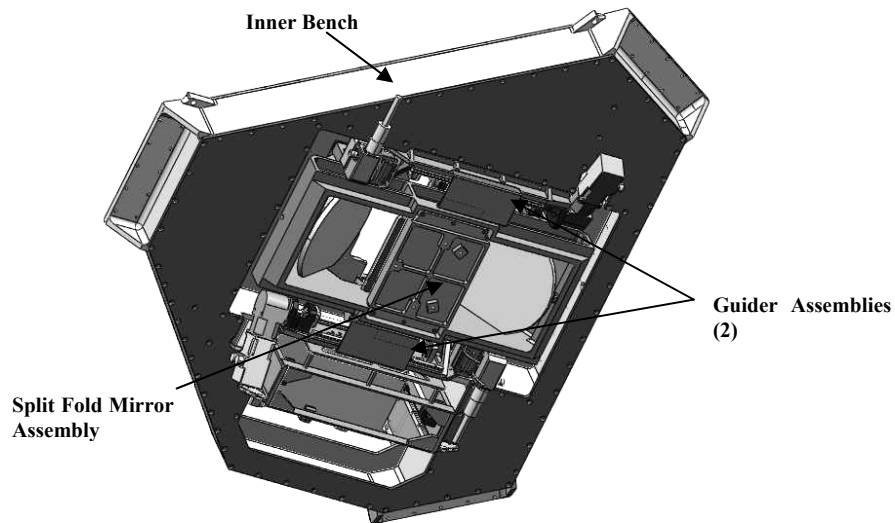


Figure 55 - Underside of Inner Bench

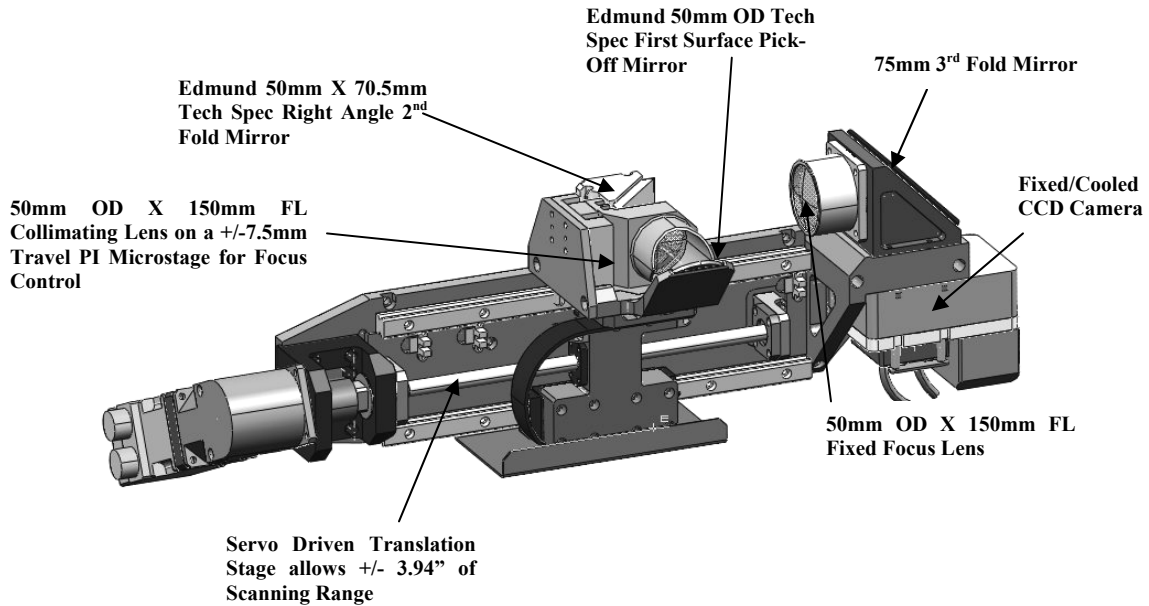


Figure 56. Guider Assembly. The total weight is 23.5 lbs.

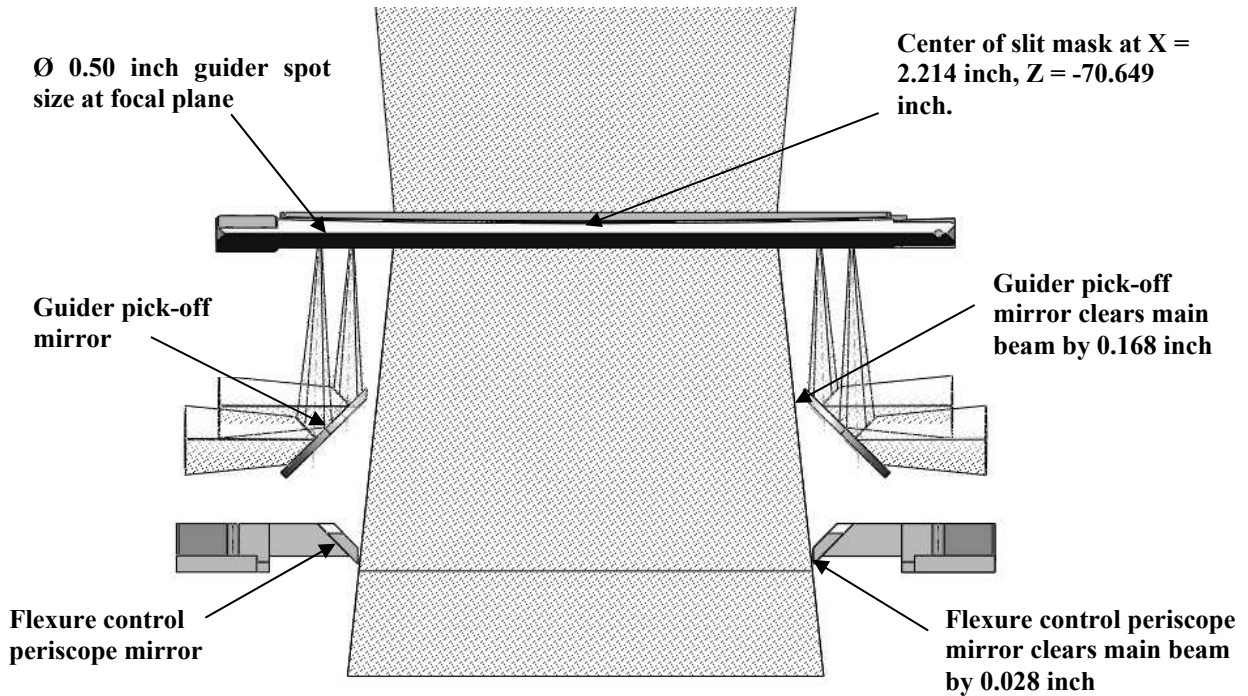


Figure 57. Guider system optical path (side view).

Due to the physical constraints of where the guiders are mounted, (see Figure 55 and Figure 59) special consideration must be given to assembly and servicing issues. The two guider assemblies are mounted underneath the inner bench alongside the split fold

mirror assembly that is part of the periscope optics that split the two Binospec beams. Installation and service of the guiders is complicated by the fact that its pick-off mirror must cantilever over the split fold mirror assembly. Therefore, the entire assembly cannot be installed from below. We separated the pick-off and collimator into a subassembly so that it can be installed and serviced through a removable port on the top surface of the bench.

In addition, the guider camera head can be removed for replacement or vacuum pump-down and the main servo may be replaced without disassembly of the guiders or removal of the split-fold mirror assembly.

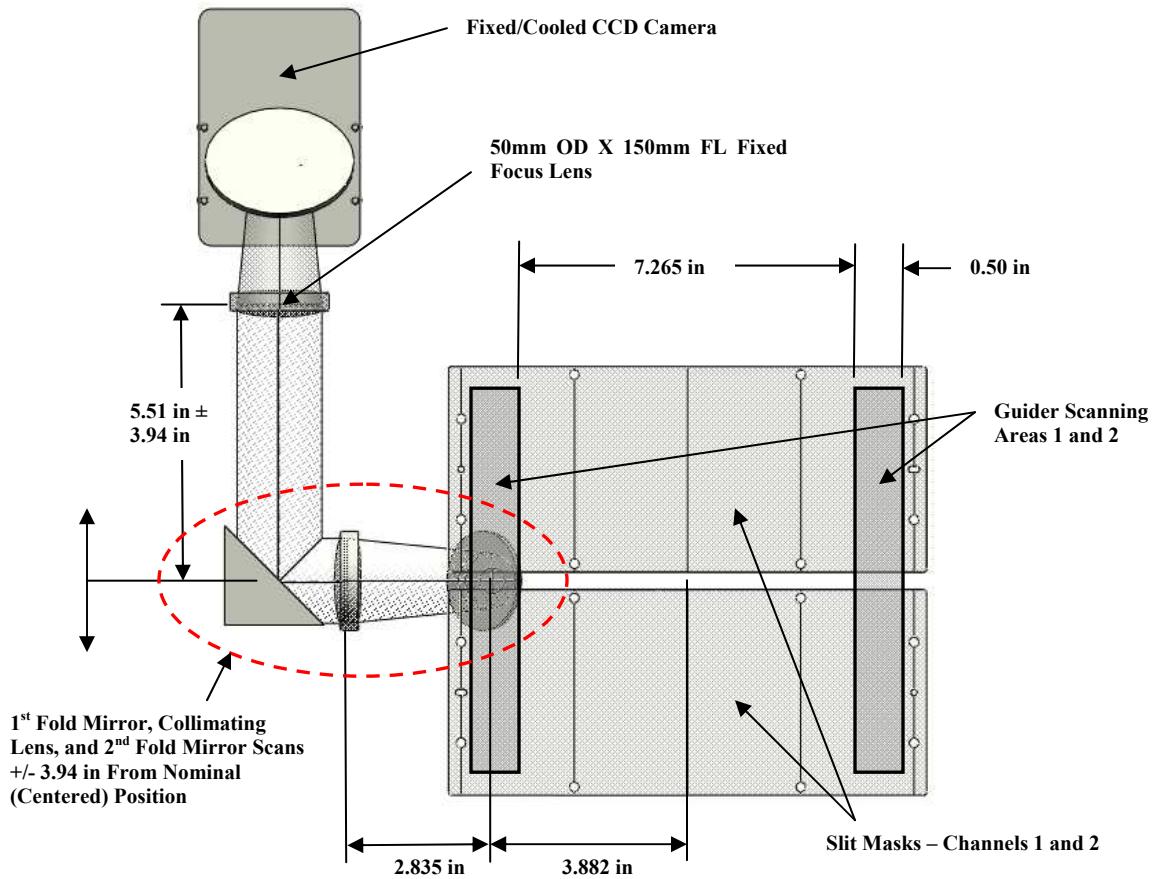


Figure 58. Guider system optical path (top view).

Access Ports from Pick-off  
Fold Mirror/Collimating  
Lens Subassembly

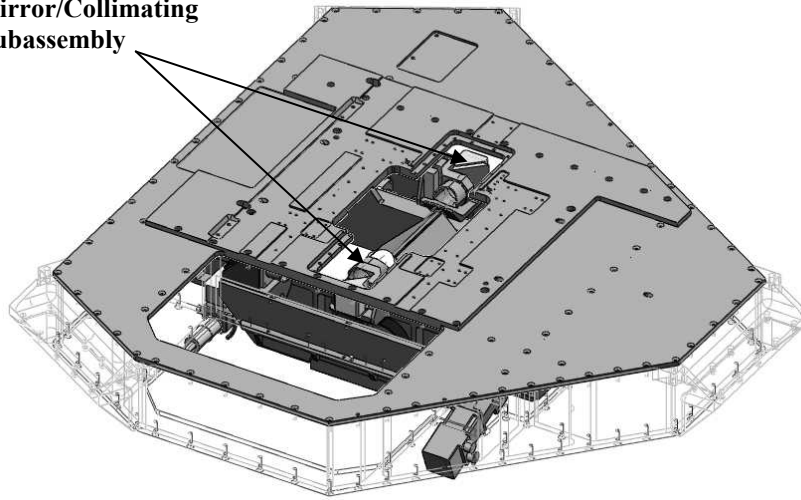
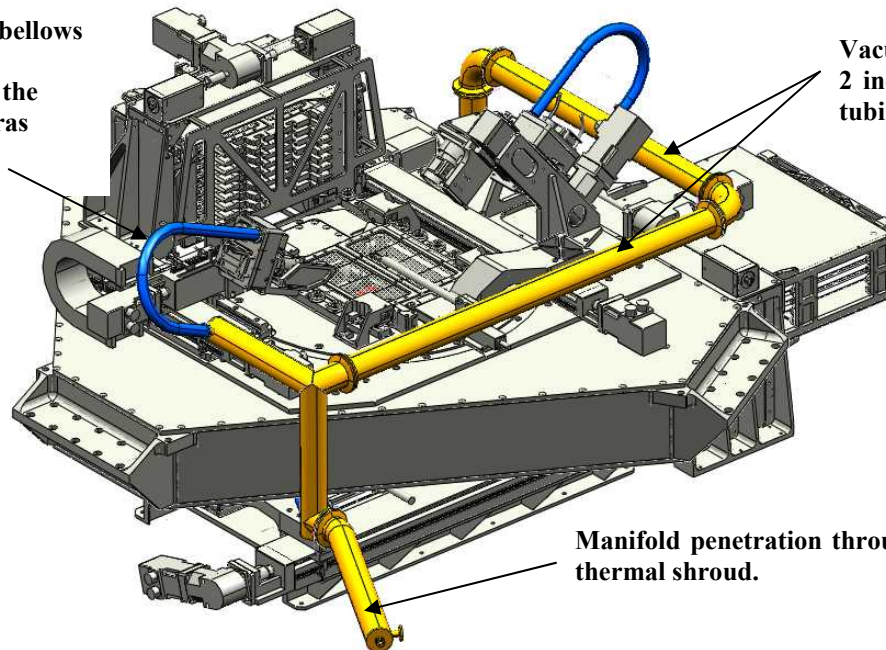


Figure 59. Access ports for guider service.

#### 4.6 Guide Camera Vacuum Manifold

We have found that to obtain the desired CCD temperature with less than two watts of thermoelectric cooler power, we need to maintain a good vacuum in the guide cameras. The leak rate past the O-rings in the guide camera quickly raises the internal pressure in the guide cameras to where convection is efficient. Therefore, the four guide cameras are connected to a common vacuum manifold (shown in Figure 60 and Figure 61) that is in turn connected to an external ion pump.

Flexible SS bellows  
connect the  
manifold to the  
guide cameras



Vacuum manifold:  
2 inch diameter SS  
tubing (yellow)

Manifold penetration through the  
thermal shroud.

Figure 60. Vacuum manifold connecting all guide cameras shown in yellow and blue.

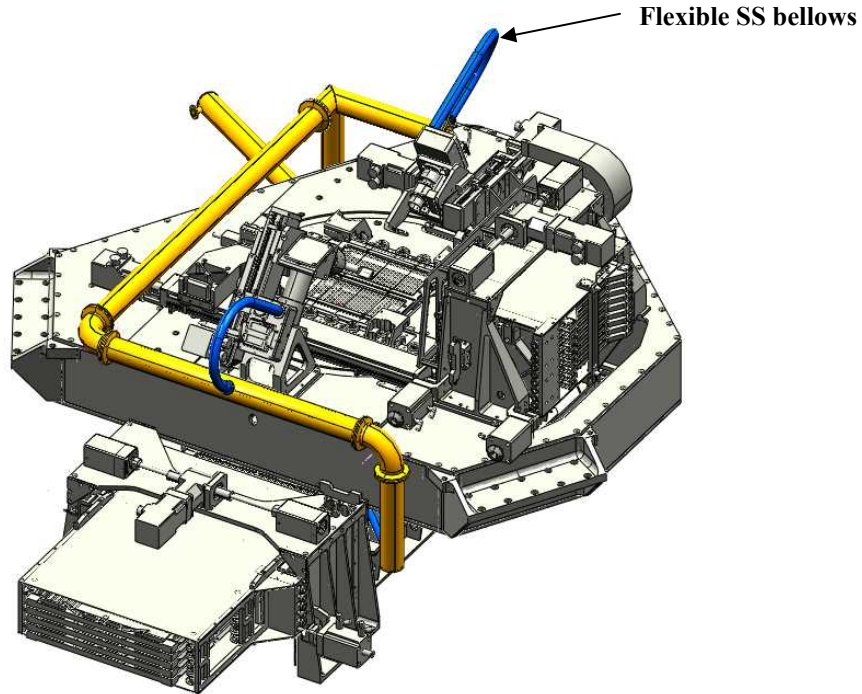


**Figure 61. Vacuum manifold (opposite view).**

The manifold is constructed of modular sections of 2 inch diameter type 304 stainless steel tubing. The sections are connected with ISO-KF-50 fittings with Viton seals. The manifold penetrates the thermal shroud to connect to an external ion pump in the guider electronics box. There is also a fitting for an external pumping system used to evacuate the system to a point where the on-board ion pump will start. At four locations, bellows connect the manifold to the guider camera bodies. All of the cameras are fixed except for the wave front sensor which moves on an XY stage in an 8.4 by 2.8 inch patrol region. The stainless steel bellows will accommodate this range of motion. The manifold will be supported off the inner bench with standoffs. The manifold weighs only about 30 lbs including clamps and support brackets.

#### **4.7 Periscope Fold Mirror Assembly**

The periscope fold mirrors are located directly beneath the slit masks as shown in Figure 62. The first fold mirrors are angled at  $45^\circ$  and the second fold mirrors are angled at  $45.43546^\circ$ . The goal of the fold mirrors is to move each optical beam off-axis by 8.25 inches parallel to the telescope optical axis, as required to provide clearance for mounting the collimator lens barrels side-by-side.

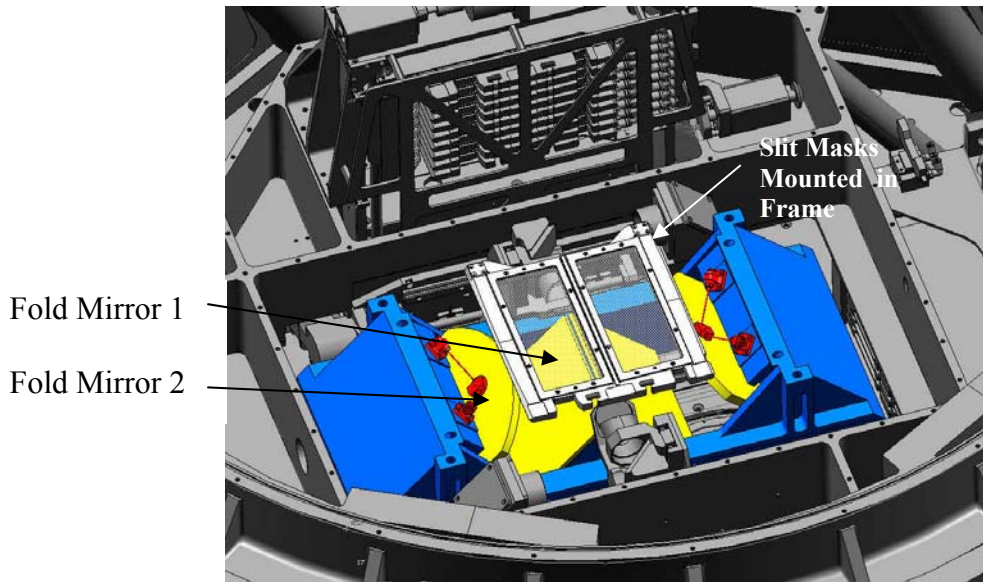


Figure 62. Periscope fold mirror assembly. The first fold mirrors form a tent assembly facing upwards. The second fold mirrors are angled down.

#### 4.8 Filter Changer Assembly

The filter changer mechanism is very similar to the slit mask changer mechanism. The filter changer consists of two major assemblies: the filter loader assembly and the filter cassette elevator assembly as shown in Figure 63 and Figure 64. The filter cassette holds six filters, each weighing about 8 lbs.

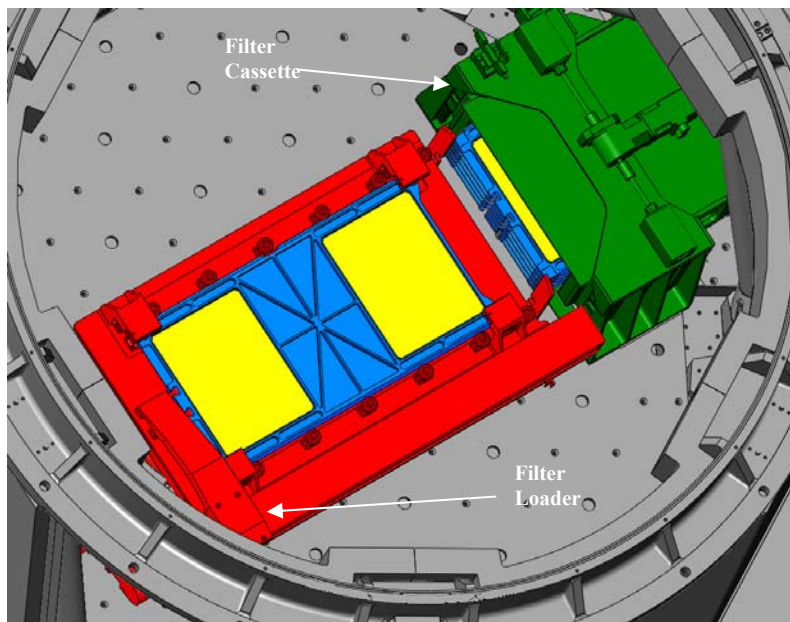
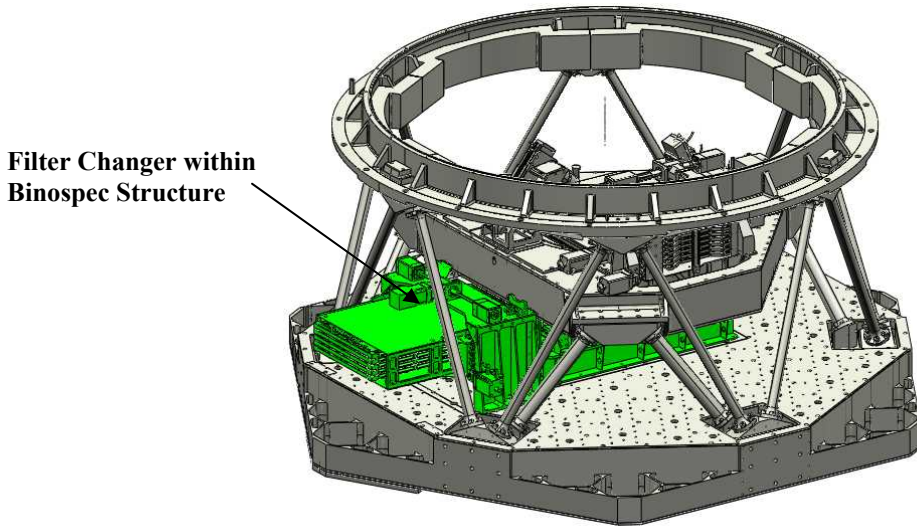
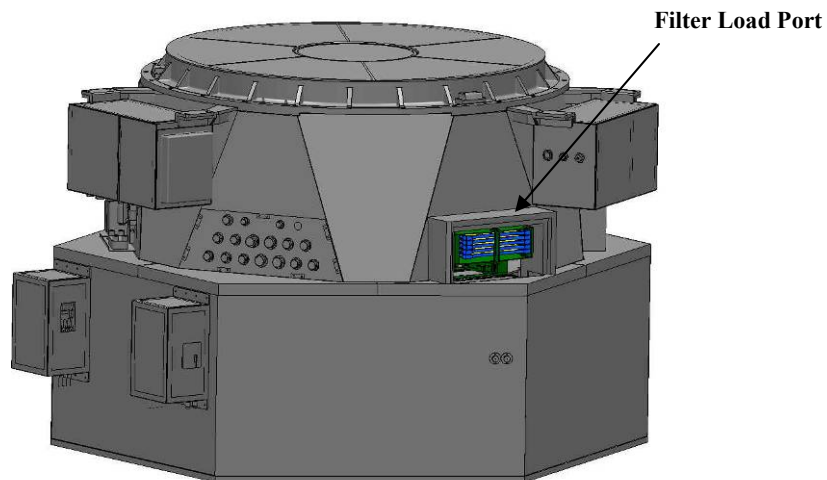


Figure 63. View showing the filter loader and storage cassette located on the top surface of the main optical bench. The filter frames are blue, the filters are yellow, and the elevator assembly is green.



**Figure 64. Filter changer on the top surface of the optical bench.**



**Figure 65. Access hatch for filter exchange.**

The filter loader assembly consists of a servo-driven, ball screw linear stage which picks a single filter assembly from the filter cassette. The linear stage pulls each filter 29.5 inches into a clamping system like that used for the slit mask.

A ball-screw driven elevator assembly indexes the filters to the load position. An optical bar-code system reads a tag on each filter frame to identify the filters present at each location within the elevator system. The drive torque required to move the 80 lb elevator (loaded with 6 filters) is 3.7 oz-in. The available continuous torque from the Compumotor NEMA 23 series servo motor is 53 oz-in. A servo-controlled THK KR4610 X 800 mm stroke linear actuator is used for the filter loader assembly.

The cassette must be loaded one filter at a time through a load port on the side of Binospec as shown in Figure 65.

## 4.9 Grating Stage

### 4.9.1 Introduction

The grating changer assemblies are shown mounted to Binospec in Figure 66. The mounted gratings are large and heavy, and moving and clamping these assemblies while maintaining low flexure is difficult. As discussed in the requirements, each arc-second of grating rotation leads to  $\sim 4 \mu\text{m}$  of image motion at the detector. Reducing grating flexure to a minimum by passive means is a high priority for our design since the grating is the most optically sensitive element in the system.

Each grating is mounted in its own bezel and, in turn, mounted on a rotary turntable. Our turntable rotates on discrete THK blocks and segmented curved rails. This approach provides superior overturning moment stiffness and significantly reduces the start-up friction associated with conventional preloaded angular contact ball or roller bearings.

### 4.9.2 Grating Storage and Loading onto Turntable

The gratings not in use are stored in fixed slots orientated radially from the turntable, similar to a railroad roundhouse. The turntable rotates to align with the storage slots in the roundhouse. A linear ball screw mechanism is used to load or unload the grating from the turntable. After the grating is selected, the turntable then rotates to the correct angle for the planned observation. Figure 67 shows the grating turntable and roundhouse storage.

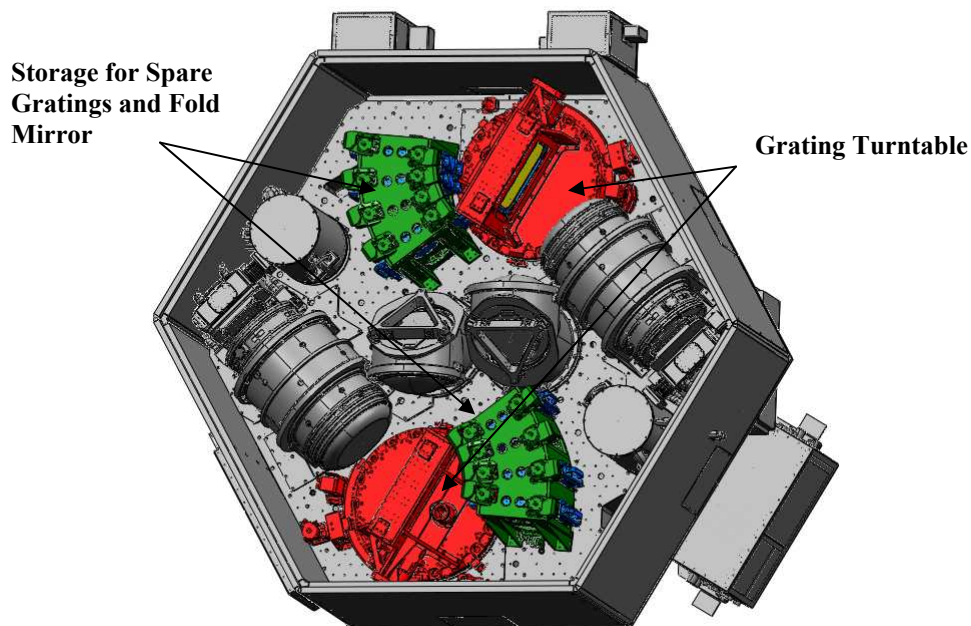
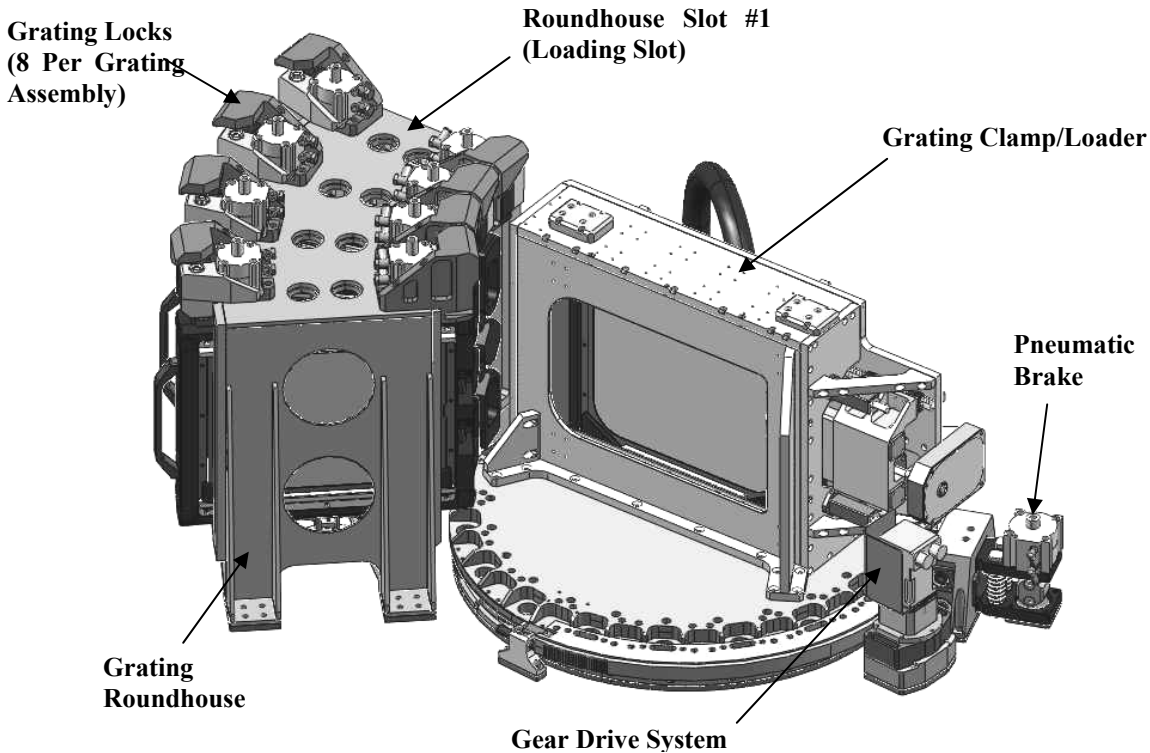


Figure 66. The grating turntables and the roundhouse storage for three gratings and one fold mirror for each beam.

There are several attractive features of this approach. (1) Only two mechanisms are required, a rotary turntable and a linear stage. (2) We have developed a very robust rotary bearing that provides high stiffness and relatively low startup-friction. (3) Storing the gratings in fixed storage slots eliminates a cassette mechanism.



**Figure 67. Grating assembly with roundhouse.**

The grating loader is a servo-driven, ball screw linear stage, which picks a single grating from the grating roundhouse assembly. The linear stage draws each grating into the clamp. When clamped, springs preload each grating assembly in six degrees of constraint, approximating a kinematic mount. The operation of this mechanism is similar in principle to the slit mask and filter changer assemblies but larger due to the increased mass of each grating. The angular pitch between gratings in the roundhouse is  $14^\circ$  and the travel of the grating into the loader mechanism is 19.7 inches.

The grating roundhouse must be loaded one grating at a time through a load port on the side of Binospec. The clamp performs a shuffle operation to transfer gratings between the load slot and its storage slot. Each of the four gratings (one mirror) is held axially in the roundhouse with two spring-loaded, pneumatic locks. The normal state of these locks is “locked”. In order for a grating to be moved into operational position, the pneumatic locks for that grating are opened, allowing the grating to be removed by the insertion mechanism. Each grating is guided along a linear path from the roundhouse into the grating clamp by rollers. Chamfered pins within the two clamps provide a preload force

of three times the weight of each grating assembly within the roundhouse. This prevents the gratings from shifting within the roundhouse during reorientation of the instrument.

### 4.9.3 Grating Assembly

The grating assembly is shown in Figure 68.



**Grating Size = 12.45 in X 9.65 in X 1.5 in (16.4 lbs)**

**Overall Size = 17.125 in X 13.125 in X 2.585 in**

**Overall Weight = 29.3 lbs**

**Clear Aperture = 11.66 in X 8.66 in**

**Mask Aperture = 12.125 in X 8.7 in (shown)**

**Distance Mask-to-Grating Surface = 0.080 in (This leaves room for black felt cloth)**

**Mask Thickness = 0.030 in**

**Teflon Support Nub Sizes: Axial (3) = 0.30 in, Vertical (2) = 0.375 in, Lateral (1) = 0.52 in**

**Figure 68. Grating assembly**

The 3g axial preload is applied by a low profile flexure plate that is fastened to the back of the frame as shown in Figure 69. The protective cover is illustrated in Figure 70.

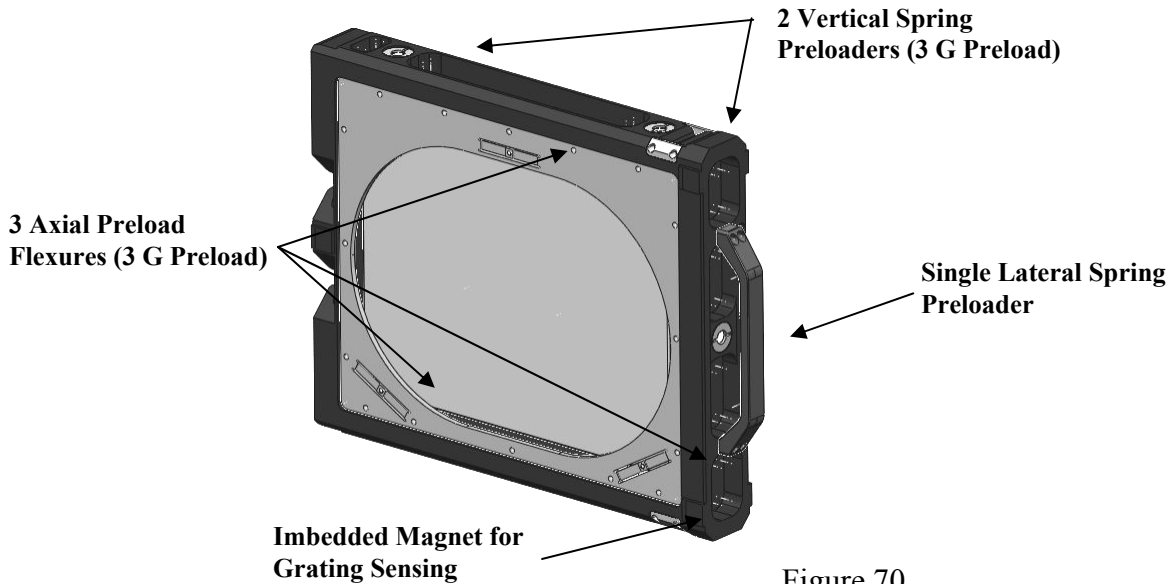


**Figure 70**

**Figure 69. Back of the grating assembly illustrating axial flexures used to preload the grating against its hardpoints and the sensing magnets.**

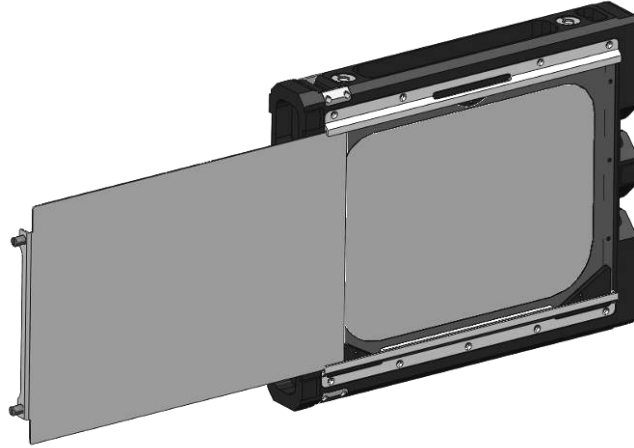


**Figure 70. Protective cover used when grating is removed from Binospec.**

An exploded view of the grating assembly is shown in Figure 71.

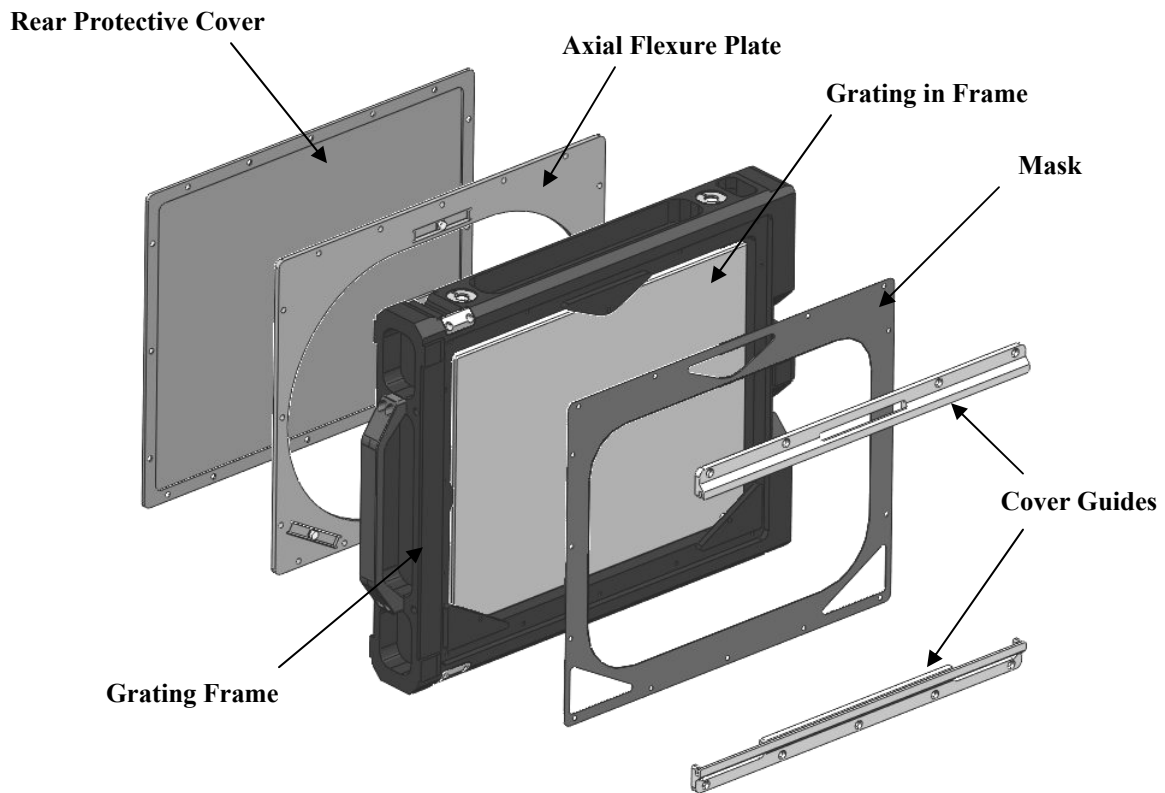


**Figure 71. Exploded view of grating assembly.**

In order to minimize the grating size, the illuminated aperture of the grating is not centered on the mechanical center of the grating as shown in Figure 72.

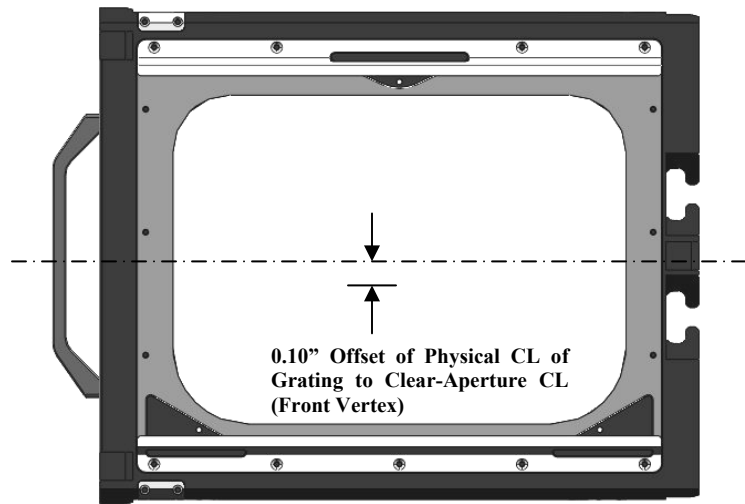


Figure 72. Illuminated portion of the grating is offset from the grating mechanical center.

#### 4.9.4 Grating Clamp and Insertion Mechanism

The grating puller assembly is driven by a THK ball screw (14 mm OD X 8 mm pitch X 500 mm stroke). The puller is guided by four THK HSR-12 linear guides on two rails. The required travel is 19.50 inches from the roundhouse to the grating clamp. A Parker single stack servo motor (part number: BE230FJNMSN with power-off brake) with 53 oz-in of available continuous torque operating through a 13.33 gear reduction drives the puller. The required torque to move this load and provide the required 87.9 lbs of preload force (3 G's) is 7.32 oz-in of torque, so that we provide a 6.24 factor of safety on the motor torque.

A clamping system (shown in Figure 73 and Figure 74) preloads the grating within the clamp to ensure that the positioning requirements are met. Spring-loaded pins within the puller are calibrated to provide 87.9 lbs (3 Gs) of lateral preloading force. As the grating is transported from the roundhouse to its operational position, it contacts a single hardpoint between the two spring loaded pins. The puller over-travels an additional 0.125 inch allowing the two compression springs to apply the precise 3-G preload on the grating. Dual preloaders provide 3 G's of preloading force in the other in-plane direction. Four normal-direction preloaders provide 3 G's of normal preload force. This mechanism operates and clamps the grating much like the slit mask and filter changer assemblies. The mass of the grating assembly is, however, much larger and the preload forces are proportionally greater.

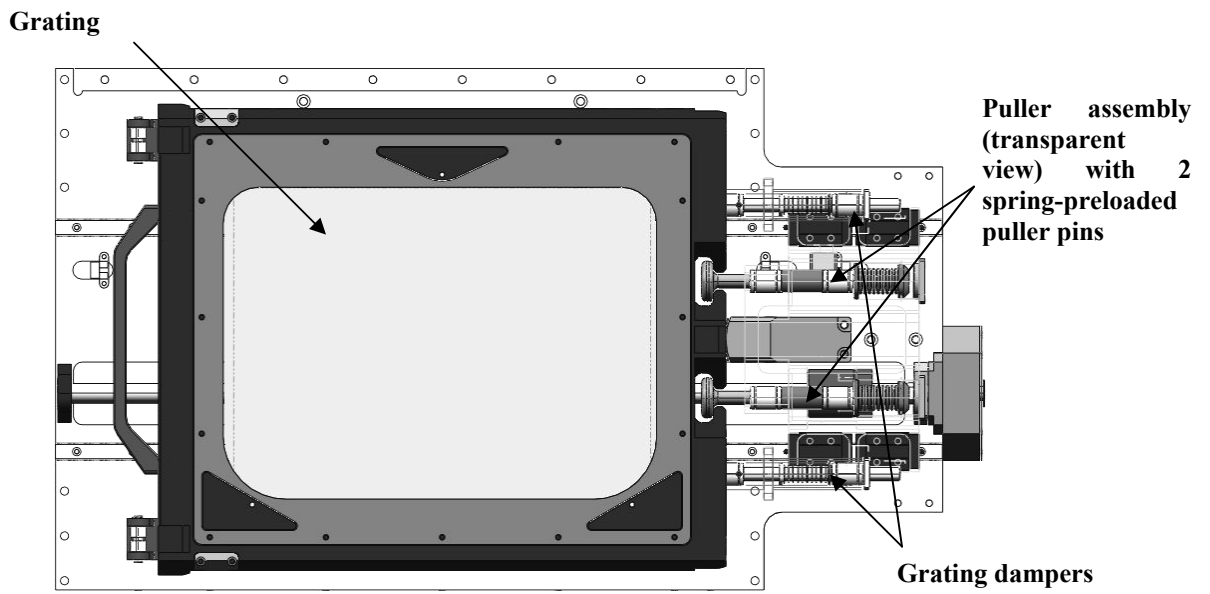


Figure 73. Grating clamping mechanism with front support structure removed.

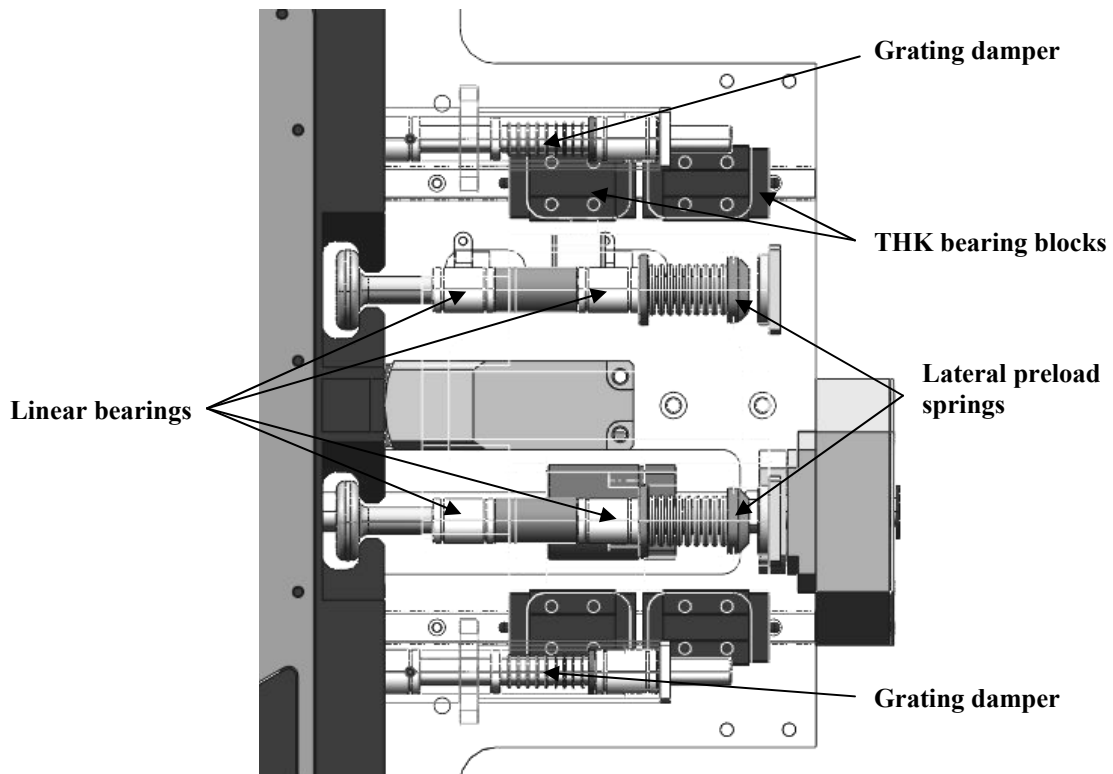


Figure 74. Close-up of the internals of the grating puller mechanism (transparent view).

#### 4.9.5 Grating Damping Mechanism

The grating damper smooths the movement of the grating as it is moved away from its clamped position. Without the damping mechanism pressing the grating against the back flange of the spring loaded pins, the grating would have a tendency to “squirt” out of the clamp in a brief moment of uncontrolled movement as the various spring loaded clamps encounter their lead-ins. The damping mechanism only comes into play during approximately the first inch of movement away from the locating pins. The dampers are visible in Figure 74.

#### 4.9.6 Grating Turntable/Bearing Assembly

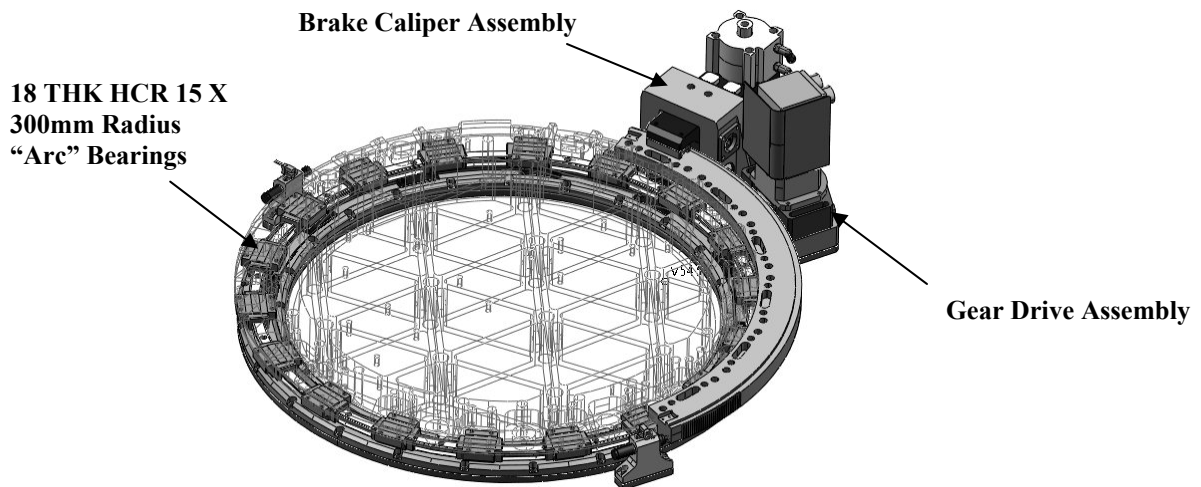


Figure 75. Grating turntable, drive and brake assembly.

Eighteen THK HCR 15 X 300 mm radii arc bearings (shown in Figure 75) are used in place of a large diameter, duplex angular-contact bearing. We compared the performance of a Kaydon 20 inch ID duplex angular contact bearing with the THK arc bearings. The THK system is found to be superior:

1. The total overturning moment stiffness of the THK arc bearing is  $10^9$  in-lb/rad. The THK system achieves this stiffness without the high preload of the duplex bearing. A preload of 0.010 inch is required in an angular contact bearing to achieve the desired stiffness.
2. The THK bearing has 1/3rd starting torque of the heavily preloaded angular contact bearing. The predicted starting torque of the THK system will be 17.7 lb-ft of torque.
3. The THK bearing eliminates the operation of press fitting a large diameter angular contact bearing.

Note: The minimum stiffness of each block (axial and radial) is  $900,000 \text{ lb in}^{-1}$ . Since we are attaching the THK 1055 steel mounting rails to an aluminum mounting surface, we plan on grinding a .015 inch gap to serve as an expansion joint between each of the six

segments of the steel bearing rail. This will compensate for the CTE mismatch between the steel and aluminum. The balls should pass over these small gaps without issue and without impacting overall system stiffness.

#### **4.9.7 Grating Gear Drive**

The total drive torque required to rotate the grating turntable is the sum of the THK block friction times the THK rail radius (17.7 lb-ft) and the moment caused by the imbalance of the load (23.5 lb-ft) or a total of 41.2 lb-ft. A 3 inch pitch diameter stainless steel spur gear (pinion) driving a stainless steel 28 inch pitch diameter spur gear (drive arc) supplies the drive torque; therefore, a tangential force of 35.3 lbs is required to drive the grating. A NEMA 23 servo motor with 53 oz-in of continuous torque drives the stainless steel pinion gear through a 120:1 harmonic drive. Calculations indicate that 11.9 oz-in of motor drive torque is required to rotate the grating in its least favorable orientation, so we have a margin of safety of 3.45 on the drive torque.

Measurements performed on a prototype friction drive grating drive confirm that this system can develop the necessary tangential force. A 3 inch diameter friction drive urethane roller was able to generate over 126 lbs of linear drive force through a 100:1 harmonic drive. The friction drive set-up was rejected, however, due to the flexibility of the urethane roller and slippage between the roller and drive arc. Both of these issues caused problems in controlling position to the desired precision.

A spur gear drive was selected instead of a worm gear drive because spur gears are the easiest to make and can be made to the highest precision. Due to the high sliding required in a worm gear, lubrication would have been necessary. We plan on using our spur gear unlubricated.

The desired positioning accuracy and repeatability of the tilt mechanism is better than 10" (.0028°). Grating tilt is measured directly with a magnetoresistive encoder with a linear resolution of 1  $\mu\text{m}$ , providing an angular resolution of 0.63". For reference, if we used the 32768 count/revolution Netzer encoder on the drive motor through the 120:1 harmonic drive and 14:3 gear, the resolution is 0.071". However, the gear system has backlash that will degrade the accuracy of the motor encoder reading. We minimize the backlash in this drive system by taking the following steps:

- a. We are using a 24 pitch, 14.5° pressure angle gear and pinion instead of a more common 20° pressure angle gear. All manufacturing and assembly tolerances being equal, 20° pressure angle gears have 41% greater backlash than 14.5° pressure angle gears.
- b. The center-to-center distance between the pinion gear and the drive arc will be on a fine adjustment so that we can minimize this as a factor in the final backlash of the system. The main sources of backlash in this gear system will be gear run-out and tooth thickness manufacturing tolerances of the pinion and drive arc.

We can reasonably expect to achieve backlash in this drive system of 0.0005 inches or 7.4" on a 28 inch pitch diameter drive arc. This number is based on an AGMA "E" backlash designation for spur gears of this size and pitch. The 28 inch PD drive arc and 3 inch PD pinion gear will be made of 300 series stainless steel. Once the grating is positioned at the desired angle of incidence, a pneumatically released caliper brake directly engages the drive-arc, holding the angular position of the turntable. This brake overcomes backlash between the pinion gear and drive-arc gear.

#### 4.9.8 Grating Clear Apertures

The grating mechanism has to operate within the configurations shown in Table 20. These include possible future gratings as well as the initial 270 gpm and 600 gpm gratings.

**Table 20. Grating configurations**

Config	Wavelength (μm)	Notes	Angle of Incidence	Angle of Diffraction	Anamorphic Mag	Vignetting
1	0.39-0.93	270 gpm	28.103°	16.987°	1.08	none
2	0.39-0.62	650 gpm	32.710°	12.290°	1.16	none
3	0.77-1.00	650 gpm	40.585°	4.415°	1.31	none
4	0.57-0.74	900 gpm	41.143°	3.857°	1.33	none
5	0.83-1.00	900 gpm	48.983°	-3.983°	1.52	7%
6	0.39-0.52	1200 gpm	39.615°	5.385°	1.29	none
7	0.88-1.00	1200 gpm	60.084°	-15.084°	1.94	27%
8	0.39-0.50	blue imaging	22.500°	22.500°	1.00	none
9	0.70-1.00	red imaging	22.500°	22.500°	1.00	none
10	0.41-0.54	g'-band	22.500°	22.500°	1.00	none
11	0.56-0.69	r'-band	22.500°	22.500°	1.00	none
12	0.69-0.83	i'-band	22.500°	22.500°	1.00	none
13	0.86-0.99	z'-band	22.500°	22.500°	1.00	none

Step CAD files were generated from ZEMAX for configurations 1, 3, 5, 7 and 8. With these we were able to verify that the grating mechanism does not block light that is not deliberately vignetted at the grating.

Front opening dimensions of the grating clamp are shown in Figure 76. The ball screw and linear bearing rails of the loading stage are not visible by the camera.

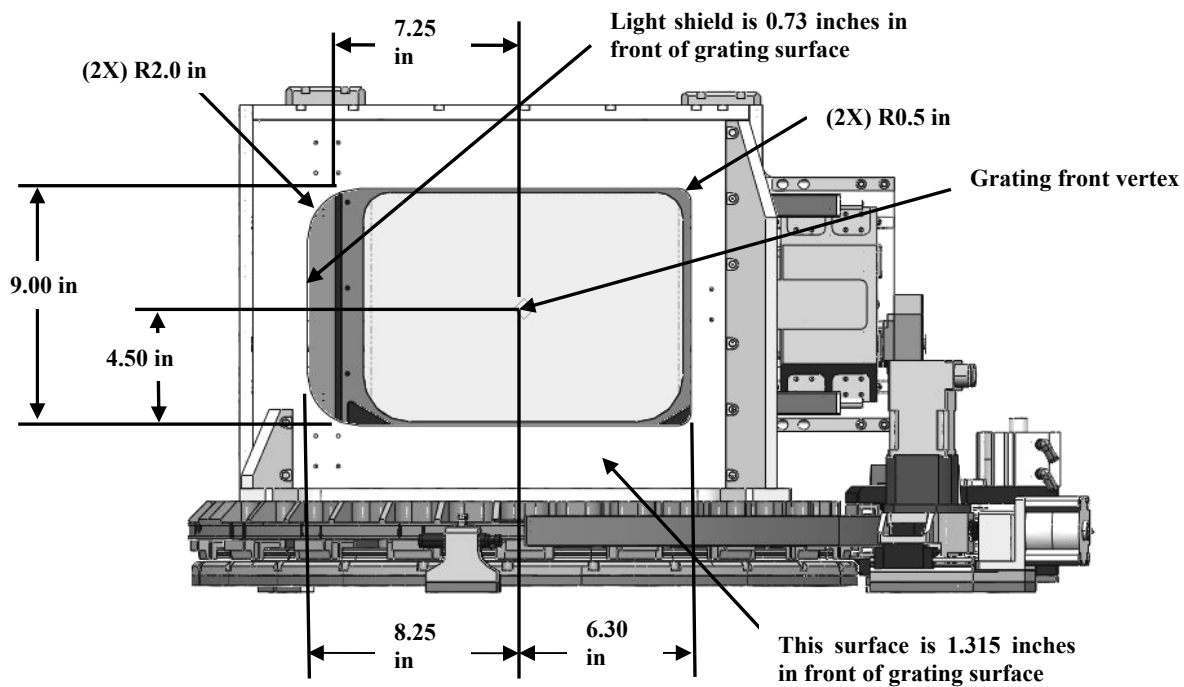


Figure 76. Grating clamp assembly front profile.

**Grating Mechanism within the Binospec Assembly:**

Figure 77 shows the grating with turntable moved to the load position.

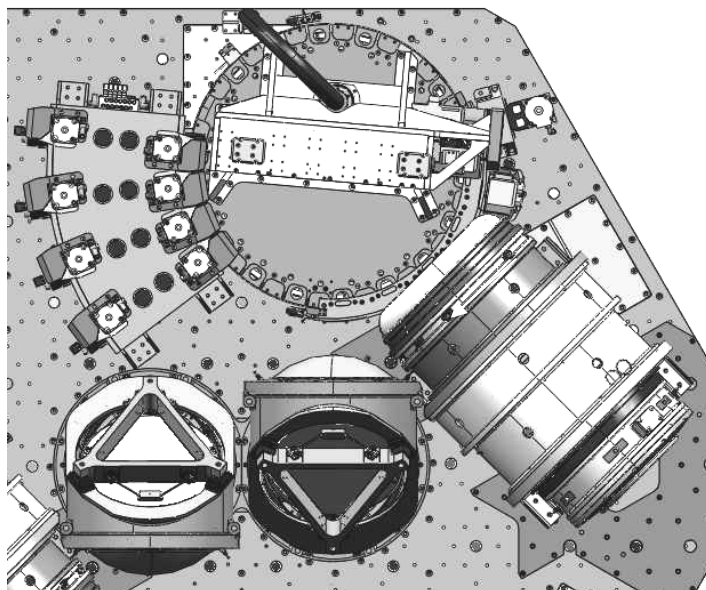
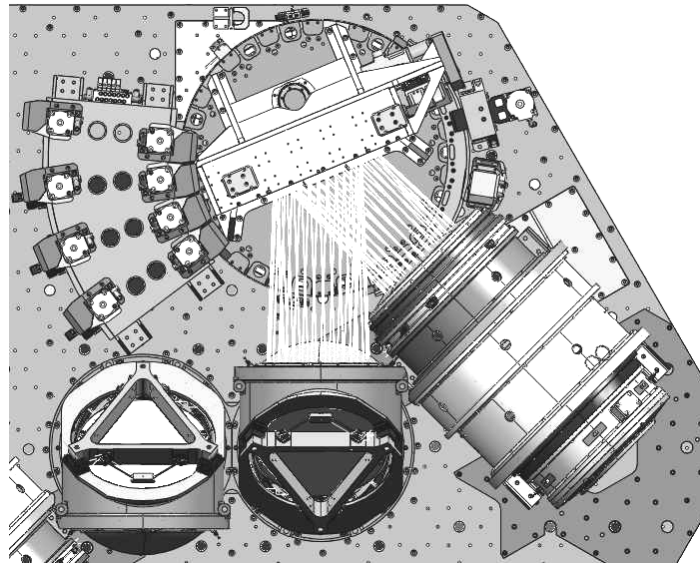
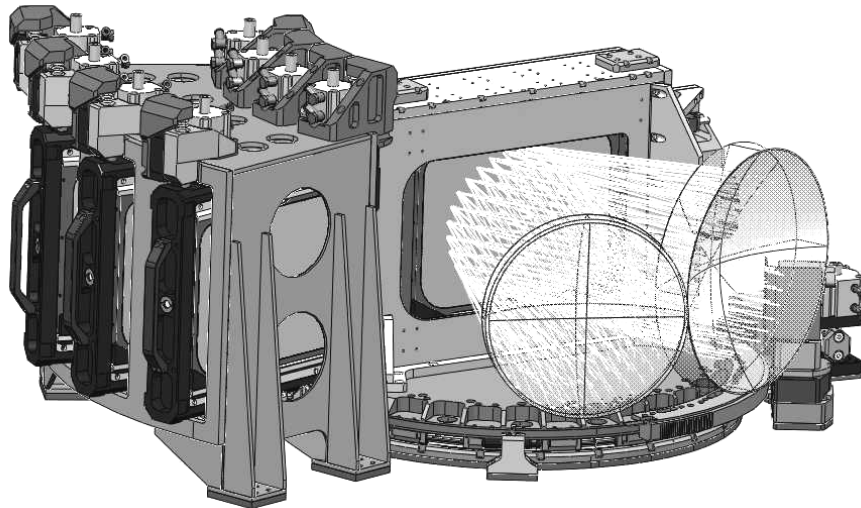


Figure 77. Grating with turntable moved to the load position.



**Figure 78. Grating with Turntable Moved to 22.5° angle of incidence (configuration 8).**

At 22.5° angle of incidence (configuration 8 as shown in Table 20) there is no vignetting of the light beam.



**Figure 79. Grating with turntable moved to 22.5° angle of incidence (configuration 8). There is no vignetting of the light beam.**

At 40.585° angle of incidence (configuration 3 as shown in Table 20), there is also no vignetting of the light beam.

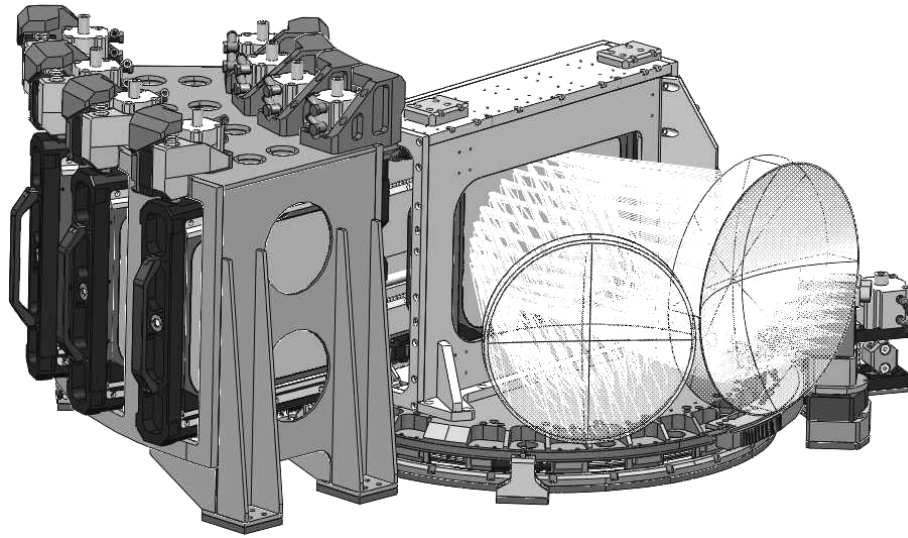


**Figure 80. Grating with turntable moved to  $40.585^\circ$  angle of incidence (configuration 3). There is no vignetting of the light beam.**

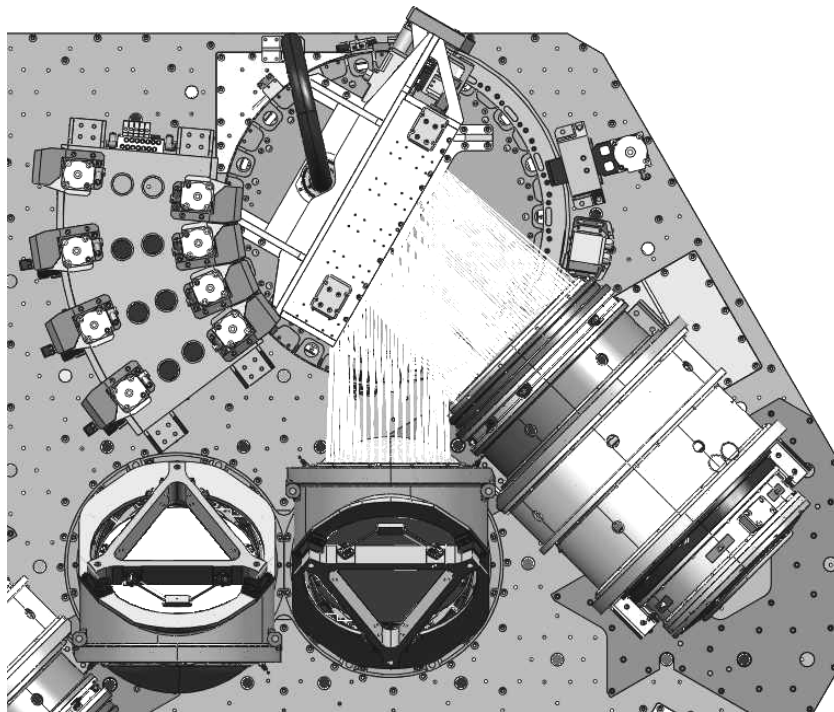


**Figure 81. Grating with turntable moved to  $60.084^\circ$  angle of incidence (configuration 7).**

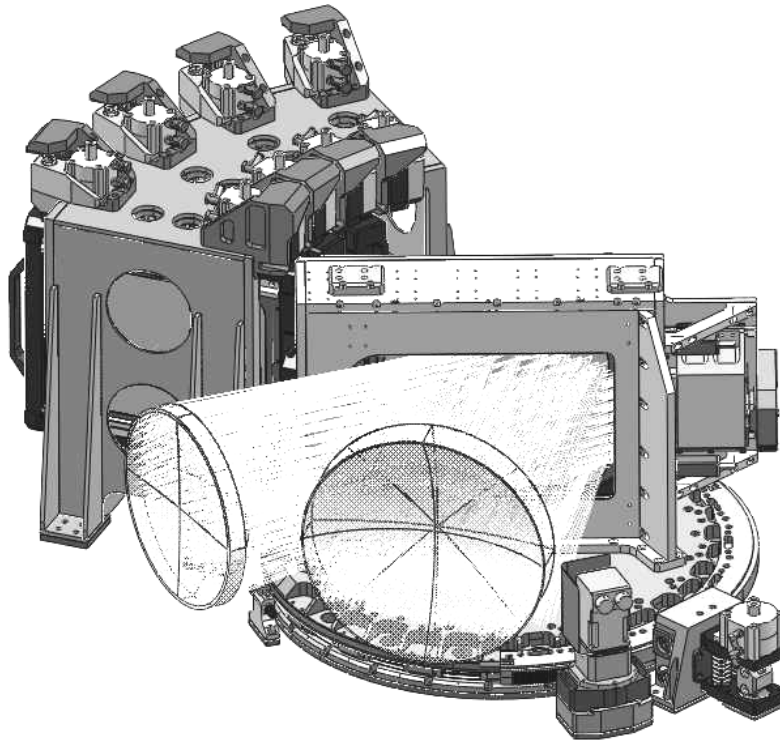


**Figure 82. Grating assembly with light beam at 60.084° angle of incidence (configuration 7).**

At 60.084° angle of incidence (shown in Figure 81 and Figure 82), vignetting of the light beam occurs at the grating. Using step CAD files generated from ZEMAX, we were able to verify that none of the light passed by the grating is vignettted by the grating structure, mounting bezel or mask.

A 25° knife edge chamfer inside of the clamp front face reduces stray light. The light shield on the left side of the opening and the grating bezel isolates the ball screw and THK rails from the camera's field of view.

The total weight of the current grating design with the roundhouse configuration is 381 lbs. This is with three gratings stored in each roundhouse and one in the clamp. There are two grating assemblies in Binospec.

#### **4.10 Science Camera and High Speed Shutter Assembly**

Figure 83 and Figure 84 show the science camera and shutter assembly located directly after the camera lens 9. The major elements of this assembly are:

1. **Camera housing:** This evacuated chamber houses the CCDs as well as the three axis piezo-driven flexure stage.
2. **Piezo stage:** A 500 μm X 500 μm X 1500 μm (focus) piezo-driven stage supports the science CCD and 2 flexure control CCDs on an invar cold plate.

3. **CCD/cold plate assembly:** The CCDs are mounted on an invar cold plate that is coupled via copper cooling foils to a main copper cooling strap. The main strap is connected to the cold plate within the LN<sub>2</sub> dewar.
4. **Ion pump:** The ion pump allows an operational vacuum level of  $5 \times 10^{-6}$  Torr or lower to be maintained within the dewar and camera housing.
5. **Vacuum gauge:** Allows remote monitoring of the vacuum within the camera housing and dewar.
6. **Isolation valve:** Allows connection of a vacuum pump to enable pump down of the system from atmospheric pressure to operational levels.
7. **Field flattener:** Lens 10 of the camera lens group is a field flattener that serves as a vacuum window. The lens is sealed against the camera housing with an o-ring. Atmospheric pressure acting over the surface area of the lens provides o-ring compression.
8. **Dewar:** The dewar holds 7.0 liters of LN<sub>2</sub>. The expected dewar hold time is 36-48 hours.
9. **High-speed shutter assembly:** The shutter is positioned directly in front of the field flattener. Dual shutter blades are actuated through ball screws by independently controller servo motors. The maximum speed of the shutter blades exceeds  $833 \text{ mm s}^{-1}$ . This allows the shutter to traverse the field in as little as 0.090 sec.
10. **LN<sub>2</sub> fill and vent ports:** Fill and vent ports for the LN<sub>2</sub> dewar are routed to the outside of the binospec thermal shroud. The dewars can be filled without removing thermal covers.

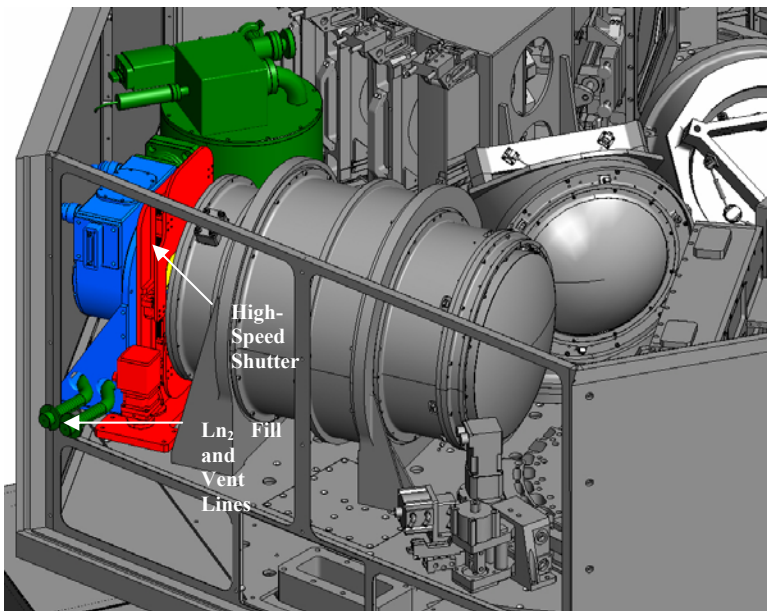
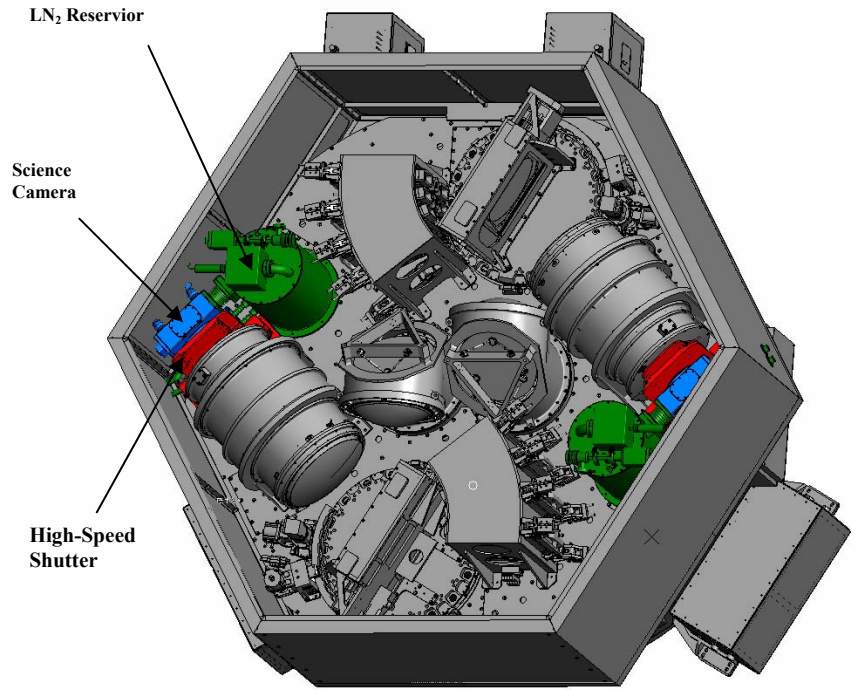
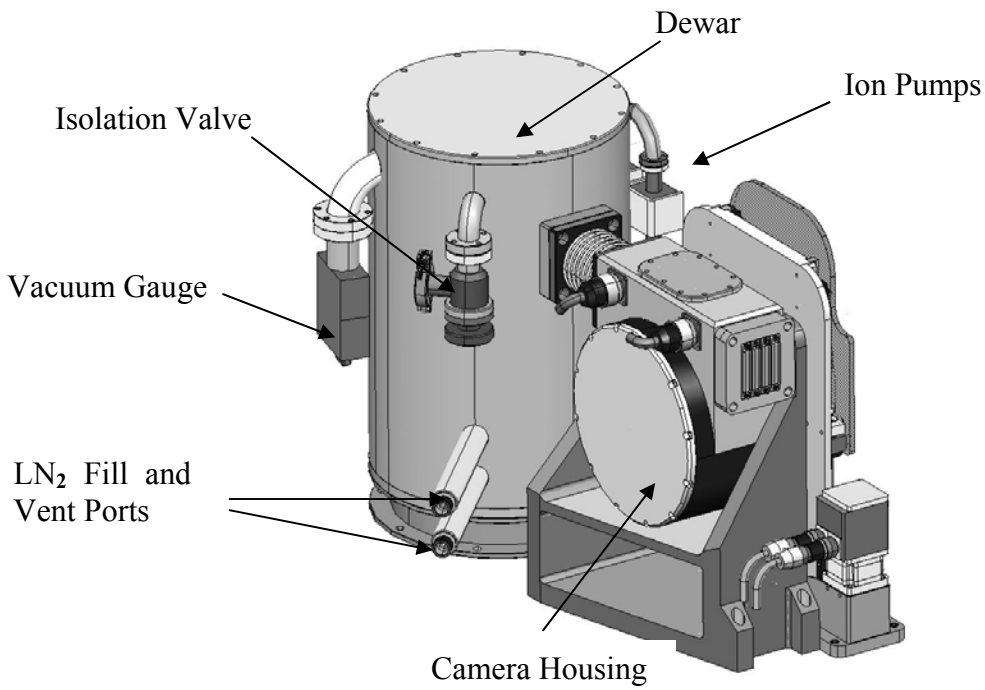


Figure 83. The high-speed shutter (red), LN<sub>2</sub> dewar (green), and detector assembly (blue).



**Figure 84. View showing the science detector, LN<sub>2</sub> dewar and high speed shutter.**



**Figure 85. Science Camera Assembly Rear View**

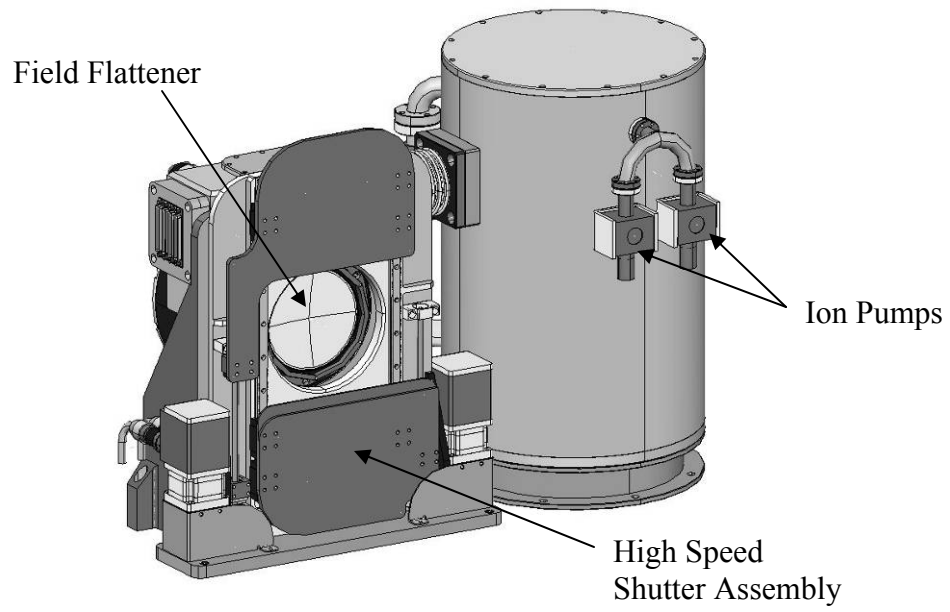


Figure 86. Science Camera Assembly Front View

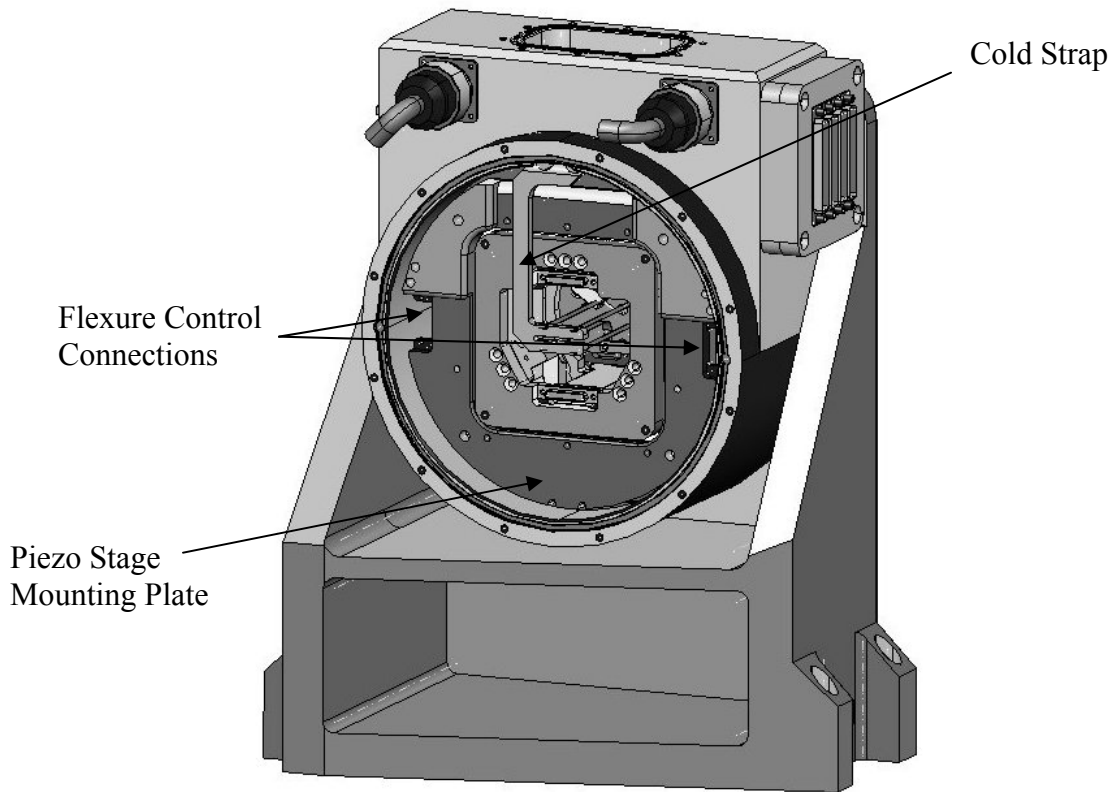
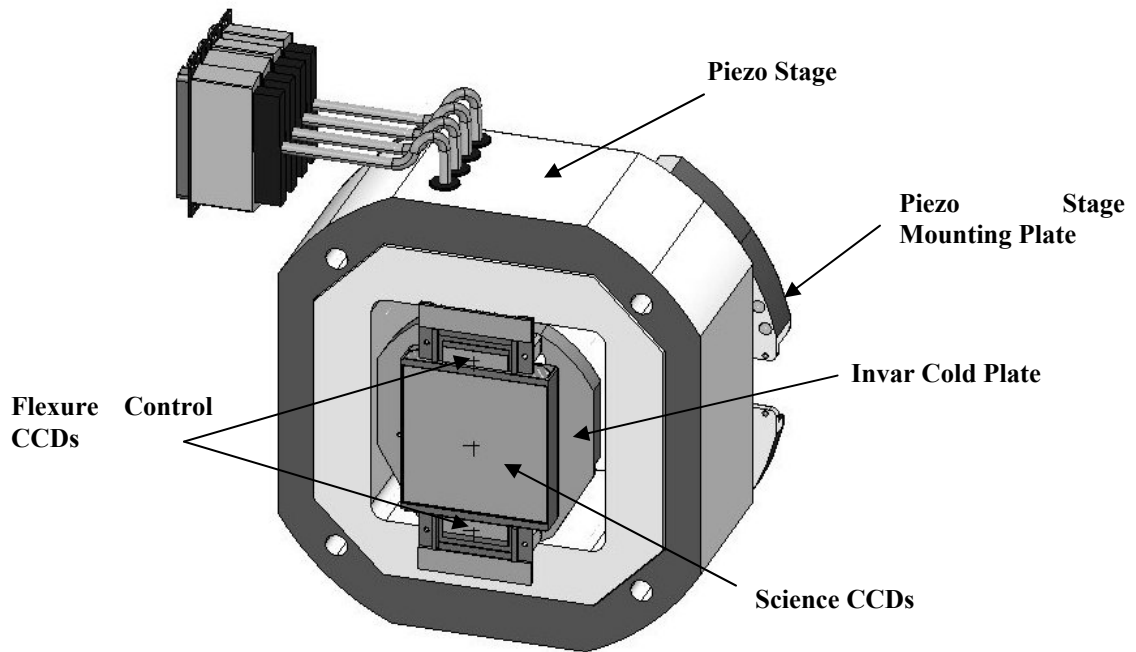


Figure 87. Rear view of the science camera assembly with the camera housing service cover removed.



**Figure 88. CCD/cold plate assembly on piezo stage**

The flexure control stage supports the science CCD as well as two flexure control CCDs. The stage provides 500  $\mu\text{m}$  x 500  $\mu\text{m}$  of X and Y travel, and 1500  $\mu\text{m}$  of focus travel for flexure compensation. PI (Physik Instrumente) supplies a variety of multi-axis nano-positioning devices for optical applications. However, they had nothing within their standard product line that met all of our requirements. We have worked with PI to develop a custom stage shown in Figure 88 that meets or exceeds all of our requirements including:

- 500  $\mu\text{m}$  of X and Y travel with 0.1  $\mu\text{m}$  resolution
- 1500 $\mu\text{m}$  of Z travel with 0.1  $\mu\text{m}$  resolution
- Overall dimensions of the stage 180 x 180 x 70 mm with rounded corners
- Center aperture of 100mm x 100mm: the CCD cold plate is supported by flexures that pass through the aperture to minimize the overall package height and balance the load about the neutral axis of the stage to minimize tilt errors. In addition, electrical and thermal connections pass through this aperture.
- Vacuum compatible to  $5 \times 10^{-6}$  Torr.
- Overall rotational stiffness of 833 Nm/rad.
- Push-pull load capacity of 6.7 lbs.

The XY portion of the device is a flexure stage actuated by PI's traditional piezoelectric actuators. The Nexline or "fingerwalker" line of actuators is used for the Z axis to achieve longer travel while meeting the stiffness and load capacity requirements. The Z motion is implemented with three Nexline actuators due to space and geometric constraints. We therefore acquire tip/tilt control of the science CCD as part of the

package. It turns out that this control is useful because flexure of the instrument causes the optical axis to be slightly tilted with respect to the CCD, and the resulting differential focus across the detector causes a slight image blur.

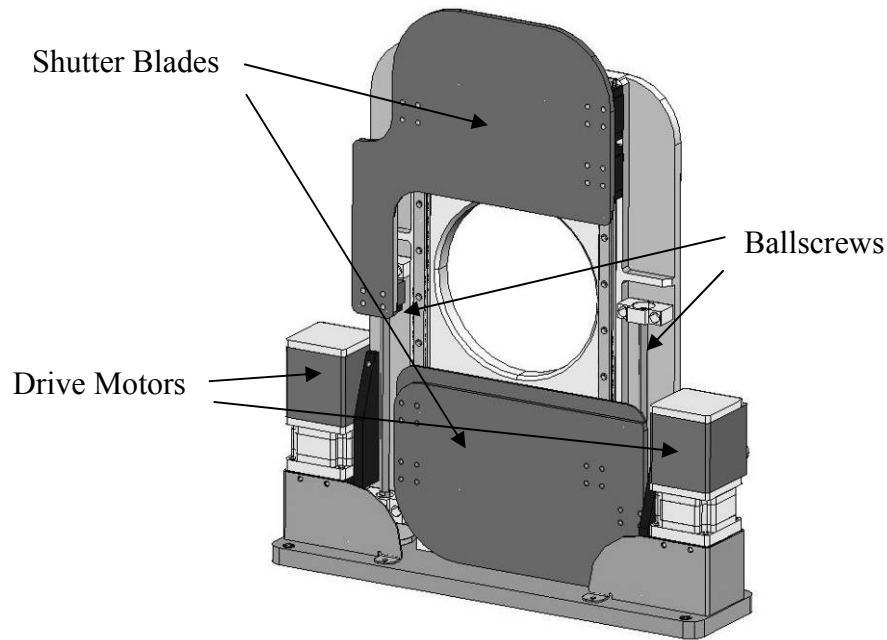


**Figure 89. High Speed Shutter Assembly**

Each shutter blade is individually servo driven to provide allow a fixed width aperture to be scanned across the science CCD. Each blade is coupled to a servomotor through a 10 mm pitch ballscrew. To reduce the overall package size, the motor is folded back 180° on the ballscrew and the torque is transmitted through two 2 inch gears. The maximum speed of the shutter blades is  $833 \text{ mm s}^{-1}$ . This allows the shutter to open in as little as 0.090 sec.

#### **4.11 Collimator and Camera Lens Assemblies**

The collimator assemblies mount to the bottom surface of the optical bench and are orientated as shown in Figure 90. The first lens in each collimator assembly is located directly beneath the filters as shown in Figure 91. Within each collimator there are nine lenses arranged in three groups and a fold mirror that redirects the light parallel to the bottom surface of the optical bench. Figure 92 shows the two camera assemblies on the main optical bench.

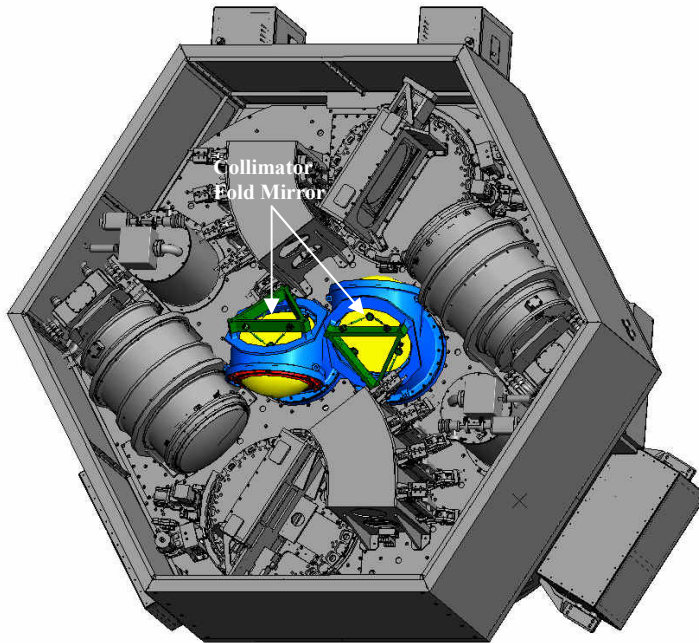


**Figure 90.** The collimators from below. A 45° mirror folds the light parallel to the optical bench.

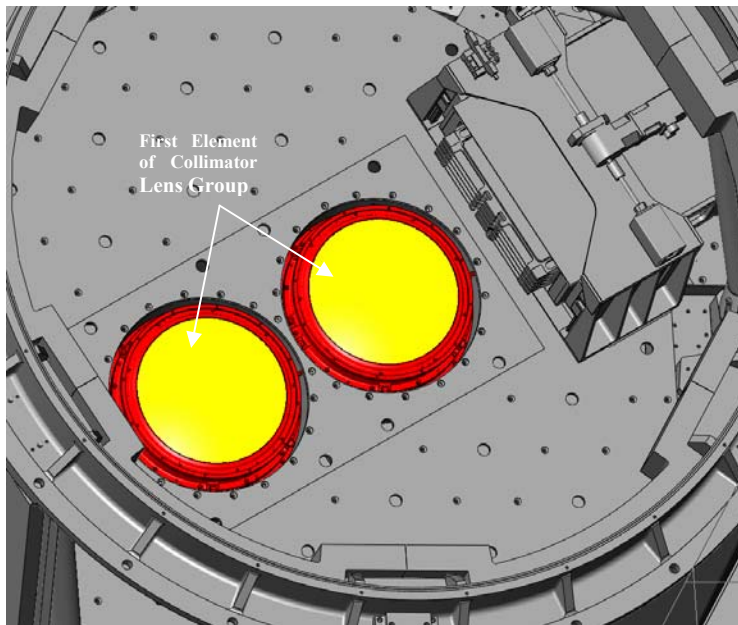


**Figure 91.** View looking from above the focal plane to show the first element of each collimator lens group mounted to the optical bench.

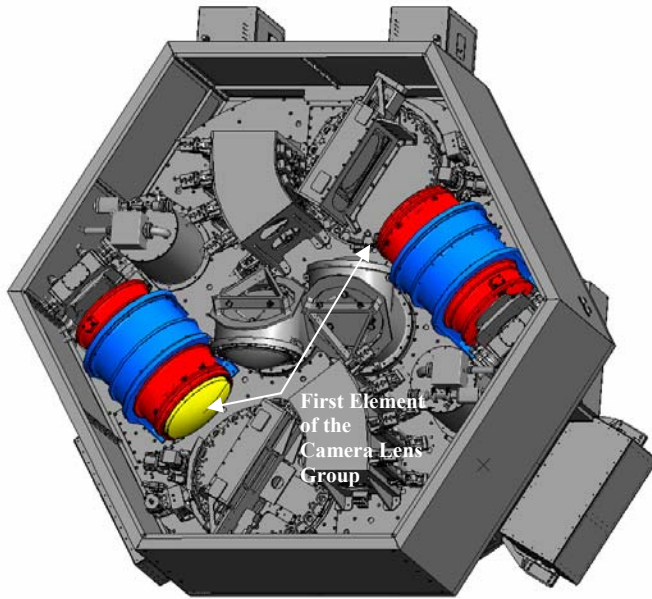


Figure 92. View looking from below that shows the two camera lens barrels.

## 4.12 Flexure Control System

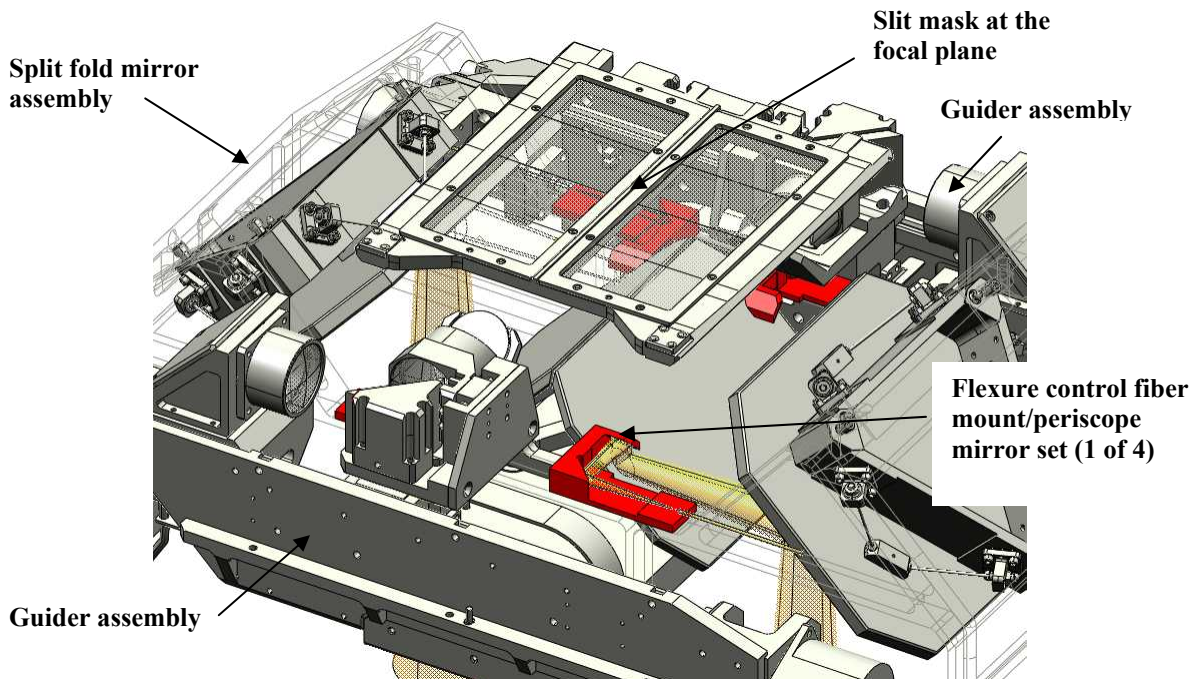


Figure 93. View of the flexure control system in relation to the split fold mirror assembly, two guider assemblies, and the slit mask. The inner bench structure is removed for clarity.

System flexure will be measured by imaging two spots of light onto flexure CCDs mounted within each CCD camera assembly. A light box containing a 6 inch integrating

sphere, wavelength calibration lamps, flat lamps, two filter wheels, a focusing lens, and a shutter will be mounted outside of the thermal enclosure of Binospec. The light from this assembly is focused onto four optical fibers, which are then routed through the thermal enclosure to mounts just below the slit see Figure 93 and Figure 94). The light leaves the four fibers, is folded by small periscope mirrors, and continues through the optical system following the same path as astronomical objects. Any movement of this light on the CCD surface can be directly attributed to structural and thermal flexure of the system. These movements will be corrected with the piezo flexure control stage on which the CCDs are mounted.

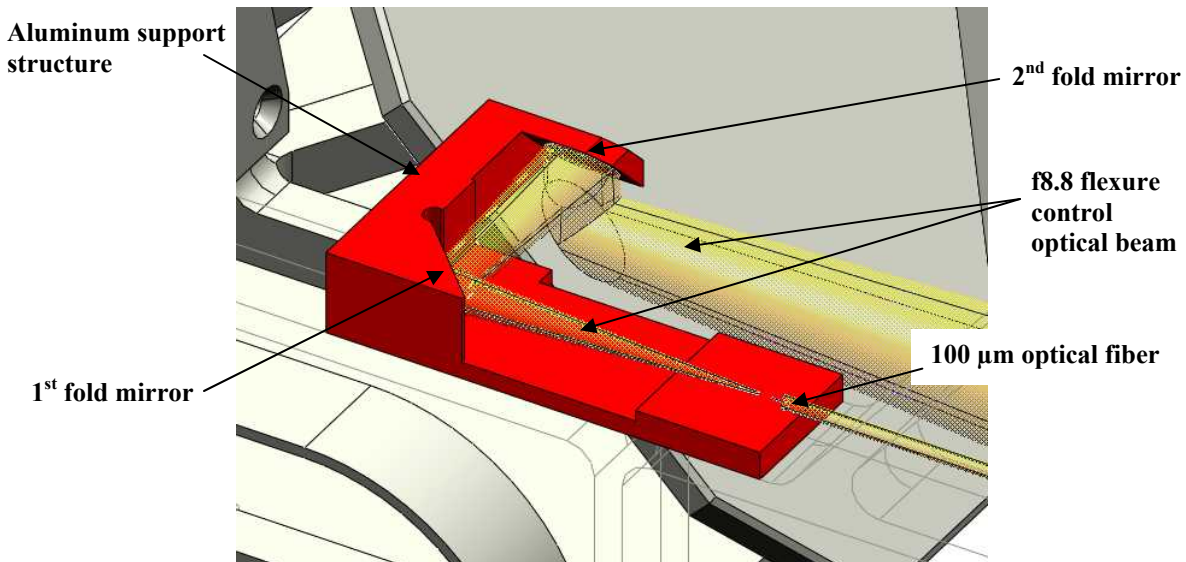


Figure 94. Close-up of flexure control periscope mirror and f8.8 beam.

### 4.13 Calibration/Derotator Assembly

The calibration/derotator subassembly serves two purposes: (1) It provides an external platform, thermally isolated from the Binospec optics, for the calibration system. The calibration system light is injected into an integrating sphere, and the light leaving the integrating is baffled and sent to a rear projection screen that illuminates the slit mask focal plane. The rear projection screen can be shuttled into and out of the optical path as commanded. (2) The calibration/derotator assembly also derotates the service umbilicals for the instrument that pass through a service port in the inner cone of the MMT primary mirror cell. These service umbilicals include:

- System main electrical power
- Fiber-optic communication
- Pneumatic supply and exhaust
- Coolant supply and exhaust

This assembly mounts to the same mounting ears on the instrument rotator bearing that support the f/5 Wave Front Sensor that is used with Hectospec/Hectochelle and Megacam. The assembly is similar in size to the existing Wave Front Sensor but is one

third the weight at about 185 lbs. Its mounting position relative to Binospec is shown in Figure 95 and Figure 96.

The minimum clearance between the calibration screen and the upper cover/entrance window of Binospec is 1.45 inches as illustrated in Figure 96. Figure 97 shows an underside view of the calibration screen when it is deployed for calibration.

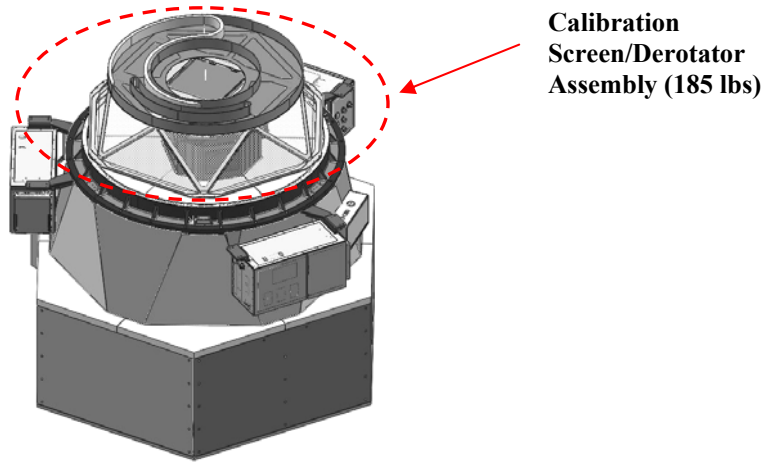


**Figure 95. Calibration screen/derotator in relation to Binospec.**

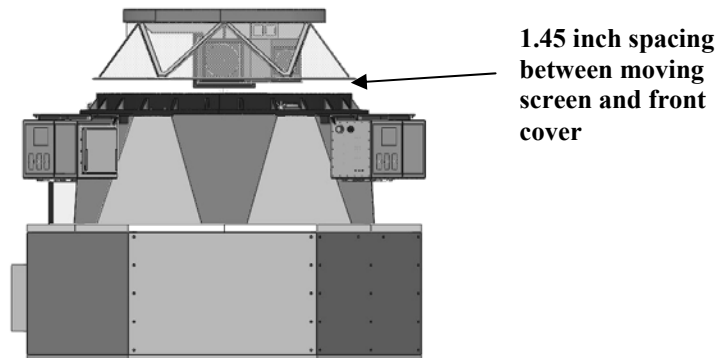


**Figure 96. Calibration screen/derotator in relation to Binospec (side view).**

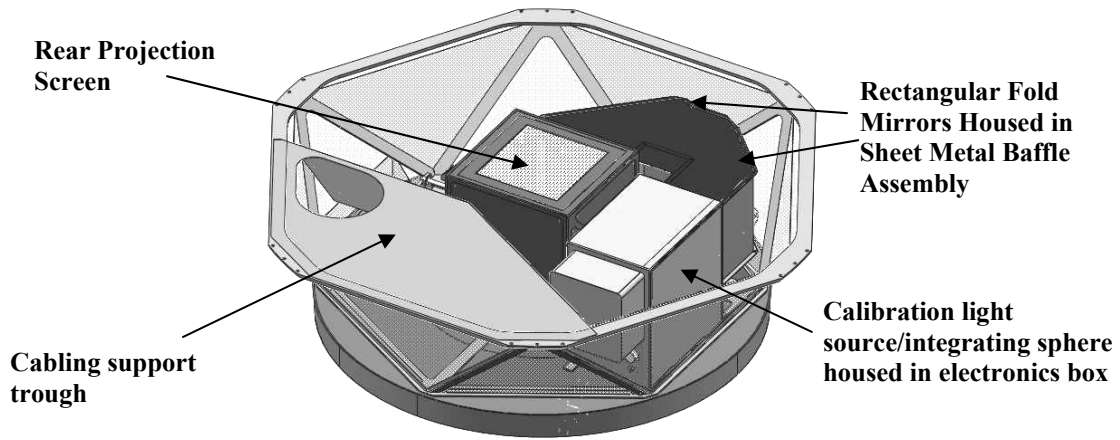


Figure 97. Inverted calibration screen/derotator assembly with screen deployed.

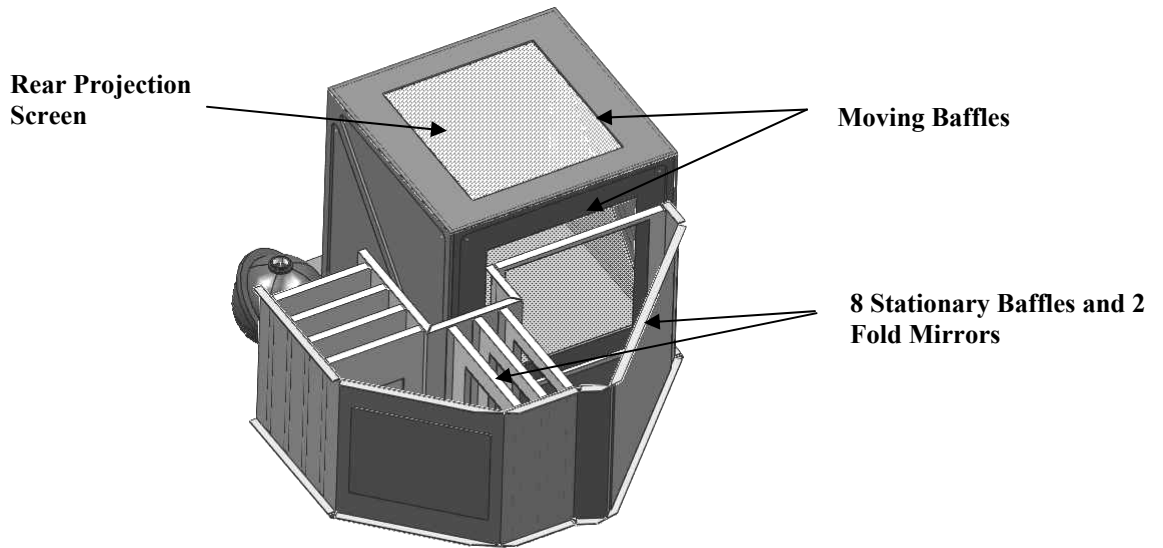
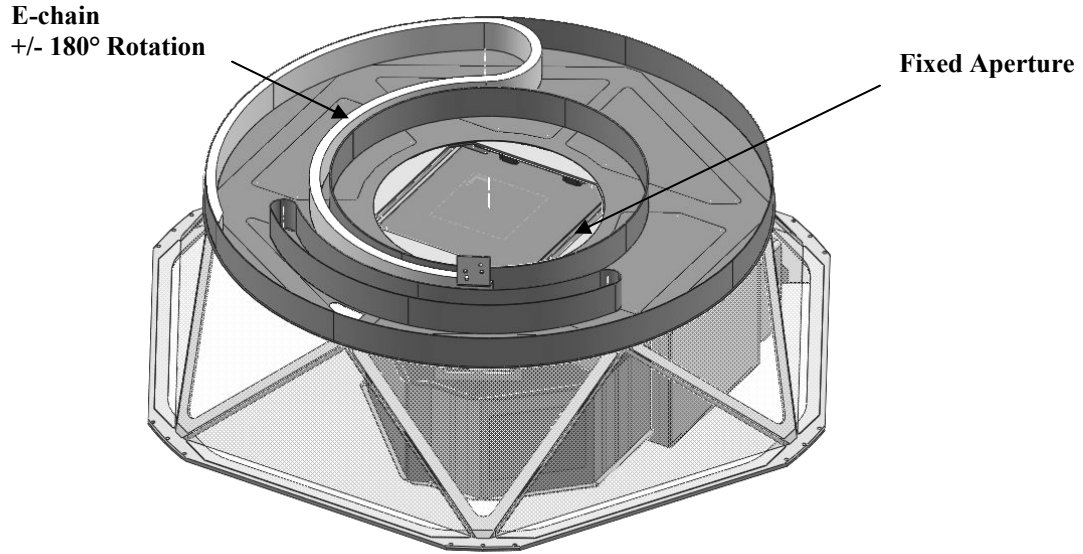
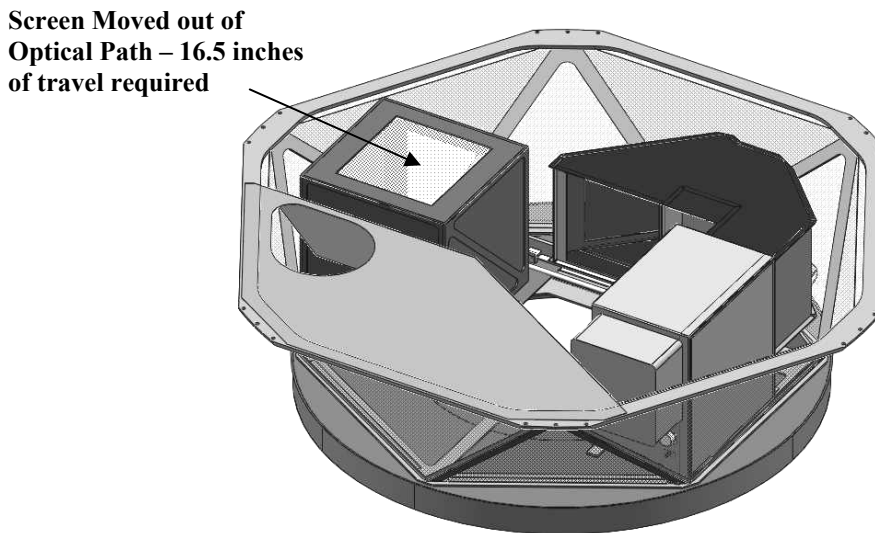


Figure 98. Baffle assembly – baffles exposed.

A baffle system, shown in Figure 98, of sheet metal construction conforms to the prescription generated by Deborah Woods on August 1, 2007.



**Figure 99. View of zenith-pointed calibration screen showing cable derotator.**



**Figure 100. Inverted calibration screen/derotator assembly with screen retracted.**

The actual and required apertures for the calibration screen are listed in Table 21 and Table 22.

Figure 99 shows an overhead view of the Calibration Screen/Derotator assembly. The cable derotator is based on the successful f/5 Wave Front Sensor design. The energy chain interfaces to connection points in the MMT Cassegrain cone. This configuration will provide a minimum of +/- 180° of rotation. The f/5 Wave Front Sensor achieves approximately +/- 200° of rotation, and we should be able to duplicate this without issue. Figure 100 shows the screen retracted for observation.

**Table 21 - Clear apertures – screen retracted.**

Position	Distance from Primary Vertex	X direction req'd (mm)	X direction actual (mm)	Y direction req'd (mm)	Y direction actual (mm)	Circular Aperture Diameter (mm)
Attic Opening*	35.23 inches	-169 mm, +235 mm	-206 mm, +241 mm	±176 mm	±206 mm	519 mm
Edge Baffle	35.96 inches	-166.9 mm +230.3 mm	+238.1 mm	NA	NA	NA
Screen Base	36.21 inches	±166.4 mm	-174.6 mm	NA	NA	NA

\*The other clear apertures are also asymmetric, but only this case was explicitly checked due to limited space. The wider opening is needed over the wave front sensor patrol region.

**Table 22 - Clear apertures – screen deployed.**

Position	Distance from Primary Vertex	X direction req'd (mm)	X direction actual (mm)	Y direction req'd (mm)	Y direction actual (mm)	Circular Aperture Diameter (mm)
Rear Projection Screen	51.98 inches	±134.4 mm	±152.4 mm	±142 mm	±152.4 mm	NA

### 4.13.1 Handling Cart

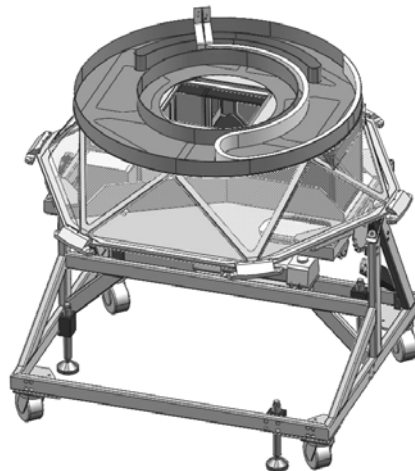


**Figure 101. Calibration screen on its handling cart**

The calibration screen assembly will be moved around on its own handling cart similar in design to the current f/5 Wave Front Sensor handling cart. The calibration screen on its

cart is shown in Figure 101. This cart design features a hydraulic actuation system which allows the instrument to be tilted 90° for a reduced storage footprint.

#### 4.13.2 Cable Connection to the Telescope

Figure 102 shows the relation of the calibration/derotator assembly and the primary mirror cell, as well as the cable attachment points.

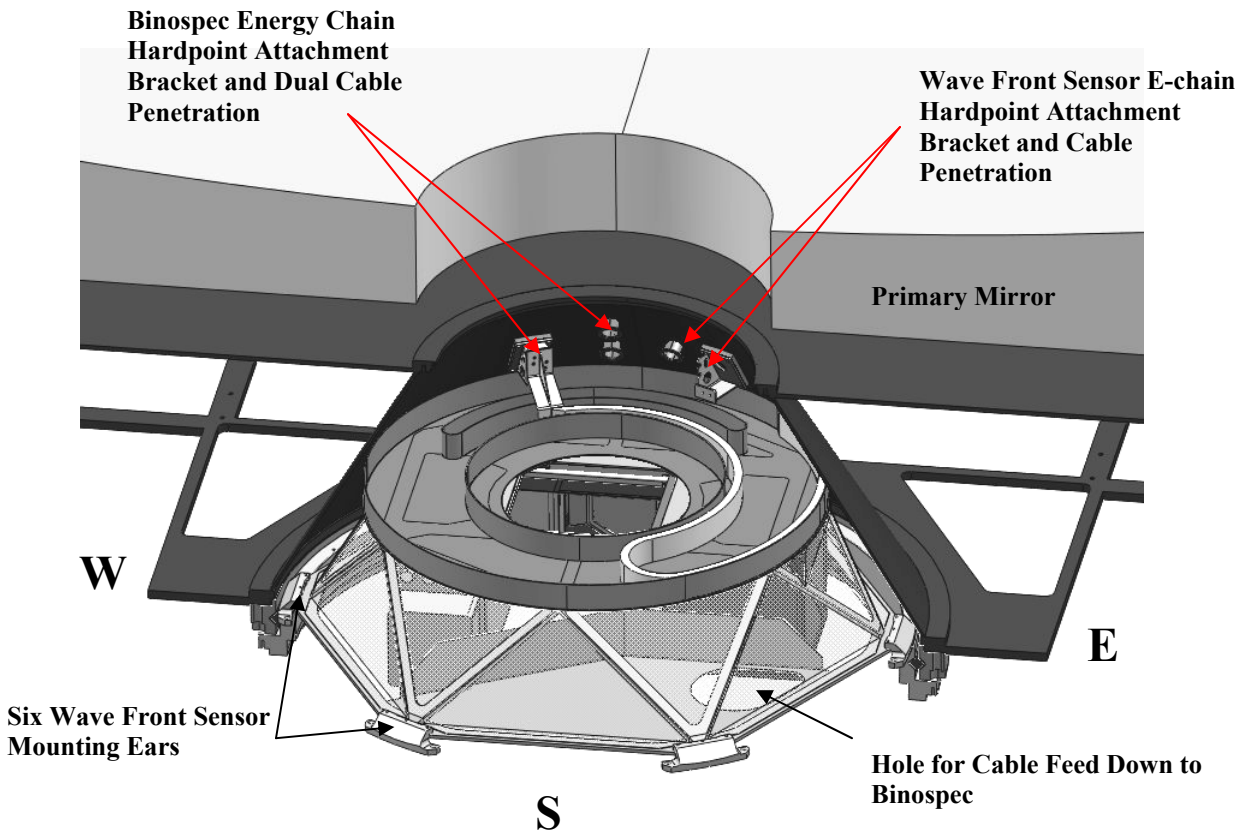
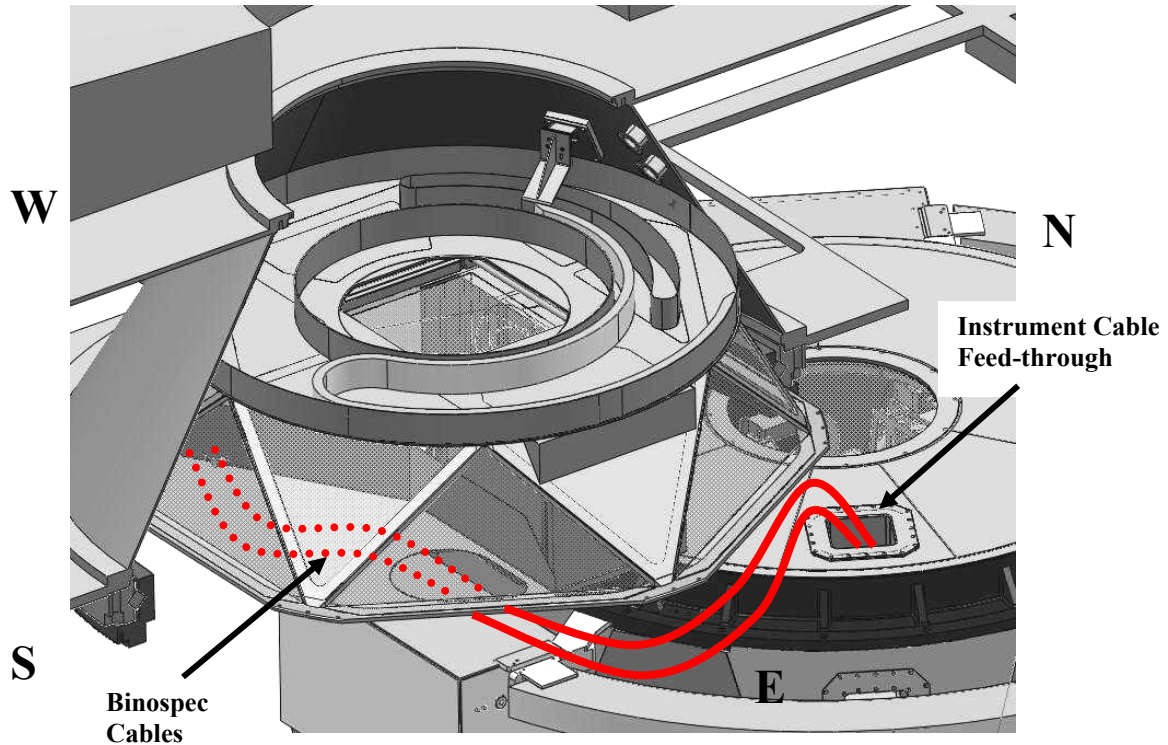


Figure 102. Calibration/derotator assembly mounted into primary mirror cell



**Figure 103. Binospec offset from IR bearing during installation**

Installation of the calibration screen and connection of cabling to the telescope and through to the instrument will proceed as follows:

1. Prior to calibration screen installation:
  - a. Ensure that the backlit screen is in the retracted position (see Figure 100). This allows a technician to look and reach up through the opening to connect the e-chain and all umbilical connections.
  - b. Ensure all Binospec cables are tucked neatly up into the cabling support trough.
2. Raise the calibration screen into position (noting the correct orientation with respect to telescope north) mating it to the wave front sensor mounting ears.
3. Install 18 mounting bolts.
4. Stand up in the clear aperture of the calibration screen and do the following:
  - a. Connect the e-chain to the designated telescope hardpoint.
  - b. Make power, communications, air and coolant connections.
5. Begin moving Binospec into position below the IR bearing. Stop once the instrument cable feed-through (see Figure 103) is just within the perimeter of the IR bearing.
6. Feed all umbilical connections from the calibration screen cable support trough through the instrument cable feed through (see Figure 103).
7. Continue moving Binospec into position underneath the IR bearing.
8. Pull all umbilical connections through the instrument cable feed through.
9. Raise Binospec to mate the mounting flange with the IR bearing and install all instrument mounting hardware.
10. Connect all umbilical connections to Binospec.

## 4.14 Thermal Covers

In order to enhance the thermal stability of Binospec, we have designed a thermal cover system that serves several functions.

- Maintains a minimum instrument thermal time constant of 36 hours
- Minimizes dust infiltration
- Minimizes stray light infiltration

In addition, the thermal cover system has been designed to provide to provide easy access to areas of the instrument which require regular access such as the slit mask, filter and grating cassettes. Covers can also be removed for complete access to internal systems for service and maintenance.

### 4.14.1 Insulating Panels

Binospec with its complete system of thermal covers installed is shown in Figure 104.

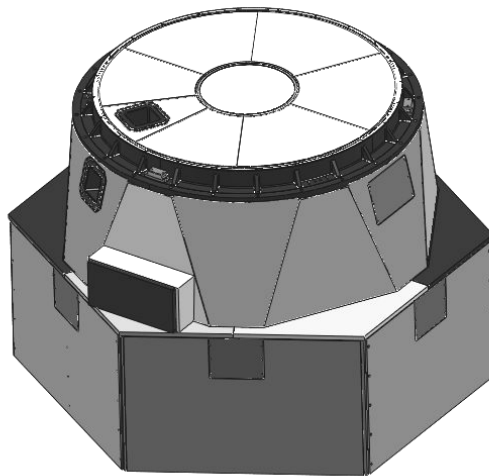


Figure 104. Binospec with all thermal covers installed.

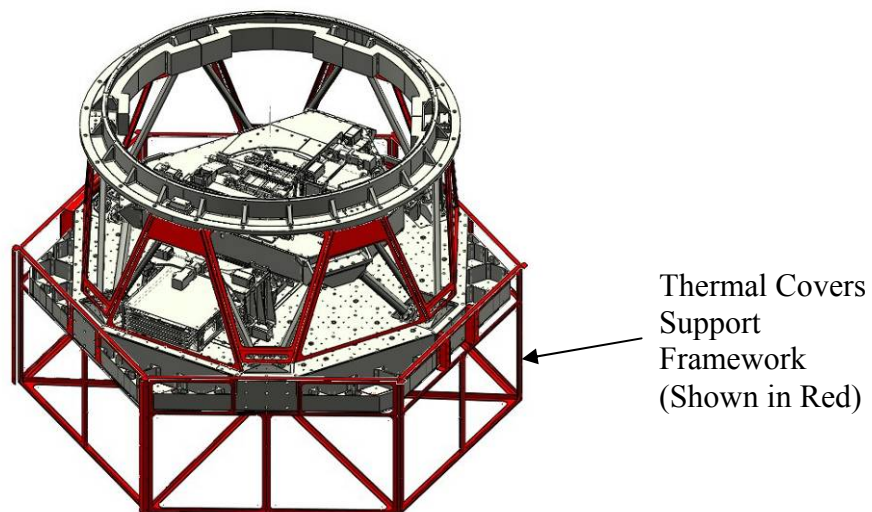
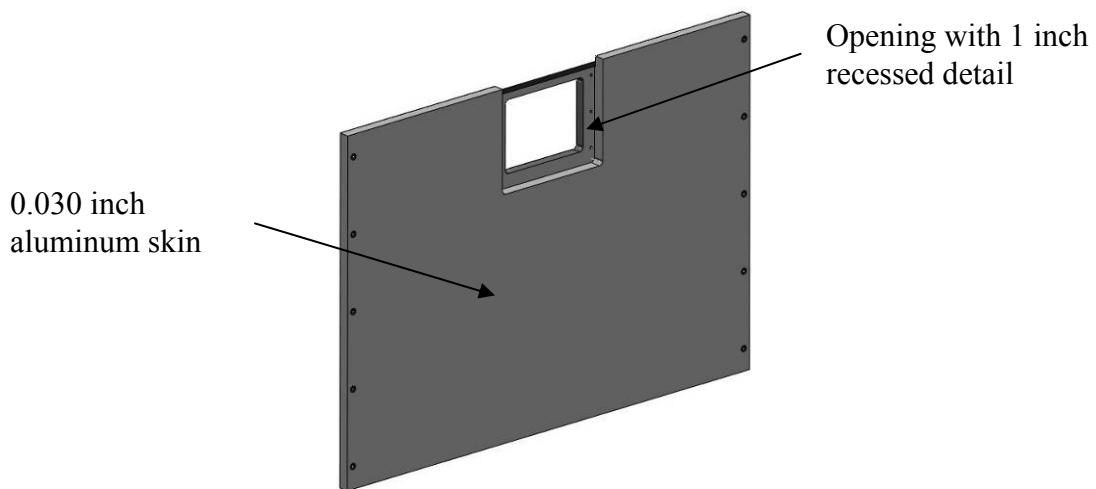


Figure 105. Binospec Thermal Covers Framework

The covers are mounted on a lightweight aluminum framework shown in Figure 105. The frame is attached directly to the main structure. Each panel is attached to the frame with captive fasteners.

A typical removable panel is shown in Figure 106. Each removable panel has an outer aluminum skin of 0.03 inch thickness. Bonded to this skin is a 2 inch thick layer of insulation. On panels, such as the one in Figure 106 that have a recessed detail, two sheets of 1 inch thick insulation are bonded back to back. This allows such details to be created simply by cutting the profile of two separate sheets and bonding them together as opposed to milling the detail into a 2 inch thick sheet. All sides of the insulation other than that bonded to the aluminum skin will be covered with a thin mylar coating as additional protection against the insulation flaking off of the cut surfaces.



**Figure 106. Typical Removable Panel**

Owens Corning 150 extruded polystyrene is used as the insulation for both the overall instrument thermal covers and also for insulating the electronics boxes. This insulation was selected for the following reasons:

- It has an R value 5.4 per inch @ 40°F (5.0 per inch @ 75°F).
- It has a relatively low density,  $\rho = 1.5 \text{ lb/ft}^3$ .
- It has continuous thin skin on the front and back surfaces minimizing particulate contamination.
- It is available in large sheets (4 ft X 8 ft) in 1, 1½, 2, 2½, and 3 inch thicknesses.
- It can be cut easily and cleanly with a sharp razor blade. The cut surfaces are smooth and do not flake off material. For extra protection, however, all surfaces not bonded to the aluminum will be covered with mylar.

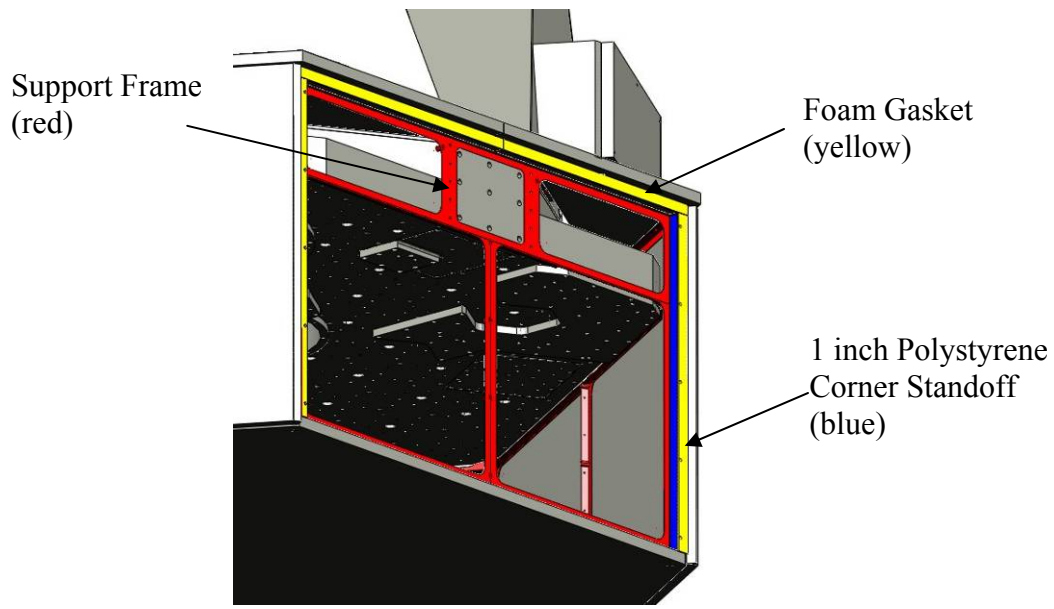


**Figure 107. Lower panel removed showing frame and foam gaskets**

Figure 107 shows details on how the sealing is achieved when the cover is removed. When the panel is attached to the frame, a thin foam seal between the frame and the panel (bonded to the frame), prevents air and dust from entering the instrument and also minimizes convection from inside the instrument to the telescope chamber.

#### **4.14.2 Access Ports**

There are specialized access ports in the thermal cover assembly for the following Binospec elements:

- Slit mask cassette
- Filter cassette
- Handling cart mounting hardpoints

The gratings are loaded into the grating roundhouse by removing the lower panel closest to the roundhouse load port.

#### **4.14.3 Motion Control Cable Thermal Transition**

Figure 108 shows a close-up of one of two transition panels on Binospec. The transition panel provides perforations that allow cables to cross from the exterior to the interior of Binospec while sealing out dust and minimizing air exchange.

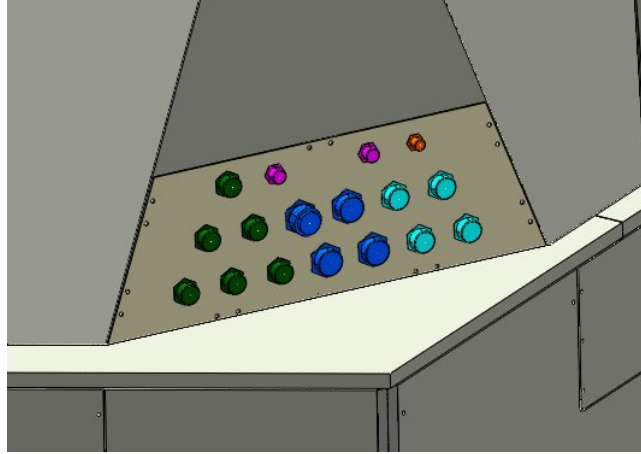


**Figure 108. One of the two electrical interface panels, located 120° apart.**

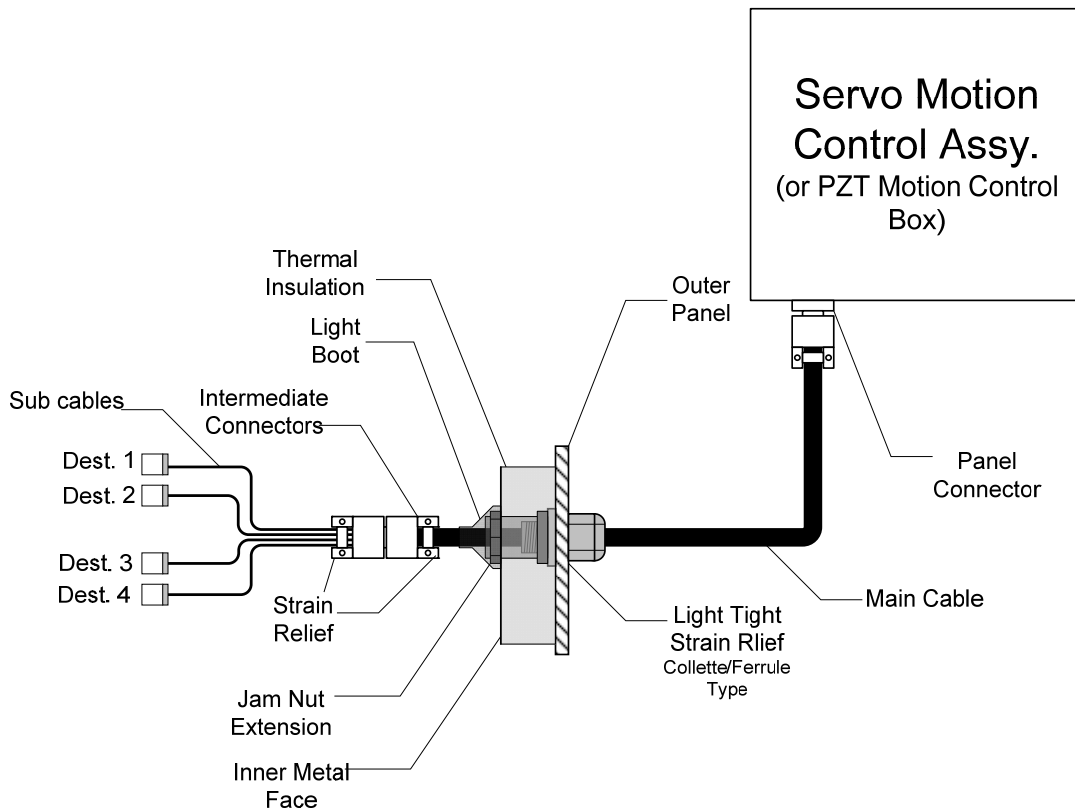


**Figure 109. Binospec cable penetration detail with collet and boot to seal against light and air leaks.** Cables will exit the servo motion control box using circular, military style connectors and cylindrical, jacketed cable. These cables will have an integral collet-type cable strain relief that is light tight after clamping (see Figure 109). The cable strain relief will mount on the external panel of the thermal shroud using a jam nut and the cable will pass through the thermal insulation to be processed into an intermediate in-line connector. A light tight boot on the inside panel of the thermal insulation will provide additional sealing against air and light leaks. The mating in-line connector will divide into four

subcables, as shown in Figure 109, which will each be routed to the destination mechanism.

Cables are grouped by function (e.g. encoder feedback, drive phases, etc.) and carry four axes. Subcable lengths will differ and be established at time of assembly. This method gives us a simple transition through the thermal barrier, light and air tight, positive cable strain relief, and the ability to disconnect mechanism cables from cables exiting the shroud for ease of service. The cables from the PZT motion control assembly will be handled in a similar fashion but the subcables will route to the two cameras.

#### 4.14.4 Thermal Model of the Motion Control Electronics Assembly

A thermal model of one of the most complex external electronics assemblies, the motion control electronics assembly, is being built to test the effectiveness of the liquid cooling system and of the extruded polystyrene insulation.

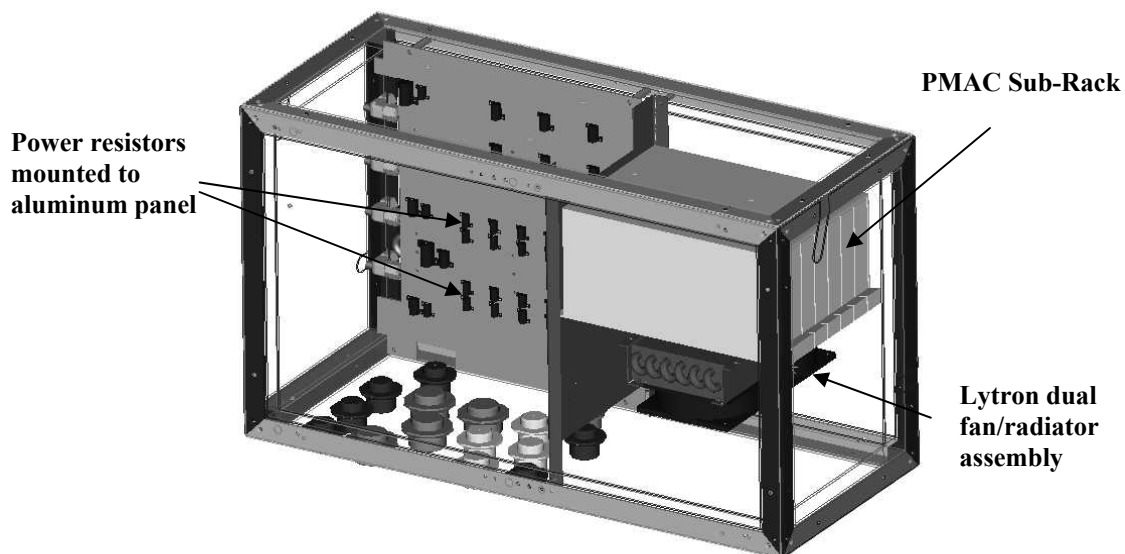


**Figure 110. Motion control electronics assembly thermal model (front view).**

The box is constructed of L-shaped aluminum bar bolted-together with sheet aluminum covers. The same Owens Corning Foamular 250 extruded polystyrene insulation used for the instrument thermal covers lines the inside of the thermal box. The insulation thickness in the box is 1 inch. All components are mounted on aluminum panels, supported by non-metallic standoffs to the aluminum outer covers. The non-metallic standoffs minimize conduction to the outside of the box.

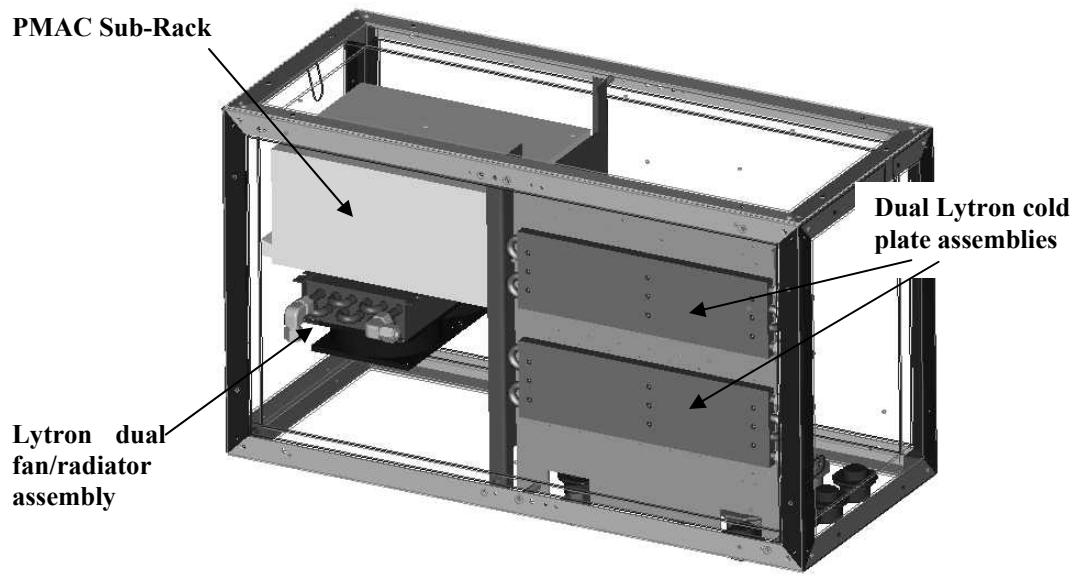


**Figure 111. Motion control electronics assembly thermal model (rear view).**

Heat extraction is accomplished by using the following:

1. A Lytron 4120 fan/radiator type heat exchanger: this unit will be able to extract approximately 25 watts per °C of coolant-to-air  $\Delta T$ . The liquid pressure drop at 0.375 gallons/min is 0.8 psi.
2. Dual Lytron CP10G20 cold plates: these units can extract 70 watts per °C of coolant-to-mounting plate  $\Delta T$ . The liquid pressure drop at 0.375 gallons/min is 0.4 psi per plate.

The total heat load of the actual MCEA box is 234 Watts. For our mock-up, this heat load will be simulated with power resistors mounted strategically throughout the box. Blocks of foam will also be inserted as required to simulate the various air-flow restrictions in the actual box.

The test has two main goals. (1) Ensure that the air temperature within the box does not exceed the maximum operational temperature rating of the most sensitive components in the box. This is the Delta Tau CPU which is rated for 50°C (122°F) ambient. (2) Ensure that the insulation does a good job of minimizing conduction of heat to the outside of the box. Ideally, all heat would be extracted through the liquid coolant.

We plan on running coolant at near-ambient temperatures to minimize condensation on metal plumbing. At the highest expected operational ambient temperature of 21°C (70°F), all of the 234 watts could be extracted using only the radiator with a modest 10°C air temperature rise. This puts the maximum expected internal air temperature of the box at 31°C (88°F), well below the maximum operational limit of the Delta Tau CPU.

Although the cooling load could theoretically be handled with the radiator alone, a cold plate will still be used. The motor drives are designed to dissipate heat to their mounting

surface making a cold plate a more practical method to extract heat from these components.

#### 4.15 Servo-Driven Stage Summary

**Table 23 – Summary of Binospec Servo Axis Details**

Axis	Max Load (lb)	Ballscrew Pitch (mm)	Gear Ratio	Req'd Torque (oz-in)	Available Torque (oz-in)	Safety Factor
Slit Mask Cassette Elevator	50	10	30:1	2.31	53	21.9
Slit Mask Insertion Stage	9	6	n/a	6.37	53	7.3
SOG – Lens Translation Stage	4.5	6	5:1	0.75	53	69.7
SOG – Camera Focus Stage (2.25 lb thrust PI micro-translation stage)	0.60	n/a	n/a	n/a	n/a	2.8
Wave Front Sensor X Translation Stage	10	6	n/a	7.1	53	6.5
Wave Front Sensor Y Translation Stage	25	6	n/a	17.7	53	2.0
WFS – Camera Focus Stage (2.25 lb thrust PI micro-translation stage)	0.30	n/a	n/a	n/a	n/a	7.5
Guider Translation Stage	6	2	n/a	1.4	53	36.9
Guider Relay Optic Focus Stage (2.25 lb thrust PI micro-translation stage)	.67	n/a	n/a	n/a	n/a	2.4
Filter Cassette Elevator	80	10	30:1	3.7	53	13.3
Filter Insertion Stage	28.5	10	5:1	7.9	53	5.7
Grating Insertion Stage	83	8	13.3:1	6.91	53	6.7
Grating Tilt Stage	41.2 ft-lb	n/a	1120:1	11.9	53	3.45
Shutter Blades	2.5	10	n/a	2.96	53	16.9
Calibration Screen	9.3	8	n/a	8.29	53	5.4

## 5 Structural Analysis

### 5.1 Introduction

Our structural design goal for the structure and optical mounts is to minimize solid body deflections of the optical elements relative to the slit mask while maintaining their internal stresses and surface deformations at an acceptable level. Motions of Binospec's optical bench relative to the MMT's optical axis are less critical since these can be guided out. In addition, we require that internal stresses in the optics and all mechanical components remain at an acceptable level when Binospec is subjected to 3g loads during shipping, assembly and handling and during 75 °F temperature changes.

Our original goal for flexure measured from the slit mask to the science CCDs was less than one pixel of image motion between zenith and horizon pointing. For an instrument of Binospec's size and weight, this goal quickly proved to be unrealistic. Our goal then became limiting the image motion to the minimum consistent with Binospec's 6000 pound weight budget while preserving image quality under all expected operating conditions. We added active flexure control to prevent the expected image motion from degrading image quality during long observations and to allow more convenient instrument calibration.

The image motions at the detector due to optical element deflections were calculated with Zemax, and are summarized in section 11.3. Lens deflections and deformations can arise from (1) gravity loads, (2) pressure head due to the lens couplant, (3) temperature changes and temperature gradients, and (4) assembly loads caused by bolting bezels together against slightly imperfect faces. The pressure head at the bottom of the largest lens when it is on edge is 0.55 psi and the corresponding load on the lens face is ~45 pounds, slightly more than the total weight of the lens. The coordinate system used for for Binospec, including the finite element analysis, is shown in Figure 112.

We summarize what we consider to be allowable stresses in each material in Table 24. For the glass and calcium fluoride lenses we allow a maximum of 500 psi. For the salt lens we allow a maximum of 100 psi. For the aluminum elements we allow a maximum stress of half the yield strength. For epoxy we allow a maximum stress 1/6 of the ultimate tensile strength of the epoxy.

Table 25 lists the weights of the Binospec components in the current 3D CAD model and the weights of components in the finite element models. Ideally these are identical, but the finite element models are not as complete, and show slightly less weight.

Table 24. Material properties.

Material	CTE, ppm/ <sup>0</sup> F	Young's Modulus (10 <sup>6</sup> psi)	Poisson's Ratio $\nu$	$\rho$ , lb/in <sup>3</sup>	Allowable Stress, psi
<b>Optics</b>					
BAL15Y	4.22	11.356	0.236	0.105	500
FSL5Y	4.94	9.021	0.229	0.089	500
PBM2Y	4.78	8.281	0.223	0.130	500
PBL6Y	4.61	8.774	0.205	0.101	500
BAL35Y	3.17	12.777	0.244	0.117	500
CAF2	10.50	11.000	0.260	0.115	500
BSM51Y	3.50	13.067	0.256	0.121	500
S-FPL51Y	7.57	10.384	0.302	0.132	500
NACL	24.40	5.798	0.252	0.078	100
Zerodur	0.00	13.200	0.240	0.091	500
<b>Nubs</b>					
Ti6Al4V	5.10	16.500	0.310	0.160	60000
Kovar	3.00	20.000	0.317	0.302	16000
304LSS	9.56	28.000	0.290	0.290	16000
4150 STEEL	6.80	29.000	0.320	0.283	16000
Invar	0.70	21.000	0.300	0.293	16000
<b>Other</b>					
Aluminum, 7050-T7451	12.80	10.60	0.330	0.098	30000
Aluminum, 6061-T6	12.80	10.60	0.330	0.098	16000
Stainless Steel 416	5.70	29.000	0.280	0.280	16000
Epoxy, Hysol 9313	16.22	0.350	0.300	0.100	1000
Teflon	80.000	0.060	0.300	0.079	1600
GE RTV560*	110.000	0.460x10 <sup>-3</sup>	~0.500	0.051	100

\* Unrestrained RTV material properties

**Table 25. Binospec Weight Summary.**

Subassembly	Weight (pounds)	
	Solid model	Finite element model
Calibration screen assembly	150	143
Calibration electronics box	42	42
Main mounting flange	597	600
Motion control electronics box	91	91
PZT electronics box	98	98
Power and communication electronics box	115	115
Entrance window assembly	92	93
Main strut assembly	310	312
Main optical bench	809	781
Collimator lens assemblies	530	508
Grating turntable assemblies	425	404
Grating round house assemblies	330	330
Camera lens assemblies	799	754
Camera, shutter, and dewar assemblies	372	380
Thermal assembly	297	297
Science CCD electronics	20	20
Flexure CCD electronics	21	21
Flexure control electronics	45	45
Interface connector panels	10	10
Filter changers and cassettes	199	204
Guide camera electronics boxes A	27	27
Guide camera electronics boxes B	35	35
Inner bench and strut assemblies	274	301
Split fold mirror assembly	41	40
Slit mask changer and cassette	117	112
Wave front sensor	35	35
Single object guider	21	21
Guider assemblies	48	48
Cables, etc.	90	0
Total weight	6040	5867

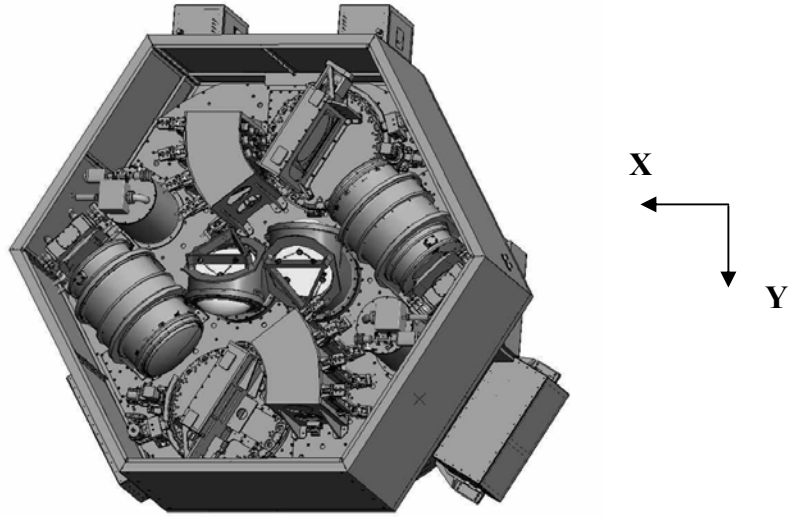


**Figure 112. Orientation of Binospec global coordinates for gravity finite analysis. The Z axis runs out of the page.**

## **5.2 Main Structure**

The Binospec support structure must hold the optical elements in excellent relative alignment at any instrument orientation. In addition, the structure must protect the optical elements and survive without damage during assembly, shipping, and handling. Figure 113 shows the Binospec support structure. The structure is comprised of a mounting flange, main struts, optical bench, inner struts and inner bench. This structure weighs ~2,000 pounds and accounts for about one third of the total instrument weight of ~6,000 pounds.

The main optical bench connects to the mounting flange with six A-frame truss members and is the structure to which most of the optics, including the collimator and camera lens groups, gratings, science cameras, and filters are attached. The inner bench connects to the main optical bench with three A-frame truss members and supports the slit masks, periscope fold mirror assembly, guiders and wave front sensor. The structure accommodates the optical design metering requirement by our specification that all materials used in the main bench, inner struts, and inner bench be aluminum, mostly 6061-T6.

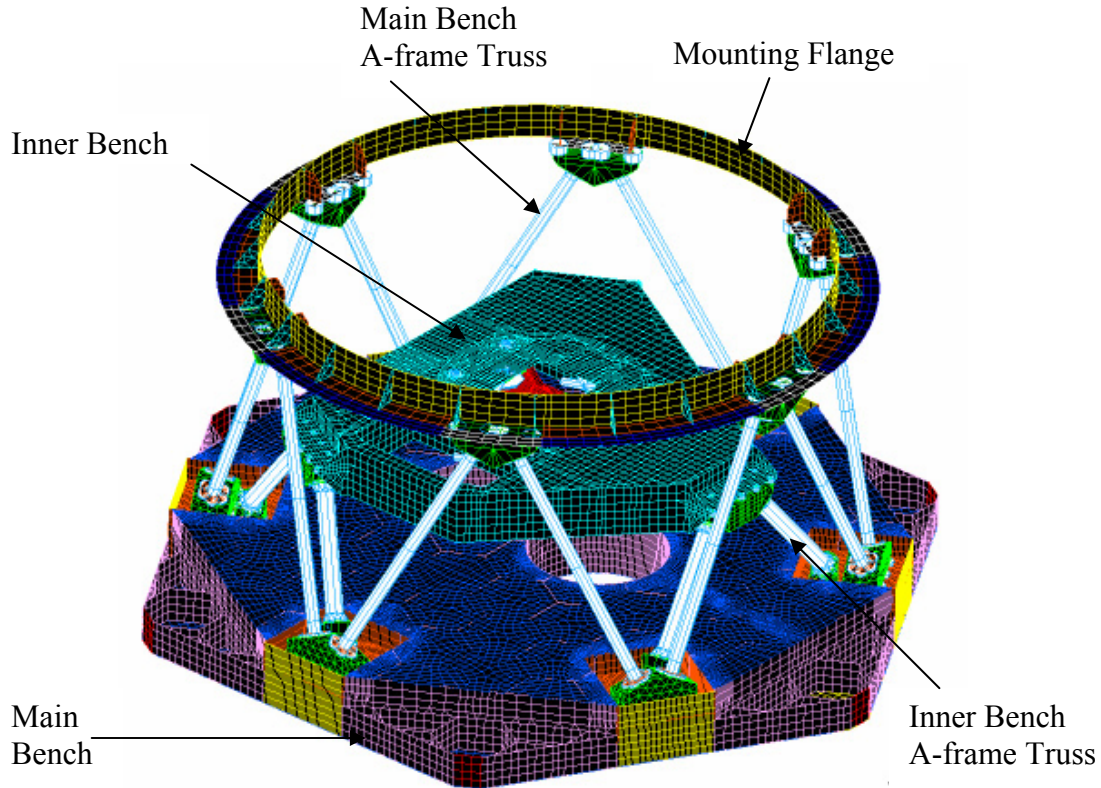


**Figure 113. Finite element model of the main support structure**

### **5.2.1 Mounting Flange**

The mounting flange is made from 400 series stainless steel to match the CTE of the telescope instrument rotator. The mounting flange also provides mounting points for the electronics boxes, upper thermal shroud, and the entrance window. The flange is nominally 1 inch thick with local areas, where the main struts attach, thickened to 1.5 inch. The vertical ring and gussets are 0.75 inch thick. The flange is bolted to the telescope at 18 points along the 72 inch bolt circle. The mount flange is constructed primarily from shell elements and is pinned to ground at each of the 18 bolt locations. The weight of the flange is 600 lbs.

### **5.2.2 Main Optical Bench**

The bench consists of two 0.30 inch thick aluminum face sheets bolted to a 7.4 inch deep aluminum honeycomb core. The face sheets are bolted to the core at the core's vertices only. The core cell spacing is 8.45 inch and the cell wall thickness is 0.18 inch. Two cylinders (0.188 inch wall with a 0.69 by 1.2 inch mounting flange) support the two collimator assemblies at the center of the bench. To spread the load of the camera lens and detector mounts, 0.70 inch thick plates are bolted to the 0.30 inch face sheets across the cells under these mounts.

Six reinforced pockets are located around the perimeter of the main bench to provide attachment surfaces for the main and inner bench struts, as well as the support cart and all lifting and handling fixtures. The pockets have a wall thickness of 0.5 inch and the strut block mounting surface is 0.75 inch thick. The interface surfaces for the handling cart and handling fixtures is 1.5 inch thick.

Figure 114 shows the finite element model for the main optical bench. The model is constructed with shell elements. Our design goal was to limit the gravity sag of the bench to the order of 0.001 inch. The total weight of the optical bench is 781 lbs.

### 5.2.3 Main A-Frame Truss Assembly

The main strut assembly consists of six A-frame truss members. The ends of each A-frame strut interface to aluminum blocks. The struts have a 1.5 inch diameter and are 30 inches long, and they are 300 series stainless steel. The 300 stainless steel was selected to minimize conduction between the mounting flange and the optical bench. The final cross-section of the struts is based on the overall stiffness as well as minimizing the weight and thermal conduction of each strut.

The struts are modeled with beam elements. Shell elements are used to represent the flanges at the ends of the struts. The blocks that mount the struts are modeled using solid elements. The total weight of the main support truss is 312 lbs.

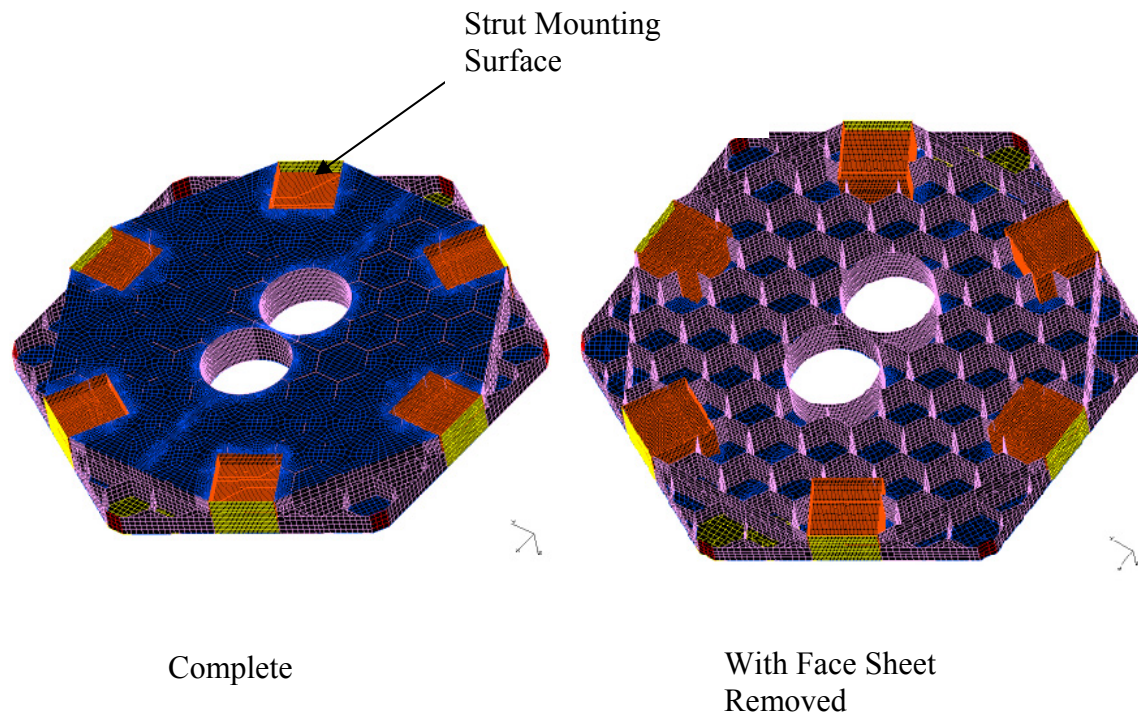


Figure 114. Finite element model of the main bench, top view.

### 5.2.4 Inner Bench

The inner bench is mounted to the main bench using three A-frame truss members. Each aluminum strut is 2 inches in diameter and 16 inches long. The aluminum bench consists of two 0.375 inch thick face sheets bolted to ribs 5.75 inch deep by 0.375 inch thick. The central area face sheet thickness is 0.6 to 0.75 inch to allow mounting the focal plane assemblies and the periscope fold mirrors. The three mounting plates that attach to the A-frame truss are 0.75 inch thick, reinforced with 0.5 inch thick gussets.

Figure 115 shows the finite element model for the inner bench. The inner bench is modeled with shell elements and the struts are modeled with beam elements. Shells are used to represent the flanges at the ends of the struts and the mounting blocks are modeled using solids. The total weight of the inner bench is 301 lbs.

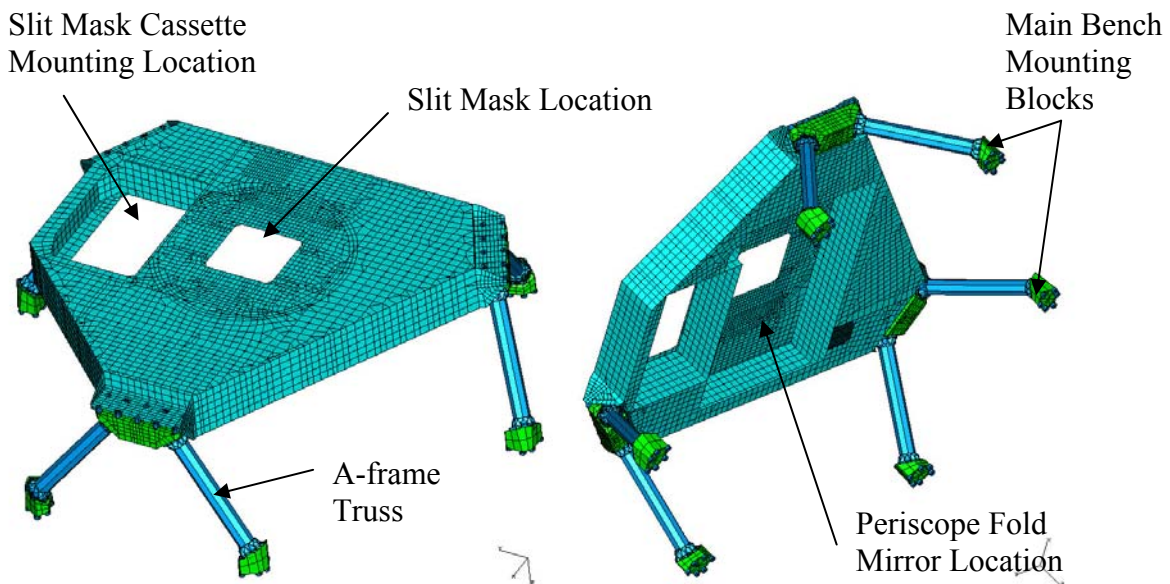


Figure 115. Finite element model for the inner bench.

### 5.2.5 Support Structure Performance

One of the critical design goals for the support structure is to provide a stiff mounting surface for all of the optical assemblies and maintain the relative alignment between the inner bench and main optical bench. Relative motion between the slit mask and any of the optical assemblies will adversely affect the image motion at the detector. Table 26 shows the maximum and the relative deflections of the two benches. The relative gravity displacements between the inner bench and the main optical bench are  $\sim 0.0006$  inch in the lateral direction and  $\sim 0.00002$  inch in the axial direction. The maximum gravity sag

across the inner bench is ~0.0013 inch and the maximum sag across the main optical bench is ~0.0018 inch. Table 27 shows the maximum principal stress in each of the structural components resulting from combined 3g gravity and 75°F temperature change.

**Table 26. Gravity displacements at the centers of the inner bench and main optical bench (10<sup>-3</sup> in.)**

	<b>Gravity X</b>	<b>Gravity Y</b>	<b>Gravity Z</b>
<b>Main Optical Bench</b>	4.40	4.31	2.23
<b>Inner Bench</b>	3.80	3.76	2.21
<b>Relative</b>	0.60	0.55	0.02

**Table 27. Maximum principal stress combining 3g shipping load and 75°F temperature change (PSI)**

	<b>Mount flange</b>	<b>Main bench</b>	<b>Main struts</b>	<b>Inner bench</b>	<b>Inner struts</b>
<b>Modeled</b>	2800	1200	5400	1200	600
<b>Allowable</b>	16000				

## 5.3 Optical Mounts

### 5.3.1 Lens Mounts (Excluding NaCl Lens)

Each lens, except the NaCl lens, is mounted into a bezel through rectangular tangent flexures epoxied to the glass. The NaCl lens mount is described in Section 5.3.4.

Table 28 lists lens materials, weights, and diameters. The flexures are integral parts of the bezels, formed by electrical discharge machining. This process eliminates trapped air pockets in the coupling fluid as well as a good deal of hardware. The flexure mounts must simultaneously meet three goals: (1) acceptable stress levels in all of the components, acceptable image motion and defocus due to lens deflections and tilts, and acceptable deformation of the optical surfaces. These goals were achieved through an iterative design process shown in Figure 116.

We initially set the stiffness of all of the mounts to produce a 200 Hz lowest mode, but reduced the stiffness of most of the mounts to reduce internal stresses and lens deformations. We limit the radial load to one pound per flexure for a 75° F temperature change. This radial force produces a 1/10 λ symmetric deformation on the most sensitive lens, collimator lens 8, and typically 1/20 λ on the other lenses. This is considerably below the surface figure tolerance for the lenses, which in turn was set to degrade the image quality by less than 2%.

The bezel (and flexure) material is heat treatable aluminum alloy 7050-T7451. This aluminum alloy is chosen for its high yield strength (57 ksi) and ultimate strength (75 ksi), good machinability, is available in plates up to 6 inches thick. The athermalization of the optical design assumed that the lens spacings are metered by an aluminum structure.

A circular nub is pressed into each flexure. After a lens is aligned to its bezel, Hysol 9313 epoxy, filled 80% by weight with Siltex 44, will be injected to bond the nub to the lens. The nominal bond thickness is 0.010 inches. The Siltex filler reduces the thermal expansion of the 9313 epoxy to about 16.2 ppm/°F without reducing the epoxy's strength. The nub material used for each lens has a thermal expansion closely matching the lens material (to 1 ppm/°F or better) to minimize thermal stresses at this bond interface. The nub materials are 304L stainless steel, Kovar, titanium, and 4150 steel.

We created four levels of finite element models: 1) a model of the nub/epoxy/glass interface for each lens, 2) a model of the lens/flexure assembly, 3) a model of the collimator and camera assemblies, and 4) a detailed model of the entire instrument.

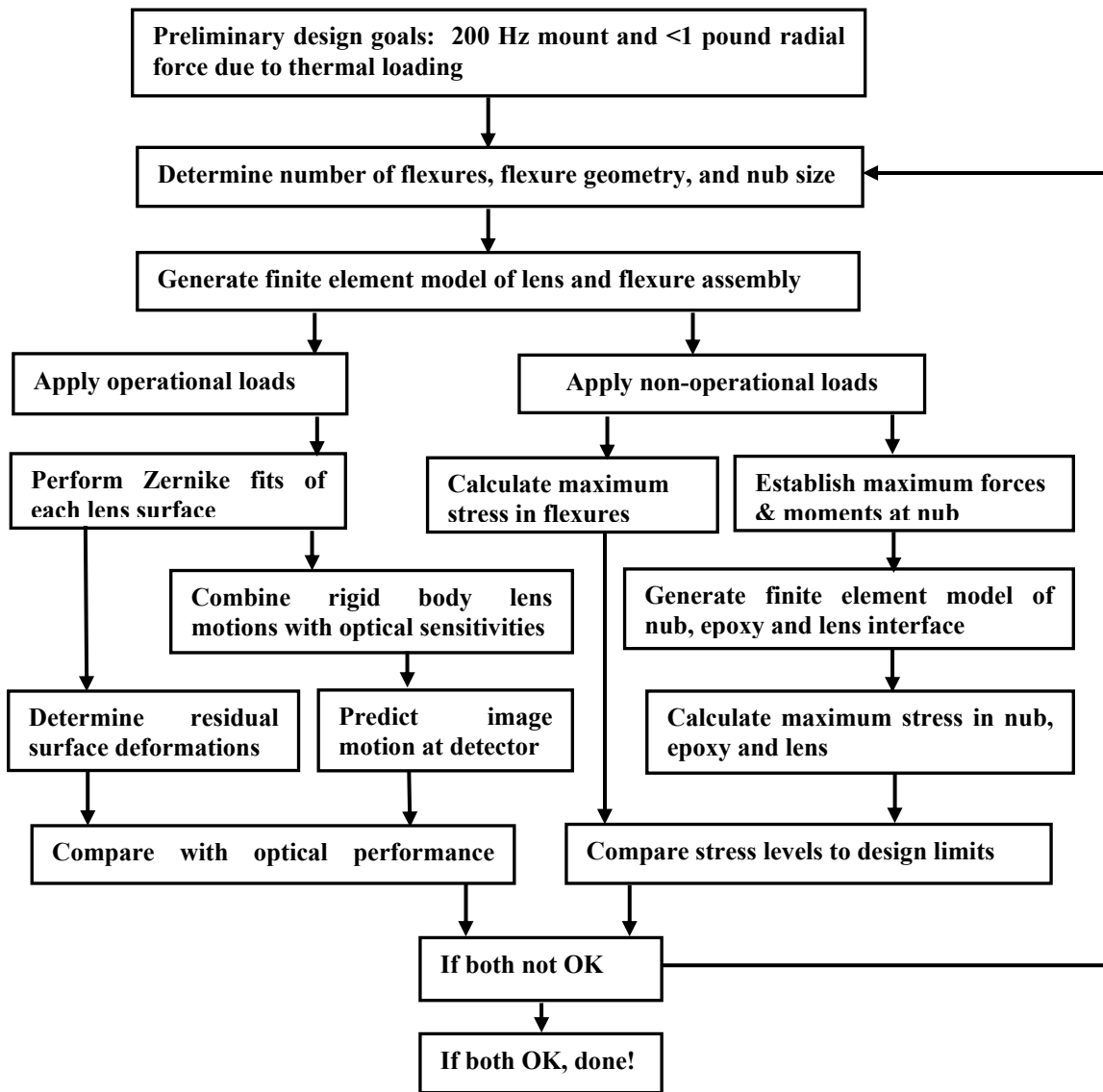
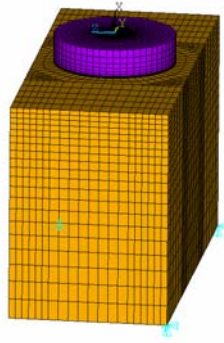


Figure 116. Design Flow Chart



**Figure 117. Finite element model of a nub/epoxy/glass bond**

Figure 117 shows the first level finite element model of the nub/epoxy/glass interface. This model was constructed with eight-node solid elements to represent the glass, the bond, and the nub. The epoxy bond, nub, and glass are modeled with four, six and 20 elements through their thickness, respectively. The mesh for the nub and glass was biased towards the epoxy layer to provide a reasonable aspect ratio for the elements. Two sets of boundary conditions were used to model the effect of mechanical and thermal loads. The results from these two load cases were combined to predict the total stress in the nub, epoxy and at the glass interface. The forces and moments applied to the nub were computed with the second level finite element model.

**Table 28. Lens geometrical and physical properties.**

	<b>Lens material</b>	<b>Weight, lb</b>	<b>Diameter, in</b>
<b>Collimator</b>			
<b>Lens 1</b>	BAL15Y	17.835	12.441
<b>Lens 2</b>	FSL5Y	27.844	12.244
<b>Lens 3</b>	PBM2Y	32.364	11.890
<b>Lens 4</b>	PBL6Y	24.626	11.181
<b>Lens 5</b>	BAL35Y	10.494	9.094
<b>Lens 6</b>	CAF2	13.823	8.622
<b>Lens 7</b>	PBL6Y	8.907	8.425
<b>Lens 8</b>	BSM51Y	10.670	11.260
<b>Lens 9</b>	CAF2	24.074	11.654
<b>Camera</b>			
<b>Lens 1</b>	BAL35Y	24.273	14.094
<b>Lens 2</b>	CAF2	40.345	14.055
<b>Lens 3</b>	CAF2	42.792	14.646
<b>Lens 4</b>	BAL35Y	31.085	14.370
<b>Lens 5</b>	CAF2	44.511	13.819
<b>Lens 6</b>	PBM2Y	26.081	13.819
<b>Lens 7</b>	S-FPL51Y	17.284	10.906
<b>Lens 8</b>	NACL	15.738	11.844
<b>Lens 9</b>	CAF2	13.073	8.583

Figure 118 shows the second level finite element model of a typical lens and flexure assembly. The lenses and the nubs are modeled with solid eight-node brick elements. The glass elements are biased towards the nub location to produce a higher fidelity mesh in this critical region. The lens is modeled with at least six elements through its thickness, and the nub is meshed with four elements along each side. The flexure is modeled with four-node shell elements with four elements along its width and 52 elements along its length.

To model the effect of the assembly loads arising from mounting flange surface irregularities,  $\cos(2\theta)$  and  $\cos(4\theta)$  axial displacement profiles were enforced at the flexure ends with a normalization of  $\pm 0.0005$  inch. These displacements are roughly double the displacements that we expect due to our final bezel flatness tolerance of 0.0005 inch. If we bolt two of these bezels together, we would expect no more than half that error to be imprinted, or  $\pm 0.00025$  inch. In analysis we scale the finite element results appropriately. The  $\cos(2\theta)$  case produced the largest surface errors, and the  $\cos(4\theta)$  case produced the maximum stress levels in the flexures, lens and epoxy. Load cases considering gravity with the pressure head, a 75 °F temperature change, and assembly loads were used to evaluate optical performance. Similar loads were used to calculate the maximum principal stress levels except that 3g shipping and handling loads were used. When computing the maximum stress levels, the forces and moments exerted on a nub were transferred from this model to the first level finite element model that has a much higher fidelity mesh.

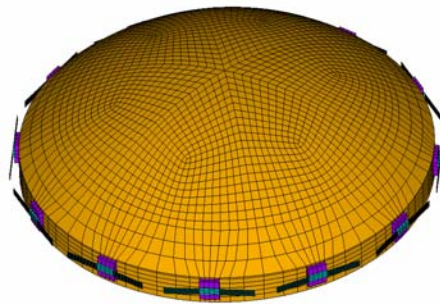


**Figure 118. Finite element model of a lens/flexure assembly**

### 5.3.2 Flexure Performance

Table 29 describes the final mount configurations for each lens assembly.

**Table 29. Mount characteristics.**

	<b>Flexure Number</b>	<b>Lowest Mode (Hz)</b>	<b>Nub Dia. (inch)</b>	<b>Nub Material</b>	<b>L (inch)</b>	<b>B (inch)</b>	<b>T (inch)</b>
<b>Collimator</b>							
<b>Lens 1</b>	9	200	0.75	Ti6Al4V	1.56	0.35	0.04
<b>Lens 2</b>	9	150	0.68	Ti6Al4V	1.54	0.33	0.04
<b>Lens 3</b>	9	150	0.70	Ti6Al4V	1.52	0.34	0.04
<b>Lens 4</b>	9	150	0.66	Ti6Al4V	1.50	0.31	0.04
<b>Lens 5</b>	9	100	0.40	Kovar	1.18	0.14	0.04
<b>Lens 6</b>	9	100	0.36x0.54	304LSS	1.10	0.14	0.04
<b>Lens 7</b>	6	150	0.58	Ti6Al4V	1.64	0.27	0.04
<b>Lens 8</b>	12	200	0.50	Kovar	1.00	0.17	0.04
<b>Lens 9</b>	12	150	0.56	304LSS	1.00	0.18	0.04
<b>Camera</b>							
<b>Lens 1</b>	12	200	0.72	Kovar	1.31	0.30	0.04
<b>Lens 2</b>	12	150	0.67	304LSS	1.30	0.28	0.04
<b>Lens 3</b>	12	150	0.80	304LSS	1.38	0.31	0.04
<b>Lens 4</b>	12	150	0.60	Kovar	1.40	0.28	0.04
<b>Lens 5</b>	12	150	0.75	304LSS	1.25	0.28	0.04
<b>Lens 6</b>	12	150	0.58	Ti6Al4V	1.35	0.25	0.04
<b>Lens 7</b>	12	150	0.46	4150 Steel	1.05	0.17	0.04
<b>Lens 8</b>	-	-	-	-	-	-	-
<b>Lens 9</b>	6	150	0.70	304LSS	1.22	0.23	0.04

Table 30 and Table 31 present the stresses at each of the lens mount components: flexure, lens, nub, and epoxy. The optimized flexures all have thicknesses of 0.040 inches; their lengths vary between 1.00 and 1.64 inches, and their widths vary between 0.14 inches and 0.35 inches. The nub diameters vary between 0.40 and 0.80 inches; one is elliptical with major axes 0.36 by 0.54 inches. To maximize the length of the flexures, we use twelve flexures for the largest diameter lenses, dropping to nine flexures for intermediate diameter lenses, and six flexures for the smallest diameter lenses.

The mount fundamental frequencies range between 100 and 200 Hz and correspond to an axial translation mode of the lens. The maximum principal stresses resulting from the worst-case combined 3g shipping loads, the  $\cos(40)$  bolt-up displacement, and a 75°F temperature change are summarized in Table 32.

**Table 30. Maximum and minimum principal stress, psi (combined gravity x / y).**

	Flexure*		Lens		Nub		Epoxy	
	max	min	max	min	Max	min	max	min
<b>Collimator</b>								
<b>Lens 1</b>	12302.0	-13919.6	423.6	-311.8	3083.1	-3222.2	750.5	-134.6
<b>Lens 2</b>	14045.8	-14237.7	264.9	-281.7	3135.3	3212.1	589.9	-187.7
<b>Lens 3</b>	11780.9	-13289.7	316.5	-267.9	3335.2	-3499.3	635.6	-169.7
<b>Lens 4</b>	9193.7	-7037.3	294.3	-202.0	2301.2	-2505.3	624.0	-121.6
<b>Lens 5</b>	11500.3	-8460.5	184.7	-289.8	1210.8	-1083.8	605.1	-265.9
<b>Lens 6</b>	4883.6	-4832.0	264.0	-404.1	2155.9	-1651.1	414.1	-345.7
<b>Lens 7</b>	10636.1	-10684.0	305.6	-218.1	1580.4	-1823.2	643.0	-163.4
<b>Lens 8</b>	20567.5	-21336.5	200.0	-367.2	2155.0	-1803.9	580.3	-325.2
<b>Lens 9</b>	14228.0	-14248.4	289.4	-413.7	2698.5	-2056.4	406.7	-425.1
<b>Camera</b>								
<b>Lens 1</b>	14402.9	-16386.5	150.2	-278.3	2419.6	-2416.9	552.9	-211.8
<b>Lens 2</b>	17165.4	-16244.8	409.2	-558.0	3073.2	-2402.3	436.7	-474.6
<b>Lens 3</b>	13715.9	-13777.1	374.4	-424.1	2755.9	-2523.9	378.0	-451.6
<b>Lens 4</b>	12376.2	-8815.0	167.0	-280.9	1837.1	-1737.9	561.6	-221.2
<b>Lens 5</b>	6692.3	-7542.5	326.9	-432.5	2397.6	-2000.2	378.2	-410.1
<b>Lens 6</b>	18253.6	-18468.2	352.2	-319.8	2585.9	-2720.6	688.0	-254.6
<b>Lens 7</b>	14765.9	-14918.1	308.3	-421.0	2092.3	-1604.0	517.1	-441.0
<b>Lens 8</b>	-	-	-	-	-	-	-	-
<b>Lens 9</b>	12954.1	-12395.1	313.9	-400.5	2189.8	-1688.9	383.2	-383.3

**Table 31. Maximum and minimum principal stress, psi (combined gravity z / -z).**

	Flexure*		Lens		Nub		Epoxy	
	max	min	max	min	max	min	max	Min
<b>Collimator</b>								
<b>Lens 1</b>	10117.6	-11668.9	384.8	-296.4	2616.1	-2735.9	712.4	-112.7
<b>Lens 2</b>	11646.4	-12773.5	208.4	-225.7	2486.2	-2559.8	542.2	-143.7
<b>Lens 3</b>	12366.5	-13507.3	261.2	-237.0	2817.6	-2945.2	587.0	-135.4
<b>Lens 4</b>	12342.2	-13329.2	304.4	-208.7	2327.1	-2532.4	630.0	-125.6
<b>Lens 5</b>	11678.0	-11306.9	120.5	-223.5	918.5	-792.8	552.9	-199.7
<b>Lens 6</b>	10696.3	-10540.6	252.1	-298.3	1928.8	-1426.2	414.3	-269.1
<b>Lens 7</b>	11886.8	-12358.4	297.3	-199.6	1380.7	-1633.0	631.1	-152.6
<b>Lens 8</b>	13283.1	-14092.8	137.7	-252.7	1626.5	-1297.2	555.9	-213.4
<b>Lens 9</b>	13037.8	-12838.7	281.8	-323.4	2139.8	-1478.9	388.9	-316.6
<b>Camera</b>								
<b>Lens 1</b>	13291.0	-13122.2	106.9	-215.0	1934.3	-1900.4	538.2	-164.4
<b>Lens 2</b>	13668.1	-13483.8	356.5	-402.2	2463.0	-1745.7	399.2	-369.5
<b>Lens 3</b>	10679.3	-10987.7	365.7	-335.8	2250.7	-1904.9	369.5	-371.6
<b>Lens 4</b>	12611.2	-13624.8	160.1	-271.7	1778.8	-1680.2	561.6	-220.9
<b>Lens 5</b>	12961.2	-13025.4	326.3	-407.6	2302.9	-1887.3	376.5	-386.8
<b>Lens 6</b>	13082.5	-13804.3	237.3	-221.4	1816.2	-1963.6	582.4	-158.0
<b>Lens 7</b>	15015.8	-15160.1	297.4	-330.8	1863.8	-1318.2	503.4	-376.7
<b>Lens 8</b>	-	-	-	-	-	-	-	-
<b>Lens 9</b>	12065.7	-11998.6	312.2	-343.7	1807.5	-1270.4	375.3	-342.2

**Table 32. Maximum principal stresses resulting from the worst-case combined 3g shipping loads, the cos(40) bolt-up displacement, and a 75°F temperature change.**

	Max Flexure Stress*	Max Lens Stress	Max Epoxy Stress	Max Nub Stress
<b>Modeled</b>	29872	424	750	3499
<b>Allowable</b>	30000	500	1000	16000

\* The flexure stresses were multiplied by a stress concentration factor of 1.4 based on the fillet radii at the ends of the flexure blades.

### 5.3.3 Assembled Collimator and Camera FE models

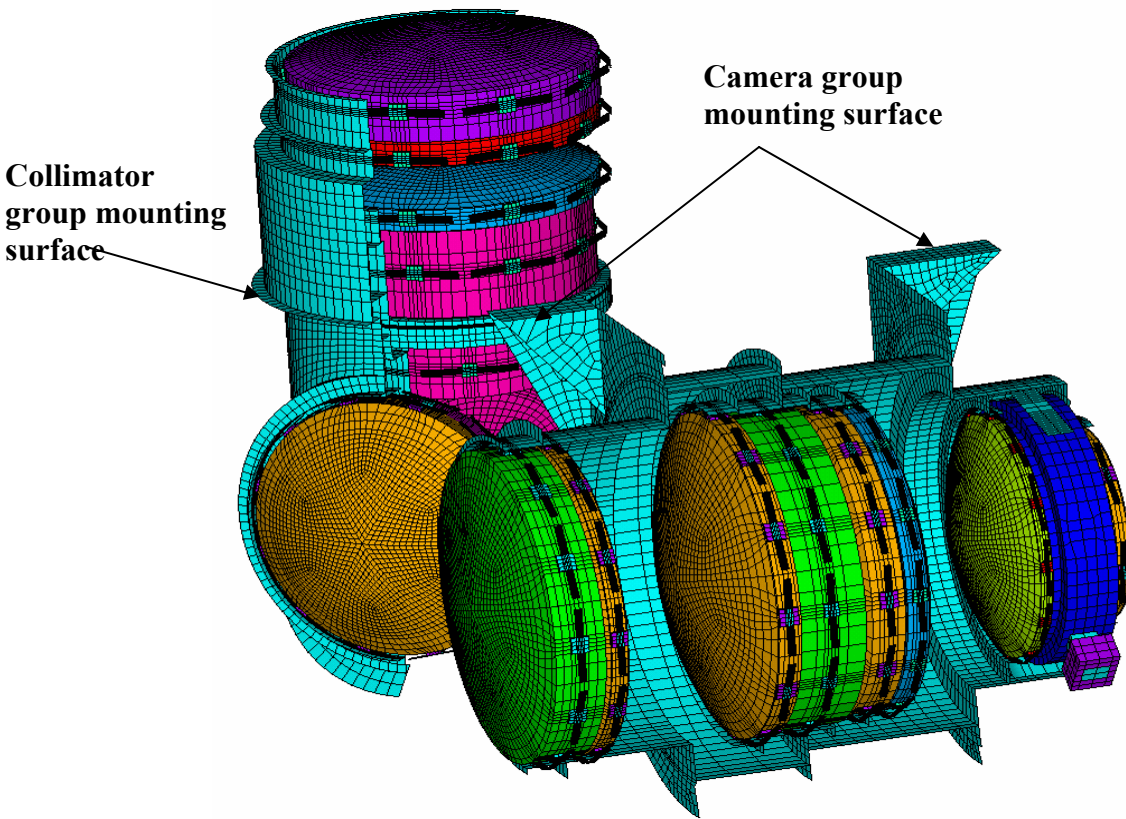


**Figure 119. Section view showing finite element model of collimator and camera assembly.**

Figure 119 presents the third level finite element model of the collimator and camera assemblies. In this model, FE models of lenses with flexures described above are supplemented with bezels, which are primarily made with shell elements; however, parts of some bezels are represented by solid elements. The third level model was used to assess the image motion and focus change of the instrument arising from the lens mounts only as a result of gravity loads application. Accordingly, the gravity loads in +X, +Y, +Z, -X, and -Y were independently applied. Based on the gravity vector orientation, the pressure head loads were added. At this stage, the mount stiffness for each lens was adjusted if required by high stress levels computed in the first and second level models. The weights of each collimator and camera assembly are 254 lbs and 377 lbs,

respectively. The first several modes of the collimator and camera assemblies correspond to the combined axial stiffness of the lens mounts and structure and vary between ~100 to 140 Hz. The first structural mode of the collimator assembly is a side to side tilt dominated by the fold mirror at ~140 Hz. The first structural mode of the camera assembly is a side to side tilt relative to the base at ~150 Hz.

### **5.3.4 NaCl Lens Mount**

The sodium chloride lens could not be mounted with bonded flexures while meeting the 100 psi stress limit for NaCl. This lens is held in its bezel using preload forces in the axial and radial directions reacted by hard points. In the axial direction, an aluminum ring with three flexures is mounted to the top of the bezel to provide a 3g preload. A ground step in the lens allows space for the axial hard points. The dimensions of the step are 0.725 in. radially and 0.385 in. axially. A single radial flexure is used to provide a 3g preload to two radial hard points. At each radial support location, the NaCl lens has three ground tangential flats. The radial distance to the flat is 5.84 in. The radial hard points are athermalized with Teflon spacers. The FE model utilizes 4-noded shell elements and 8-noded brick elements. The connection between the flexures and lens was represented using 4-noded contact elements.

#### **5.3.4.1 Axial Preload**

A finite element model of the axial preload ring for the NaCl camera lens is shown in Figure 120. The axial flexure width is 0.65 in. and each flexure blade is 2.4 in. long. The nub length is 0.8 in., giving a total flexure length of 5.6 in. The blade thickness is 0.092 in., the nub thickness is 0.25 in. and the ring thickness is 0.50 in. Teflon pads 0.125 in. thick are press fit to the nubs and hard points at their interface with the lens. The flexures were sized so that a 0.02 in displacement on each flexure would produce the desired 3g preload on the lens. Constraint equations were used to specify that the relative displacements of the nodes be equal to the enforced displacement of 0.02 in.

#### **5.3.4.2 Radial Preload**

A schematic of the radial support is shown in Figure 121. The radial preload flexure has a rectangular cross-section 1.1 in. wide, with each blade 2.4 in. long and 0.1 in. thick. The nub is 0.92 in. long and 0.42 in. thick. An aluminum cylinder with a 1.125 in. diameter is used for the hard point supports. Teflon pads 0.125 in. thick are press fit to the flexure nub and hard points at their interface with the lens. The rest of the bezel is 1.1 in. thick everywhere except for local areas that are 0.25 in. thick around the radial preload flexure and hard points. The flexures were sized such that a 0.03 in. displacement on the flexure would produce a 3g preload on the lens. Constraint equations were used to specify the relative displacements of the nodes be equal to the enforced displacement of 0.03 in.

The lens is supported in its axial direction at the nodes corresponding to the locations of three axial hard points. A pressure corresponding to the 3g preload produced by the axial flexure interface ring is applied at the corresponding nodes on the other side of the lens. At the two hard point locations, Teflon spacers 1.133 thick are located between the O.D. of the bezel and the end of the aluminum cylinders that supports the lens. These spacers

were sized to athermalize the NaCl lens relative to the aluminum bezel to maintain centration over the entire 75°F temperature swing.

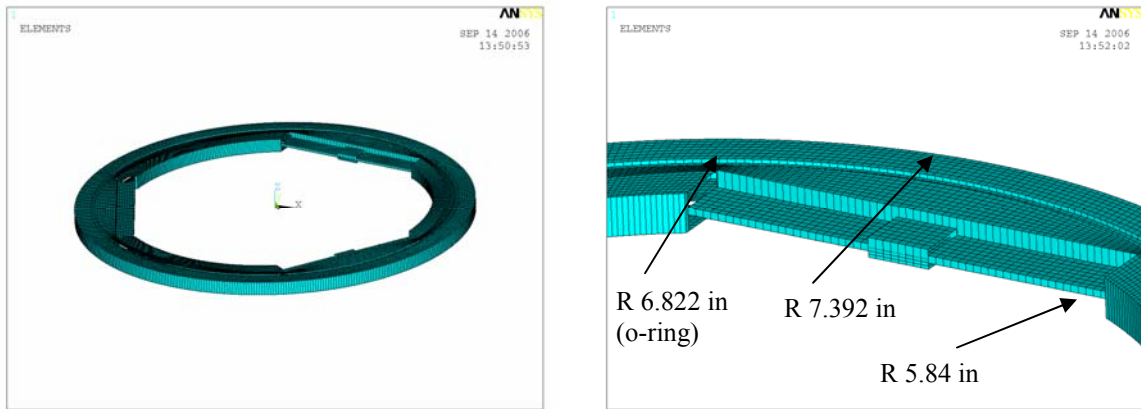


Figure 120. Finite element model of the axial preload ring for NaCl lens mount.

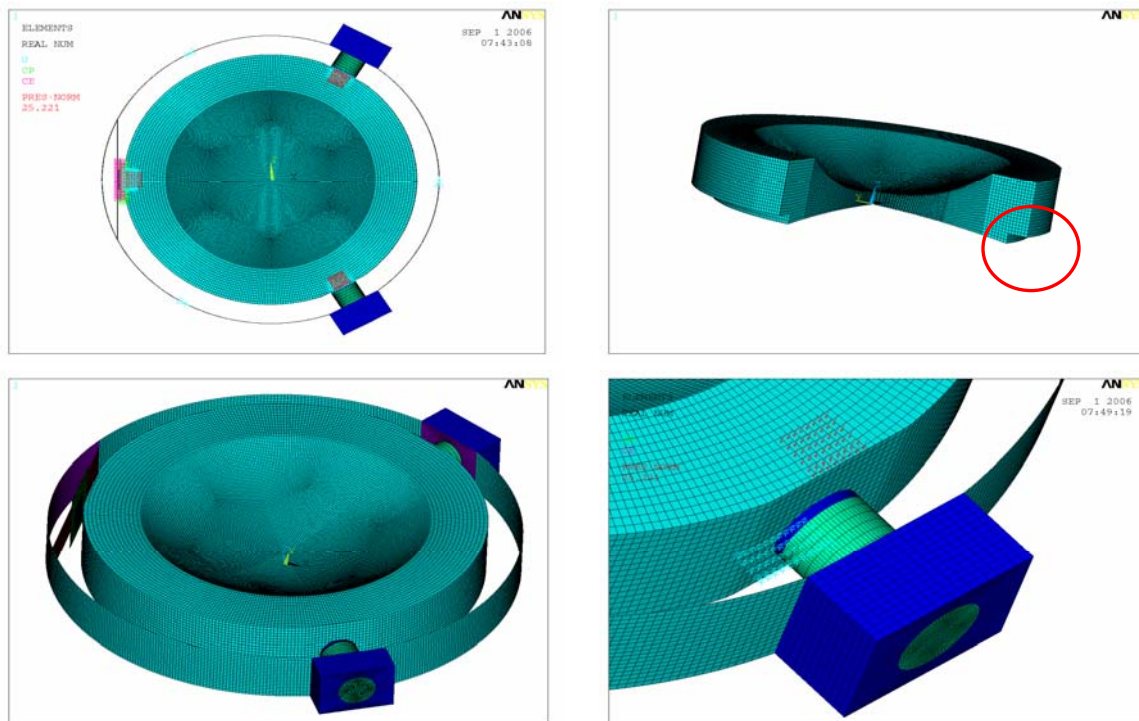


Figure 121. FE model of NaCl camera lens in its radial support mount.

### 5.3.4.3 NaCl Lens Mount Performance

The NaCl lens model was subjected to the flexure preload, lateral and axial gravity, and 75°F temperature soak. Table 33 summarizes the maximum stresses in the most severe load combinations. Since this lens is supported at three points in the axial and radial directions, and completely submersed in couplant oil, there are no additional loads from

bolt-up or pressure head. Results also show that temperature changes have minimal effect. The 3g preload produced  $\sim 0.2 \lambda$  of trefoil surface error, which is insignificant.

**Table 33. Maximum principal stresses (psi) for the NaCl lens resulting from the 3g preload and 3g shipping loads combined with 75°F soak.**

	Max Flexure Stress*	Max Lens Stress
Modeled	26600	95
Allowable	30000	100

\* The flexure stresses were multiplied by a stress concentration factor of 1.4 based on the fillet radii at the ends of the flexure blades.

### 5.3.5 Fluid Couplant Seal Analysis

The finite element model of the lens couplant seal for collimator lens 8 is shown in Figure 122. The 0.0075 inch thick Teflon seal has an 11.26 inch ID, an 11.83 inch OD, and a 0.52 inch unfolded radial width. The seal is modeled with shell elements. We evaluated the seal performance by calculating the seal forces resulting from gravity, pressure head, and a 75 °F temperature change. The forces were applied to the lens around its perimeter to predict the lens surface deformation. The results for other lens seals are similar.

For a  $-75$  degree °F temperature change, the radial seal load on the lens is  $0.09 \text{ lb in}^{-1}$  and produces  $\sim 1/25\lambda$  of surface deformation. For 1g axial and lateral gravity, the total seal loads are small, 0.017 lbs and 0.22 lbs. respectively, and the lens deformations are negligible. The lens tilt produced by the pressure head over the face of the seal is  $\sim 4.5 \times 10^{-6}$  radian,  $\sim 10\%$  of the total lens tilt. The maximum Teflon stress is  $\sim 450$  psi resulting from the 75°F temperature change and is located at the bond interface between the seal and lens. The Teflon stress resulting from 3g pressure head is  $\sim 1080$  psi. These stresses are well below the 1600 psi design allowable.

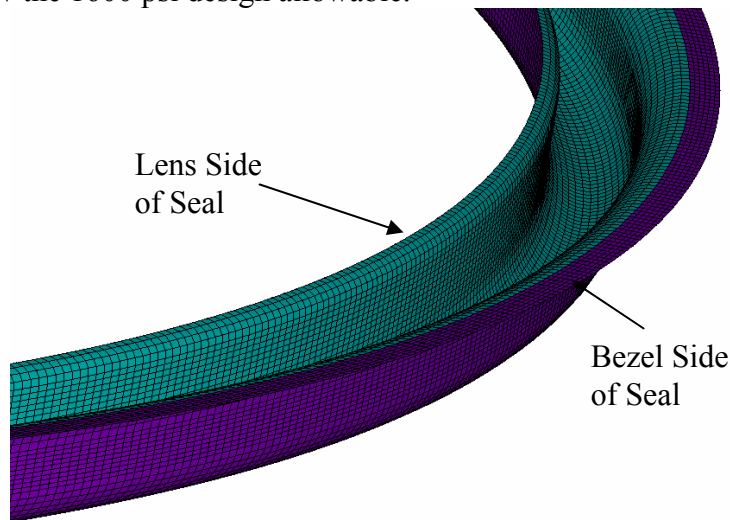


**Figure 122. Couplant seal finite element model.**

### 5.3.6 Fold Mirrors

Table 34. Fold mirror geometrical and physical properties

	Weight (lb)	Thickness (inch)	Dimensions (inch)
<b>Periscope</b>			
<b>Fold Mirror 1</b>	1.87	0.35	9.1 x 6.83
<b>Fold Mirror 2</b>	3.77	0.50	9.8 x 9.0
<b>Collimator</b>			
<b>Fold Mirror 3</b>	11.04	1.00	12.43 circular

There are three fold mirrors in the Binospec collimator optics. Two of the fold mirrors constitute a periscope configuration to separate the dual beams of the instrument. The third fold mirror is located within the collimator lens group. The fold mirrors and mounts are designed to be robust to minimize surface deformations and image motion resulting from gravity and thermal loads. The fold mirror substrates are Zerodur. The mounts and support structure are aluminum to meter the optical spacings as defined in the optical prescription. Table 34 lists the weight and geometry of the fold mirrors.

#### 5.3.6.1 Fold Mirror Finite Element Trade Studies

Three types of finite element models were used to analyze the fold mirrors and their mounts: (1) detailed axisymmetric models of the nub/epoxy/glass joints, (2) highly detailed models of the flexured mirror assembly, and (3) simplified fold mirror assemblies integrated into the complete instrument model. The detailed models were used to determine the optimal axial support location of the nub along the thickness of the mirror and to establish geometric features such as mirror thickness, bond diameter, and bond thickness.

For fold mirrors 2 and 3, the most important load case for the detailed models is the 75°F temperature change. The temperature change produces a local bump and slope errors on the mirror surface directly above the nub due to the CTE mismatch between the glass, epoxy and nub materials. We optimized the lens thickness and nub diameter to minimize this thermal distortion while simultaneously minimizing the stress levels. Fold mirrors 1 and 2 are near the telescope (and collimator focus), and their slope errors are negligible. For fold mirror 3, the RMS surface slope errors in a pupil are  $0.5 \times 10^{-6}$  radians. The resulting contribution to the image blur is small, 1.1  $\mu\text{m}$  RMS diameter.

#### 5.3.6.2 Periscope Fold Mirrors 1 and 2

Fold mirror 1 is located close to the focal plane where space is very limited. The mirror is 0.35 in. thick and is supported from the back using three 0.020 in thick RTV560 pads 0.59 inches in diameter. The pads are spaced 120° apart on a 6 inch diameter circle. To optimize the peak to valley displacement, the mirror is offset by 0.060 in. relative to the center of the RTV support. Both first fold mirrors attach to a common aluminum support truss. This truss is made from members that have a cross section of 0.4 in. by 0.5 in. Shell elements are used to represent the mirror and beam elements for the RTV pads and support truss. The detailed analysis for fold mirror 1 is fully documented in SAO

Memorandum, "Binospec First Fold Mirror Analysis" by Henry Bergner, dated April 16, 2007.

The second fold mirror is 0.5 in. thick and supported from the back with three aluminum bipod flexures. The flexures are 2.2 inches long and have a diameter of 0.08 inch. The flexures connect to an Invar block/nub that is bonded to the mirror. The 0.010 thick bond of silica filled Hysol 9313 epoxy dimensions is 0.5 inch in diameter. The flexures are equally spaced 120° apart on a 6.6 inch diameter circle. The bases of the flexures are attached to a triangular aluminum base frame with a cross section of 1.75 by 0.25 inches. The model consists of shell elements representing the mirror and beam elements for the Invar nubs and the bipod flexures. The triangular base frame is modeled using shell elements. The detailed analysis for fold mirror 2 is fully documented in SAO Memorandum "Binospec Second Fold Mirror Analysis" by Henry Bergner, dated April 10, 2007.

The finite element assembly model for periscope fold mirrors 1 and 2 is shown in Figure 123. The weight of the assembly is 40.1 lbs. The entire assembly mounts to the underside of the inner bench at 4 places shown. The support housing is made from 0.25 inch thick aluminum except for local areas that were thickened to 0.95 inch around the attachment points. There are 1.0 by 0.25 inch thick reinforcing ribs located at the top and bottom along the sides of housing. The fold mirror 1 support truss is mounted to a light weighted platform with a deck and rib thickness of 0.25 in.

### **5.3.6.3 Collimator Fold Mirror 3**

The finite element model of the collimator fold mirror/flexure assembly is shown in Figure 124. The 1 inch thick mirror is supported from the back with three aluminum bipod flexures. The flexures are 2.76 inch long and 0.14 inch in diameter. The flexures connect to an Invar block/nub that is bonded to the mirror. The 0.010 inch thick silica filled Hysol 9313 epoxy bond is 0.8 inch in diameter. The flexures are spaced 120° apart on an 8.7 inch diameter circle. The flexure bases are attached to a triangular aluminum base frame with a cross section of 2.0 by 0.6 inches. Invar blocks 1.1 in. thick were placed between the triangular base frame and the support structure to compensate for the image shift and focus error introduced by the differential CTE of the Zerodur mirror and the aluminum frame. Shell elements were used to represent the mirror and beam elements for the Invar nubs and the bipod flexures. The triangular base frame and Invar blocks were modeled with solid elements. The detailed analysis for fold mirror 3 is documented in SAO Memorandum, "Binospec: On Stresses and Surfaces Deformations Arising from Collimator Fold Mirror Mounting" by Vladimir Kradinov, dated April 5, 2007.

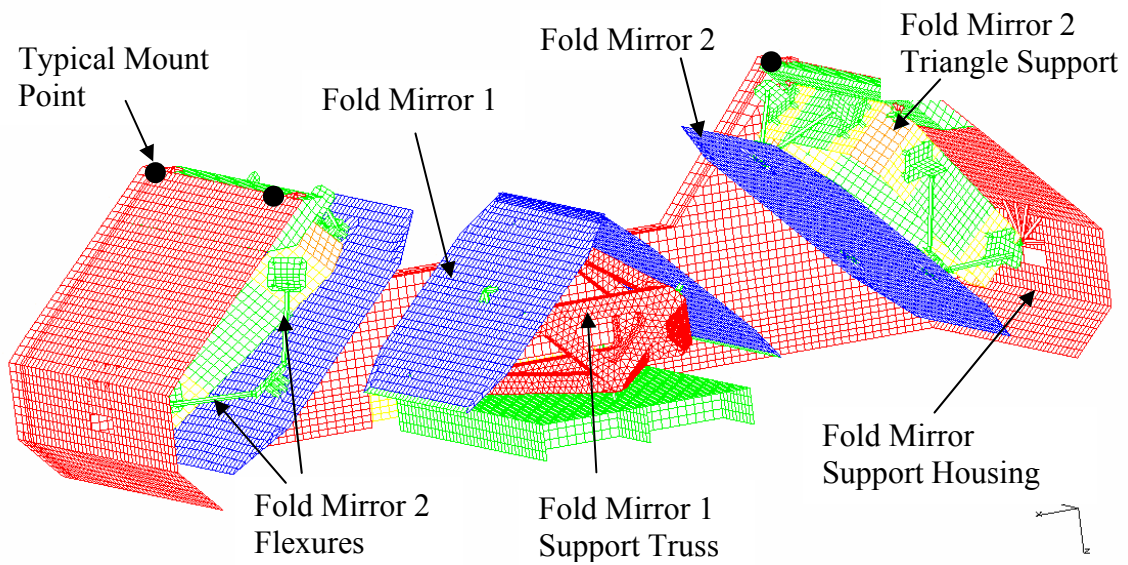


Figure 123. Section view of Periscope Fold Mirror FE model.

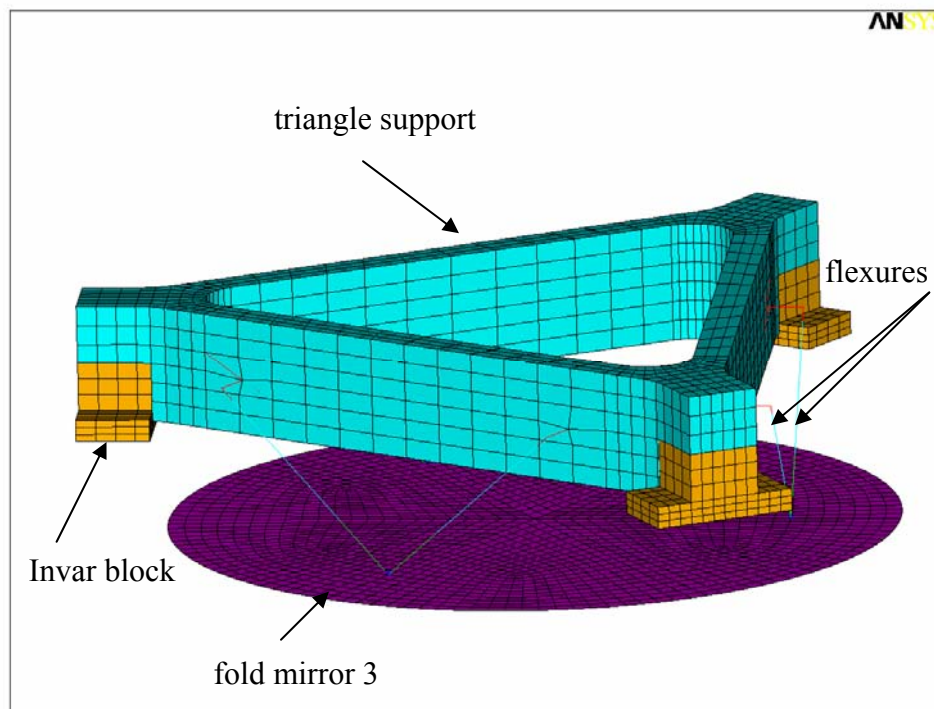


Figure 124. Collimator fold mirror 3 mounted on three bipod flexures.

### 5.3.6.4 Fold Mirror Mount Performance

Table 35 is a summary of the mount details. Fold mirror 1 has a fundamental frequency of 141 Hz and corresponds to an axial rotation mode. Folds 2 and 3 have fundamental frequencies of 240 Hz and 250 Hz, respectively that correspond to a tip-tilt mode.

**Table 35. Fold mirror flexure mount characteristics**

	<b>Lowest Mode (Hz)</b>	<b>Bond Thickness (inch)</b>	<b>Bond Material</b>	<b>Nub Diameter (inch)</b>	<b>Nub Material</b>	<b>Flexure Description</b>
<b>Periscope</b>						
<b>Fold 1</b>	141	0.020	RTV 560	0.59	Al 6061-T6	RTV pads
<b>Fold 2</b>	240	0.010	Hysol 9313	0.50	Invar	6 rods, 2.20 in. long, 0.08 in. dia. Al 7050-T7451
<b>Collimator</b>						
<b>Fold 3</b>	250	0.010	Hysol 9313	0.80	Invar	6 rods, 2.76 in. long, 0.14 in. dia. Al 7050-T7451

The maximum stress levels calculated for the fold mirrors, bond materials (epoxy or RTV), nubs and flexures are summarized in Table 36. Stresses listed result from combined 3g shipping and handling loads and 75°F soak.

**Table 36. Maximum Principal Stress for Combined 3g Shipping and 75°F Thermal Soak, psi**

	<b>Max Flexure Stress*</b>	<b>Max Mirror Stress</b>	<b>Max Epoxy Stress</b>	<b>Max RTV Stress</b>	<b>Max Nub Stress</b>
<b>Modeled</b>	4144	290	800	30	437
<b>Allowable</b>	30000	500	1000	100	16000

\* The flexure stresses were multiplied by a stress concentration of 1.4 based on the fillet radii at the ends of the flexure blades.

### 5.3.7 Finite Element Models of the Grating Assembly

Each grating is mounted into a bezel using a six degree of freedom mount. A linear ball screw stage inserts the bezel into an open frame structure that is attached to a rotary turntable that controls the grating angle and wavelength setting. The bezel is held into the frame with 3g forces provided by the ball screw in the lateral direction and preloaded rollers in the axial and vertical directions. These forces are reacted by precision hard points. We reduced the grating blank thickness to 1.5 inches to allow for the storage of up to 4 gratings per channel. A thinner blank also results in less weight for the mechanisms to translate and potentially reduces mount deflections.

To minimize the grating tilt resulting from gravity loads, we established overturning moment stiffness for the rotary bearing of  $10^9$  in-lb radian<sup>-1</sup>. We concluded that THK blocks and curved rails would provide the desired stiffness with the least amount of start-up torque and meet our space constraints. The overturning moment stiffness of the rotary bearing is provided by 18 discrete THK HCR15 curved blocks equally spaced on a 23.62 inch diameter circle.

### 5.3.7.1 Grating Blank

The 1.5 inch thick Zerodur gratings are 12.45 inches long and 9.65 inches tall and weigh 16.4 lbs each. Normally, the Richardson Grating Lab specifies a 2 inch thick blank for a grating of this size, due to concerns about deformations from epoxy shrinkage during the grating replication and from gravity during use. A detailed study of the grating blank thickness is described in SAO Memorandum, “Binospec Grating Deflections, rev.3” by Vladimir Kradinov, dated April 9, 2007. We find that the epoxy shrinkage deformations are small,  $\sim 1/10 \lambda$  for the 2 inch thick grating and  $1/6 \lambda$  for the 1.5 inch thick grating. If the epoxy layer is uniform, epoxy shrinkage produces a small and negligible fixed symmetric focus deformation. We have also modeled the gravity deformation of the grating, and found that the 1.5 inch thick grating deforms 56% more than a 2 inch thick grating under gravity. For the 1.5 inch thick grating, the P-V surface error is  $0.4 \lambda$ , but the RMS slope errors are small,  $0.85 \times 10^{-6}$  radians (0.175”). The image blur caused by this surface error is  $2.7 \mu\text{m}$  RMS diameter.

To represent the six degree of freedom grating mount, a 3g preload is applied in the axial, lateral and vertical directions as shown

Figure 125. The forces are reacted by corresponding hard points on the opposite sides of the grating. The lateral and vertical preloads applied to the grating blank above are provided by spring plungers and the axial preloads are supplied by flexures. The axial flexures are 0.40 inch wide and the flexure blades are 1 inch long. With a 0.3 inch wide nub, the total flexure length is 2.3 inches.

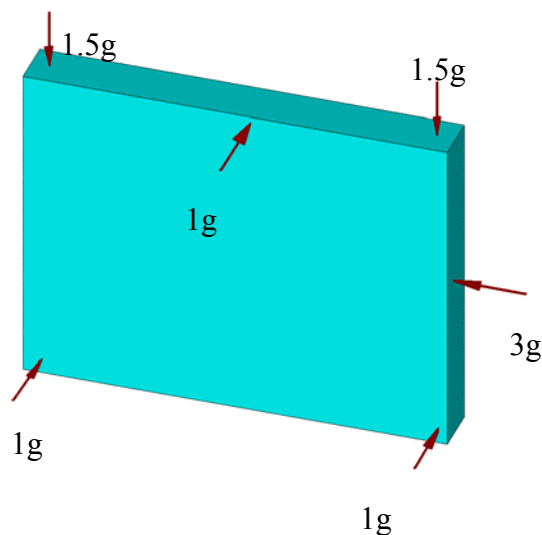
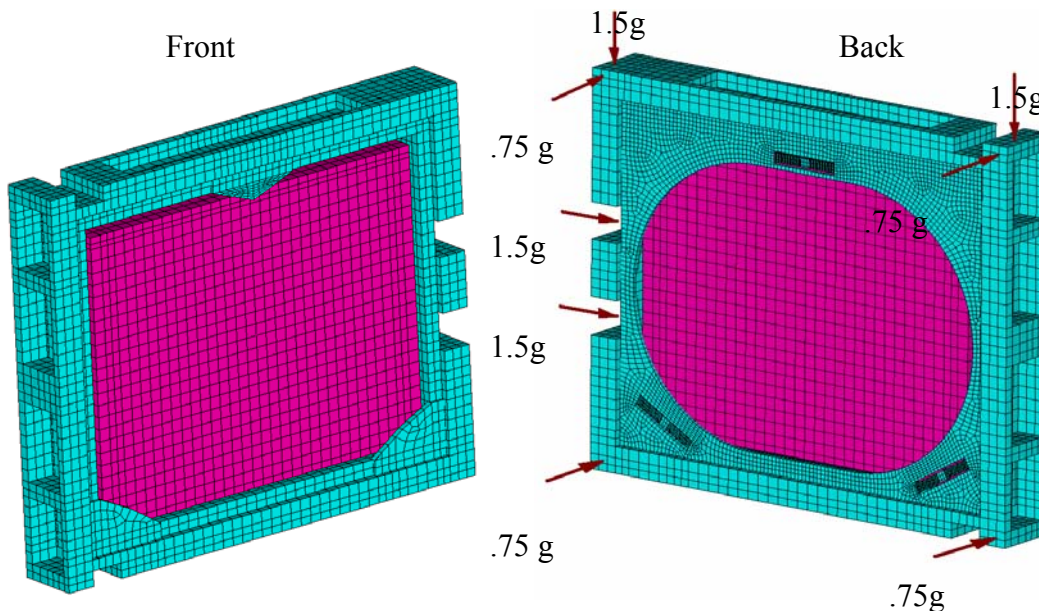


Figure 125. Finite element grating mesh and boundary conditions showing the six DOF mount with 3g preload.



**Figure 126. Finite element model of grating bezel assembly with 3g clamp forces applied.**

The axial flexure blade thickness is 0.058 inch, with a 0.125 inch thick nub. Teflon pads 0.125 inch thick are press fit to the nubs and the hard points to prevent glass to metal contact. The pad diameters are 0.30, 0.37, and 0.52 inch for the axial, vertical, and lateral pads, respectively. A 0.014 inch axial flexure displacement produces the desired 3g preload.

The finite element model of the grating bezel is shown in Figure 126. The bezel is mounted in an aluminum open frame structure that is attached to the rotary turntable. There are four axial and two vertical preload forces each reacted by hard points on the opposite side of the bezel. In the lateral direction, two preload forces are reacted by a single central hard point.

The finite element model of the grating assembly is shown in Figure 127. The ~0.5 inch thick plate structure is modeled with shell elements. The weight of the puller mechanism is ~11.5 lbs and is modeled using solid elements. The ~11.5 lb weight of other components, including guide rollers and the ball screw is uniformly distributed over the frame structure. The total weight of the structure supported by the rotary bearing is 155 lbs.

The top platform of the rotary turntable is light weighted using an open back triangular core pattern. Each triangular cell has a repeating section of 3.5 in. The rib height and thickness are 2.5 inch and 0.375 inch, respectively, and the face sheet is 0.5 inch thick. The light weight platform is represented in the finite element model as a solid plate using shell elements with a calculated equivalent solid thickness of 1.867 in. and density of 0.0557 lb/in<sup>3</sup>.

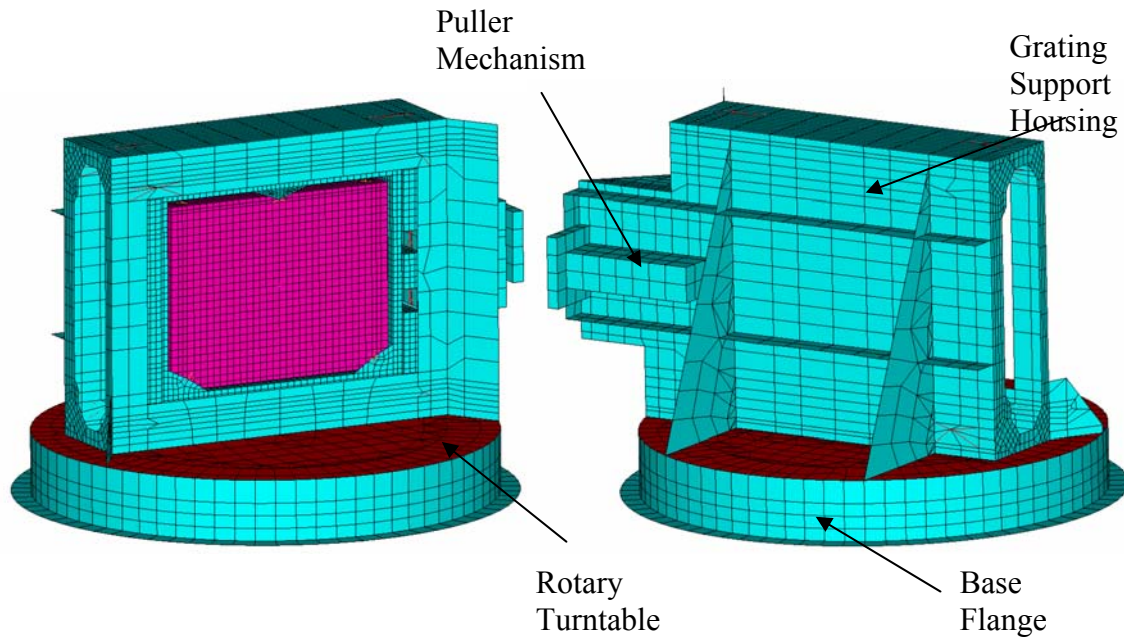


**Figure 127. FEA Model of Grating assembly.**

The rotary bearing is modeled with spring elements representing the THK blocks. One end of the spring attaches to the top platform the other end attaches to the base flange. Each block has a spring rate of  $900,000 \text{ lb in}^{-1}$  in the axial and radial directions. A tangential restraint is located at the OD of the turntable to represent the rotary brake. The base flange is made from shell elements 1 inch thick. The bottom of the flange is pinned to ground at 24 locations evenly spaced around the perimeter.

### 5.3.7.2 Grating Performance

The fundamental frequency of the grating assembly is 187 Hz. This mode corresponds to a tip-tilt of the grating relative to the base. Maximum principal stresses resulting from the 3g preload and 3g shipping loads combined with 75°F soak are shown in Table 37. Since the grating is supported by six DOF mount, there are no additional loads from clamping. Temperature changes have minimal effect.

**Table 37. Maximum principal stresses (psi) resulting from the 3g preload and 3g shipping loads combined with 75°F soak.**

	Max Flexure Stress*	Max Mirror Stress
<b>Modeled</b>	28740	464
<b>Allowable</b>	30000	500

\* The flexure stresses were multiplied by a stress concentration of 1.4 based on the fillet radii at the ends of the flexure blades.

### 5.3.8 Science Camera

The Binospec science camera consists of three structural components: (1) a support structure, (2) a vacuum housing, and (3) a CCD/cold plate assembly that mounted to the

PI flexure control stage. The finite element model of the science camera assembly is shown in Figure 128.

The camera support structure is made from aluminum with a 1 inch thick base and 0.5 inch thick front plate and gussets, and is mounted to the main optical bench at four locations. The structure is modeled with shell elements, and the mount points are pinned to ground. The aluminum vacuum housing has a minimum 0.6 inch thick wall. The removable back cover (not shown) is a flat plate with a 0.29 in. minimum thickness. The small circular and rectangular openings on top are electrical feed through ports that will be sealed with hermetic connectors. Solid elements were used to represent the complex geometry of the vacuum housing.

The field flattener (camera lens 10) is made from BSM51Y and mounts to the front of the vacuum housing. An O-ring is located between the axial ground surface of the lens and vacuum housing to create the seal. The field flattener is mounted to its bezel using a continuous (0.5 in. by 0.25 in. thick) ring of RTV560. The RTV ring is sized to athermalize the lens in the radial direction and to provide axial compliance to allow for the compression of the O-ring when vacuum is applied.

Figure 129 shows the details of the cold plate assembly that mounts to the aluminum PI flexure control stage. The science CCD and the two flexure control CCD's are attached to a common 0.375 inch thick Invar cold plate. The temperature of the cold plate is maintained at -202 °F (-130 °C). The cold plate is connected to a 0.5 inch thick aluminum support plate with three titanium flexures. The aluminum support plate is attached to the flexure control stage at four points.

The titanium flexures decouple the thermal loads resulting from the CTE mismatch and provide a low conductive path between the Invar cold plate and aluminum support. The flexures are 1 inch long, 0.50 inch wide, and 0.03 inch thick. The base of the flexure extends an additional 1.5 inch with has a stiff section 1 inch wide and 0.25 inch thick. This extension allows the cold plate assembly to fit within a circular aperture inside the flexure control stage. The goal is to minimize the imbalance of the cold plate assembly about the neutral axis of the stage to reduce gravity tilts of the CCDs.

The 3.26 lb weight of the cold plate assembly is supported by the stage with a CG offset of 1.28 inch. The estimated stage weight is 8.36 lbs. The flexures are modeled using shell elements. The support and cold plate are modeled using solid elements. The science and flexure control CCDs are represented as lumped masses. The stage is currently modeled using rigid elements, but the stage's rotational stiffness will be added to the finite element model when these data are supplied by the vendor.

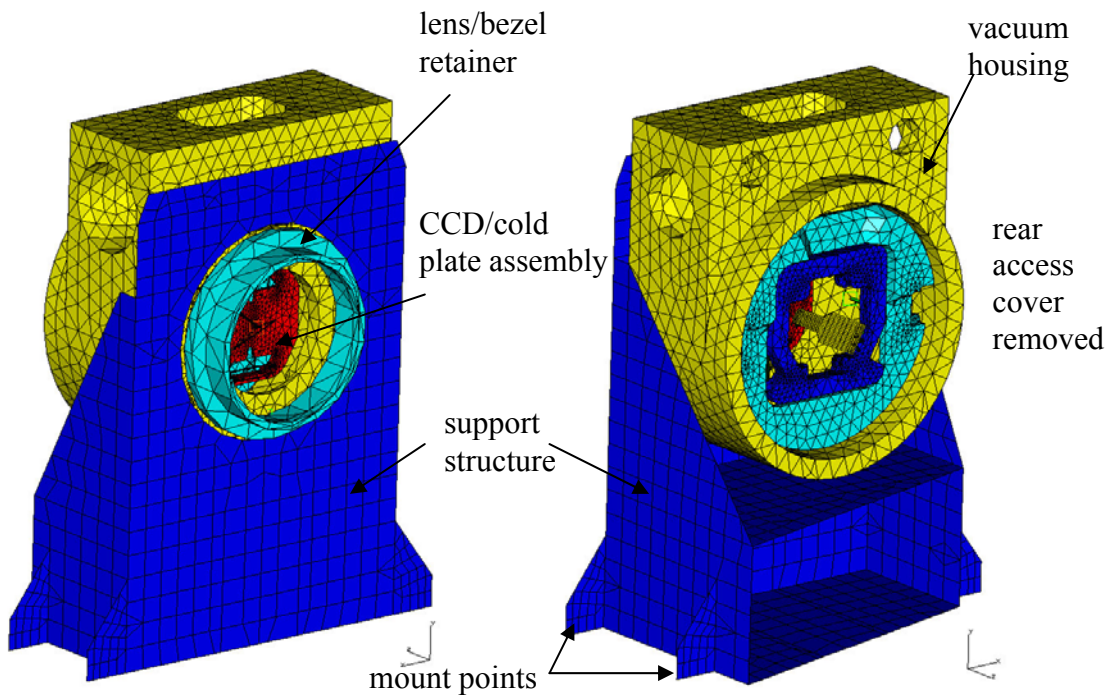


**Figure 128. Binospec camera finite element model with rear cover removed.**

The total weight of the camera assembly is 64.8 lbs. The finite element model was subjected to gravity, thermal and vacuum loads. The thermal loads include a 75° F ambient temperature change and a -202° F linear gradient across the titanium flexures. A 14.7 psi pressure was applied to the vacuum housing as well as the field flattener. The fundamental frequency of the camera assembly is 208 Hz. This mode corresponds to a front to back tilt of the support structure relative to the base.

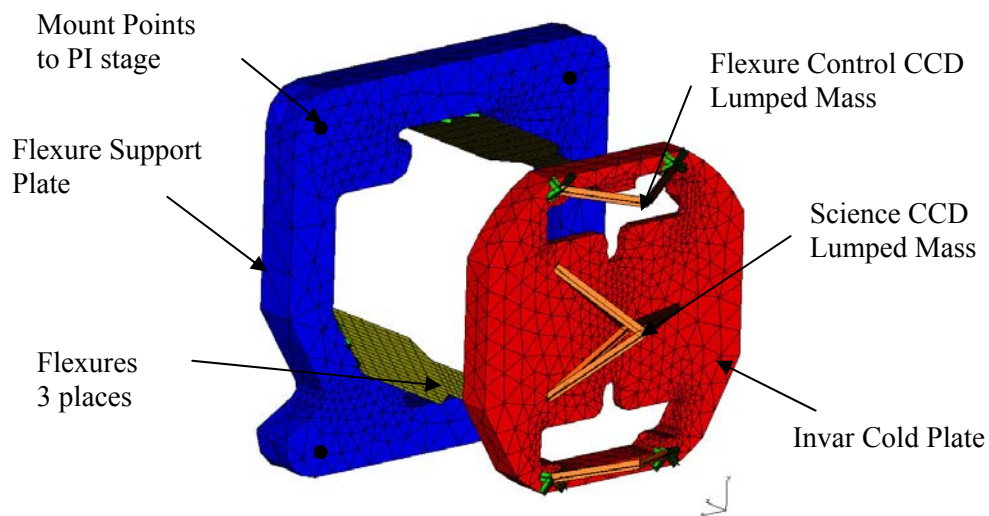


**Figure 129. Finite element model of the cold plate and flexure control stage.**

Table 38 shows the maximum stress in the flexures and the field flattener resulting from combined 3g shipping, 75°F temperature change, -202°F temperature gradient and -14.7 psi vacuum load. The resulting gravity deflections at the science CCD are ~0.00022 inch. The maximum relative motion between the science and flexure control CCDs is ~28 μin.

**Table 38. Maximum principal stresses (psi) resulting from 3g shipping loads combined with thermal and vacuum loads.**

	<b>Max Flexure Stress*</b>	<b>Max Lens Stress</b>
<b>Modeled</b>	7600	490
<b>Allowable</b>	60000	500

\* The flexure stresses were multiplied by a stress concentration of 1.4 based on the fillet radii at the ends of the flexure blades.

## 5.4 System Level Finite Element Model and System Performance

The system level finite element model represents the entire instrument, including detailed models of the mounting flange, main and inner optical benches, detailed collimator and camera lens assemblies, periscope fold mirrors, grating assembly, and science camera. Those components that do not directly contribute to the system optical performance or structural integrity are modeled as lump mass elements, including: the electronic boxes, thermal shroud, grating round house, filter assembly, calibration screen assembly, and the slit mask mechanism. The total number of elements is 805,560; the total number of nodes is 967,043. The system model is used to predict the image motion and focus changes at the science CCD when the complete instrument experiences gravity and thermal loads.

The fold mirror optical surfaces are represented by highly detailed shell element meshes. The collimator and camera lens optical surfaces are represented with highly detailed solid element meshes. The slit mask is modeled as a single node connected with RBE3 to four corners of the slit mask opening in the inner optical bench. The science detector surface is also modeled with a single node on the end of stiff beams mounted to the Invar cold plate.

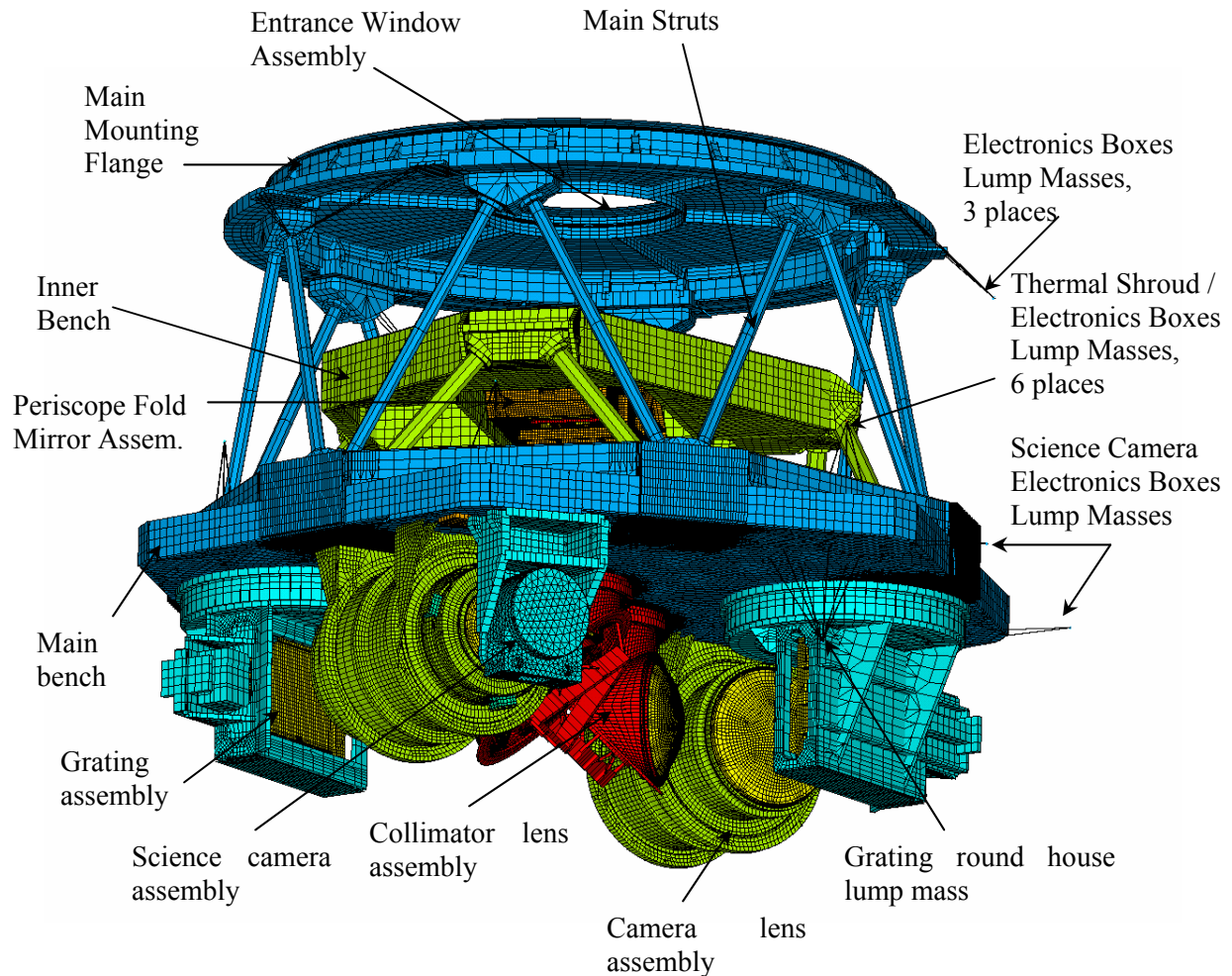


**Figure 130. Finite element model of the complete Binospec.**

#### **5.4.1 Predicting Image Motion and Surface Deformation with Bisense**

We developed a program, Bisense, to analyze finite element results and extract image motions and focus changes at the detector using the optical sensitivities in section 11.3, as well as to fit Zernike polynomials to the deformed optical surfaces for detailed analysis with Zemax. Bisense is primarily written in C++, supplemented with some heritage FORTRAN code.

Bisense uses data from several sources. A system prescription file produced by Zemax is used to define the optical system geometry. The optical sensitivities for each optical surface in the system are read from the file reproduced in section 11.3. The finite element geometry, deflection data, and group data defining the optics are read from an ANSYS file or IDEAS Master's Series universal file. Finally, a small input text file is read to relate the Zemax data to the finite element data.

Deformations of individual optical surfaces are fit by 36 Zernike terms. To aid visualization of the results, the Zernike fits can be output in a format compatible with the finite element software. The Zernike data can also be output to a format compatible with Zemax for further ray tracing analysis.

For evaluating a complete instrument, the user interactively selects particular load cases and optical surfaces to be used in the analysis. Bisense determines the lateral and focus displacement of the beam at the detector for each optical surface, and then determines the total lateral and focus displacement at the detector by summing contributions from all of the optics, in a minute or less. Bisense can therefore be used to quickly assess the effects of structural changes on the optical performance of the system.

### 5.4.2 Analysis of Surface Deformations

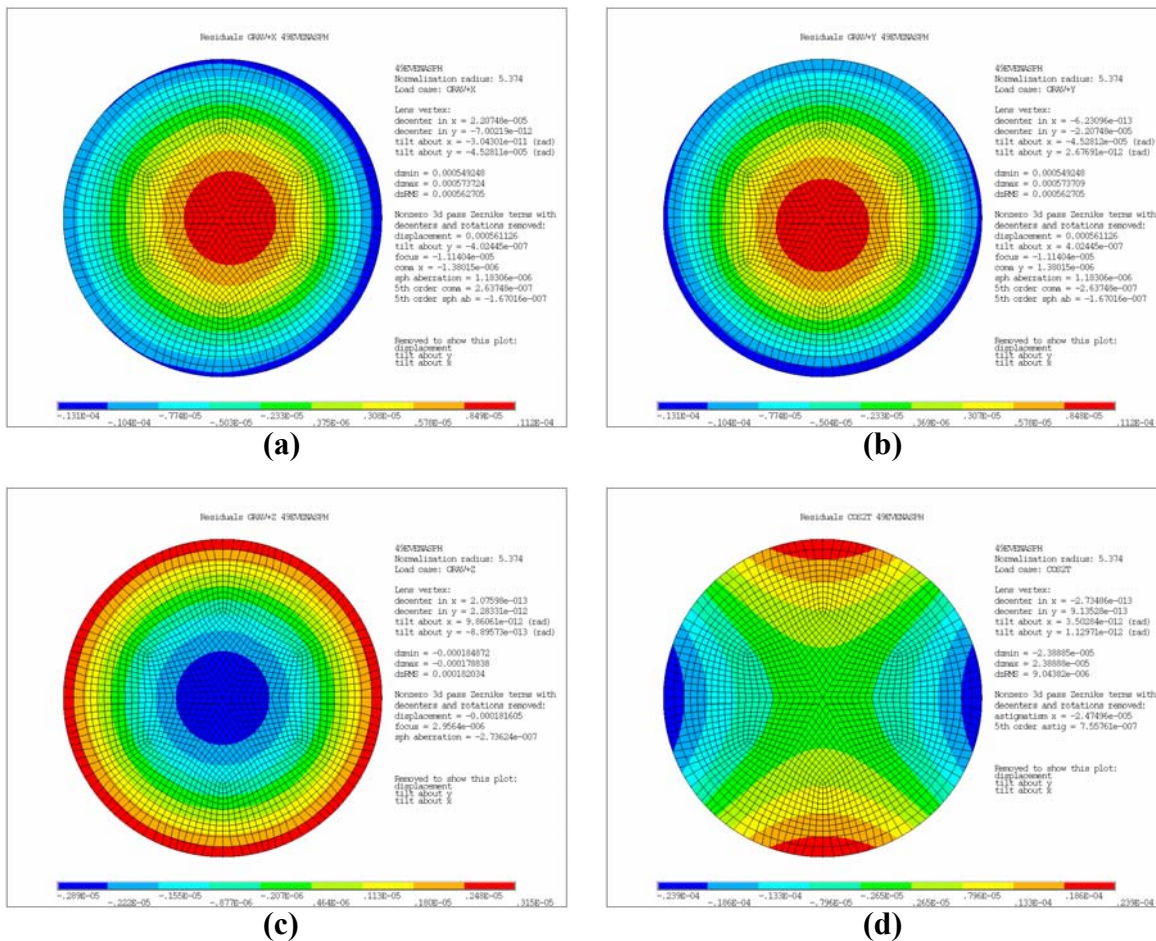


Figure 131. Analysis of finite elements results for the deformed surface of collimator lens 8. All units are inches.

A sample output from the Bisense program for one of the most critical lenses, collimator lens 8, is shown in Figure 131. Residual deformation plots (after piston and tilts have been removed) corresponding to gravity  $-X$  (a), gravity  $-Y$  (b), gravity  $-Z$  (c), and  $\cos(20)$  load (d) are presented in the figure (couplant pressure is included in all cases).

### 5.4.3 Predicted Image Motion

Figure 132 shows the image motion at the detector due to gravity acting on the complete instrument, including the lens assemblies, fold mirrors, gratings, structure and mechanisms at telescope elevation angles of 0, 30, 60, and 90°. Figure 133 shows the focus shifts due to gravity acting on the complete instrument. Figure 134 displays the same data as Figure 133, but referenced to zero gravity rather than gravity acting on the zenith-pointed instrument.

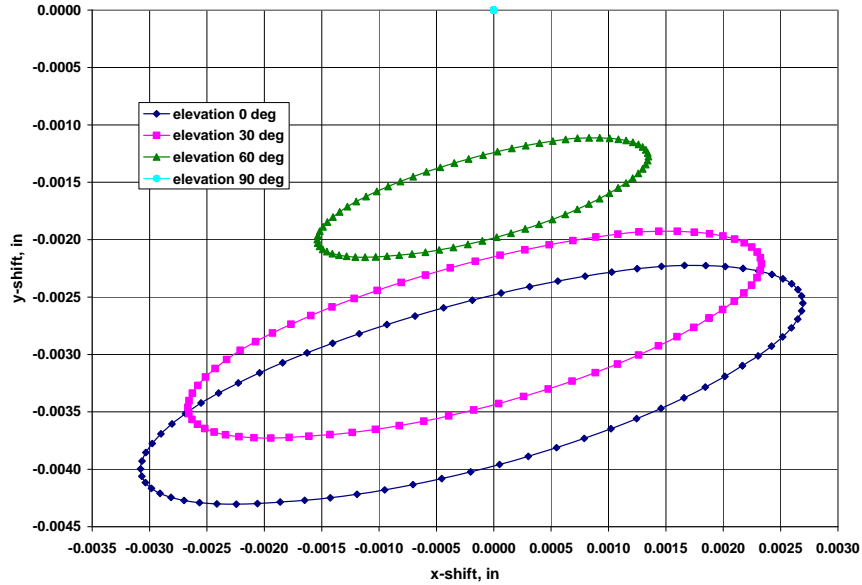


Figure 132. Image motion at the detector due to gravity acting on the complete instrument.

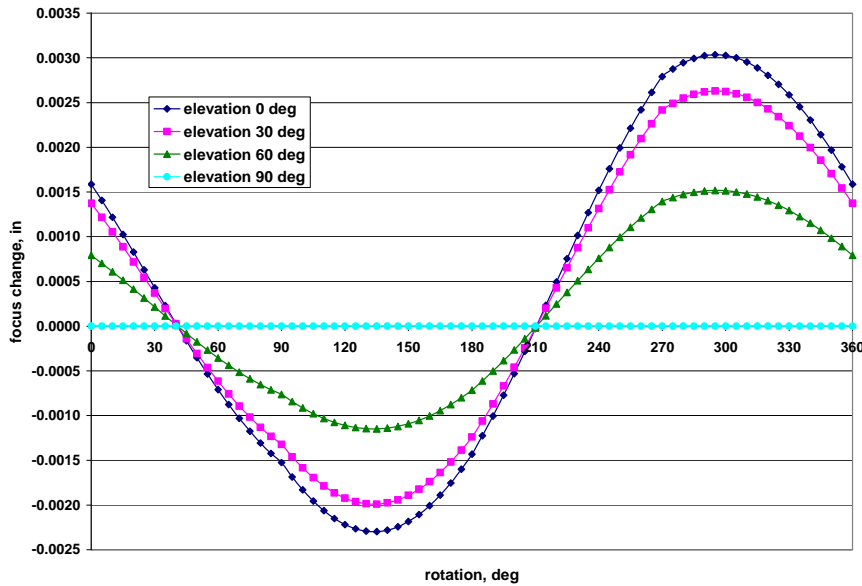


Figure 133. Focus change at the detector due to gravity acting on the complete instrument.

To evaluate the major contributors to image motion and focus changes, the worst case image motion was summed for major system groups as indicated in Table 39. The

maximum X and Y shifts at the detector are approximately -0.0031 and -0.0043 inch, respectively. The maximum focus shift is 0.003 inch.

**Table 39. Worst case contributions to the image motion and focus changes at the CCD. These include the effect of moving from zenith to horizon pointing at the rotator angle that produces the largest relative image motion.**

Group	X Motion at CCD	Y Motion at CCD	Focus Change
Slit mask	$1.14 \times 10^{-3}$	$1.37 \times 10^{-3}$	$-2.92 \times 10^{-4}$
Fold mirrors	$4.92 \times 10^{-4}$	$-1.11 \times 10^{-3}$	$-7.51 \times 10^{-4}$
Collimator	$-2.31 \times 10^{-3}$	$-8.73 \times 10^{-4}$	$1.51 \times 10^{-3}$
Grating	$-2.52 \times 10^{-4}$	$-2.78 \times 10^{-3}$	-
Camera	$-7.96 \times 10^{-3}$	$-2.54 \times 10^{-3}$	$7.36 \times 10^{-3}$
Detector	$5.80 \times 10^{-3}$	$1.63 \times 10^{-3}$	$-4.79 \times 10^{-3}$
Total	$-3.08 \times 10^{-3}$	$-4.30 \times 10^{-3}$	$3.04 \times 10^{-3}$

The camera lens group is the largest contributor to image motion, followed by the detector. The numbers in the table do not directly reflect the motions of the individual assemblies with the exception of the detector. The detector's maximum X motion is a summation of the rigid translation of the optical bench (~0.0045 inch), tilt of the detector mount due to the surface slope at the edge of the bench (~0.001 inch), and the mount stiffness (~0.00025 inch).

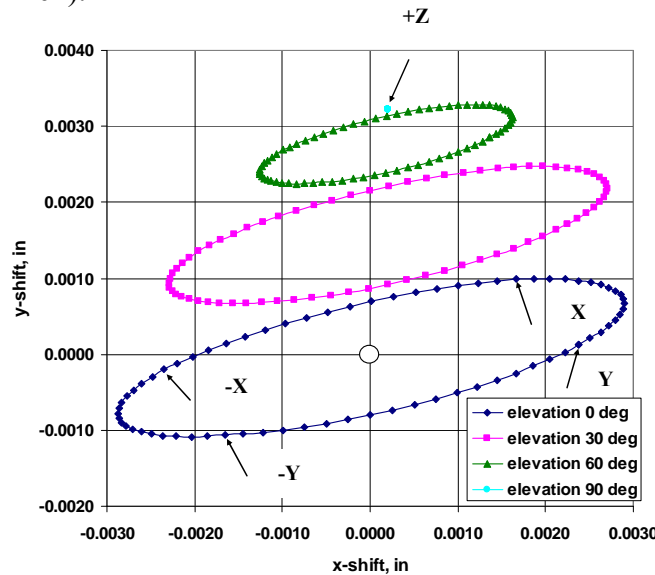


**Figure 134. Image motion at the detector relative to an unperturbed system with no gravity. Note that the largest Y image motion (perpendicular to dispersion) relative to the unperturbed system occurs for a zenith pointed instrument, and the largest X image motion (parallel to dispersion) occurs for a horizon pointed instrument. This predicted image is for the optical beam located at +X. The corresponding deflections will occur for the opposite X and Y gravity for the other optical beam.**

## 5.5 Predicted Image Motion and Image Quality from Zemax

The Bisense analysis discussed in section 5.4 gives a useful prediction of image motion and focus changes at the detector due to system flexure, but has two limitations. (1) the image motions and focus changes are correct only for light incident at the center of the field and do not allow us to study differential image motions that will limit the performance of the flexure control system. (2) We would also like to verify that the lens tilts, decenters, and surface errors introduced by system flexure cause an acceptable loss in image quality. We therefore have analyzed the finite element predictions of surface shifts, tilts, and Zernike aberrations directly with the Zemax model of the optics to calculate the spot motions and focus changes across the field and the changes in image quality. Since this work was performed by a scientist, we jump into metric units.

We perform this analysis on the cases of gravity orientations  $\pm X$ ,  $\pm Y$ ,  $+Z$ . We examine residual spot displacements across the field after an overall flexure correction is applied. We also study the RMS image diameters across the field after the system is refocused. For the image quality study, we also look at the surface errors caused by lens bezel bolt-up errors ( $\cos(2\theta)$  and  $\cos(4\theta)$  terms). To model the effect of the assembly loads arising from mounting flange surface irregularities,  $\cos(2\theta)$  and  $\cos(4\theta)$  axial displacement profiles were enforced at the flexure ends with a normalization of  $\pm 0.0005$  inch.

### 5.5.1.1 Importing the Finite Element Data

The first step is to import the element displacements, tilts, and Zernike aberration terms into the Zemax model. We wrote a Zemax macro to read in the text file containing the finite element data, insert those terms into the appropriate places in the model, and compute the spot positions and image quality at the detector for a range of wavelengths and field angles. We carried out this analysis for the 270 line grating configuration in a wavelength range of 3900 to 9312Å.

In order to include the Zernike aberration coefficients, we change each surface to type “Zernike Fringe Sag”, except for surface 55, the diffraction grating. We have not included the effects of the grating surface deformations in this analysis. Our Zemax macro uploads the Zernike coefficients into the appropriate locations in the Extra Data Editor, which holds the Zernike aberration coefficients for each surface defined as a Zernike Fringe Sag type. The normalization radii for the Zernike coefficients are the same as those listed in the sensitivity matrix data in section 11.3 and vary from surface to surface.

We verify the performance of the Zemax macro by comparing the spot motion computed for flexure terms for one surface at a time with the values in section 11.3 for on-axis illumination at 6600Å. The spot motions predicted by the Zemax model agree well with the sensitivity matrix for each surface individually, and for all of the surfaces collectively, equivalent to the Bisense analysis.

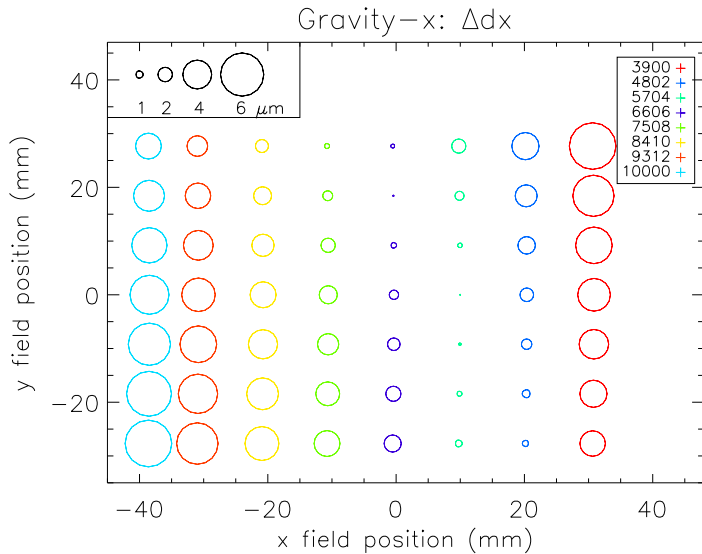
### 5.5.1.2 Image Motion Results

Table 40 shows the maximum, minimum, and the half-width of the range of spot motion measured for wavelengths between 3900 and 10,000Å at the full range of field angles perpendicular to dispersion. The last two columns list the maximum differential flexure that cannot be compensated by the flexure control system. We choose the flexure correction that minimizes the largest uncorrected displacements. The gravity  $-X$  load produces the largest uncorrected flexure.

**Table 40. Summary of spot motion for the different gravity orientations.**

	Max. dx ( $\mu\text{m}$ )	Min. dx ( $\mu\text{m}$ )	Max. dy ( $\mu\text{m}$ )	Min. dy ( $\mu\text{m}$ )	$\pm\Delta dx$ ( $\mu\text{m}$ )	$\pm\Delta dy$ ( $\mu\text{m}$ )
<b>Gravity +X</b>	55.0	45.2	5.2	-2.6	4.9	3.9
<b>Gravity -X</b>	-43.3	-55.5	-1.9	-3.0	6.1	0.6
<b>Gravity +Y</b>	40.9	33.5	27.2	24.1	3.7	1.5
<b>Gravity -Y</b>	-34.4	-39.5	-23.5	-30.8	2.5	3.7
<b>Gravity +Z</b>	7.5	2.9	70.5	65.9	2.3	2.3

Figure 135 shows the residual spot displacements following flexure correction for the  $-X$  gravity. We note that some of the spots that are shown on the plots fall outside the detector area,  $x = \pm 30.7$  mm,  $y = \pm 27.7$  mm. The spots that are significantly outside the detector area are plotted to show the trend but are not counted in the analysis.



**Figure 135. The uncorrected flexure for the  $-X$  gravity load. The diameters of the points are coded to show the magnitude of the residual uncorrected flexure. This gravity load produces the largest uncorrected flexure.**

### 5.5.1.3 Flexure Effect on Focus

We measure the effects on the image quality from the distortions in the lenses caused by gravity-induced flexure and by mounting surface imperfections. We make a single focus adjustment to the Zemax model after including the flexure terms. The focus adjustment attempts to reproduce the focus chosen for the unperturbed system. Table 41 summarizes the focus adjustment for each of the gravity orientations. The total range of focus motion needed to compensate for gravity-induced flexure is 109.2  $\mu\text{m}$  (0.0043 inch.)

**Table 41. Focus applied to bring the pattern of RMS spot diameters into the closest possible agreement with the unperturbed system. The initial system focus value is not zero.**

Case	Focus Value ( $\mu\text{m}$ )
Refocus unperturbed system	-43.2
Gravity +X	-76.2
Gravity -X	24.1
Gravity +Y	-85.1
Gravity -Y	6.4
Gravity +Z	-64.8
Range of motion	109.2

### 5.5.1.4 Flexure Effect on Image Quality

Table 42 shows the RMS image diameter averaged over wavelength and field angle (3900 to 9312  $\text{\AA}$  and at collimator Y field angles of  $\pm 7.5'$ ) for the various load cases. Table 43 gives the RMS image diameter at each wavelength and field angle. The  $-X$  and  $-Y$  orientations suffer from the largest image quality degradation of the load cases studied. Most of the image quality loss is a defocus along the dispersion direction because the gravity-induced flexure causes a slight tilt of the optical axis with respect to the CCD. For this reason, the tip/tilt capability of the PI flexure control stage turns out to be valuable as shown in Table 42. The required tilt corrections are small,  $\sim 0.02^\circ$ .

**Table 42. Image Quality Averaged Over Wavelength and Field Angle.**

Case	RMS Image Diameter ( $\mu\text{m}$ ) (no CCD Tilt)	RMS Image Diameter ( $\mu\text{m}$ ) (with CCD Tilt)	Image Blur Diameter ( $\mu\text{m}$ ) (no CCD Tilt)	Image Blur Diameter ( $\mu\text{m}$ ) (with CCD Tilt)
Unperturbed	13.3		0	0
Gravity +X	13.4	13.0	1.6	0
Gravity -X	14.6	13.6	6.0	2.8
Gravity +Y	13.2	13.1	0	0
Gravity -Y	14.3	13.4	5.3	1.6
Gravity +Z	13.4	13.1	1.6	0
Cos(2 $\Theta$ )	14.7		2.2*	2.2*
Cos(4 $\Theta$ )	13.7		1.2*	1.2*

\*Scaled down by a factor of 2 to reproduce the expected  $\pm 0.00025$  inch displacements rather than the modeled  $\pm 0.0005$  inch displacements, and by  $\sqrt{2}$  to account for the fact that all of the enforced displacements were modeled as coherent rather than random. Image blur diameters are assumed to add in quadrature.

**Table 43. RMS Image Diameter as a function of wavelength and field angle for the various finite element load cases. The best CCD tilt (typically  $\sim 0.02^\circ$ ) has been applied.**

Wavelength (Å)	Field angle (arcmin)						
	(5.616, 0.000)	(5.616, 3.750)	(5.616, -3.750)	(5.616, 6.000)	(5.616, -6.000)	(5.616, 7.500)	(5.616, -7.500)
<b>Initial</b>							
0.3900	9.2	10.1	10.1	10.8	10.8	13.4	13.4
0.4802	10.0	14.9	14.9	17.4	17.4	18.7	18.7
0.5704	6.5	6.7	6.7	10.3	10.3	14.6	14.6
0.6606	20.7	14.7	14.7	9.4	9.4	10.3	10.3
0.7508	25.9	19.6	19.6	13.3	13.3	11.4	11.4
0.8410	21.2	16.5	16.5	12.4	12.4	11.8	11.8
0.9312	10.8	9.9	9.9	10.3	10.3	12.5	12.5
<b>Gravity +X</b>							
0.3900	8.7	9.9	10.1	10.6	10.6	13.0	12.7
0.4802	11.2	15.9	16.2	18.5	18.8	19.6	20.0
0.5704	6.4	7.4	7.6	11.4	11.6	15.6	15.9
0.6606	19.5	13.7	13.5	8.8	8.5	10.4	10.4
0.7508	24.5	18.2	18.0	11.9	11.5	10.5	10.3
0.8410	19.6	15.0	14.7	11.1	10.7	11.2	11.0
0.9312	10.0	9.8	9.6	10.7	10.6	13.2	13.4
<b>Gravity -X</b>							
0.3900	10.0	10.9	10.8	11.3	11.3	13.7	13.9
0.4802	10.9	15.9	15.7	18.6	18.4	20.1	20.0
0.5704	6.4	7.4	7.3	11.6	11.5	16.2	16.1
0.6606	20.2	14.4	14.6	10.0	10.3	11.8	12.0
0.7508	25.4	19.2	19.5	13.4	13.8	12.4	12.8
0.8410	20.6	16.0	16.3	12.5	12.9	12.7	13.0
0.9312	9.9	9.5	9.8	10.5	10.7	13.0	13.0
<b>Gravity +Y</b>							
0.3900	10.1	11.1	10.5	12.9	10.8	16.4	13.1
0.4802	9.0	12.7	15.2	15.1	18.2	16.6	19.7
0.5704	7.2	6.2	7.6	9.0	11.6	13.2	16.3
0.6606	20.5	15.1	13.8	10.0	8.9	10.3	11.3
0.7508	25.0	19.5	17.8	13.7	11.4	11.8	11.1
0.8410	19.6	15.9	14.3	12.6	10.7	12.3	12.0
0.9312	9.7	10.0	9.7	11.2	11.4	13.5	14.5
<b>Gravity -Y</b>							
0.3900	10.0	10.9	11.2	11.0	12.8	12.9	16.1
0.4802	9.8	15.8	13.4	18.6	15.6	19.9	17.0
0.5704	6.9	7.8	6.5	11.8	9.4	16.2	13.4
0.6606	20.6	14.2	15.5	9.5	10.7	11.4	10.8
0.7508	25.5	18.6	20.3	12.4	14.8	11.6	12.8
0.8410	20.4	15.2	16.9	11.5	13.7	12.1	13.1
0.9312	9.9	9.5	10.1	10.7	11.2	13.5	13.3
<b>Gravity +Z</b>							
0.3900	9.8	10.4	11.0	12.2	11.3	15.9	13.3
0.4802	8.9	12.0	15.7	14.1	18.8	15.5	20.3
0.5704	7.2	5.4	8.1	7.8	12.1	12.1	16.7
0.6606	20.9	15.6	14.3	10.2	9.5	9.9	11.6
0.7508	25.7	20.3	18.5	14.3	12.1	12.0	11.4
0.8410	20.4	16.6	14.9	12.9	11.1	12.1	11.9
0.9312	9.7	9.5	9.3	10.2	10.7	12.4	13.7

### **5.5.1.5 Discussion of Zemax Analysis**

Looking at Table 42 and Figure 134 we see that the worst image blur arises during the largest  $-X$  image motion at the detector. In local coordinates, the  $X$  axis at the CCD runs perpendicular to the dispersion direction. The  $-X$  gravity case that we analyzed doesn't give the largest  $-X$  image motion for a horizon pointed instrument; the worst case gives ~20% larger deflections. However, we won't use the instrument below an elevation of ~30°, and Figure 134 shows that the largest  $-X$  image motion at a 30° elevation is identical to that for the  $-X$  gravity case that we analyzed. We conclude that the results in Table 42 are representative.

The keen eyed reviewer will note that the image motions shown in Figure 134 are 10-15% higher than those shown in Table 40. This difference arises from the fact that the Zemax analysis was carried out with a slightly earlier version of the system finite element model that reflected somewhat less weight. The performance of the collimator and camera optical mounts is identical in both models, so the larger deflections in the newer model should cause no more image blur. Nonetheless, we scale our worst expected image blur due to gravity, 2.8  $\mu\text{m}$ , up to 3.2  $\mu\text{m}$  for the summary in section 7.

## **5.6 Subassembly Finite Element Analysis**

We performed finite element analysis of the critical mechanical subassemblies, including the slit mask and filter storage cassettes, the grating roundhouse, the entrance window assembly, the thermal shroud, and the calibration/derotator assembly. Although the performance of these subassemblies does not influence the optics, our goal is to maintain reasonable flexure and stress levels to avoid damage to filters, gratings, and etc. and to assure reliable mechanism operation. Below, we present some representative analyses.

### **5.6.1 Slit Mask and Filter Elevator Assemblies**

Each elevator assembly stores the slit masks or filters while not in use and positions the cassettes to allow for component interchange. The assembly must remain structurally intact during operation and positively engage the cassettes, with minimal assembly deflection. The model was subjected to a total load of 3g gravity combined with a 3g preload of cassettes against their mounting rollers.

Figure 136 and Figure 137 show the finite element models for the slit mask and filter cassette elevators, respectively. The frames consist primarily of shell elements. Beam elements were used to represent the cassettes and elevator stage mechanisms. The slit masks and filters were represented as lumped masses. The modeled weight is 63 lbs for the slit mask assembly and 112 lbs for the filter assembly.

A maximum stress of 4200 psi was found in the slit mask elevator, with a maximum deflection of 0.018 inches. For the filter elevator, the maximum stress is 2400 psi, with a maximum deflection of 0.006 in.

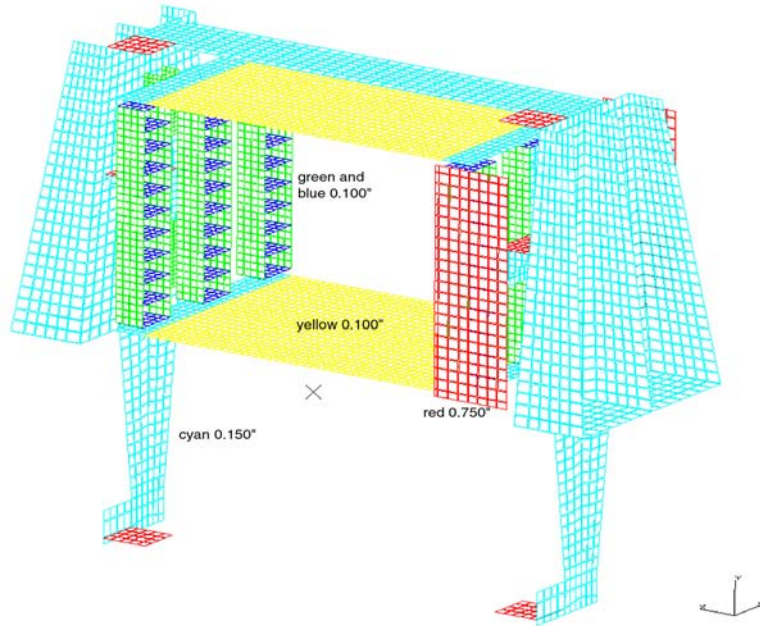


Figure 136. Finite element model for the slit mask elevator assembly.

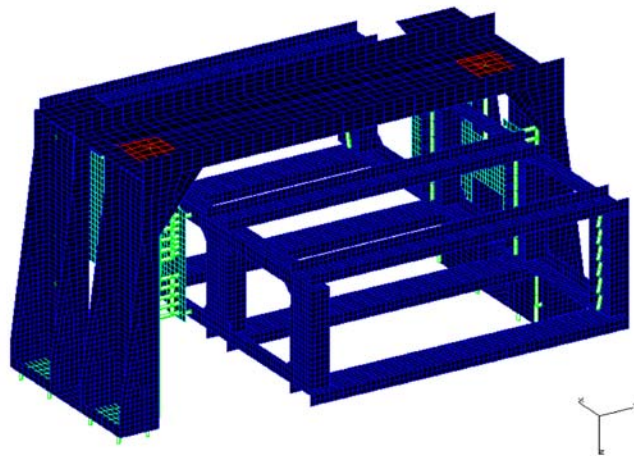


Figure 137. Finite element model for the filter cassette elevator assembly.

### 5.6.2 Grating Storage

The grating roundhouse stores the gratings while not in use. The roundhouse weighs 165 lbs including the weight of four grating assemblies, each weighing 24 lbs. The finite element model includes the gratings, rollers, grating locks, and support frame as shown in Figure 138. The structure is modeled with shell elements. Beam elements were used to represent the gratings and roller assemblies. The model was subjected to a total load of 3g gravity combined with 3g preload of the gratings against their mounting rollers.

The maximum stress is 3000 psi and the maximum deflection is 0.004 inch at the center of the top plate.

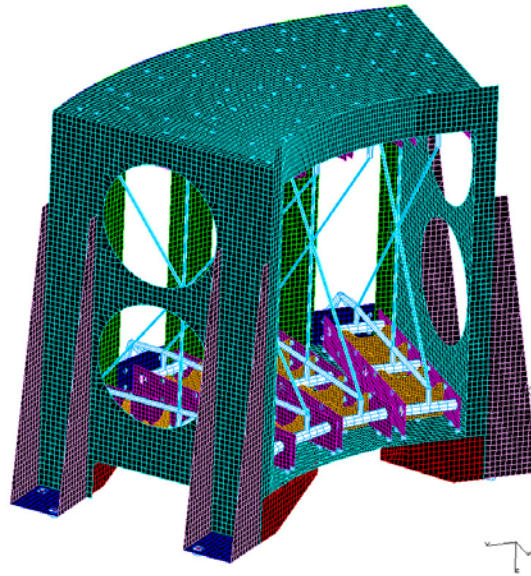


Figure 138. Finite element model of the grating roundhouse assembly.

## 5.7 Shipping and Handling

Binospec consists of many optical, mechanical and structural assemblies that must survive shipping and handling. We set the maximum shipping and handling loads at 3g. During shipment of previous f/5 instruments to the MMT the measured loads on isolated platforms were always less than 2g.

The critical handling load cases that we considered are: hoisting Binospec, rotating it 180°, and mounting it on its support cart upside down for service. The requirement is that the maximum stress in each material must not exceed the allowable levels summarized in Table 24.

### 5.7.1 Shipping Isolation System

Figure 139 shows the finite element model of Binospec installed on the handling cart for shipping and maneuvering in the lab and on the MMT observatory floor. During shipping, there will be one Aeroflex coil isolator (model number CB-1900-12) mounted at each of the four corners underneath the cart. The isolators are 8.5 by 10.25 inches, and by 20.5 inches long. The isolators were sized to limit the response of the instrument to 3 g for a vertical drop height of 5.5 inches. The instrument response is summarized in Table 44.

**Table 44. Binospec Isolation System Performance**

Load direction	Transmitted Load	Drop height	Isolated Displacement
Vertical	3.0g	5.5 in	2.5 in

### 5.7.2 Hoisting for Assembly and Maintenance

Figure 140 shows Binospec in its hoist configuration. The hoist frame includes a hoist point, and spherical bearings that decouple moment loads at the two main optical bench attachment locations. Figure 141 shows Binospec rotated upside down and mounted to the cart. In this configuration, Binospec is supported at six locations along the mounting flange.

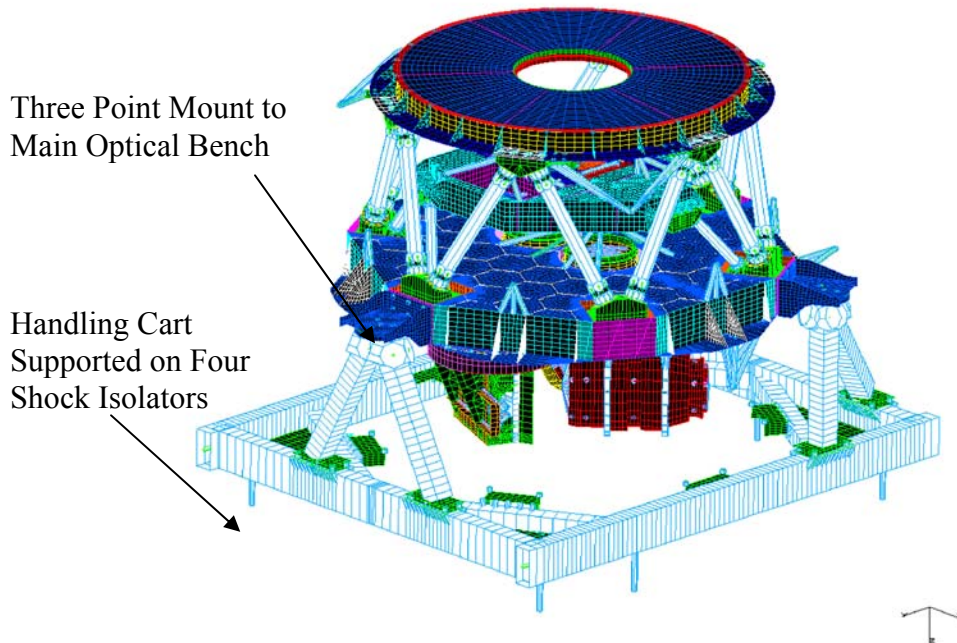


**Figure 139. Finite Element Model for Shipping on Cart.**

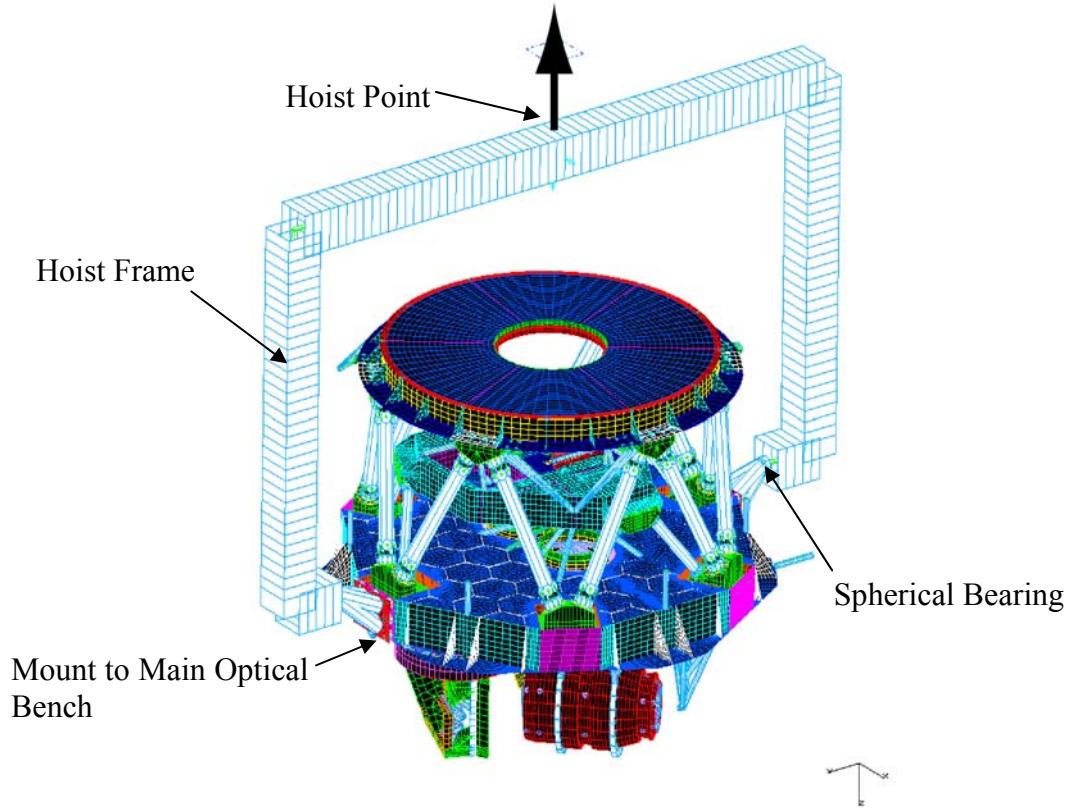


Figure 140. Finite element model for vertical hoisting.

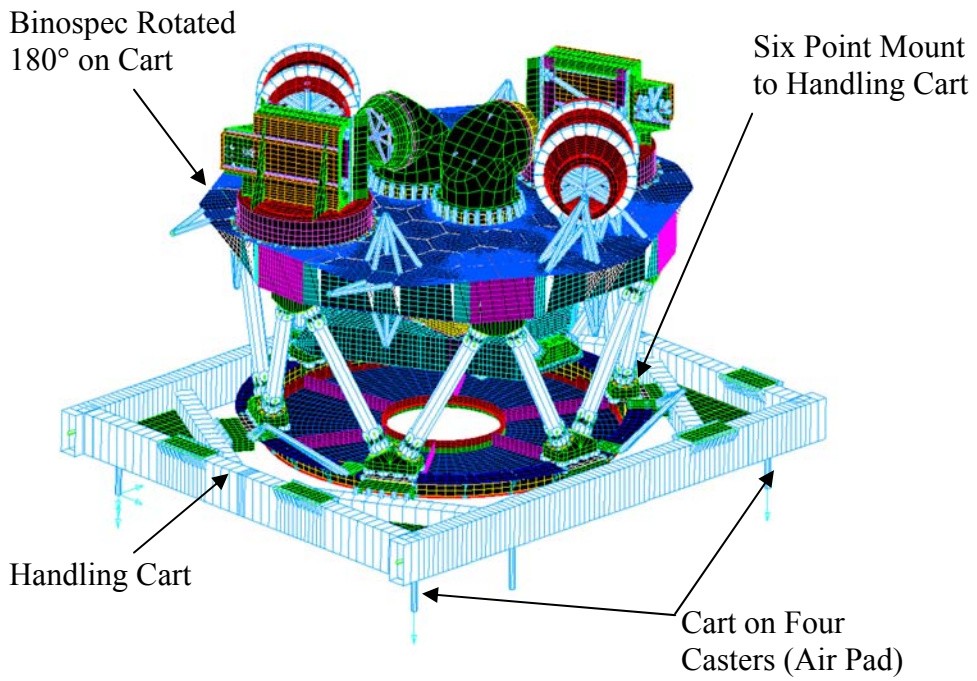


Figure 141. Finite element model for Binospec inverted on its cart.

Table 45 lists the maximum stress in the mounting flange, main optical bench, and inner bench. The highest stress levels shown are in the main bench at the cart or hoist attachment locations. The maximum stress of 4200 psi occurs during hoisting.

**Table 45. Binospec Stress Summary.**

<b>3g load case configuration</b>	<b>Load direction</b>	<b>Stress (psi)</b>		
		<b>Mounting flange</b>	<b>Main optical bench</b>	<b>Inner bench</b>
Binospec mounted on support cart	lateral	780	3900	282
	vertical	780	2370	330
Binospec hoisting and rotation	lateral	168	460	48
	vertical	1200	4200	600
	upside down	1140	3960	450
Binospec mounted upside down on support cart	vertical, upside down	2160	750	360
Allowable		16000		

## 6 Optics Assembly

### 6.1 Lens Fluid Seals

#### 6.1.1 Introduction

The optical design of Binospec includes 12 lens multiplets that are coupled with Cargille Laser Liquid 5610. This couplant is siloxane based (silicone) with an index of refraction  $n_D=1.5000$  (5893Å) at 25°C. The athermal optical design takes advantage of the couplant's index change with temperature ( $dn/dT$ ) and is sensitive to the index value. This section discusses the materials and methods that will be used to form a fluid seal that is strong and does not influence the optical performance. The seal must be reliable and not interact chemically with the couplant.

#### 6.1.2 Material Compatibility with the Lens Couplant

To ensure the long term reliability of the optical system, all materials that come in contact with the LL5610 were tested to make sure that they do not contaminate the couplant and that the couplant does not degrade their mechanical properties. Strict quality control in handling the samples was observed in order to prevent false readings due to cross contamination. Table 46 lists materials that are being used that were tested for compatibility with Cargille LL5610. Tests were done that looked for an index or transmission change in the fluid and also for a change in the material durometer. See memo 28 October, 2007 summarizing the details of the materials tests.

**Table 46. Materials compatible with LL5610**

Bare Al
Ni Plated Al
Teflon Coated O-Ring 1
NaCl Windows
Viton O-Ring
Teflon O-Ring CE
Hysol 9313 Epoxy w/Siltex 44
FEP Formed Seal
FEP Formed Seal Chemically Etched
Outgassed LL5610

**Table 47. Materials incompatible with LL5610**

	<b>Incompatibility</b>
GE655 RTV	Index 1.5000 -> 1.5133 and Transmission Change
Sylgard 184 RTV	Index 1.500 -> 1.5110 and Transmission Change
GE560 RTV Red	Durometer decrease (55 to 30)
Sylgard 184 JZ Batch 21	Index 1.5000->1.5113 and Transmission Change
Sylgard 184 JZ Batch 22	Index 1.5000->1.5137 and Transmission Change
Buna-Nitrile O-Ring	Transmission Change

### 6.1.3 Multiplet Lens Seal Manufacturing

Polyimide and Teflon films were considered for seal material. We selected 7.5 mil FEP Teflon Type A. Thinner seals are too hard to handle and thicker seals are not sufficiently compliant. A Teflon surface treatment of sodium ammonia from Porter Process Inc. allows adhesives to stick to the Teflon. The adhesive that will be used for seal bonding is Loctite Hysol 9313 mixed 80% by weight with Siltex 44 silica powder and outgassed by standard methods. Samples were soaked in L5610 and then subjected to bond failure testing, see memo 27 October 2007. Figure 142 shows how the Teflon stretches before the bond fails. The Teflon began to stretch noticeably at 15 lbs per inch and failed before the bond.



Figure 142. Teflon bond failure tests. The Teflon stretches considerably before the bond fails in shear.

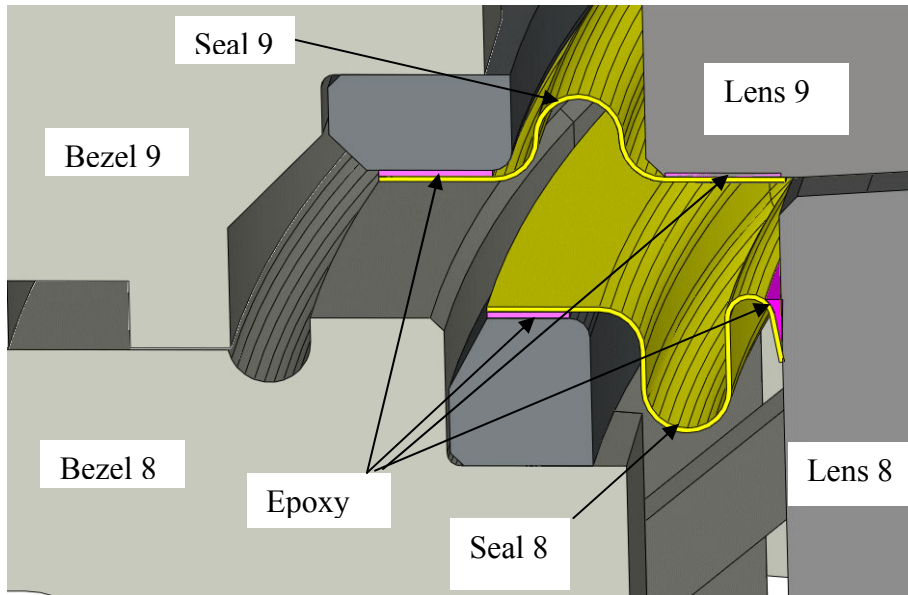
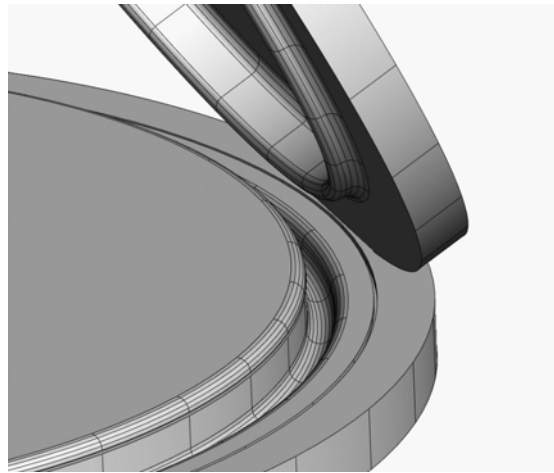


Figure 143. Detail of lens seal geometry.

Space constraints, fabrication limits, bond application and finite element analysis has led

us to the seal shapes shown below in Figure 143. This shape minimizes the seal load on the lenses. We use two seal profiles depending on where the seal is bonded to the lens. The length of the seal between the lens and the bezel determines the seal compliance. The method of forming the seals into their required shape involves a top/bottom mold as shown in Figure 144. The Teflon is placed between the mold pieces and the sandwich is heated to 550°F. Seals produced in this fashion have uniform thickness and display ~0.5% shrinkage relative to the mold dimensions.



**Figure 144. Two part Teflon seal mold.**

The seal is bonded to the lens using a precision syringe controlled by a pressure regulated dispenser. The lens and the seal are rotated at a constant speed while the epoxy is dispensed at a controlled rate. This procedure is shown in Figure 145.

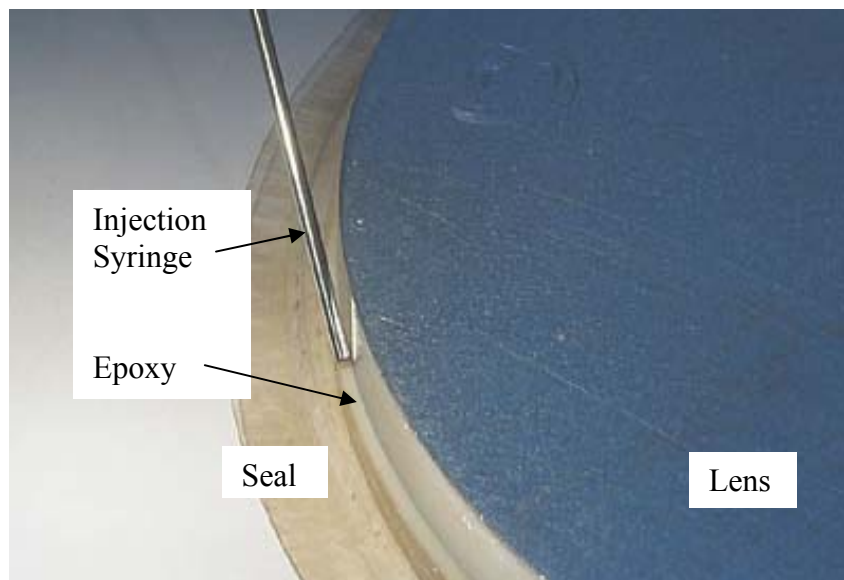


**Figure 145. The Teflon seal is bonded to the lens with epoxy that is injected at a constant rate while the lens and seal are rotated at a constant speed. This procedure yields a very neat and strong seal.**

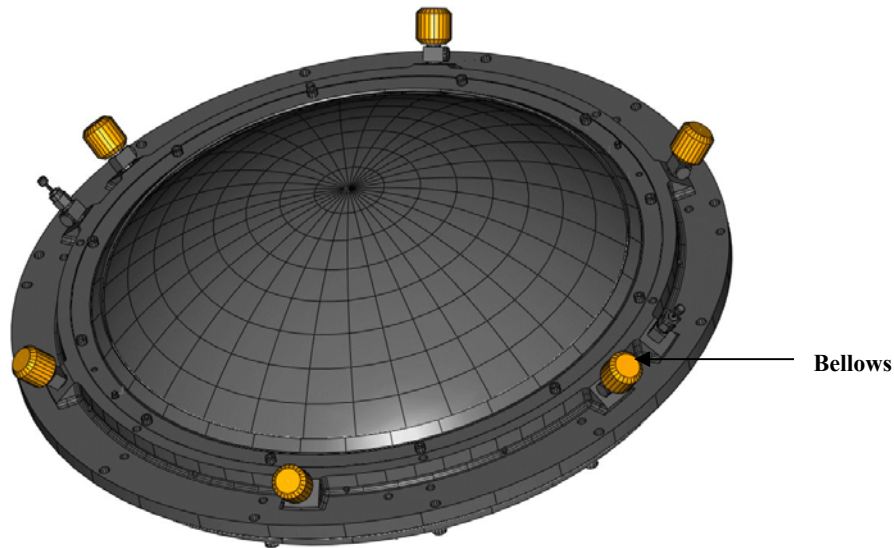
### 6.1.4 Fluid Thermal Contraction Compensation

LL5610 has a volume coefficient of thermal expansion ( $8 \times 10^{-4}$  per  $^{\circ}\text{C}$ ) that is an order of magnitude larger than that of aluminum ( $6.9 \times 10^{-5}$  per  $^{\circ}\text{C}$ ), so that as a fluid-coupled lens group is cooled from room temperature, a vacuum will be pulled by the decrease in couplant volume if a fluid reservoir is not provided. We plan to provide fluid reservoirs in the form of small Teflon bellows. As an illustration of the magnitude of the problem, we present two cases: (1) a small couplant volume between collimator lenses 8 and 9, and (2) a much larger couplant volume in the collimator quintuplet (lenses 4 through 7). Table 48 summarizes the results for an extreme  $42^{\circ}\text{C}$  temperature change. The required bellows volume is the difference between the gap and fluid volumes plus a safety factor. Further details can be found in Joe Zajac's "Fluid Gap Modeling" memo October 29, 2007)

**Table 48. Lens group volume changes for a  $42^{\circ}\text{C}$  temperature change**

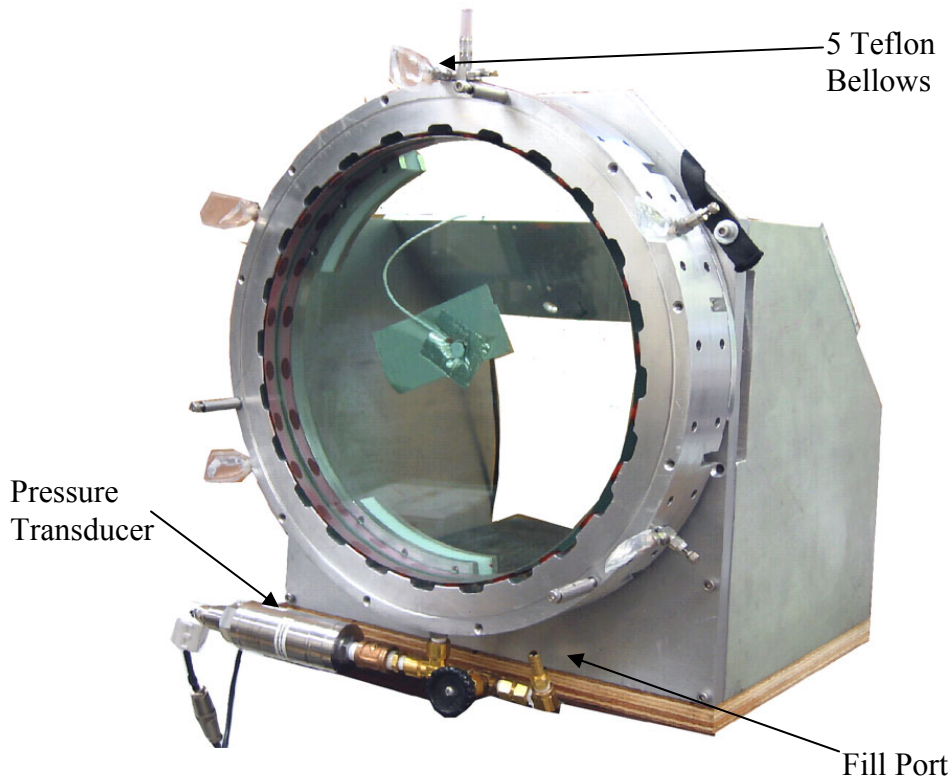
Collimator Lenses	Delta Gap (in <sup>3</sup> )	Delta Fluid (in <sup>3</sup> )
8 - 9	-0.165	-0.34
4 - 7	-0.46	-1.58

Figure 146 shows the arrangement of bellow for a typical lens group. The bellows are distributed around the circumference so that there is a bellows near the top of the group in any gravity orientation. If we provided a single bellows and it happened to be near the bottom, the pressure head across the lens would counteract its function, and the fluid volume change would occur by deforming the seal at the top of the lens group.



**Figure 146. Typical arrangement of fluid bellows around a multiplet. The Teflon bellows are protected in metal enclosures.**

### 6.1.5 Prototype Doublet



**Figure 147. Prototype doublet lens assembly.**

In order to test prototype Teflon seals, seal bonding techniques, and the performance of Teflon thermal compensation bellows, we built a prototype lens doublet and bezel assembly. The prototype was simplified by using flat glass plates spaced by 0.010 inches instead of lenses and by substituting RTV pads for the flexure mounts that we have adopted. The fluid gap was filled with LL5610 and the measured pressure head was the expected 0.625 psi. We learned that outgassing the LL5610 significantly reduces bubbles when filling the doublet. We filled the doublet with LL5610 from the bottom with the top open to provide a vent. Figure 148 shows that over a 76 °F (42 °C) temperature drop, the thermal compensation bellows kept the pressure head constant within 0.07 PSI.

### 6.1.6 Seal Load on Glass

To verify the finite element analysis of the seal load on a lens, a seal was bonded between a lens surrogate and a bezel, with no lens mount between the bezel and the surrogate lens. The force required to translate the bezel while holding the lens surrogate stationary is a good measure of the force applied by the seal for relative lateral shifts. We measure a force of ~6.6 lbs per 0.001 inch of relative lateral shift. We expect relative lateral displacements due to flexure of ~0.00004 inch and the resulting loads of ~0.26 lb are small.

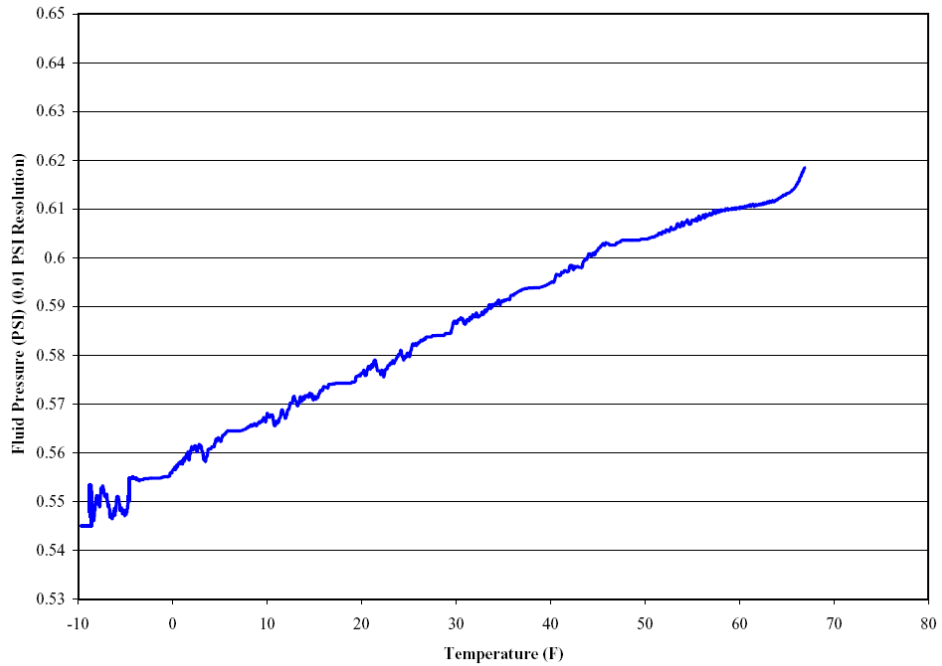


**Figure 148. Pressure head change in prototype doublet fluid for 76 °F (42 °C) temperature drop. The thermal compensation bellows kept the pressure head constant within 0.07 PSI.**

## 6.2 Optical Assembly with the Opticentric Lens Alignment Machine



**Figure 149. Opticentric lens alignment machine**

Aligning the lenses to their bezels requires precision alignment in five degrees of freedom: tip, tilt, and position along three axes. Since the optical center of the lens is not exactly the mechanical center, the most precise alignment requires optical detection of the lens axis. We looked into building an alignment machine but the estimated engineering costs were more than the purchase price of the commercial Opticentric machine shown in Figure 149.

The Opticentric uses two autocollimators to view both surfaces of a lens simultaneously. The autocollimator signals are digitized and recorded as the lens is rotated on an air bearing stage. If the lens is not exactly on the axis of the air bearing stage, the autocollimator return describes a circle with radius proportional to alignment error. The lens is centered and tilted until both autocollimator circles are acceptably small. The Opticentric comes with software to display and analyze the autocollimator data. We have developed a fixture to hold and position the lens and bezel on the Opticentric. In Figure 150, the collimator lens 9 is shown on three Teflon supports.

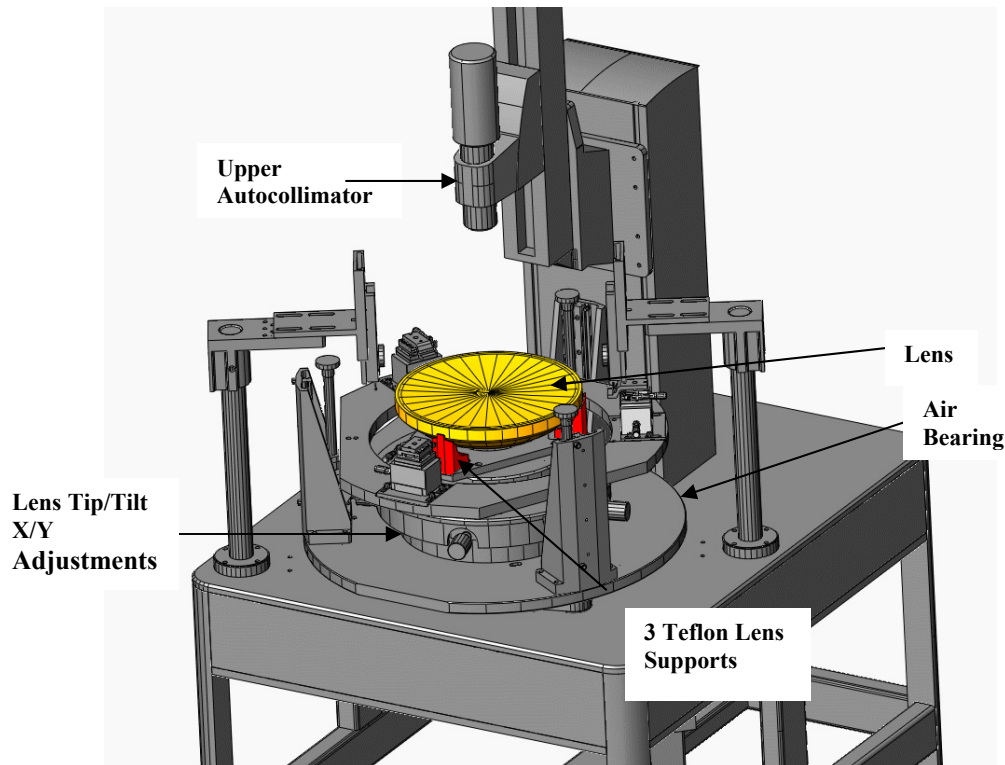


Figure 150. Opticentric lens and bezel fixture.

The **first step** of the lens to bezel alignment is to align the optical axis of the lens to the rotary axis of the air bearing using the tip/tilt and X/Y adjustments.

In the **second step**, the autocollimator linear encoder is set to zero when the autocollimator is focused at the vertex of the lens. This is called the “cat’s eye” position.

The **third step** in the alignment begins by raising the bezel support above the lens and placing the bezel on the three point adjustable mount as shown in Figure 151. Two dial indicators are then used to center the bezel on the rotary axis and to adjust the bezel so the reference surface of the bezel is perpendicular to the rotary axis.

In the **fourth step** we place the bezel at its proper height with respect to the lens using a special fixture with a mirror that allows the Opticentric autocollimator to pick up an axial surface that is precisely referenced to the bezel's axial reference surface. The special gauge is shown in Figure 152.

**Step five** in the alignment is to recheck the lens and bezel alignments with respect to the air bearing axis, and **step six** is to bond the lens to the bezel.

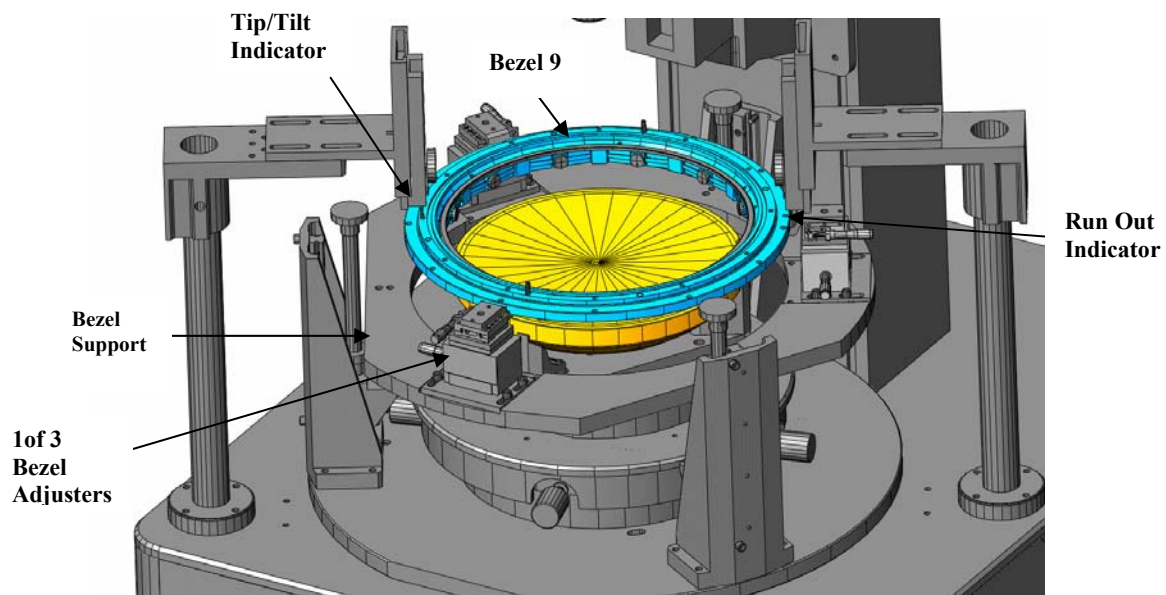
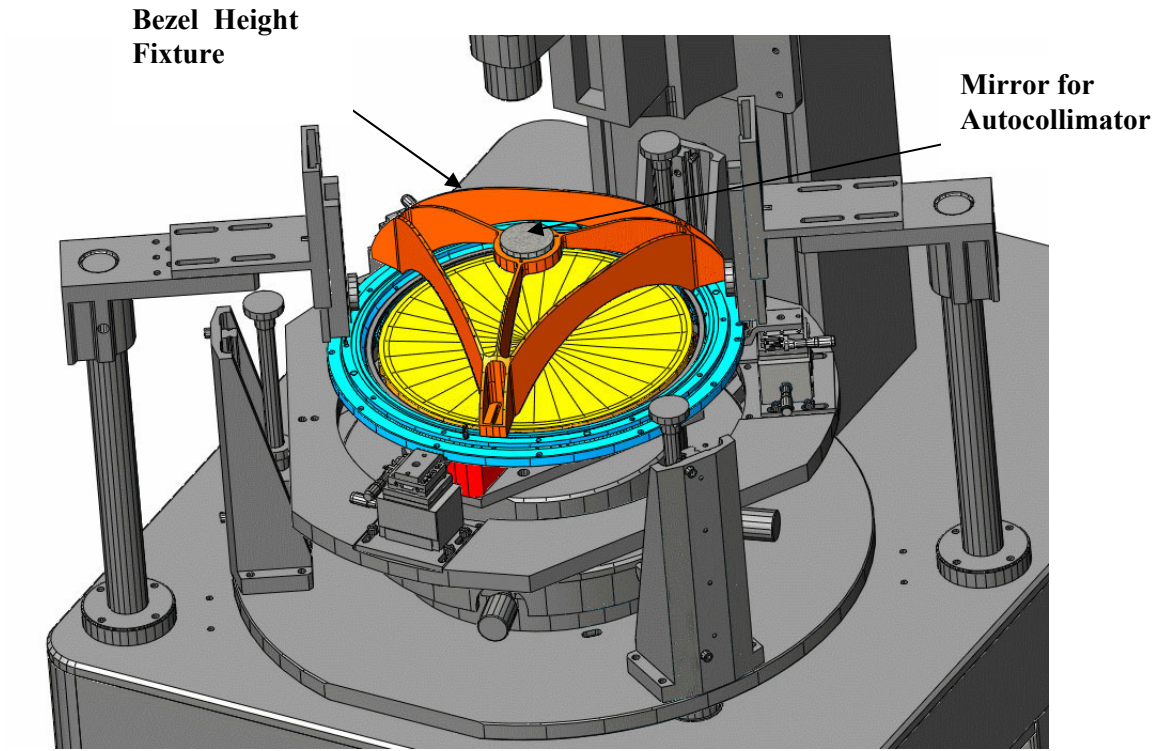


Figure 151. The lens bezel is placed on its support and vertical and radial runout is measured with two dial gauges, and then zeroed out with adjustments.

### 6.2.1 Radius of Curvature Measurement

While measuring the radius of curvature of a lens surface is not a required part of our alignment procedure, the Opticentric allows us to verify the radius of curvature supplied by the optician. With a converging lens of a suitable focal length to account for the travel of the autocollimators in the axial direction, the collimated beam can be focused on the surface of the optic. This is known as the cat's eye position, illustrated in Figure 153. If the autocollimator is then moved closer to the lens until the reflected beam off the first surface is in focus at the camera, the distance translated is the radius of curvature of the lens. The accuracy of this measurement depends on the focal ratio of the converging lens and the encoder resolution. Faster focal ratio lenses will yield a shallow depth of field and a greater accuracy in focusing on the cat's eye position. Our tests have shown that with a 100mm FL lens, the surface can be repeatedly located within 1  $\mu\text{m}$ . The linear encoder is accurate to 2  $\mu\text{m}$ .



**Figure 152.** The tripod fixture used to set the axial position of the bezel. The upper autocollimator is focused on a mirror attached to fixture. The mirror is precisely registered to the bezel's axial reference surface.

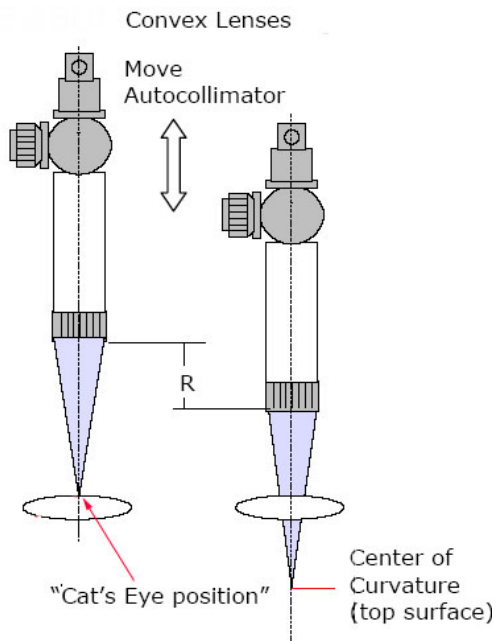


**Figure 153.** Convex Lens Radius Measurement

## 6.2.2 Lens Thickness Measurement

This measurement provides another convenient means of checking the optician's work. The cat's eye position of the top and bottom surfaces of the lens can be measured with the upper and lower autocollimators respectively. Then the lens is removed and one autocollimator is translated so that its beam is at the focus of the opposite autocollimator. The translated distance is the lens thickness.

## 6.3 Collimator and Camera Assembly Tolerances

### 6.3.1 Axial and Radial Lens Assembly Requirements

We can derive a requirement for the assembly tolerance based on the loss of image quality due to misalignments. Only a few surfaces, listed in Table 49, contribute significantly.

**Table 49. Sensitive surfaces for radial alignment.**

Lens	Surface	Image Blur for 0.001 inch Decenter (RMS diameter in microns)
Collimator 7	2	2.4
Collimator 8	1	1.8
Collimator 9	2	3.6
Camera 1	1	0.9
Camera 6	2	1.5
Total (in quadrature)		5.0

Although a decenter and tilt are equivalent for a spherical surface, and are zeroed equivalently in the lens alignment process, we must consider the error introduced by the fact that the bezel reference surface is tilted slightly with respect to the optical axis as the bezels are assembled into a complete collimator and camera assembly.

**Table 50. Sensitive surfaces for tilt alignment**

Lens	Surface	Image Blur for 0.06 milliradian Tilt (RMS diameter in microns)
Collimator 7	2	0.8
Collimator 8	1	0.5
Collimator 9	2	1.7
Camera 1	1	0.3
Camera 6	2	1.5
Total (in quadrature)		2.2

The image quality for a perfectly aligned and manufactured lens system is  $\sim 12 \mu\text{m}$  RMS diameter. Referring to Table 49 and Table 50, if we set a radial assembly tolerance such

that each surface is centered to 0.001 inch and has a tilt less than 0.06 milliradians, we would expect to degrade this intrinsic image quality by to 13.2  $\mu\text{m}$  RMS diameter, or by  $\sim 10\%$ . We view this loss as acceptable and therefore set our centration tolerance at 0.001 inch and our tilt tolerance at 0.06 milliradians.

The axial assembly tolerances are much less stringent since we can compensate for the first order effect of axial errors on the image quality: defocus. However, the incremental cost to hold these tolerances to the same level as the radial tolerances is modest, so the optical effect of these errors will be insignificant.

### 6.3.2 Sources of Lens Assembly Errors

Our goal is to understand and control all of the factors that determine the alignment of the collimator and camera lens assemblies. There are three sources of error: (1) the initial manufacture of the bezels and support structure (2) the reassembly tolerances of the bezels and support structure, and (3) the accuracy of aligning the lenses to the bezels. The errors are in the radial, axial and tilt directions.

#### 6.3.2.1 Collimator and Camera Bezel Reference Surfaces

We have developed a procedure for manufacturing the collimator and camera lens bezel assemblies that minimizes tolerance build-up. There are three lens groups in the cameras and collimators, neglecting lens 10 in the camera, the dewar window. For both the collimator and camera lens assemblies, we establish radial and axial reference surfaces on bezel 4, which is located in the central lens group. During the manufacture of the collimator and camera bezels we align each bezel in the radial direction to 0.00025 inches successively to those reference surfaces and then drill and pin each bezel. When we reassemble the bezel stack, we return to this initial alignment tolerance to within the 0.00025 inch radial clearance of the pins relative to their holes.

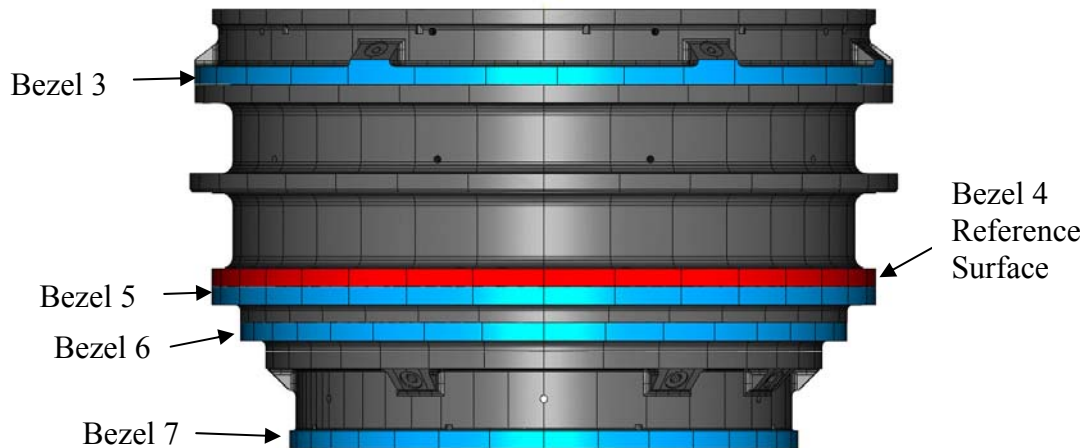


Figure 154. Edge view of the bezels for the middle collimator lens group showing the radial alignment surfaces (blue) and the radial reference surface (red).

The axial tolerance build-up is limited by the tolerances for machining each bezel. The bezel thickness is held to  $\pm 0.0005$  inch, and the opposite faces of each bezel are parallel to  $\pm 0.0005$  inch parallelism of. Adjustment shims between lens groups allow us reestablish the axial position of the outer lens groups relative to the axial reference surface on the middle lens group, to a tolerance of 0.0005 inch.

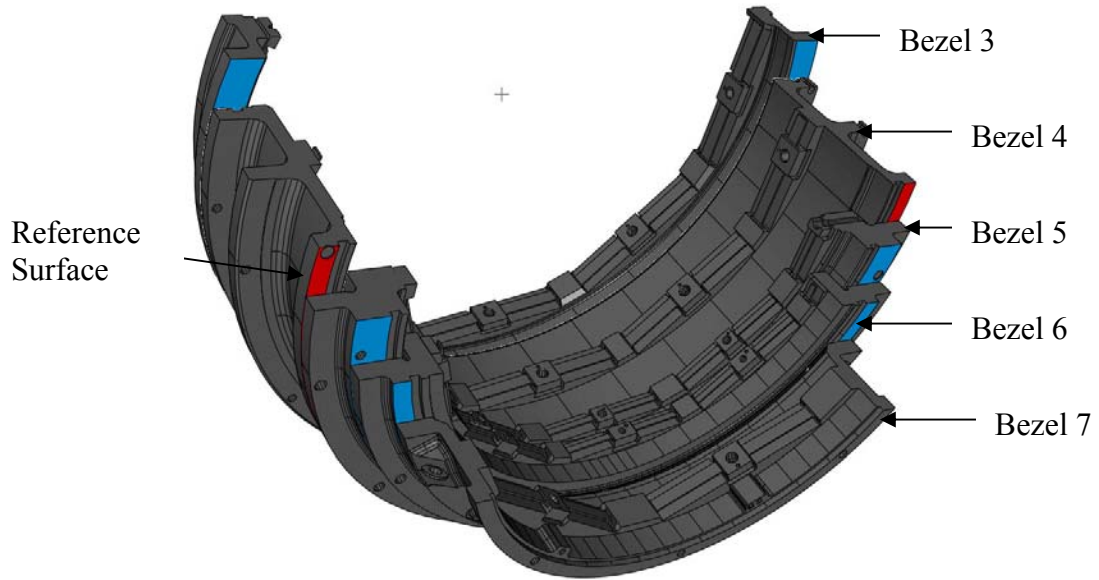


Figure 155. Bezels for the central lens group of the collimator showing the axial reference surface (red) and the remaining axial surfaces (blue).

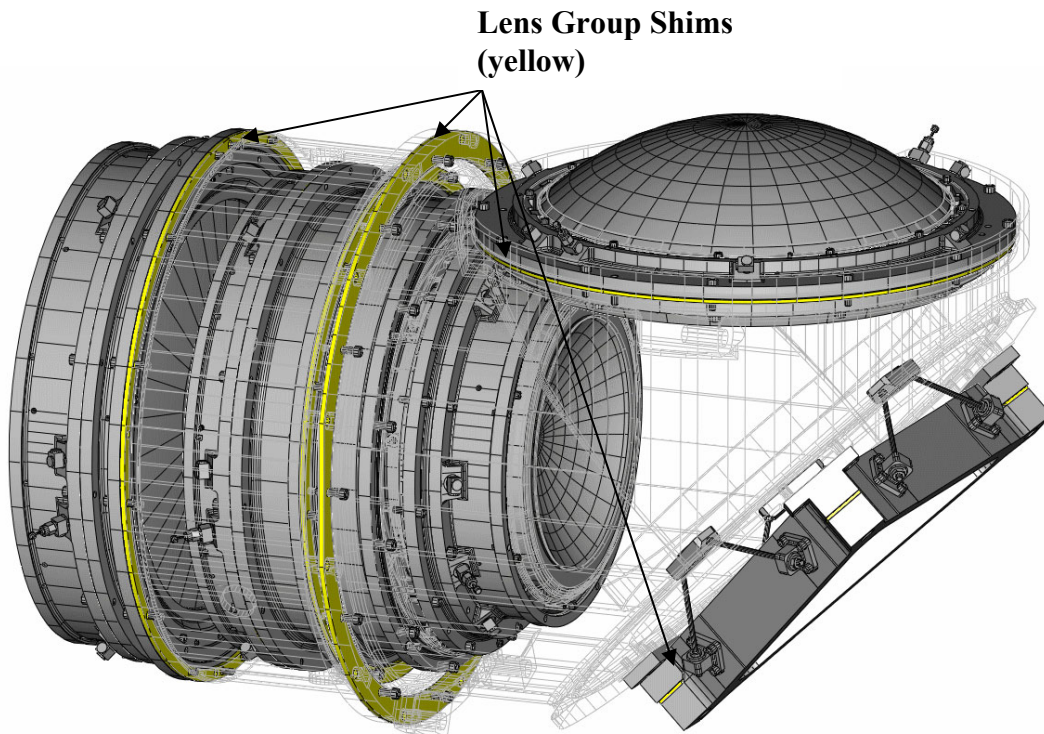
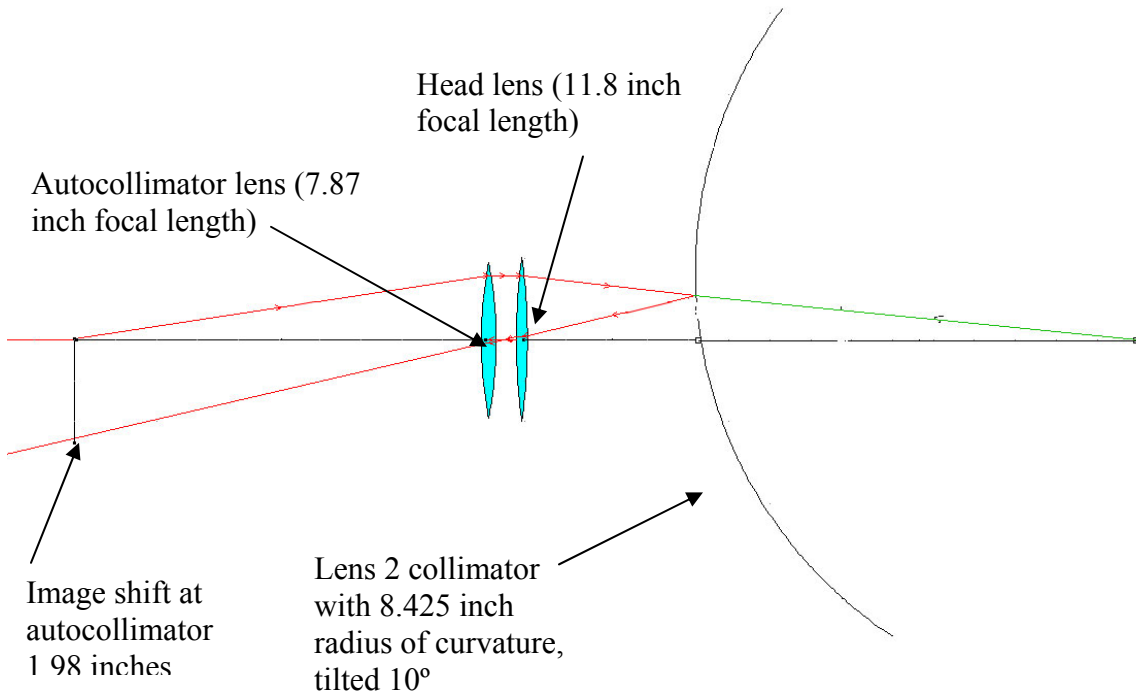


Figure 156. The complete collimator lens assembly showing the three lens groups and, in shadow, the structure that holds these lens groups in alignment. The axial shims are shown in yellow.

Three lens groups in the cameras and collimators are held together by a support structure shown in Figure 156. For lens mounting, the structure is disassembled into individual lens bezels and the lenses are mounted one by one into their bezels. The structure is then re-assembled with the lenses installed.

### 6.3.2.2 Opticentric Resolution

The Opticentric's 200 mm focal length autocollimators are used to detect decenters and tilts of the lenses with respect to its rotary axis. CCD cameras on each autocollimator with analysis software aid in the alignment. A head lens, chosen to accommodate the focal length of the Binospec lens being aligned and the 17.7 inch travel of the autocollimator, is used to focus the autocollimator light at the center of curvature of the optical surface. The CCD camera at the autocollimator focus has 0.00025 inch pixels and we are able to resolve image shifts at better than the  $\frac{1}{4}$  pixel level. The Opticentric resolution depends on the ratio of head lens focal length to the collimator focal length. A sample setup is shown in Figure 157.



**Figure 157. Detecting lens tilts or shifts with the Opticentric.** An exaggerated lens tilt of  $10^\circ$  produces an image shift of 1.98 inches at the detector. For a convex surface, the head lens focal length is the lens radius of curvature plus the distance between the head lens and the Binospec lens under test.

If a spherical mirror with radius of curvature  $R$  is illuminated by a pinhole at its center of curvature, the image of the pinhole at the center of curvature will move by  $2\alpha$  if the mirror is shifted in plane by  $\alpha$ , and by  $2R \tan(\Theta)$  if the mirror is tilted by  $\Theta$ . The image relayed to the autocollimator focus will move by this amount scaled by the ratio of focal lengths of the relay optics (the autocollimator and head lenses). The Opticentric sensitivity can be determined from the following relations, where  $F_a$  is the autocollimator

lens focal length,  $F_h$  is the head lens focal length,  $R$  is the lens radius of curvature, and  $S$  is the image shift at the autocollimator CCD:

For lens tilt  $\Theta$ :  $S = 2 (F_a/F_h) R \tan(\Theta)$

For lens translation  $\alpha$ :  $S = 2 (F_a/F_h) \alpha$

As the Opticentric rotary stage is rotated by  $360^\circ$ , the image will move along a circle of radius  $S$  at the autocollimator detector.

### 6.3.2.3 Radial Errors

Table 51 and Table 52 summarize the expected total radial tolerances for the assembled collimators and cameras, respectively. We add a series of tolerances, described below, in quadrature to arrive at the total.

The outer edge of each bezel is a reference surface and the edge of bezel 4 is the primary alignment datum. During manufacture each bezel is positioned radially with respect to the primary alignment datum to within 0.00025 inch and then pinned. This error is referred to as the **Initial Assembly Accuracy**.

The bezels are separated for lens installation, and when reassembled, the clearance between the pin and the pin hole can cause a radial shift of 0.00025 inch. This is referred to as **Pin Tolerance**.

The Opticentric machine is used to assemble the lenses to the bezels. The resolution of the Opticentric machine depends on the curvature of the surface reflecting the autocollimator beam. We expect to align the lens to the rotary axis to this tolerance, listed as **Opticentric Resolution**. We do not count this error again in the tilt table since de-center and tilt are can't be decoupled for a spherical surface. The accuracy with which we position the bezel to the rotary axis is another source of error referred to as **Alignment Bezel to Opticentric**.

In the collimator, we have to account for the installation tolerance of the fold mirror causing a beam deviation, and the re-assembly tolerance of the fold mirror support mount to the primary support mount causing radial shifts.

### 6.3.2.4 Axial Errors

In Table 53 and Table 54 we summarize the expected total axial tolerances for the assembled collimators and cameras, respectively. We add a series of tolerances, described below, in quadrature to arrive at the total.

The bezels are machined to a tolerance of 0.0005 inch in thickness. When the bezels are stacked up, axial errors accumulate accordingly. This error is referred to as the **Machine Tolerance Bezel X Thickness**.

Adjustment shims between lens groups allow us reestablish the axial position of the outer lens groups relative to the axial reference surface on the middle lens group, to a tolerance of 0.0005 inch. This is referred to as **Shim Tolerance**.

We use the Opticentric to axially align the lens to the bezel. The technique is to install a fast focal ratio lens on the upper autocollimator and focus to the cat's eye position on the surface of the lens. This has shown to be repeatable to 0.00004 inch. The linear encoder is accurate to 0.00008 in, so the difference between two position measurements is good to ~0.00013 inches. This is referred to as the **Opticentric Axial Resolution**.

We use a bezel height fixture to pick up the reference surface of the bezel with the autocollimator. This fixture holds a flat mirror a measured height above the reference surface of the bezel. The **Bezel Height Tool Measurement Accuracy** is how well we expect to measure this height with a coordinate measuring machine.

### 6.3.2.5 Tilt Errors

In Table 55 and Table 56 we summarize the expected total tilt tolerances for the assembled collimators and cameras, respectively. We add a series of tolerances, described below, in quadrature to arrive at the total.

The bezels are machined to a tolerance of 0.0005 inch in parallelism. When the bezels are stacked up, errors occur due to the tolerance in the parallelism. This error is referred to as the **Mechanical Assembly Tolerance Parallelism**.

The lens is aligned to the Opticentric's rotary axis and the error in this alignment is accounted for in the radial section since tilt and decenter cannot be separated.

**Alignment Bezel to Opticentric** is the tilt of the bezel with respect to the Opticentric's rotary axis. It is assumed that there is a 0.0005 inch tilt across the diameter of the bezel.

For the collimator there are also perpendicularity manufacturing tolerances that affect the tilt on the fold mirror support with respect to the reference surface.

**Table 51. Collimator Radial Error Analysis**

Description	Source of Error	Value Surface 1 (inches)	Value Surface 2 (inches)
Lens 1	Opticentric Resolution	0.00013	0.00002
	Initial Assembly Accuracy Bezel 1 Edge K to Reference Bezel 4 Edge B	0.00025	0.00025
	Pin Tolerance Bezel 1 to Bezel 2	0.00025	0.00025
	Pin Tolerance Bezel 2 to Primary Support Mount	0.00025	0.00025
	Pin Tolerance Primary Support Mount to Bezel 4	0.00025	0.00025
	Alignment Bezel to Opticentric	0.00025	0.00025
	<b>Total RSS Error</b>	<b>0.00057</b>	<b>0.00056</b>
Lens 2	Opticentric Resolution	0.00005	0.00019
	Initial Assembly Accuracy Bezel 2 Edge H to Reference Bezel 4 Edge B	0.00025	0.00025
	Pin Tolerance Bezel 2 to Primary Support Mount	0.00025	0.00025
	Pin Tolerance Primary Support Mount to Bezel 4	0.00025	0.00025
	Alignment Bezel to Opticentric	0.00025	0.00025
	<b>Total RSS Error</b>	<b>0.00050</b>	<b>0.00053</b>
Lens 3	Opticentric Resolution	0.00008	0.00008
	Initial Assembly Accuracy Bezel 3 Edge D to Reference Bezel 4 Edge B	0.00025	0.00025
	Pin Tolerance Bezel 3 to Bezel 4	0.00025	0.00025
	Alignment Bezel to Opticentric	0.00025	0.00025
	<b>Total RSS Error</b>	<b>0.00044</b>	<b>0.00044</b>
Lens 4	Opticentric Resolution	0.00002	0.00002
	Alignment Bezel to Opticentric	0.00025	0.00025
	<b>Total RSS Error</b>	<b>0.00025</b>	<b>0.00025</b>
Lens 5	Opticentric Resolution	0.00003	0.00002
	Initial Assembly Accuracy Bezel 5 Edge E to Reference Bezel 4 Edge B	0.00025	0.00025
	Pin Tolerance Bezel 5 to Bezel 4	0.00025	0.00025
	Alignment Bezel to Opticentric	0.00025	0.00025
	<b>Total RSS Error</b>	<b>0.00043</b>	<b>0.00043</b>
Lens 6	Opticentric Resolution	0.00003	0.00005
	Initial Assembly Accuracy Bezel 6 Edge F to Reference Bezel 4 Edge B	0.00025	0.00025
	Pin Tolerance Bezel 6 to Bezel 5	0.00025	0.00025
	Pin Tolerance Bezel 5 to Bezel 4	0.00025	0.00025
	Alignment Bezel to Opticentric	0.00025	0.00025
	<b>Total RSS Error</b>	<b>0.00050</b>	<b>0.00050</b>
Lens 7	Opticentric Resolution	0.00002	0.00002
	Initial Assembly Accuracy Bezel 6 Edge G to Reference Bezel 4 Edge B	0.00025	0.00025
	Pin Tolerance Bezel 7 to Bezel 6	0.00025	0.00025
	Pin Tolerance Bezel 6 to Bezel 5	0.00025	0.00025
	Pin Tolerance Bezel 5 to Bezel 4	0.00025	0.00025
	Alignment Bezel to Opticentric	0.00025	0.00025
	<b>Total RSS Error</b>	<b>0.00056</b>	<b>0.00056</b>
Lens 8	Opticentric Resolution	0.00005	0.00039
	Initial Assembly Accuracy Group 3 Mounting Center on Fold Mirror Support T to Reference Bezel 4 Axial Mounting Surface A and Centerline B	0.0005	0.0005
	Initial Assembly Accuracy Bezel 8 Edge P to Bezel 9 Edge N	0.00025	0.00025
	Initial Assembly Accuracy Bezel 9 Edge N to Group 3 Mount T	0.00025	0.00025
	Positioning of Fold Mirror Beam Deviation at Vertex of Lens	0.00032	0.00035
	Pin Tolerance Bezel 8 to Bezel 9	0.00025	0.00025
	Pin Tolerance Bezel 9 to Group 3 Mount on Fold Mirror Support	0.00025	0.00025
	Pin Tolerance Fold Mirror Support to Primary Support Mount	0.00025	0.00025
	Pin Tolerance Primary Support Mount to Bezel 4	0.00025	0.00025
	Alignment Bezel to Opticentric	0.00025	0.00025
	<b>Total RSS Error</b>	<b>0.00089</b>	<b>0.00098</b>
Lens 9	Opticentric Resolution	0.00038	0.0005
	Initial Assembly Accuracy Group 3 Mounting Center on Fold Mirror Support T to Reference Bezel 4 Axial Mounting Surface A and Centerline B	0.0005	0.0005
	Initial Assembly Accuracy Bezel 9 Edge N to Group 3 Mount T	0.00025	0.00025
	Positioning of Fold Mirror, Beam Deviation at Vertex of Lens	0.00035	0.00050
	Pin Tolerance Bezel 9 to Group 3 Mount on Fold Mirror Support	0.00025	0.00025
	Pin Tolerance Fold Mirror Support to Primary Support Mount	0.00025	0.00025
	Pin Tolerance Primary Support Mount to Bezel 4	0.00025	0.00025
	Alignment Bezel to Opticentric	0.00025	0.00025
	<b>Total RSS Error</b>	<b>0.00091</b>	<b>0.00090</b>

**Table 52. Camera Radial Error Analysis**

Description	Source of Error	Value Surface 1 (inches)	Value Surface 2 (inches)
<b>Lens 1</b>	Opticentric Resolution	0.00013	0.00002
	Initial Assembly Accuracy Bezel 1 Edge J to Reference Bezel 4 Edge B	0.00025	0.00025
	Pin Tolerance Bezel 1 to Bezel 2	0.00025	0.00025
	Pin Tolerance Bezel 2 to Support Plate Front	0.00025	0.00025
	Pin Tolerance Support Plate Front to Support Barrel	0.00025	0.00025
	Pin Tolerance Support Barrel to Bezel 4	0.00025	0.00025
	Alignment Bezel to Opticentric	0.00025	0.00025
	<b>Total RSS Error</b>	<b>0.00063</b>	<b>0.00061</b>
<b>Lens 2</b>	Opticentric Resolution	0.00005	0.00055
	Initial Assembly Accuracy Bezel 1 Edge H to Reference Bezel 4 Edge B	0.00025	0.00025
	Pin Tolerance Bezel 2 to Support Plate Front	0.00025	0.00025
	Pin Tolerance Support Plate Front to Support Barrel	0.00025	0.00025
	Pin Tolerance Support Barrel to Bezel 4	0.00025	0.00025
	Alignment Bezel to Opticentric	0.00025	0.00025
	<b>Total RSS Error</b>	<b>0.00056</b>	<b>0.00079</b>
<b>Lens 3</b>	Opticentric Resolution	0.00008	0.00019
	Initial Assembly Accuracy Bezel 3 Edge D to Reference Bezel 4 Edge B	0.00025	0.00025
	Pin Tolerance Bezel 3 to Bezel 4	0.00025	0.00025
	Alignment Bezel to Opticentric	0.00025	0.00025
	<b>Total RSS Error</b>	<b>0.00044</b>	<b>0.00044</b>
<b>Lens 4</b>	Opticentric Resolution	0.00008	0.00001
	Alignment Bezel to Opticentric	0.00025	0.00025
	<b>Total RSS Error</b>	<b>0.00026</b>	<b>0.00025</b>
<b>Lens 5</b>	Opticentric Resolution	0.00008	0.00016
	Initial Assembly Accuracy Bezel 5 Edge E to Reference Bezel 4 Edge B	0.00025	0.00025
	Pin Tolerance Bezel 5 to Bezel 4	0.00025	0.00025
	Alignment Bezel to Opticentric	0.00025	0.00025
	<b>Total RSS Error</b>	<b>0.00044</b>	<b>0.00046</b>
<b>Lens 6</b>	Opticentric Resolution	0.00020	0.00002
	Initial Assembly Accuracy Bezel 6 Edge F to Reference Bezel 4 Edge B	0.00025	0.00025
	Pin Tolerance Bezel 6 to Bezel 5	0.00025	0.00025
	Pin Tolerance Bezel 5 to Bezel 4	0.00025	0.00025
	Alignment Bezel to Opticentric	0.00025	0.00025
	<b>Total RSS Error</b>	<b>0.00054</b>	<b>0.00050</b>
<b>Lens 7</b>	Opticentric Resolution	0.00008	0.00024
	Initial Assembly Accuracy Bezel 6 Edge M to Reference Bezel 4 Edge B	0.00025	0.00025
	Pin Tolerance Bezel 7 to Support Plate Rear	0.00025	0.00025
	Pin Tolerance Support Plate Rear to Support Barrel	0.00025	0.00025
	Pin Tolerance Support Barrel to Bezel 4	0.00025	0.00025
	Alignment Bezel to Opticentric	0.00025	0.00025
	<b>Total RSS Error</b>	<b>0.00056</b>	<b>0.00061</b>
<b>Lens 8</b>	Opticentric Resolution	0.00008	0.00002
	Initial Assembly Accuracy Bezel 8 Edge N to Bezel 4 Edge B	0.00025	0.00025
	Pin Tolerance Bezel 8 to Bezel 7	0.00025	0.00025
	Pin Tolerance Bezel 7 to Support Plate Rear	0.00025	0.00025
	Pin Tolerance Support Plate Rear to Support Barrel	0.00025	0.00025
	Pin Tolerance Support Barrel to Bezel 4	0.00025	0.00025
	Alignment Bezel to Opticentric	0.00025	0.00025
	<b>Total RSS Error</b>	<b>0.00062</b>	<b>0.00061</b>
<b>Lens 9</b>	Opticentric Resolution	0.00003	0.00063
	Initial Assembly Accuracy Bezel 9 Edge P to Bezel 4 Edge B	0.00025	0.00025
	Pin Tolerance Bezel 9 to Bezel 8	0.00025	0.00025
	Pin Tolerance Bezel 8 to Bezel 7	0.00025	0.00025
	Pin Tolerance Bezel 7 to Support Plate Rear	0.00025	0.00025
	Pin Tolerance Support Plate Rear to Support Barrel	0.00025	0.00025
	Pin Tolerance Support Barrel to Bezel 4	0.00025	0.00025
	Alignment Bezel to Opticentric	0.00025	0.00025
	<b>Total RSS Error</b>	<b>0.00066</b>	<b>0.00091</b>

**Table 53. Collimator Axial Error Analysis**

<b>Description</b>	<b>Source of Error</b>	<b>Value (inches)</b>
<b>Lens 1</b>	Bezel Height Tool Measurement Accuracy	0.00025
	Mechanical Assembly Tolerance Shim Bezel 1 Reference R to Bezel 4 Reference A	0.0005
	Alignment Lens to Bezel	0.0005
	Opticentric Axial Resolution	0.00013
	<b>Total RSS Error</b>	<b>0.00076</b>
<b>Lens 2</b>	Bezel Height Tool Measurement Accuracy	0.00025
	Mechanical Assembly Tolerance Shim Bezel 2 Reference R to Bezel 4 Reference A	0.0005
	Alignment Lens to Bezel	0.0005
	Opticentric Axial Resolution	0.00013
	<b>Total RSS Error</b>	<b>0.00076</b>
<b>Lens 3</b>	Bezel Height Tool Measurement Accuracy	0.00025
	Machine Tolerance Bezel 4 Mounting Surface of Bezel 3 C to Bezel 4 Reference A	0.0005
	Alignment Lens to Bezel	0.0005
	Opticentric Axial Resolution	0.00013
	<b>Total RSS Error</b>	<b>0.00076</b>
<b>Lens 4</b>	Bezel Height Tool Measurement Accuracy	0.00025
	Alignment Lens to Bezel	0.0005
	Opticentric Axial Resolution	0.00013
	<b>Total RSS Error</b>	<b>0.00057</b>
	<b>Lens 5</b>	Bezel Height Tool Measurement Accuracy
Alignment Lens to Bezel		0.0005
Opticentric Axial Resolution		0.00013
<b>Total RSS Error</b>		<b>0.00057</b>
<b>Lens 6</b>		Bezel Height Tool Measurement Accuracy
	Machine Tolerance Bezel 5 Thickness	0.0005
	Alignment Lens to Bezel	0.0005
	Opticentric Axial Resolution	0.00013
	<b>Total RSS Error</b>	<b>0.00076</b>
<b>Lens 7</b>	Bezel Height Tool Measurement Accuracy	0.00025
	Machine Tolerance Bezel 5 Thickness	0.0005
	Machine Tolerance Bezel 6 Thickness	0.0005
	Alignment Lens to Bezel	0.0005
	Opticentric Axial Resolution	0.00013
	<b>Total RSS Error</b>	<b>0.00091</b>
<b>Lens 8</b>	Bezel Height Tool Measurement Accuracy	0.00025
	Pin Tolerance Center Mounting Flange to Primary Support Mount	0.00025
	Pin Tolerance Primary Support Mount to Fold Mirror Support	0.00025
	Shim Tolerance Reference Surface M Bezel 8 to Surface U Fold Mirror Support	0.0005
	Alignment Lens to Bezel	0.0005
	Opticentric Axial Resolution	0.00013
	<b>Total RSS Error</b>	<b>0.00084</b>
<b>Lens 9</b>	Bezel Height Tool Measurement Accuracy	0.00025
	Pin Tolerance Center Mounting Flange to Primary Support Mount	0.00025
	Pin Tolerance Primary Support Mount to Fold Mirror Support	0.00025
	Shim Tolerance Reference Surface M Bezel 9 to Surface U Fold Mirror Support	0.0005
	Alignment Lens to Bezel	0.0005
	Opticentric Axial Resolution	0.00013
	<b>Total RSS Error</b>	<b>0.00084</b>

**Table 54. Camera Axial Error Analysis**

<b>Description</b>	<b>Source of Error</b>	<b>Value (inches)</b>
<b>Lens 1</b>	Bezel Height Tool Measurement Accuracy	0.00025
	Mechanical Assembly Tolerance Shim Bezel 1 Reference K to Bezel 4 Reference A	0.0005
	Alignment Lens to Bezel	0.0005
	Opticentric Axial Resolution	0.00013
	<b>Total RSS Error</b>	<b>0.00076</b>
<b>Lens 2</b>	Bezel Height Tool Measurement Accuracy	0.00025
	Mechanical Assembly Tolerance Shim Bezel 2 Reference K to Bezel 4 Reference A	0.0005
	Alignment Lens to Bezel	0.0005
	Opticentric Axial Resolution	0.00013
	<b>Total RSS Error</b>	<b>0.00076</b>
<b>Lens 3</b>	Bezel Height Tool Measurement Accuracy	0.00025
	Machine Tolerance Mounting Bezel 3 Surface C to Bezel 4 Reference A	0.0005
	Alignment Lens to Bezel	0.0005
	Opticentric Axial Resolution	0.00013
	<b>Total RSS Error</b>	<b>0.00076</b>
<b>Lens 4</b>	Bezel Height Tool Measurement Accuracy	0.00025
	Alignment Lens to Bezel	0.0005
	Opticentric Axial Resolution	0.00013
	<b>Total RSS Error</b>	<b>0.00057</b>
<b>Lens 5</b>	Bezel Height Tool Measurement Accuracy	0.00025
	Alignment Lens to Bezel	0.0005
	Opticentric Axial Resolution	0.00013
	<b>Total RSS Error</b>	<b>0.00057</b>
<b>Lens 6</b>	Bezel Height Tool Measurement Accuracy	0.00025
	Machine Tolerance Bezel 5 Thickness	0.0005
	Alignment Lens to Bezel	0.0005
	Opticentric Axial Resolution	0.00013
	<b>Total RSS Error</b>	<b>0.00076</b>
<b>Lens 7</b>	Bezel Height Tool Measurement Accuracy	0.00025
	Shim Tolerance Bezel 7 Reference Surface R to Bezel 4 Reference A	0.0005
	Alignment Lens to Bezel	0.0005
	Opticentric Axial Resolution	0.00013
	<b>Total RSS Error</b>	<b>0.00076</b>
<b>Lens 8</b>	Bezel Height Tool Measurement Accuracy	0.00025
	Shim Tolerance Bezel 7 Reference Surface R to Bezel 4 Reference A	0.0005
	Machine Tolerance Bezel 7 Reference Surface R to Bezel 8 Reference Surface U	0.0005
	Alignment Lens to Bezel	0.0005
	Opticentric Axial Resolution	0.00013
	<b>Total RSS Error</b>	<b>0.00091</b>
<b>Lens 9</b>	Bezel Height Tool Measurement Accuracy	0.00025
	Shim Tolerance Bezel 7 Reference Surface R to Bezel 4 Reference Surface A	0.0005
	Bezel 8 Thickness	0.0005
	Alignment Lens to Bezel	0.0005
	<b>Total RSS Error</b>	<b>0.00091</b>

**Table 55. Collimator Tilt Error Analysis**

<b>Description</b>	<b>Source of Error</b>	<b>Value (Radians)</b>
<b>Lens 1</b>	Mechanical Assembly Tolerance Parallelism Bezel 1 Reference R to Bezel 4 Reference A Alignment Bezel to Opticentric <b>Total RSS Error</b>	3.33E-05 1.66E-05 <b>0.00004</b>
<b>Lens 2</b>	Mechanical Assembly Tolerance Parallelism Bezel 1 Reference R to Bezel 4 Reference A Alignment Bezel to Opticentric <b>Total RSS Error</b>	3.33E-05 1.66E-05 <b>0.00004</b>
<b>Lens 3</b>	Machine Tolerance Parallelism Bezel 4 Reference C to Bezel 4 Reference A Alignment Bezel to Opticentric <b>Total RSS Error</b>	3.44E-05 1.72E-05 <b>0.00004</b>
<b>Lens 4</b>	Alignment Bezel to Opticentric <b>Total RSS Error</b>	2.24E-05 <b>0.00002</b>
<b>Lens 5</b>	Alignment Bezel to Opticentric <b>Total RSS Error</b>	1.86E-05 <b>0.00002</b>
<b>Lens 6</b>	Machine Tolerance Bezel 5 Parallelism Alignment Bezel to Opticentric <b>Total RSS Error</b>	3.96E-05 1.98E-05 <b>0.00004</b>
<b>Lens 7</b>	Machine Tolerance Bezel 6 Parallelism Machine Tolerance Bezel 5 Parallelism Alignment Bezel to Opticentric <b>Total RSS Error</b>	3.96E-05 3.62E-05 1.98E-05 <b>0.00006</b>
<b>Lens 8</b>	Machine Manufacturing Tolerance Bezel 8 Mounting Surface U on Fold Mirror Support Perpendicular to Bezel 4 Reference Surface A Bezel 9 to Mounting Surface U Alignment Bezel to Opticentric <b>Total RSS Error</b>	3.5E-05  3.5E-05 1.75E-05 <b>0.00005</b>
<b>Lens 9</b>	Machine Manufacturing Tolerance Bezel 8 Mounting Surface U on Fold Mirror Support Perpendicular to Bezel 4 Reference Surface A Bezel 8 Parallelism Alignment Bezel to Opticentric <b>Total RSS Error</b>	3.5E-05  3.5E-05 1.75E-05 <b>0.00005</b>

**Table 56. Camera Tilt Error Analysis**

<b>Description</b>	<b>Source of Error</b>	<b>Value (radians)</b>
Lens 1	Mechanical Assembly Tolerance Parallelism Bezel 1 Reference K to Bezel 4 Reference A Alignment Bezel to Opticentric <b>Total RSS Error</b>	3.03E-05 1.51E-05 <b>0.00003</b>
Lens 2	Mechanical Assembly Tolerance Parallelism Bezel 1 Reference K to Bezel 4 Reference A Alignment Bezel to Opticentric <b>Total RSS Error</b>	3.03E-05 1.51E-05 <b>0.00003</b>
Lens 3	Machine Tolerance Parallelism Bezel 4 Reference C to Bezel 4 Reference A Alignment Bezel to Opticentric <b>Total RSS Error</b>	2.88E-05 1.44E-05 <b>0.00003</b>
Lens 4	Alignment Bezel to Opticentric <b>Total RSS Error</b>	1.48E-05 <b>0.00001</b>
Lens 5	Alignment Bezel to Opticentric <b>Total RSS Error</b>	1.48E-05 <b>0.00001</b>
Lens 6	Machine Tolerance Bezel 5 Parallelism Alignment Bezel to Opticentric <b>Total RSS Error</b>	3.05E-05 1.52E-05 <b>0.00003</b>
Lens 7	Shim Tolerance Bezel 7 Reference Surface R to to Bezel 4 Reference A Alignment Bezel to Opticentric <b>Total RSS Error</b>	3.27E-05 1.63E-05 <b>0.00004</b>
Lens 8	Shim Tolerance Bezel 7 Reference Surface R to to Bezel 4 Reference A Machine Tolerance Bezel 7 Reference Surface R to Bezel 8 Reference Surface U Alignment Bezel to Opticentric <b>Total RSS Error</b>	3.27E-05 3.27E-05 1.63E-05 <b>0.00005</b>
Lens 9	Shim Tolerance Bezel 7 Reference Surface R to to Bezel 4 Reference A Bezel 8 Parallelism Alignment Bezel to Opticentric <b>Total RSS Error</b>	3.27E-05 3.27E-05 1.63E-05 <b>0.00005</b>

### 6.3.2.6 Summary Discussion of Collimator and Camera Assembly Tolerances

Referring Table 51 through Table 56, we conclude that we will be able to meet our centration tolerance of 0.001 inch and our tilt tolerance of 0.06 milliradians.

## 7 Summary Image Quality Error Budget

Now that the contributors to the image quality error budget have all been discussed and quantified, we can take stock of the final expected image quality. In section 2.14 we set a goal of 10  $\mu\text{m}$  or less for all of these terms added in quadrature. Our calculations show that we should reach this goal, and in fact have some margin.

**Table 57. Summary of contributions to image blur diameter**

<b>Contribution to Image Blur</b>	<b>Image Blur Diameter (<math>\mu\text{m}</math>)</b>
Lens Manufacture	4.7
Lens Alignment	5.5
Lens Bezel Bolt-up Errors	2.5
Grating Gravity Deformation	2.7
Fold Mirror Gravity Deformation	1.1
Lens Gravity Deformation	3.2
Total Image Blur From Above	8.8
Margin	4.7
Error Budget	10.0

## 8 Electronics

### 8.1 Introduction

The Binospec electronics design goals are: meeting the science requirements, assuring instrument and personnel safety, low power consumption to assure thermal stability of the optics, low weight to meet a tight weight budget, high reliability, minimal cabling, elimination of extraneous light, reuse of existing hardware and software designs where appropriate, and serviceability. We provide diagnostics in each system to simplify servicing. We maximize the use of commercial components to minimize cost and risk.

The six functional blocks in the Binospec electronics are: 1) power control and communication, 2) motion control, 3) calibration/flexure control, 4) detector electronics, 5) detectors, and 6) mechanism. Figure 158 shows the external system components.

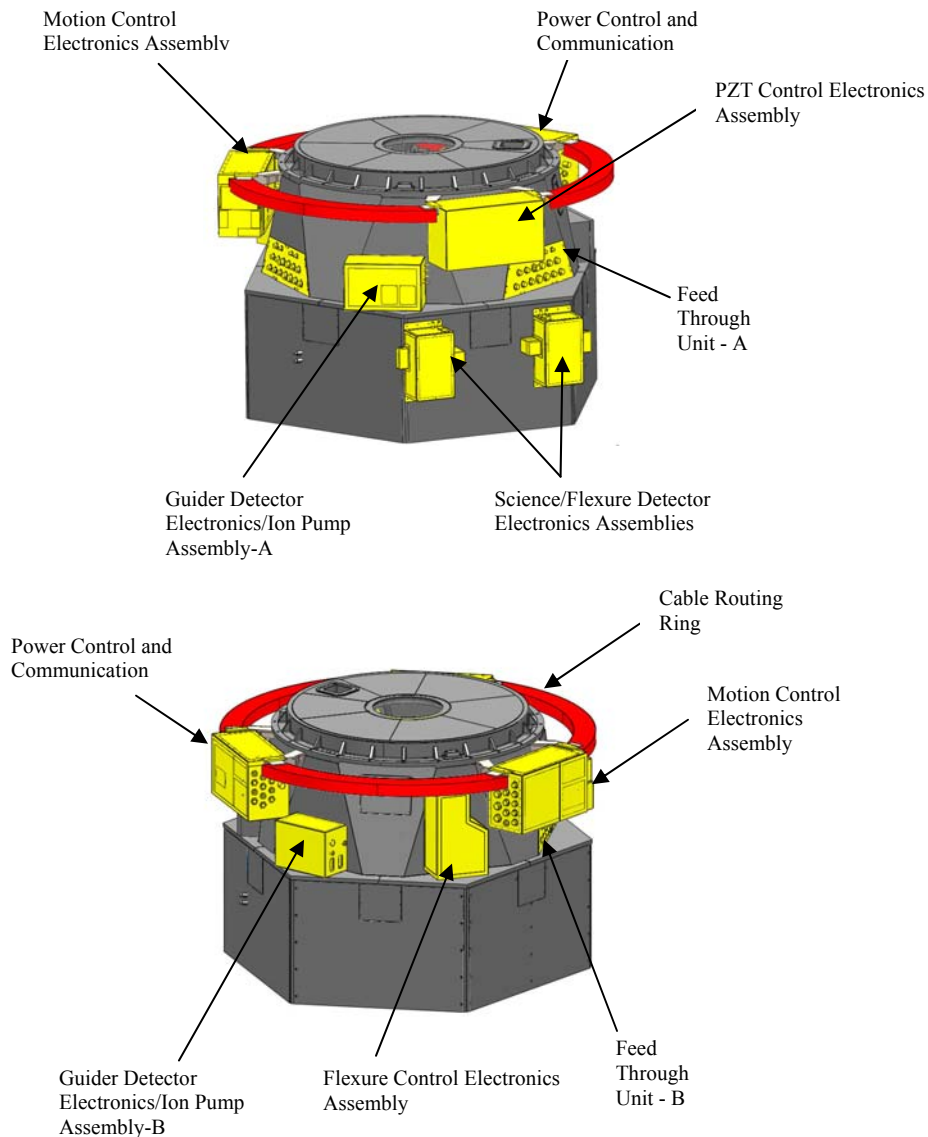
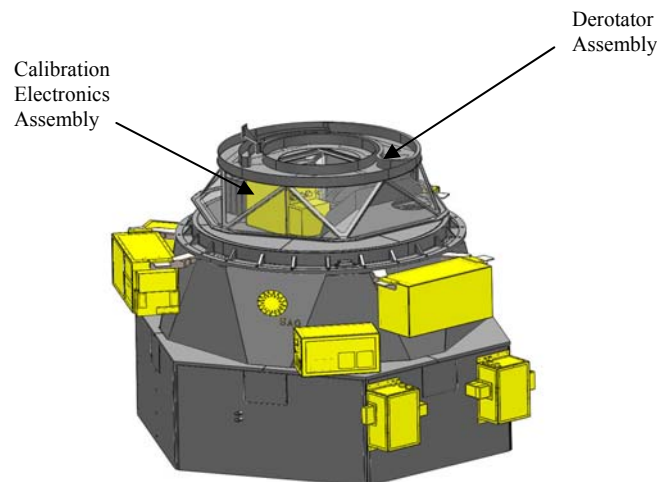


Figure 158. Binospec's electronic modules seen from opposite sides. The red halo is a cable trough.

1. The **power control and communications electronics assembly** contains AC power conditioning, over-voltage and over-current protection, low voltage DC power supplies for other subassemblies, power switching relays, Ethernet switchgear, and analog and digital input/output modules for power control and housekeeping telemetry.
2. There are two **motion control electronics assemblies**. One assembly contains a digital signal processor-based multi-axis motion controller (Delta Tau PMAC) and the servo motor drives. The other assembly contains four single-axis piezoelectric stage controller/drivers for X-Y position control and six axes of PI Nexline PZT controller/drivers for Z (and tip/tilt) control of our two focal plane CCD mosaics.
3. There are two **calibration electronics assemblies**, one for flexure control and one for internal wavelength and flat-field calibration. These can be seen in Figure 158 and Figure 159, respectively.
4. The **detector electronics** include two multi-board modules for the readout of the science and flexure control CCDs at the focus of the camera optics. In addition, there are two, dual channel modules for the control and readout of the four guider/wave front sensor cameras. These assemblies also house two ion pump controllers for our two science cameras and a single ion pump controller and pump for the four guider/wave front sensor cameras.
5. The **detectors** for all of the cameras are located within Binospec's thermal covers.
6. The **positioning mechanisms** are a mix of brushless motor/ball screw stages, small brush motor driven stages, piezoelectric, and pneumatic actuators. These mechanisms are all located within Binospec's thermal covers.



**Figure 159.** The calibration/derotator assembly and its electronic module located in a separate module.

The connections between those components internal to Binospec's thermal covers and the external electronics are made through two large thermally isolated feed through panels. Cables from detectors and detector electronics assemblies are routed through two separate feed throughs to minimize the cable length.

## **8.2 Electronics Functional Requirements and Subsystems Layout**

### **8.2.1 General System Electrical Requirements**

The Binospec systems electronics requirements are:

1. Motion control of all mechanisms to the accuracy, range of motion, and functionality requirements
2. Controlled power delivery to all components and subsystems requiring AC or DC power
3. Communication between mechanisms requiring software control and the off-instrument control computer.
4. Diagnostic monitoring

### **8.2.2 Specific Electrical Requirements**

1. Precision control of 22 servo motor axes (including one in the calibration/derotator unit), plus redundant position feedback encoders on the grating tilt mechanisms, plus 3 spares, with digital incremental encoder position feedback, end of travel limit switches and fiducial switches, as needed.
2. Control of 10 axes of low voltage piezoelectric actuators (four X/Y and six + Z/tip/tilt) with capacitive sensor analog absolute position feedback.
3. Control of 24 channels (12 to extend, 12 to retract) of solenoid valves for pneumatic actuators for 21 cylinders. Each cylinder has two end of travel limit switches for feedback (42 in total) that are read by PMAC digital inputs. These channels are controlled by PMAC digital outputs driving 24V solid state relays.
4. Control of 15 sets of actuator brakes (and 3 spares). These brakes are controlled by PMAC digital outputs (on ACC24 boards) driving 24V solid state relays.
5. Two sets of switched four DC power supplies (5V,  $\pm 15V$ , 24V, 30V) for science/flexure camera electronics.
6. Switched DC power for four guider cameras and the associated thermoelectric coolers (8V and 48V).
7. Two channels of switched DC motor drive power.
8. System 12V and 24V DC general purpose switched power for commercial components, including DA/AD modules, communications switch gear, etc.)
9. Communications support consisting of Ethernet, RS-232, Controller Area Network (CAN Bus), 1-Wire<sup>TM</sup>, and RS-485 to interface devices for control, data handling, temperature monitoring, and housekeeping telemetry.

### 8.2.3 Electrical Subsystems Layout

Figure 160 shows Binospec's electrical interconnection layout.

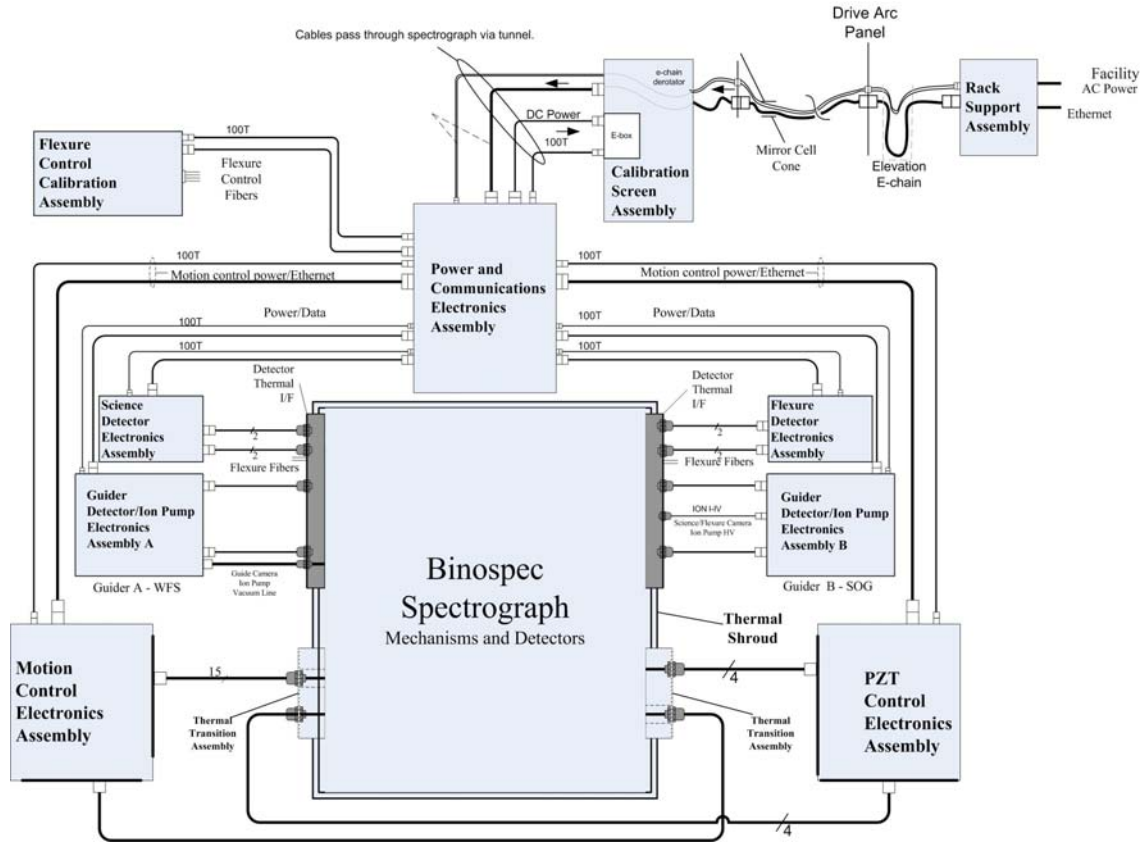


Figure 160. Binospec electrical interconnection layout.

### 8.2.4 Grounding

The electrical grounding system for Binospec is shown in Figure 161. The MMTO quiet power ground, Q, connects to the system racks in the west instrument room from the power panel. This ground is connected to the rack structure for safety/shield ground. Instrument power cable shield and two discrete wire grounds are brought to the power and communications assembly via the calibration/derotator module. Separate hot, neutral, and safety ground conductors are brought to the instrument for the motion control, motor power, and detector electronics. All electronics assemblies will be isolated from the instrument structure. The instrument structure will connect electrically to the telescope structure which is, in turn, grounded to the facility quiet power ground via straps. The detector electronics utilize isolated power supplies and will have a local ground (Ground A). Ground A will be referenced to Ground Q using a 10 megohm resistor. The PZT focal

plane assembly actuator will be isolated from the detector assembly chassis and from the focal plane assembly.

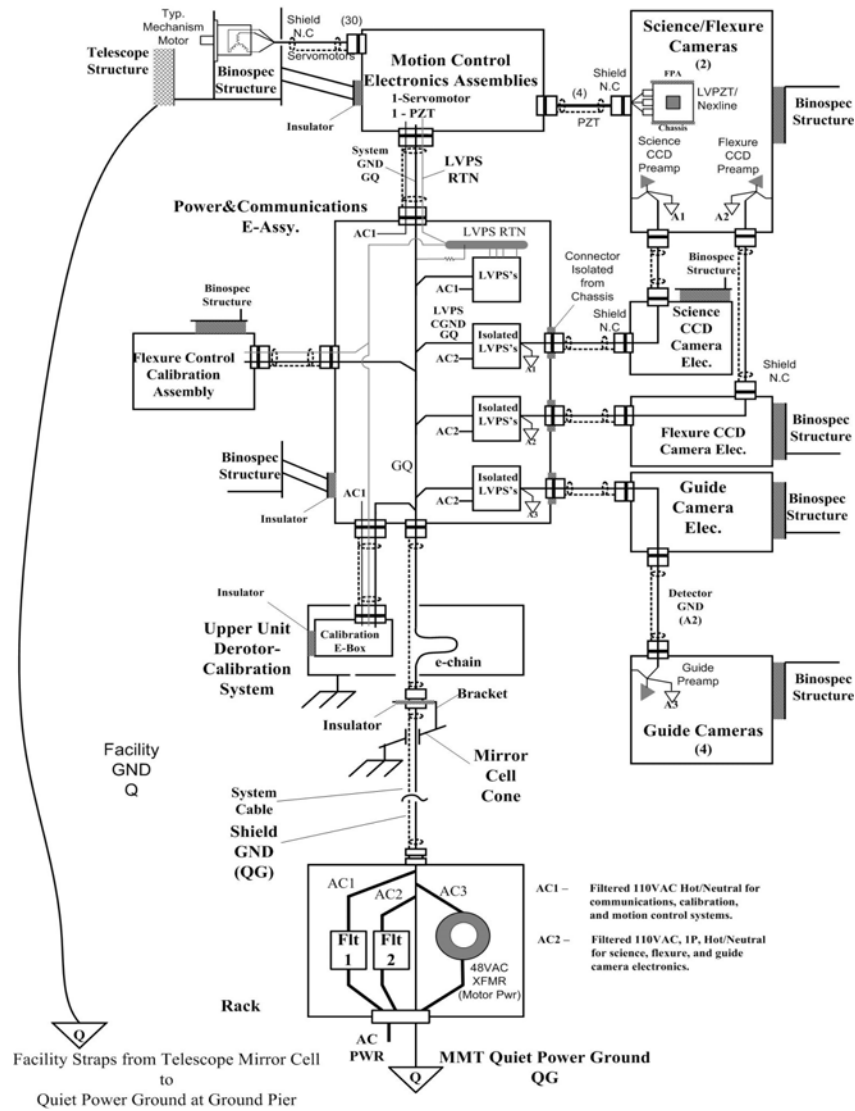


Figure 161. Binospec’s electrical grounding system.

### 8.3 Power Control and Communication Assembly

The power control and communication assembly provides filtered, protected, controlled AC and low voltage DC system power and communications resources to the other subassemblies of the instrument. It contains low voltage DC power supplies, Ethernet switchgear, solid state and electromechanical relays, terminal blocks, circuit overvoltage and current protection devices, and industrial I/O and A/D Ethernet interfaced modules for providing software control and parameter monitoring. The block diagram for the power control and communication assembly is shown in Figure 162. Figure 163 is a CAD model of the interior of this assembly.

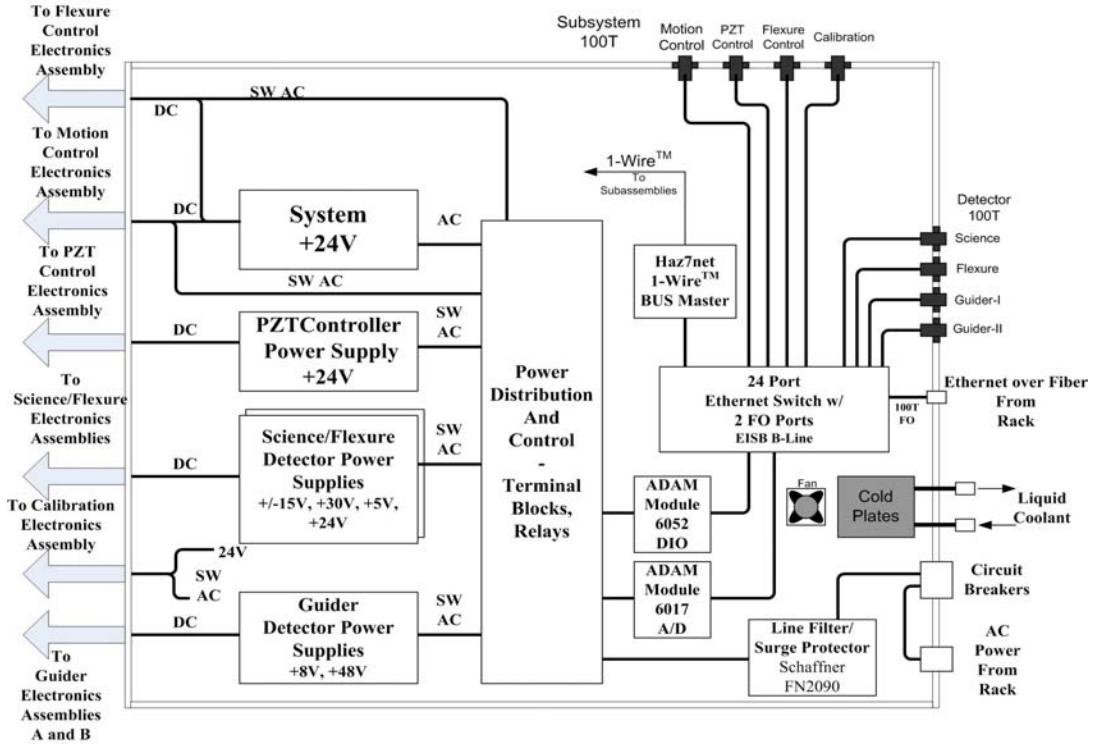


Figure 162. Power control and communication assembly block diagram.

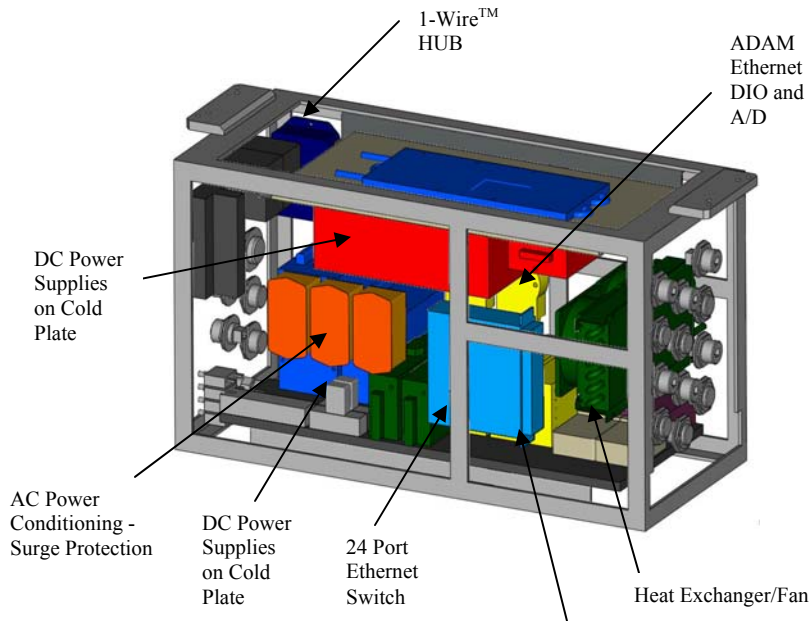


Figure 163. Power control and communications assembly packaging.



## 8.4.2 Motion Control Electronics Components and Subassemblies

The Delta Tau PMAC (Programmable Multi-Axis Controller) system is a powerful DSP-based motion control system that we have used in several prior instruments. The Binospec PMAC uses the compact PCI geometry (cPCI) and controls up to 24 motion axes with one CPU. The Binospec PMAC has 64 general purpose, opto-isolated inputs and 32 outputs that we use for status monitoring and discrete control.

The complete PMAC rack assembly includes seven Delta Tau cPCI cards (1-CPU, 6-four axis controllers, 1-I/O board), one cPCI bus power supply, one 8-slot passive motherboard, and custom interface boards. An additional 24 isolated inputs and 24 outputs for discrete control are provided on an Ethernet interfaced Delta Tau accessory unit as spares.

We monitor motor, electronics, and structure temperatures with Dallas DS18S20 digital 1-Wire temperature sensors accessed through an Ethernet to 1-Wire™ module.

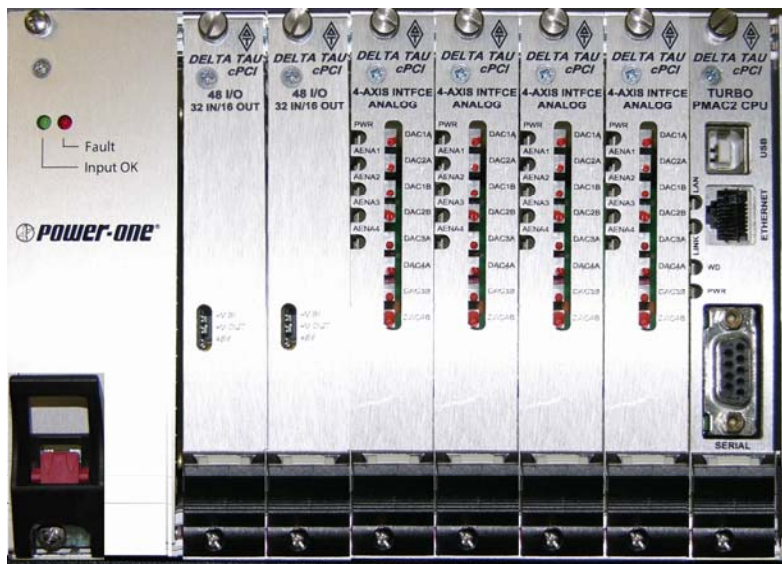


Figure 165. A typical Delta Tau PMAC cPCI electronics rack.

## 8.4.3 Servo Motor Drives and Switched Relay Outputs

Forty eight solid state relay switched 24V outputs are provided to control the pneumatic solenoids and the servo motor brakes, including nine spares. Twenty four Copley Controls Accelnet Micropanel servo drives, shown in Figure 166, are used to drive 17 brushless servo motors and four brush servo motors with three spares.

The Copley Accelnet drive is compact, lightweight, and can be remotely configured for brush or brushless motor operation at any current level up to 12A peak, 3A continuous at

20 to 90 VDC. Communication with the drive takes place over either RS232 or CAN networks for configuration, control and status read-back. Communication is not interrupted while the drive is enabled. This communication allows us to determine input states, position, velocity, drive current, amplifier temperature, etc., independent of the PMAC. We will use CAN bus communication because that allows us to daisy chain the drives to reduce cabling and interface board complexity. Optional hardware addressing allows for drive replacement without software configuration. The Copley determines position and velocity information from the motor encoder signals, which are buffered and passed through to the PMAC. Since the selected brushless motor does not have integral Hall effect sensors for commutation, the Accelnet drives will be commutated from encoder signals.

The Accelnet also provides nine general purpose digital inputs (one is preprogrammed to be the amp enable) and four general purpose digital outputs. A programmable amplifier fault can be configured to fault in various latched or non-latched modes based on selectable fault conditions. All drive DSP and PWM clocks will be synchronized for EMI considerations.

Rotary encoders are used for position feedback for most of the actuators. We have selected Netzer BE25 capacitive encoders for their low power dissipation and zero light emission. The Netzer BE25 provides a proprietary serial output in addition to conventional A/B/I differential outputs. We will interrogate each encoder with a microcontroller upon power up to obtain the absolute shaft position for commutation and send this information to the appropriate Copley Accelnet drive via the CAN network. This information primes the drive for commutation without a drive “wake and wiggle” move to establish the motor’s rotor position.



**Figure 166 Copley Accelnet Micropanel servo motor drive.**

### 8.4.4 Interface Printed Wiring Board

The main interface printed wiring board provides the signal interface between the mechanisms, the servo drives, and the PMAC. Mezzanine boards that mount on the interface board provide a number of important functions: (1) signal buffering and over voltage protection, (2) a safe to move interlock, and (3) commutation of the Netzer encoder-equipped motors. The safe to move interlock has access to limit switch status, motor temperature flags, and emergency stop status, servo drive status, pneumatic solenoid status, and brake control signals to determine when mechanisms can be safely moved. For example, the slit mask puller mechanism can only be safely moved into the slit mask elevator when the elevator is in the empty position. An FPGA will be used to control the interlock.

System voltages and currents will be monitored through the interface board by A/Ds in the PMAC. Voltages that are critical to the PMAC operation will be monitored by industrial MODBUS interfaced A/D modules. Digital status lines will be monitored by PMAC inputs and MODBUS module I/O. Motor phase currents, bus voltage, encoder position, and HALL sensor states will be monitored using drive motor interface through the Controller Area Network (CAN) interface.

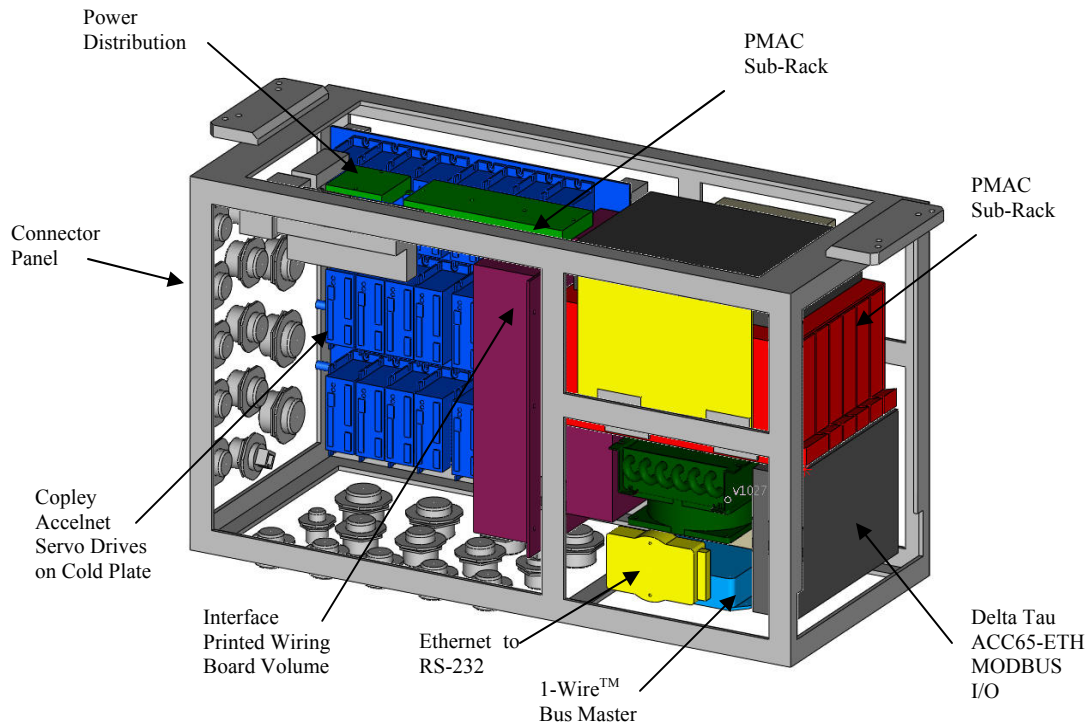


Figure 167. Interior of the motion control electronics assembly.

### 8.4.5 Communications

In order to minimize cabling between boxes, there will be an Ethernet switch in the motion control assembly, providing 10/100T Ethernet to the PMAC chassis, Ethernet to RS-232 converter, 1-Wire™ master, and the MODBUS I/O and A/D modules (housekeeping). We use a Harting 3080-A2 8-port compact, industrial Ethernet switch.

The Ethernet to RS-232 converter unit provides RS-232 channels for communications with: (1) the first Copley Accelnet drive which acts as a CAN bus gateway, (2) two barcode readers used to identify slit masks and filters, (3) the PMAC serial interface used to configure the PMAC CPU, (4) the encoder interface microcontroller, and (5) a diagnostic port.

#### **8.4.6 Motion Control Electronics Assembly Packaging**

The motion control electronics boxes are designed to achieve minimum size and weight while maintaining serviceability. Figure 167 shows the interior of a Motion Control e-box.

### **8.5 Piezoelectric Motion Control Assembly**

The two science CCDs are mounted a three-axis Physik Instrumente (PI) stage for flexure control. The focus (Z) motion of the selected stage uses Nexline inchworm-type actuators due to the required 1.5 mm travel. Due to geometrical and space constraints, three small Nexline actuators were chosen for the focus drive so we have tip/tilt control of the focal plane as well. The X and Y motions are each driven by a single conventional piezo stack. We use a total of four Physik Instrumente E-625 LVPZT motion controller/drivers and two (three axis) PI Nexline controller/drivers. Communications with the PI controllers takes place over an RS232 connection. User-defined motion profiles can be generated and run by the local controller and synchronized to the PMAC system via discrete input/output lines. The controller/driver electronics implement all the required feedback, drive, and I/O. Controllers of the same type are linked together for communications. Figure 168 and Figure 169 show the two PI controllers.



**Figure 168. PI E-625 Single-Axis Low Voltage Piezoelectric Subsystem**



**Figure 169. PI E-755 Nexline Single-Axis Piezoelectric Subsystem**

The piezoelectric control assembly also contains a 24V power supply, an Ethernet switch, and Ethernet to RS-232 converters. A block diagram of the piezoelectric motion control electronics assembly is shown in Figure 170 and a CAD model of the assembly is shown in Figure 171.

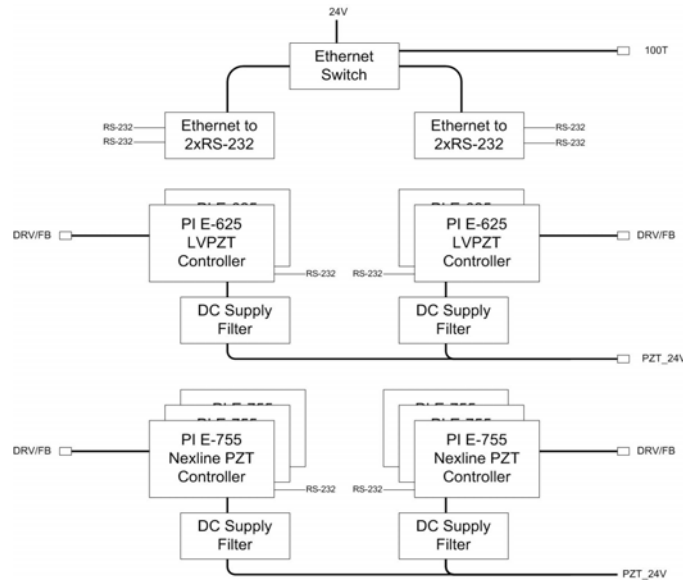


**Figure 170 Piezoelectric motion control assembly block diagram.**

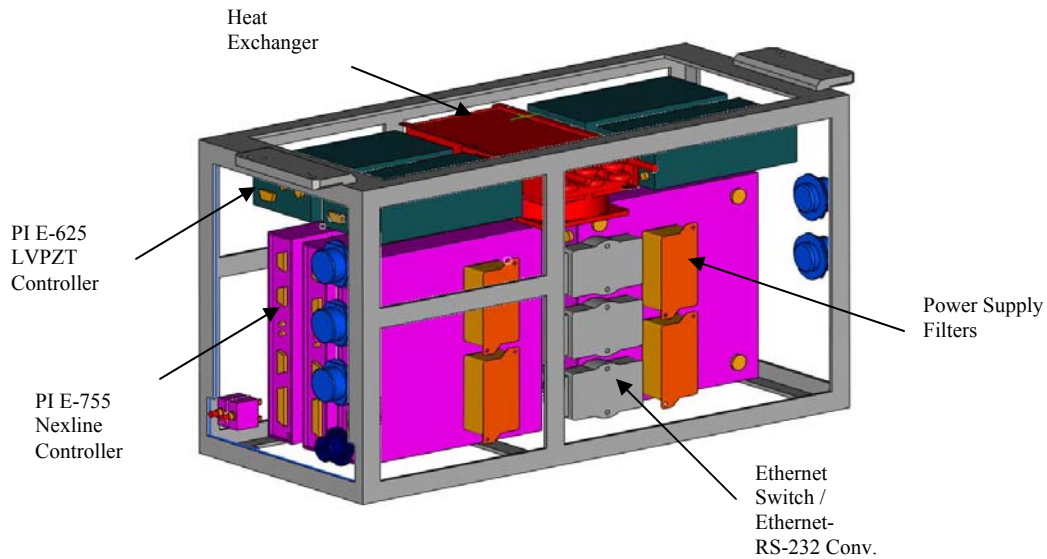


Figure 171. CAD model of the piezoelectric motion control assembly.

## 8.6 Calibration Electronics

### 8.6.1 Derotator/Calibration Assembly

The derotator/calibration assembly provides a set of software controllable calibration light sources (two hollow cathode lamps and an incandescent lamp) to be used for flatfield and spectral calibration. A single mechanism in the assembly moves a mirror and rear projection screen to inject calibration light onto the slit mask. Motion control is provided by a single Copley Accelnet Micropanel drive identical to those used for other instrument mechanisms. This drive is not under PMAC control and the drive itself is used to close the control loop. The drive is commanded by RS-232 via an on-board Ethernet to RS-232 server. An Accelnet programmable output will control the motor brake through a relay. Drive and lamp power is controlled by an industrial MODBUS I/O module via relays. Figure 172 shows the calibration assembly electronics block diagram and Figure 173 is a CAD model of the assembly.



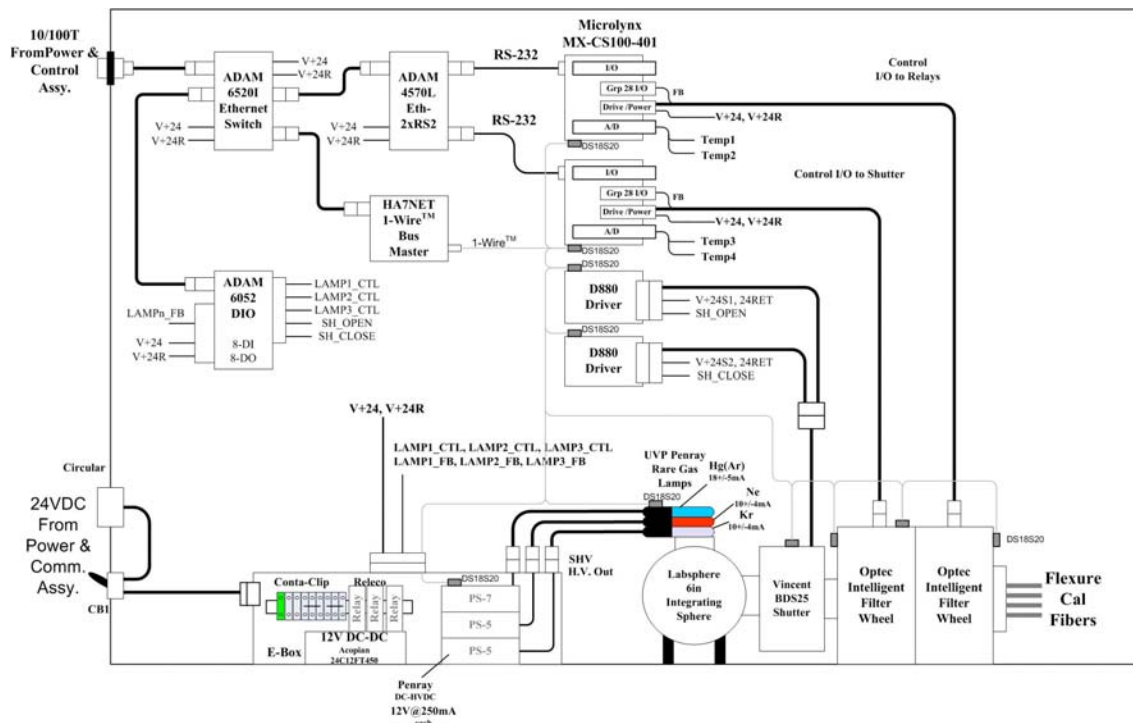
## 8.6.2 Flexure Control Calibration Assembly

The flexure control calibration assembly consists of three Penray type spectral lamps mounted in an integrating sphere, two filter wheels, and a shutter. The lamps, filter wheels and shutter are under software control. The assembly receives 24 VDC and 100T Ethernet from the power and communications electronics assembly.

The supplied commercial filter wheel controller was found to be unreliable so it has been replaced by an Intelligent Motion Systems MicroLynx step motor indexer (see Figure 174). These drives have been used successfully in other SAO instruments for stepper motor control. MODBUS discrete I/O and A/D converters are used to implement power control and analog housekeeping. The Vincent shutter is a bistable unit which is driven open by solenoid, stays open with zero power, and closes with a second solenoid. Shutter solenoids are controlled by output from MicroLynx I/O boards under software control. The electrical block diagram for the Flexure Control Calibration Assembly is shown in Figure 175.

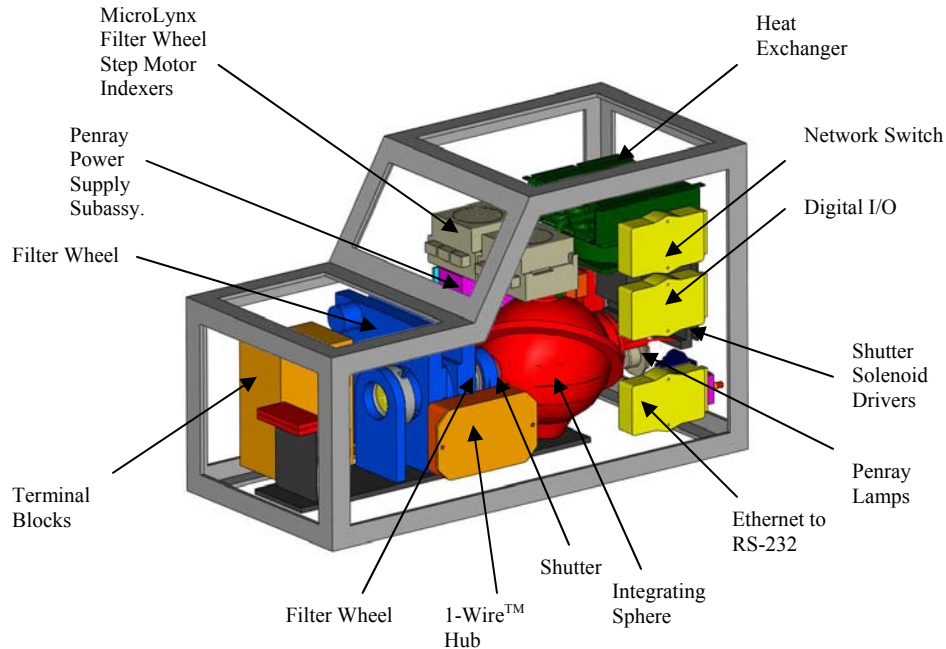


Figure 174. Intelligent Motion Systems MicroLynx step motor indexer.



**Figure 175. The electrical block diagram for the flexure control calibration assembly.**

Figure 176 shows a CAD model of the flexure control electronics assembly package.



**Figure 176. CAD model of the flexure control electronics assembly package.**

## **8.7 Science/Flexure Detector Electronics Assembly**

### **8.7.1 Overview**

The electronics to run the two large science imagers (E2V 4K X 4K baseline) and the four flexure control CCDs (E2V CCD42-10) are two separate but very similar systems. The two science imagers, each with four output ports, will be run from one 8-channel system, with both science imagers being read out simultaneously. The other system will run asynchronously from the first and be configured as a 4-channel system (one per alignment CCD), with all four CCDs read out simultaneously. All boards and spares will be interchangeable between the two systems.

### **8.7.2 Partitioning**

Because of space limitations imposed by the mechanical design, it is not possible to mount the CCD control electronics in very close to the imagers. Noise pickup is minimized with a new differential preamplifier design. The preamplifier is designed to mount directly on the hermetic connector on the dewar wall, and serves not only to provide a clean differential video but also filters bias voltages for the imagers. The video signal processing boards have been modified to accept this differential video instead of the single-ended connections used in past systems.

### 8.7.3 Camera Board Sets

Each camera controller has one I/O board, one timing board, one driver board, and one or two 4-channel A/D boards. All boards are 6U VME format mechanically but interface to a proprietary bus. The I/O board uses an in-house designed data buffer/converter to allow transport of detector data via Ethernet. The timing board features flexible downloadable programming and generates all of the logic-level timing signals to scan out the CCDs and run the analog signal processors on the A/D boards. The driver board translates the CCD timing signals to CCD operating voltages and also generates all required CD bias voltages. The A/D board(s) process the analog CCD signals and digitize them for presentation to the I/O board. A custom backplane routes signals to the required destinations and also serves as the mount for all power and signal connectors, to and from the controller.

### 8.7.4 Card Cages and Power Requirements

The flexure CCD controller, the smaller of the two systems, mounts in a standard 6U VME card crate measuring approximately 5.1 x 10.5 x 8.3 inches. The extra A/D board in the science CCD controller adds 0.8 inches (5.9 x 10.5 x 8.3 inches).

All power supplies are linear, except as noted below, so an amount of heat approximately equal to the controller dissipation will also need to be removed from the power supplies themselves.

**Table 58. Power supplies and power dissipation for CCD controllers.**

DC Voltage	Flexure CCD Controller	Science CCD Controller
+5 V	0.80 A (4.0 W)	0.80 A (4.0 W)
+15 V	0.66 A (9.9 W)	0.92 A (13.8 W)
-15 V	0.64 A (9.6 W)	0.80 A (12.0 W)
+30 V	12 mA (0.36 W)	20 mA (0.6 W)
+24 V (switcher)	115 mA (2.8 W)	115 mA (2.8 W)

### 8.7.5 Packaging

A CAD model of the detector electronics assembly packaging is shown in Figure 177.

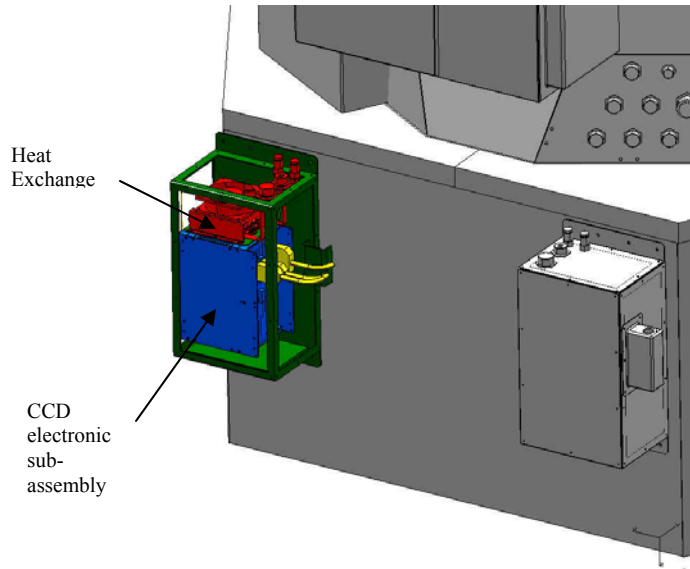


**Figure 177.** A CAD model of the detector electronics assembly packaging.

## **8.8 Guider Detector Electronics Assembly**

### **8.8.1 Overview**

The two guider camera electronics assemblies contain the control and readout electronics for the four thermoelectrically-cooled CCD guider cameras. We have adapted an existing electronics design from the Carnegie Institution to allow the guider head to be placed remotely from the readout electronics. The SAO version is equipped with a copper Ethernet (100T) interface rather than the proprietary fiber optic interface of the Carnegie version. This modification reduces the number of data fibers to be routed off Binospec.

### **8.8.2 Readout Electronics**

The readout electronics consist of five printed circuit boards (power, clocks, signal processing, timing generator, and amplifiers), interfaced to a motherboard. We house this system in an aluminum box measuring approximately 6.25 x 3.75 x 3.25 inches. Control signal input and output of video data is via Ethernet. Internal voltages are derived from a single 48V DC power input, and total power dissipation is approximately 12 watts.

### **8.8.3 Remote CCD Head**

We use an E2V CCD47-20, a thinned backside-illuminated frame-transfer CCD with 1024 x 1024 active pixels (13 um square). It is housed in a vacuum-tight aluminum box measuring approximately 4.75 x 3.25 x 1.75 inches (not including the small vacuum valve and electrical connector). Internal cooling of the CCD to -20 °C or better is provided by a 3-stage Melcor thermoelectric cooler, with the heat conducted through the the housing to the Binospec structure. The power dissipation of the thermoelectric cooler is less than 2 watts.

The remote CCD head connects to the readout electronics box via a multi-coax cable. To better buffer the CCD output signals for remote operation, small preamplifiers have been added inside the vacuum box for the two video channels. Tests have shown no performance degradation with cable lengths up to six feet, but the Binospec design requires cables 12 to 13 feet. We will shortly test the electronics with longer cables. If 12 to 13 foot cables degrade the clock signals significantly, we will add additional buffering electronics at the guider head. If required, these additional electronics will add ~0.1 watt of power dissipation per camera.

### 8.8.4 Operation

The guider may be used at full resolution or in binned mode. In addition, smaller regions of interest may also be specified. At full resolution, the maximum frame rate is approximately 0.5 Hz, and is correspondingly greater for binned operation (~2 Hz, binned 2 x 2). For regions of interest of 50 pixels square, maximum frame rates of 5 Hz are possible. Maximum exposure times are limited by dark current buildup in the CCD, but exposures exceeding 100 seconds are possible.

### 8.8.5 Packaging

CAD models of the packaging for the two guider detector electronics assemblies are shown in Figure 178 and Figure 179. Assembly A contains two guider camera control electronics boxes, one ion pump controller, and ion pumps for a vacuum manifold that connects to the guider cameras. Assembly B contains two guider camera control electronics boxes and two ion pump controllers for the science/flexure detectors. Both units utilize DeviceNet interfaced A/D modules to monitor ion pump current and voltage.

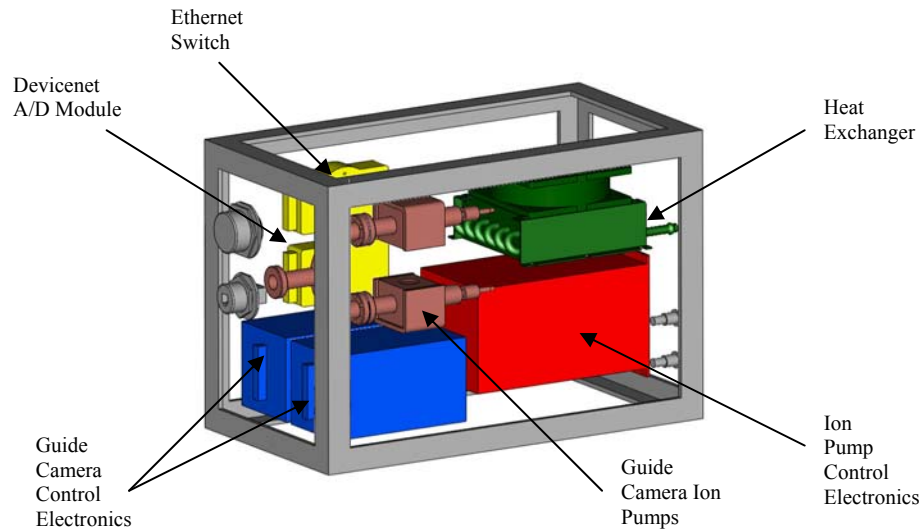
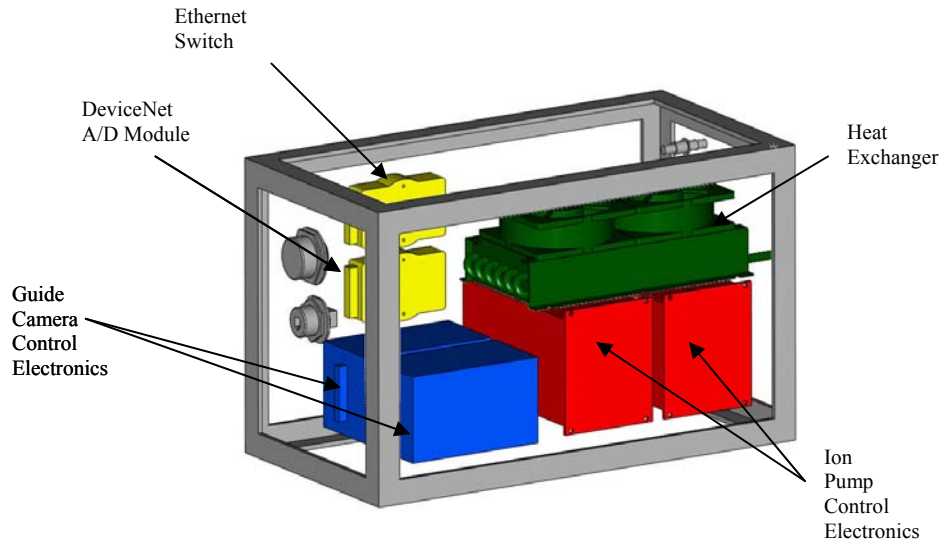


Figure 178. Guider Detector Electronics Assembly A Packaging



**Figure 179. Guider Detector Electronics Assembly B Packaging**

## 8.9 Thermal Impact of Electronics

The electronics affect the thermal design of Binospec in three ways: 1) power dissipation of component within the instrument thermal envelope, 2) penetration of the thermal envelope by electrical wires and associated connectors, and 3) power dissipation of electrical components and subsystems outside of the thermal envelope. Table 59 gives power dissipation estimates for each external electrical assembly. Most of this power is removed by liquid coolant and heat exchangers.

Electrical components inside the thermal envelope include Hall-effect limit and home switches on each mechanism axis, incremental position encoders used on each mechanism axis, motor windings, motor brakes, pneumatic solenoid valves, and temperature sensors. Table 60 lists the power dissipation, quantity used in the instrument, and the estimated duty cycle for each of these components.

**Table 59. Power dissipated in external electrical assemblies.**

Subassembly	Qty	Average Power (W)	Comment
Motion Control Electronic Assembly	1	234	
PZT Control Electronic Assembly	1	170	PZT moving
Power and Communications Electronic Assembly	1	187	
Science Detector Electronics Assembly	1	35	
Flexure Detector Electronics Assembly	1	28	
Guider Detector Electronics Assembly-A	1	34	
Guider Detector Electronics Assembly-B	1	29	
Flexure Control Electrical Assembly	1	30	
Calibration Assembly	1	38	
<b>Total for external subassemblies</b>		<b>785</b>	

**Table 60. Power dissipated by electrical components inside Binospec’s thermal envelope.**

<b>Function</b>	<b>Qty</b>	<b>Power mW</b>	<b>Duty Cycle</b>	<b>Total Avg. Power – W</b>	<b>Comment</b>
EOT Limit Switch	80	75	0.02	0.12	Stage limits & fiducials. (Hall)
Cylinder EOT	46	0	1.0	0	Magnetic reed
Temperature Sensors	64	4	1.0	0.256	Qty. estimated.
Parker Motor Encoders	18	175	1.0	3.15	Netzer encoder
Parker Motor Windings	18	20,000	0.02	7.2	420mA avg. current @48VDC. From mechanism spread. Duty cycle 2% est.
Parker Motor Brakes	18	9120	0.02	2	Bi-level drive used to reduce active power.
PI Microstage Encoder/Limits	4	465	1.0	1.9	5.1 V @ 93 mA
PI Microstage Windings	4	2000	0.02	0.16	
Grating Tilt Encoder	1	250	0	0	Used only for calibration.
Pneumatic Solenoid Valves	24	432	0.02	0.21	
LVPZT Mechanism	2	167	0.95	0.333	Z-axis Nexline PZT actuator requires 0 holding power.
Science/Flexure Camera Assembly	2	1800	1.0	3.6	
Guider Detector Camera Assembly	4	2000	1.0	8	
Barcode Reader	2	2000	0.01	0.04	Used during setups
<b>Total Power Inside Thermal Envelope</b>				<b>27W</b>	

The thermal transition unit is a feed through panel that allows connection of the exterior system motion control cables to the interior of the thermal shroud. Cables from the motion control electronics assemblies are of the following types:

1. Motor drive/thermostat
2. Motor feedback (encoder)
3. Mechanism limit/temperature/pneumatic solenoid drive
4. Pneumatic solenoid drive
5. Grating tilt position/miscellaneous
6. PZT drive/feedback

Detector cables similarly pass through secondary transition panels close to the detectors due to cable length restrictions. Cable conductor sizes are selected to minimize the overall copper area penetrating the thermal shroud while preserving electrical functionality and reliability. Collet-type cable feed throughs will be used on all electrical cables to reduce the thermal path through the outer panel compared to metal connectors. The 360° clamping action of this type of fitting will slightly deform the cable jackets, creating a light trap and preventing a convection path. Boots, fitted on the inside of the thermal panels on all cables, will back up the function of the collets. Detector cabling and Ethernet data lines penetrate the thermal shroud, using the same scheme. The total equivalent cross sectional area of copper wire penetrating the thermal envelope, calculated by adding up all individual wire cross sectional areas is 2.2 cm<sup>2</sup>. Figure 180 shows the main thermal transition unit connector layout.

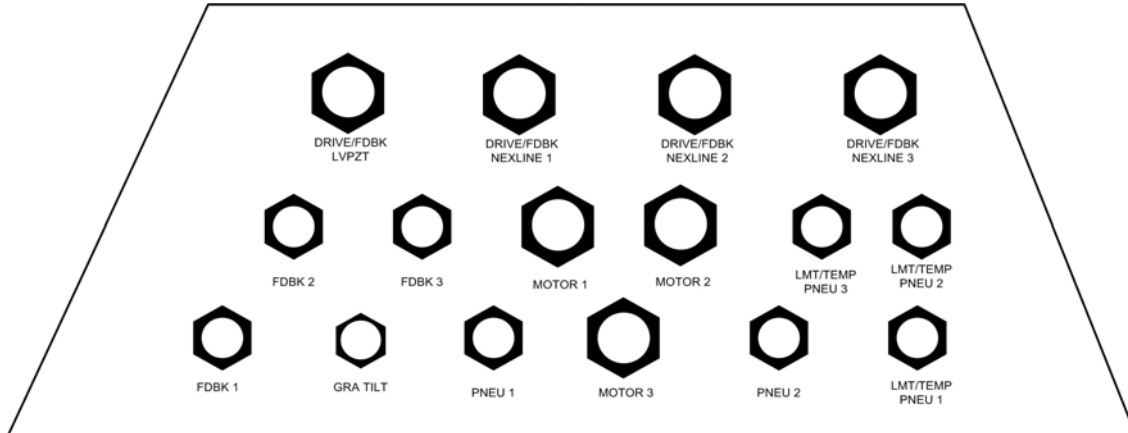


**Figure 180. Thermal transition unit panel layout. Feed throughs are grouped by function: FDBK feed throughs contain encoder, Hall sensor, and motor thermostat signals for four axes. MOTOR feed throughs contain motor phase lines for four axes. LMT/TMP/PNEU feed through contain stage limit sensor signals, temperature sensor signals for four axes as well as signals for one pneumatic actuator, including limit feedback. One set of these feed through services mechanisms located on the upper optical bench, one set services the middle bench, and two sets service mechanisms on the lower optical bench. The PNEU feed throughs contain signals for pneumatic actuator drive and feedback for mechanisms located on the lower bench. LVPZT and NEXLINE connectors carry signals from the PI piezo stages in the detector assembly. GRA TLT carries analog encoder signals from the Renishaw encoder on the grating tilt mechanism to the motion control box. Where possible, we maintain 10% spare conductors in each cable.**

## 9 Software

### 9.1 Introduction and Heritage

SAO has been operating instruments at the converted 6.5m MMT for seven years, starting with the Minicam imager at the f/9 focus in 2000. We have commissioned seven instruments at the MMT: two optical imagers (Minicam and Megacam), two fiber-fed multi-object spectrographs (Hectospec and Hectochelle), an infrared imager (SWIRC), a Shack-Hartmann wave front sensor and the f/5 refractive corrector. We have developed mature instrument control systems, a common observing environment, and a robust computer system to support multi-instrument observing.

Binospec will use the same Delta Tau PMAC control electronics to drive motors and report status information that we have used for past instruments. We have written software to configure PMACS for a wide range of motion control. The ADAM Ethernet-based data acquisition modules are identical to those used in MMIRS and the Magellan Megacam topbox. The Binospec science camera electronics are similar to Hectospec's and Hectochelle's, and we have mature software for these CCD cameras. The observing GUI will need to accommodate both imaging and spectrographic modes of operation similar to MMIRS. Components for this GUI will be drawn from the Megacam and Hectospec and Hectochelle camera interfaces and will be similar to that used for MMIRS.

MMIRS and Binospec will be the first MMT instruments (other than the AO instruments) to implement continuous wave front sensing; this change will require the development of new software interfaces with the telescope control system. The Binospec guiding software will draw heavily on the systems developed for Megacam, Hectospec/Hectochelle and MMIRS.

The PMAC motion control server, the guide server and the log file server programs are configured from data tables. These programs can therefore be quickly configured for Binospec hardware testing. As Binospec assembly and test proceeds, higher level instrument-specific functions will be written using this foundation. The software that controls instrument operation at the telescope must be developed specifically for Binospec.

### 9.2 Software Architecture

#### 9.2.1 Client-Server Architecture

Programs in the system are divided into three general categories: servers, clients, and stand-alone programs. This division is conceptual and not functional. Many servers are clients themselves, obtaining status values or sending commands to other servers to implement high level functions in the system.

Servers expose the control and status of individual electro-mechanical systems via a network protocol. Clients can connect to multiple servers to present the status of the entire system and coordinate the internal actions of the instrument and its external interactions with the telescope and other systems.

The servers in our software architecture generally interface to real hardware that is controlled. They may directly control internal hardware, provide a uniform interface to external resources, or provide a very high level service that is itself the combination of control and status from other software components. Many are very simple mappings of a mechanical device's function to the network. Others such as the CCD Camera or Guide Server implement high level data management policies and image processing functions.

Client programs may be graphical user interfaces that present the instrument status to the operator and provide buttons and menus to configure the instrument state. Other clients are simple command line scripts that perform configuration and automate procedures. The clients operate by connecting to the server programs that represent the instrument hardware, setting and getting published values, or calling registered server commands. In addition to the major user interface programs used to control the instrument during observations (described below), there are dozens of command line scripts available to monitor and control any aspect of the instrument. These scripts are typically used in the characterization, calibration, and integration of the instrument.

Client/server design forces software to be broken into manageably sized modules. Each module can be tested separately and is isolated from others by the commands that it registers and the values it publishes. Each module may publish a few very high level commands that are used by user interfaces and script clients during instrument operation as well as many low level commands and status values that facilitate hardware troubleshooting and repair.

The network protocol used for message passing was developed at SAO and is a simple ASCII over TCP publish/subscribe system. The protocol has several features that make it easy to use. 1) The protocol is ASCII. 2) Telnet communication to any server allows the user to easily query status and invoke commands. 3) Client subscription to status values results in the server publishing data to the clients when these status values change, allowing an event driven programming style that combines easily with Tcl/Tk. 4) C and Tcl interface libraries make it easy to register commands and publish values that clients can access. The client interface library provides robust connections that are automatically reestablished when the server end goes down. Our message passing library "msg" is used to bind all the software components together into a system.

### **9.2.2 Software Languages**

We have purposely limited our software development languages to C and Tcl/Tk. During the development of the Megacam, Hectospec, and Hectochelle instrument software, we used C for control servers and Tcl/Tk for user interfaces. As we gained experience with instrument integration and developed interfaces with external facility software some important server programs were developed in Tcl. Now, Tcl is our first choice for server and interface development, with only low level hardware interface code being written in C. System libraries are packaged to be callable from either C or Tcl. This approach has proven to be robust, flexible and portable. Major components of our software are run under SunOS, Linux and Windows XP.

### 9.3 Software Block Diagram

This section outlines the basic functions and relationships of the programs in the Binospec software system. The software is made up of several client and server programs that cooperate to control the hardware and implement the procedures needed to observe with the instrument. Figure 181 shows the relationships and major communications paths between these programs. The upper left corner of the figure shows the major observer interfaces to the system. Below that a square box encloses the external software interfaces with the telescope. The center of the figure shows the core control software programs. The large box running down the right side shows the Binospec hardware.

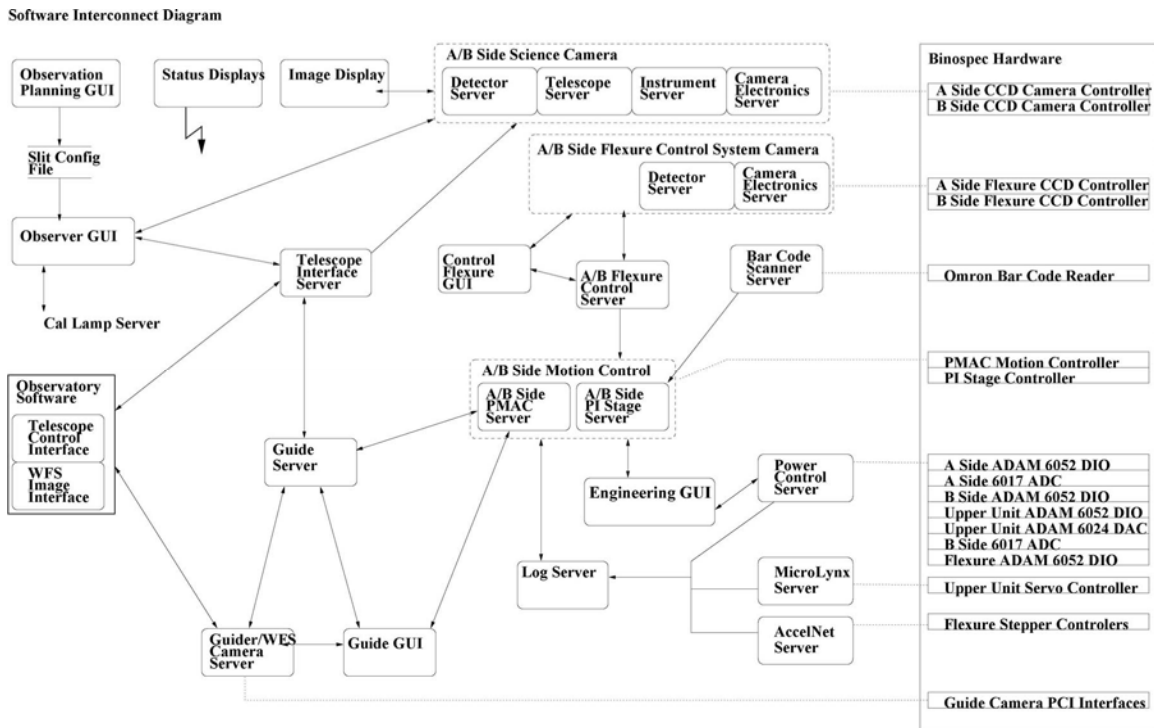


Figure 181. Program relationships and communications paths.

### 9.4 Observation Planning and Mask Design Program

The mask design program will be used by observers to plan their observations and to optimize instrument configurations. It performs two main functions, one to organize and record the proposed spectrograph configurations and two, to optimize the slit mask design for a given field. It is similar in function to the xfitfibs program used to plan fiber fields in Hectospec/Hectochelle observing. The mask design program will be based on the existing Magellan IMACS software; we intend to enhance this program to allow multiple mask optimization. In the current architecture that we use for Hectospec fiber fitting, the fitting engine is a command line program written in C. This allows it to be tested and debugged without repeatedly pressing buttons in the GUI. This same strategy, separating the smarts from the user interface will be used to develop Binospec mask fitting program. The fiber configuration software currently runs on Linux and SunOS.

Our software architecture allows this software to be ported to Windows and Mac OS X, but these operating systems are currently not supported. These additional platforms will be supported in the future.

## **9.5 Graphical User Interfaces**

### **9.5.1 Observing GUI**

The observer's graphical user interface represents the instrument to the observer. From this interface the observer is able to start and stop the instrument systems, configure the spectrograph and take sequences of images with the CCD camera. The configuration information recorded during using the mask program is loaded into the user interface when the corresponding mask is selected. The interface allows complete control of the spectrograph configuration for each science image, including mask selection, grating selection, filter selection, exposure time, and telescope offset.

Three main user interface programs are currently used to operate the f/5 instruments. Mice, the Megacam ICE interface, Spice, the Spectrograph ICE interface and Hobserve, the fiber positioner control interface. For operation of the Binospec a merged version of these interfaces will be developed to allow operation of the instrument as both an imager and a spectrograph and to allow the observer to follow setup and configuration procedures. The Binospec observing GUI will share significant portions of its code with these programs.

It is typical for complex astronomical instruments to have routine procedures that must be repeatedly performed during an observing night. Without a software interface to guide the operator and perform the necessary bookkeeping, executing these procedures accurately and consistently is difficult. The Binospec observing interface will help follow the procedures necessary for operating Binospec.

The current spectrograph configuration and status will be displayed in the upper quarter of the interface window. This area is intended as a text parameter display, showing the user the current values of each important parameter or status value. This panel is always available to the observer.

Under the configuration and status area we place a selectable series of notebook tabs. Each tab allows the operator to perform a specific activity. It is intended that all the buttons and information that the observer needs to complete a task will be contained within a single tab, routinely switching from one tab to another during a single activity should not be necessary. From left to right the current set of tabs include: Start Up, Mask On Deck, Mask Setup, Spectrograph Setup, Start/Stop, and Shutdown.

The Start up/Shutdown procedures for Binospec are relatively simple, consisting of three buttons each. To start up Binospec and make it ready for observing the observer would select the Start Up tab and press the three buttons there in sequence "Power On", "Start

Servers” and “Home Stages”. Shutdown is equally simple. The observer selects the “Shutdown” tab and presses the three buttons there in sequence, “Stow Stages”, Stop Servers” and “Power Off”.

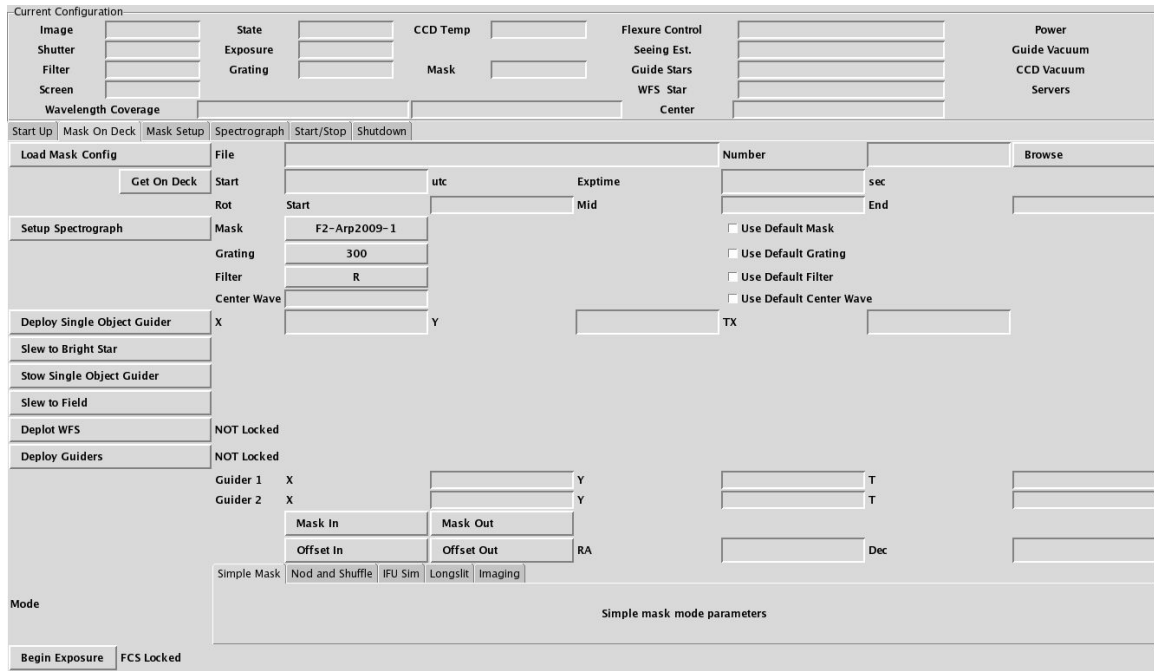


Figure 182. The prototype Binospec observing GUI.

The “Mask On Deck” tab provides a place for the observer to look ahead to the next field before the current field is completed. This tab is a duplicate of the “Mask Setup” tab without any of the buttons that command the spectrograph or telescope. A field configuration can be loaded and the tab displays all of the information about a planned field (RA, Dec, mask selected, observing mode etc.).

Guide star acquisition and mask alignment are the most complex procedures that are routinely needed by the observer. This is done from the “Mask Setup” tab. The procedure is implemented as a series of steps that the observer follows by pressing each button in sequence down the left side of the page. Important status information and parameters for each step are shown in the area to the right of each button. The buttons are normally displayed in a color similar to the background. As each step is successfully completed the button for the next step in the procedure is highlighted in green. If a step fails that button is highlighted in yellow to indicate that further action is needed before proceeding. It should be noted that the highlighting is only a guide, any action may be skipped or repeated as needed by the observer. This allows flexible operation of the instrument in exceptional circumstances while making normal procedure flow obvious.

Along the bottom is another row of set up sub tabs. This allows the display of parameters and additional setup steps necessary for a particular observing mode. Currently these include “Simple Mask”, “Nod & Shuffle”, “IFU Sim”, “Imager” and “Long Slit”.

The “Spectrograph” tab allows the spectrograph to be operated at a lower level than the normal “Mask Setup” tab. From here the filter, mask, grating and grating angle can be specified directly (not from an input field file) and exposures can be made.

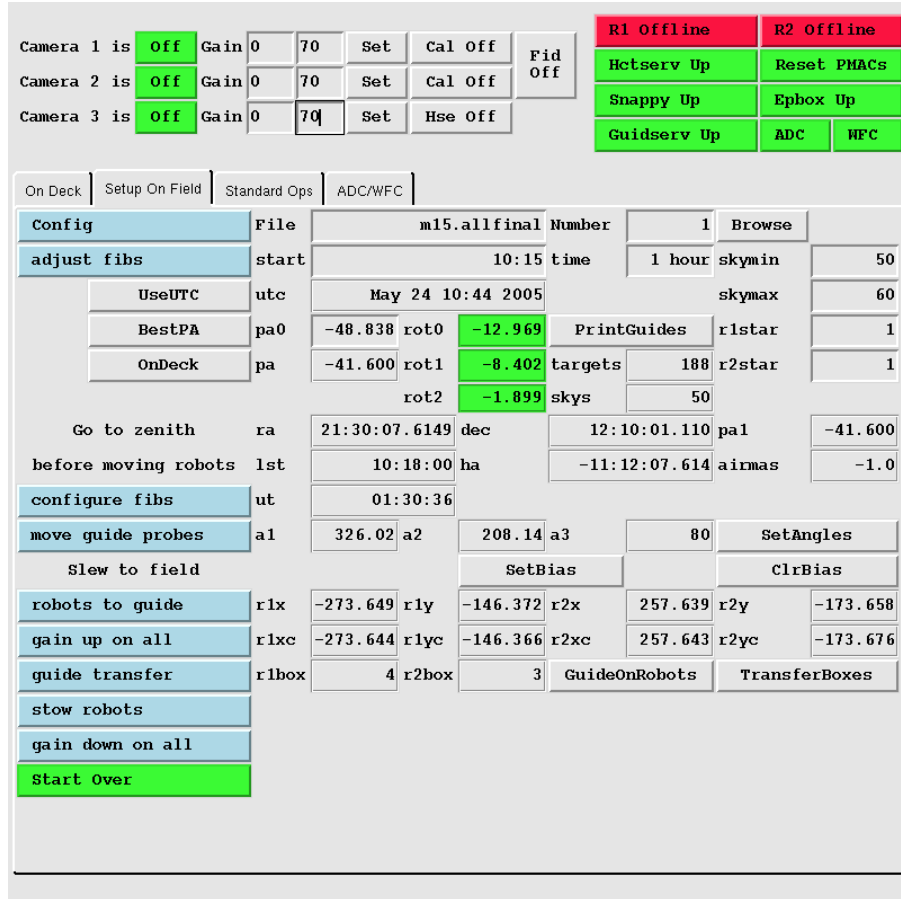


Figure 183. Hectospec observing interface for robot control.

In Figure 183 we show the existing user interface used with the Hectospec instrument to configure the fibers and register the guide stars. The interface shows important status across the top. The bottom half of contains a setup tabs for important instrument procedures. In the tab shown a set of buttons down the left hand side guides the operator through the steps in fiber configuration and guide star registration. The right half of the tab shows the various bookkeeping values that the interface is tracking for the operator.

### 9.5.2 Image Display

The ds9 image display program is used to display science images. The science camera server automatically loads images after they have been read out from the CCD camera. This state of the art fits image display program was developed by the High Energy Astrophysics Division enclosed cooperation with the MMT instruments software group. Figure 184 shows a Megacam image automatically displayed at the observer’s console after the exposures complete.

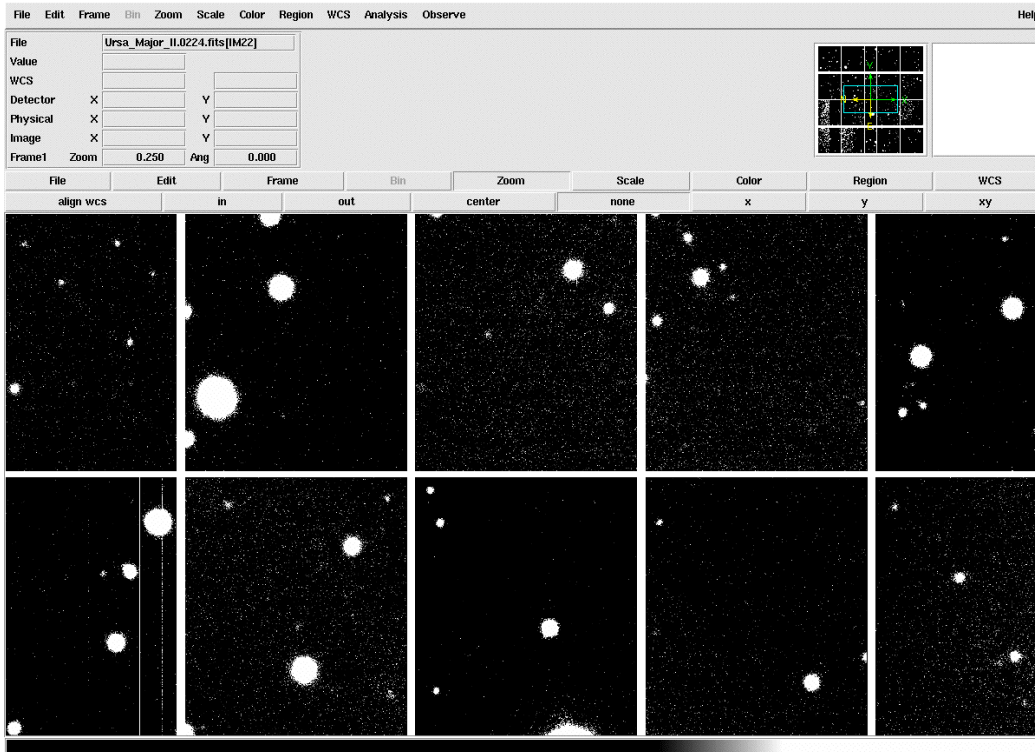


Figure 184. Megacam image displayed by ds9

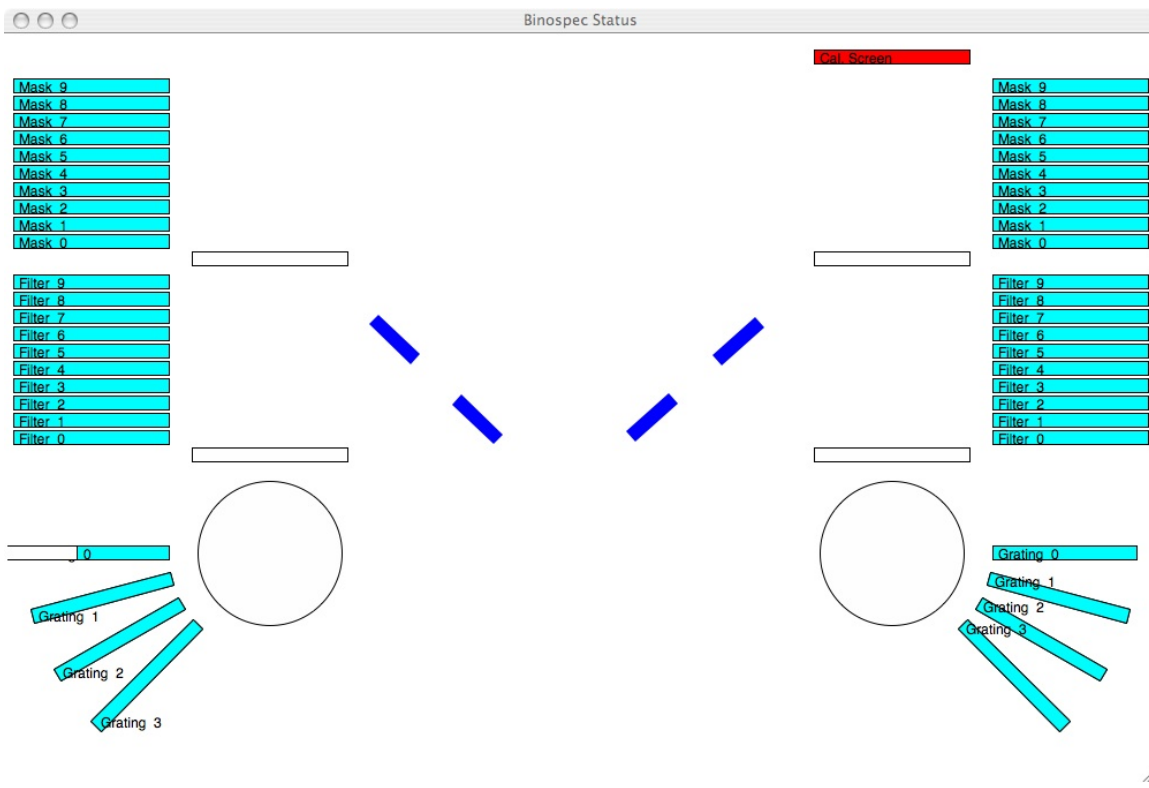


Figure 185. Binospec status display cartoon.

### 9.5.3 Status/Axis Cartoon Display

In contrast to the upper part of the observing interface GUI the status cartoon shows the operator a graphical schematic of the current instrument state. The prototype for the Binospec display is shown in Figure 185. One spectrograph beam is illustrated on either side of the display window with the currently selected mask, filter and grating. This display is connected to the motion control server for each axis and shows the relative axis positions as they move in real time. This gives the operator concrete feedback as configurations are changed.

### 9.5.4 Guide and Flexure Control GUI

The guide GUI provides image display, graphical feedback, analytical feedback, and interactive guide box positioning for the guide cameras. Figure 186 shows the Hectospec guide GUI. A common guide GUI program is already in use for Megacam, Hectospec and Hectochelle. Its configuration is read from the appropriate guide server. It is based on the ds9 image display program and is tightly integrated with the guide server and the guide cameras. Because ds9 is itself written in Tcl we have been able to use the message protocol to tightly integrate these programs and provide near real time guide image display to the operator.

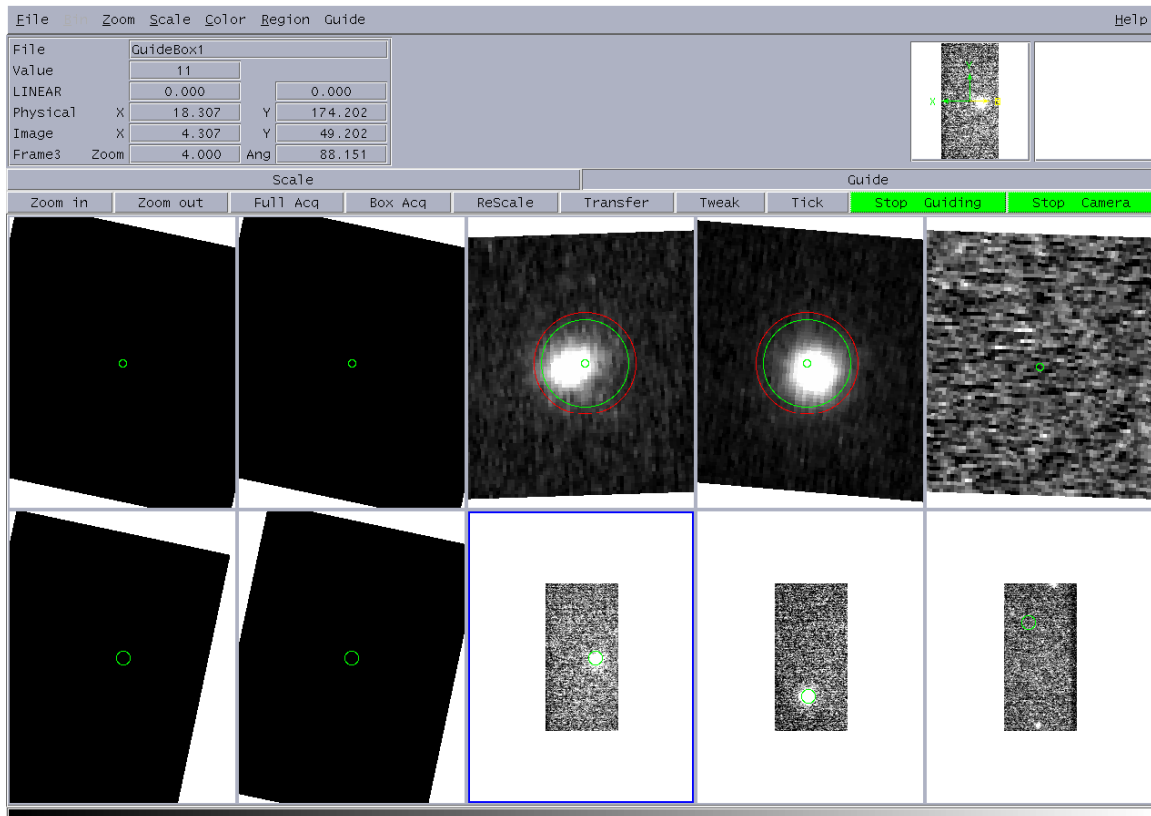


Figure 186. Hectospec guide GUI that provides the basic functions needed for Binospec.

### 9.5.5 Motion Control Engineering GUI

The engineering GUI exposes the lowest level of the instrument's mechanical operation. This interface is typically used to debug mechanical issues, tune the server loop, and qualify an axis before using it with higher level integrated control software. All axes can be moved individually or in conjunction with related axes from this interface. In addition the server parameters and status of all motors and axes are displayed graphically through the interface. Figure 187 shows the top level interface window for the mask changer prototype. The status and positions of the insertion arm and elevator axes are displayed. The mask assembly motion debugging window is shown in Figure 188. Here, an entry box is available to enter a pair of positions for each axis and buttons can be pressed to move between the two positions. Axis control parameters can be adjusted from the parameter read out window shown in Figure 189. This GUI is also able to read out axis motion data and display it as a position verses time plot. This display, shown in Figure 190, is indispensable in tuning axis performance.

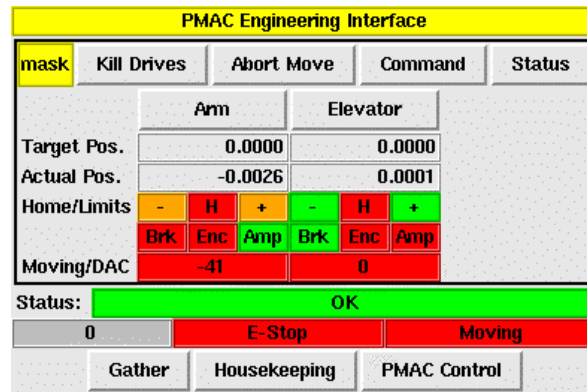


Figure 187. Slit mask changer prototype testing GUI

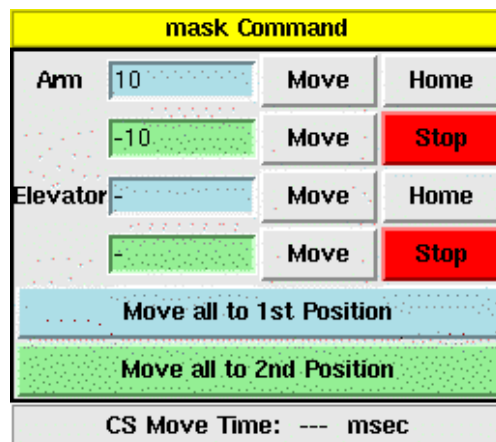


Figure 188. Mask assembly test software GUI.

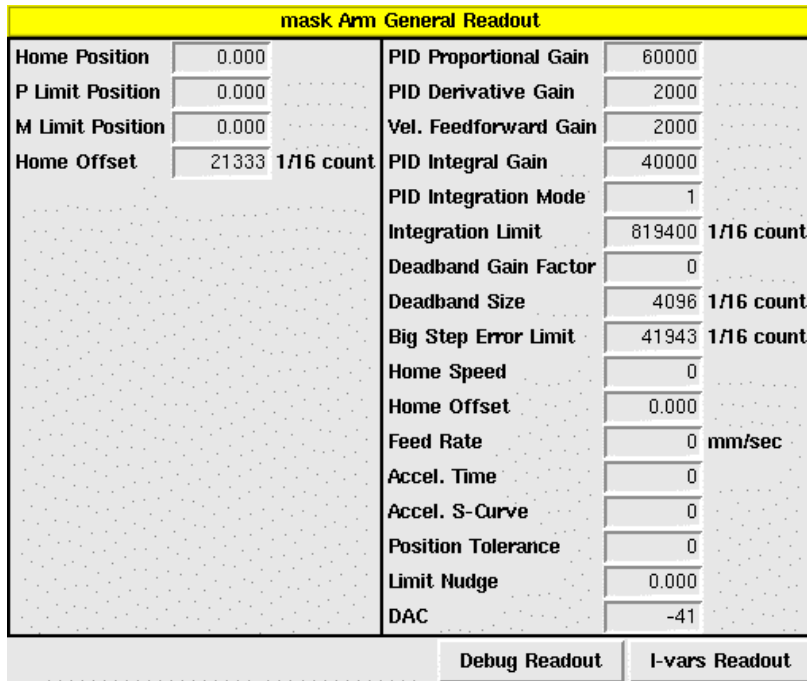


Figure 189. Parameter display and control window.

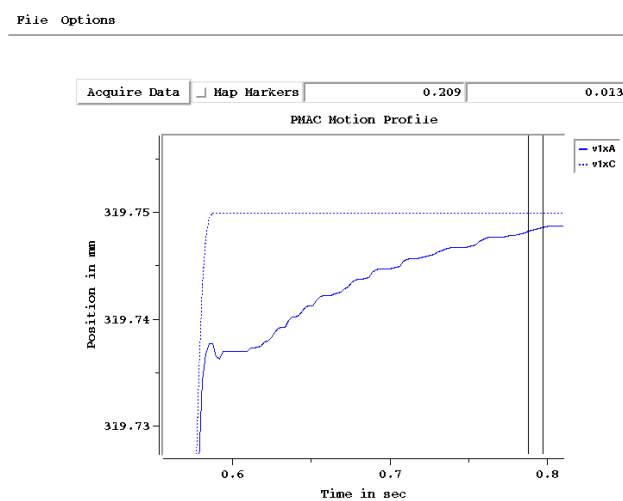


Figure 190. Motion plot used for servo tuning. The actual and commanded trajectories are plotted.

## 9.6 Servers

### 9.6.1 Telescope Guide Server and Flexure Correction Server

The guide server program obtains images from a guide camera that compares the image centroids to the expected image positions and sends corrective offsets to remove the detected errors. In its standard application, the guide images are obtained from an instrument guide camera, and the corrections are azimuth and elevation telescope motions. A second version of the program will be used to make instrument flexure corrections. For flexure control, guide images are read from the flexure control CCDs and X, Y, and focus adjustments to the focal surface position are sent to the motion control server.

The guide server program is currently used with Megacam, Hectospec, and Hectochelle. The program is extensively configurable for various camera sizes, positions, rotation angles and pixel scales. It is capable of computing position, rotation and focus errors using inputs from multiple guide cameras; there are five on the Hectospec/Hectochelle fiber positioner). Its use as the telescope guiding controller for Binospec at the MMT should not present any issues. To allow the guide server program to be used for flexure control, the Binospec motion control server will be enhanced to accept the guide offset commands that are normally sent to the telescope. It will implement these commands as offsets to the focal surface position. Few changes to the guide server code should be required.

The guide server program is able to command telescope offsets in an instrument coordinate system and to simultaneously adjust the guide box centers to match the commanded telescope offsets. This capability allows precision guided offsets to be routinely made by the instruments, and will form the basis of the nod and shuffle and IFU simulation observing modes for Binospec.

### 9.6.2 A/B Side Science Camera Server

This server provides all the functions necessary to configure a science camera and its supporting hardware (e.g. filter selection, shutter control), perform an exposure, read out the data and write a standard FITS data file with complete header keywords recording the telescope, instrument and detector readout information.

The CCD camera server is based on the IRAF ICE data acquisition software and shares its client server architecture. This heritage allows the system to be operated from the IRAF ICE command line interface although this is not typically run at the MMT.

The science camera server program consists of four servers bundled into a single executable. The three main servers for the detector, instrument, and telescope are taken directly from NOAO's ICE servers and can be run directly from an IRAF/ICE client interface. The only modification to the traditional ICE architecture is the writing of the final science data FITS file. The data file is written directly by the detector server rather than by the client. In addition the ICE socket protocol, the server supports an SAO **msg** protocol interface that provide both status and control functions that allows the server to

conform to our software architecture. Normal Binospec observing will use the **msg** interface to this server. The fourth server in the CCD camera server is the CCD control interface. This is a direct interface to the CCD controller itself and allows special command codes to be entered and status to be read back directly.

The science camera software for Binospec is identical to that used in Hectospec/Hectochelle. The only foreseen modifications will be for the implementation of reverse charge shift commands that the Binospec camera will support. This new capability will be used to implement the nod and shuffle mode in Binospec.

### **9.6.3 A/B Side Flexure Control System Camera Server**

The flexure control system camera server controls the flexure control CCD camera hardware and provides camera configuration and FITS images to the flexure control server. The standard CCD camera server software provides a **msg** interface for the two hardware guide boxes supported by the CCD camera and used in the Megacam CCD guide camera. The flexure control system may have more than two fiducial images on each camera. If a larger number of images must be acquired, the code will be modified to section a larger image into multiple virtual guide boxes.

### **9.6.4 Telescope Interface Server**

The telescope interface server provides a standard messaging protocol interface for our software to access telescope information and control telescope functions. It is a translation layer where the telescope model and coordinate systems expected by our system can be implemented on top of the model provided directly by the facility. This interface is currently in use at the MMT. There, this service is a thin layer presenting the MMT telescope model fairly directly with only a few rough edges smoothed over.

### **9.6.5 Guider and Wave Front Sensing Camera Servers**

The guider and wave front camera servers provide FITS images to the guide server and wave front correction programs. Each of the three guide cameras and the wave front sensor camera are controlled and readout by software developed for the MMIRS project and currently in use in the Megacam WFS and TRES project. This software directly supports the **msg** interface protocol needed to provide FITS images to the SAO guide server and MMT wave front programs.

### **9.6.6 A/B Side Motion Control Server**

All requests for moving stages that are controlled by the PMAC are sent to the motion control server. Our software for utilizing PMAC motion control systems is very mature and easily configurable. The low level motion control commands and parameters for each axis are easily configurable. The server and its corresponding graphical user interface and command line commands are created from an ASCII configuration file that declares the names of the axes and the PMAC motors to which they connect. Various configuration files will be used during the development of an instrument as test assemblies are evaluated until the final instrument configuration is integrated and tested.

The motion control server will handle requests for focal plane motion by commanding the PI stage controllers. These axes are commanded via networked RS-232 converters.

Each group of axes which control a particular assembly (filter changer, mask changer, grating changer) will be coordinated by a small submodule of the server. These assembly level modules implement high level commands for each assembly, allowing selection of filters, masks and gratings by name. When a filter or mask is selected, the proper sequence of motions will be made to return any current item to the cassette and deploy named item. The same code is used for both the filter and mask changers, with some modifications it will be used for the grating changer.

### **9.6.7 Bar Code Reader, Power Control Server**

Binospec has power switches for various devices, bar code readers, temperature sensors and other miscellaneous points of control and status values. We have developed a framework to allow these values to be set and reported using the **msg** protocol. Many Ethernet and RS232 serial devices have been incorporated into this framework, including the ADAM 6052 and ADAM 6017 used in the Binospec instrument. This server allows status value to be named with a meaningful mnemonic. The value can then be queried or set using this name.

### **9.6.8 Microlynx Stepper Control Server**

The two Micorlynx stepper motor controllers used in the flexure control light box to position filter wheels are controlled from this server via an RS232 connection. The server will have commands to home and move each filter wheel as well as a command to index the wheel to a particular filter. Microlynx controllers have been used in several projects at SAO and the MMTI software group has direct experience with them.

### **9.6.9 Accelnet Servo Drive Server**

The reflective screen in the upper unit illumination system is moved into and out of position with an Accelnet servo drive. These drives are capable of driving servo motors directly without sophisticated servo controller equipment (such as the PMAC used in the rest of the system). They can be commanded via an RS232 interface. A single stand alone Accelnet drive is used in the Binospec upper unit and will be controlled by this server. Commands to home and move the axis will be implemented.

### **9.6.10 Log Server**

The log server maintains several periodic log files containing columns of status values obtained from the other instrument servers. The log server connects to each server that contains values that are to be logged, queries these values at a periodic rate and writes the values to a log file. The **msg** protocol allows it to log any values that are published by another server. This software has already been developed and is in use for the MMIRS project. The configuration file allows multiple logs to be written at specified rates and several values from various servers may be written into each log. The “server” is really a client of other servers in the system, but as it runs in the background and is started up automatically with the rest of the system we think of it as a server.

## **10 Project Management, Budget, and Schedule**

### **10.1 Overview**

Binospec is the last of a suite of instruments built at SAO for use at the f/5 focus of the 6.5 meter MMT. The construction of these instruments is funded by the Major Scientific Instrumentation (MSI) line item in the Smithsonian Institution's federal budget. The MSI line item previously supported the conversion of the telescope from the original Multiple Mirror Telescope. The funding level for MMT instruments is limited by the Congressional appropriation to the Institution, and is currently slightly under \$2 million per year.

Binospec's delivery schedule is driven by the availability of funding and not the technical readiness of the design. The detailed design and mechanism prototyping will be essentially completed by mid FY08. At that time we will be ready to begin procurement of the remaining optics, major mechanical hardware, and CCDs. Maintaining the desired construction and procurement pace requires funding at a greater level than is currently anticipated from the MSI. With augmented funding the team is confident it can deliver this instrument in the summer of 2011.

### **10.2 Management and Cost Estimating**

The project is managed on a daily basis, in close consultation with the PI (Daniel Fabricant), by the project engineer (Robert Fata) and a project manager (Leslie Feldman), assisted by a financial administrator. Robert Fata has been with the project since inception. Leslie Feldman has had broad financial responsibility for all MMT instrument programs since inception, but assumed project manager duties in January 2006. The financial administrator position was created in 2001 to support all procurement activities, and the Binospec portion is 35% FTE. This structure ensures detailed cost oversight of the project with coordination between the technical and financial requirements of the project.

The project engineer and project manager are in close contact, meeting or speaking by phone on a regular basis. They have responsibility for meeting design and financial goals set by the PI. They both communicate routinely with Central Engineering management to ensure needed personnel are assigned to the project.

SAO has a large Central Engineering group which is managed as a cost center, with formal requests for labor approved at the beginning of each month and authorized on an as-needed basis after that. Negotiations with Central Engineering management for labor assignments are handled by the project engineer and project manager in consultation. All assigned labor must be approved in writing by the project manager, to ensure funding is available.

The mechanical and electrical groups communicate daily. Formal meetings with members of the two groups and the project manager occur on a regular basis to make sure that all team members understand the implications of design decisions. These groups

communicate regularly with the PI, and issue technical memos and financial reports on a regular basis. The entire team meets three to four times per year in internal reviews to evaluate progress and discuss outstanding issues.

A major “cost to complete” exercise began in 2006 with a detailed analysis of manpower requirements and procurement costs. The program work breakdown structure was updated. Labor estimates for each task were produced by the lead Binospec engineer for the appropriate discipline and reviewed by Binospec’s management team. Projected labor costs include expected cost of living adjustments. The 2006 budget was revised and updated based on final design activities in 2007. Several major procurement packages were sent to vendors for quotes. Each subassembly estimated cost was reviewed and revised as necessary to reflect the current design.

Expense monitoring compares yearly estimated expenses against actual costs. This process allows us to understand how well we estimated, and also allows us to rebudget as necessary to meet the challenges of instrument development. All requests for procurement are approved by the project manager and processed by the project administrator. These procedures ensure that spending oversight is complete and up-to-date.

We present two budgets and schedules. The fast schedule projects a mid 2011 delivery, and the slow schedule projects a mid 2013 delivery. The fast schedule requires a funding augmentation of \$1.9 million in FY09 and \$1M in FY10. The slow schedule assumes constant MSI funding at the current level of ~\$2 million per year. This slow schedule requires that major procurements be split or not completed until FY12, and extended engineering support. We estimate that total costs rise by ~\$1.5 million with the less aggressive delivery schedule.

### **10.3 Major Schedule Milestones for FY2011 delivery**

FY08	Complete electronic prototyping and start major procurements
FY09	Complete major procurements and begin assembly
FY10	Integration and testing
FY11	Delivery and Commissioning

## 10.4 Costs to Complete with FY11 Delivery

**Table 61. Binospec budget overview for fast schedule.**

<b>Budget Item</b>	<b>FY08</b>	<b>FY09</b>	<b>FY10</b>	<b>FY11</b>	<b>TOTALS</b>
Central Engineering	\$1,133,001	\$1,199,317	\$1,206,026	\$690,121	\$4,228,466
Optics/Mounts/Fixtures	360,000	976,000	362,000	0	1,698,000
Mechanical Hardware	200,000	898,000	225,000	0	1,323,000
Main Structure	0	0	533,000	0	533,000
CCDs	0	50,000	230,000	0	280,000
Electronics/Motors	72,299	306,800	69,200	4,000	452,299
Assembly/Integration /Test	0	350,000	0	0	350,000
Project Management	30,000	29,900	45,800	35,700	141,400
Delivery and Commissioning	0	0	279,000	45,000	324,000
<b>TOTAL COST</b>	<b>\$1,795,300</b>	<b>\$3,810,017</b>	<b>\$2,950,026</b>	<b>\$774,821</b>	<b>\$9,330,165</b>
Expected MSI Total	\$1,795,300	\$1,943,000	\$1,943,000	\$1,943,000	\$7,624,300
Other Funding Sources		\$1,867,017	\$1,007,026		\$2,874,043

**Table 62. Central Engineering hours, fast schedule.**

	<b>FY08</b>	<b>FY09</b>	<b>FY10</b>	<b>FY11</b>	<b>TOTAL HOURS</b>
Project Engineer	1674	1560	1524	680	6492
Lead Electrical Engineer	900	837	837	480	4929
Lead Mech Engineer	1674	1360	1674	760	7142
Lead Mech Designer	1674	1380	1232	520	6480
Mechanical Engineer	160	88	1036	0	1684
Structural Engineer	80	0	0	0	1160
Structural Engineer	998	0	100	0	980
Mechanical Designer	960	0	160	0	2908
Electrical Engineer	630	1394	1256	480	5918
Electrical Engineer	0	960	0	0	1200
Electrical Designer	900	480	0	0	2080
Electrical Technician	300	1674	1256	480	5643
Electrical Technician	530	837	1256	480	3650
Electrical Technician	0	837	0	0	1674
Instrument Technician	0	1054	2080	480	3614
Lead Software Engineer	960	960	960	480	4272
<b>TOTAL HOURS</b>	<b>11440</b>	<b>13421</b>	<b>13371</b>	<b>4840</b>	<b>43072</b>

**Table 63. Optics, mounts, and fixtures, fast schedule.**

	<b>FY08</b>	<b>FY09</b>	<b>FY10</b>	<b>FY11</b>	<b>TOTAL</b>
Spherical lenses	300000				
Coat lenses		300000			
Gratings		236000			
Fold mirrors		120000			
Lens, bezel support fixtures	42000	20000			
Seal molds	18000				
Lens bezels		250000	250000		
Assembly fixtures		50000			
Alignment fixtures			50000		
Filters			62000		
Subtotal	360000	976000	362000	0	1698000

**Table 64. Mechanical hardware, fast schedule.**

	<b>FY08</b>	<b>FY09</b>	<b>FY10</b>	<b>FY11</b>	<b>TOTAL</b>
Split Mirror Assembly		75000			
Thermal Shroud, Upper		0	50000		
Thermal Shroud, Lower		0	50000		
Camera Assembly		100000			
Collimator Assembly		100000			
Guider Assembly		40000			
Slit Mask Loader Assembly		40000			
Grating Assembly	200000	60000			
Filter Changer Assembly		70000			
Entrance Window Assembly		40000			
Wave Front Assembly		25000			
Single Object Guider/Acq.		20000			
Detector Assembly		150000			
Flexure Control Stage, etc.		166000	50000		
Thermal System (Chiller)		12000			
Calibration Screen Assembly		0	75000		
Main Structure		533000			
Telescope Simulator Refurb		350000			
Subtotal	200000	1781000	225000	0	2026000

**Table 65. CCDs**

	<b>FY08</b>	<b>FY09</b>	<b>FY10</b>	<b>FY11</b>	<b>TOTAL</b>
Science grade		230000			
Alignment and flexure		50000			
Guide camera (purchased in FY07)		0			
Subtotal	0	280000	0	0	280000

**Table 66. Electronics and motors, purchased parts**

	<b>FY08</b>	<b>FY09</b>	<b>FY10</b>	<b>FY11</b>	<b>TOTAL</b>
Camera Electronics		15000			
Motion Control Electronics	31500	171300	61700		
Instrument Mechanisms		10600			
Power and Communications Electronics	11300	7500			
Cables (Wire and Connectors)	3300	1100			
System Support Spares	1300	5200			
Science/Flexure Detector Electronics		45000			
Guide Detector Electronics	7300	17300			
Flexure Control Assembly	2100	5000			
Upper Unit Calibration	1300	3000			
Thermal Transition Unit	4200	2800			
Test Fixtures		3000	5000	2000	
Prototype Development	5000	5000	2500	2000	
Electronics Boxes, Structures	5000	15000			
Subtotal	72299	306800	69200	4000	452299

**Table 67. Program management and support.**

	<b>FY08</b>	<b>FY09</b>	<b>FY10</b>	<b>FY11</b>	<b>TOTAL</b>
Program Management (federal support)	0	0	0	0	0
Financial Administrator	23900	24900	25800	6700	104300
Miscellaneous Travel	3000	5000	20000	29000	60000
CDR Travel	4100				4000
Subtotal	30000	29900	45800	35700	141400

**Table 68. Delivery and Commissioning**

	<b>FY07</b>	<b>FY08</b>	<b>FY09</b>	<b>FY10</b>	<b>FY11</b>	<b>TOTAL</b>
Instrument Shipping Container				25000		
Electronics, Misc. Shipping Crates				4000		
Truck to MMT					15000	
Other Shipping					6000	
Slit Mask Cutter				250000		
Commissioning Travel					24000	
Subtotal	0	0	0	279000	45000	324000

**10.5 Table 69. Major Schedule Milestones for FY2013 delivery**

FY08	Complete electronic prototyping, figure spherical lenses
FY09	Coat lenses, begin bezel procurement, continue subsystem build
FY10	Complete optics procurements; procure non-science CCDs
FY11	Procurement of main structure, science CCDs, and simulator
FY12	System assembly and test
FY13	Complete assembly and test, delivery and commissioning

## 10.6 Costs to Complete with FY13 Delivery

	<b>FY08</b>	<b>FY09</b>	<b>FY10</b>	<b>FY11</b>	<b>FY12</b>	<b>FY13</b>	<b>TOTALS</b>
Central Engineering	1133001	913100	909400	677000	1096300	992000	5720801
Optics/Mounts/Fixtures	360000	620000	606000	50000	62000	0	1718000
Mechanical Hardware	200000	236000	225000	350000	0	100000	1111000
Main Structure	0	0	0	533000	0	0	533000
CCDs	0	0	50000	230000	0	0	280000
Electronics/Motors	72299	144900	122800	91300	129000	104000	540299
Assembly/Integration/Test	0	0	0	0	350000	0	350000
Project Management	30000	29000	29800	11700	26700	31700	158900
Delivery/Commissioning	0	0	0	0	279000	45000	324000
Total Cost	1795300	1943000	1943000	1943000	1943000	1272700	10736000
Total from MSI	1795300	1943000	1943000	1943000	1943000	1943000	11510300

## 10.7 Costs Through FY07

	<b>Expenditure to Date</b>
Central Engineering	\$4,103,768
Optics/Mounts/Fixtures	3,066,825
Mechanical Hardware	232,988
Main Structure	62,136
CCDs	48,376
Electronics/Motors	201,506
Assembly/Integration/Test	0
Project Management	309,905
Delivery/Commissioning	0
Total through FY07	8,025,504

# 11 Appendices

## 11.1 Description of Slit Mask Geometry

The purpose of this memo is to document the shape and position of the Binospec slit masks. The area of each slit mask that will contain slits is shown in Figure 191.

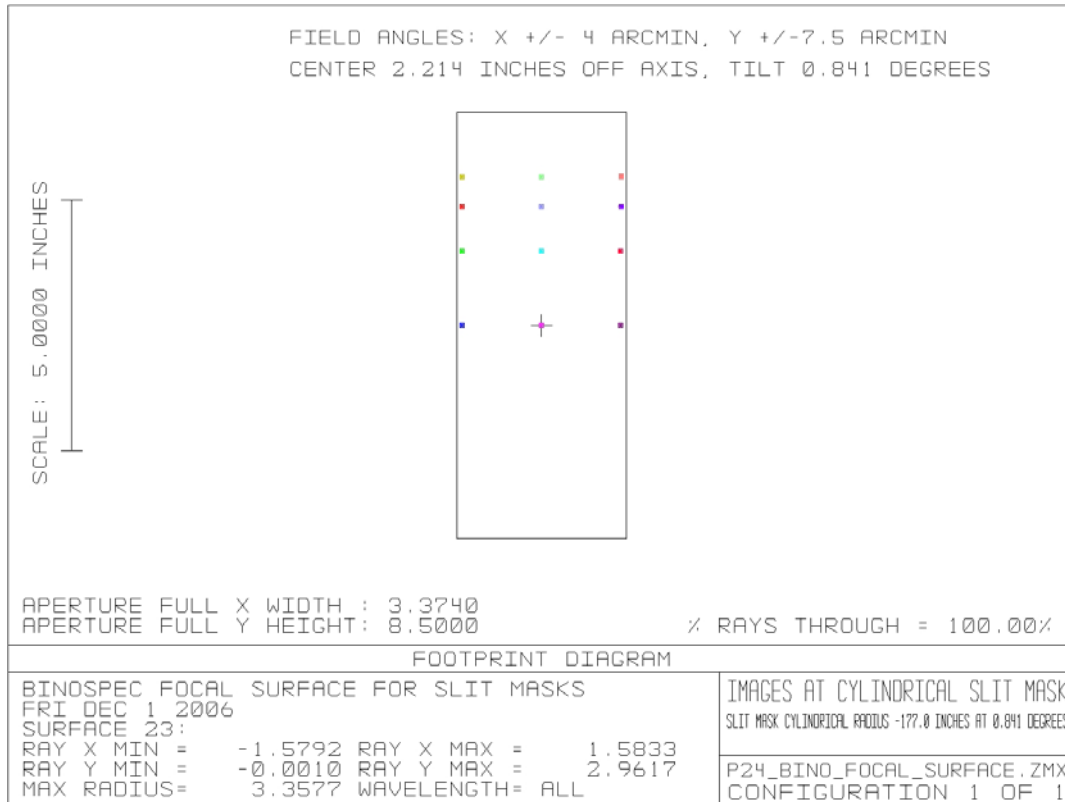


**Figure 191. One half of the “active” area of the slit masks. The active area is that area occupied by slits. Only positive Y field angles are shown. Units are inches.**

The telescope focal surface is a hyperboloid of revolution with a vertex radius of curvature of -134.01575 inches and a conic constant of -665. The images on this surface are shown in Figure 192.

We are approximating the hyperbolic telescope focal surface with tipped cylindrical surfaces for each beam. The tip is about the long axis of the slit mask at the center of each individual slit mask. The cylindrical bend is about the short axis of the slit mask, symmetric about its center. In Figure 193, the images using the best cylindrical radius for the nominal tip of the optics (0.72°) is shown. In Figure 194, we allow both the cylindrical radius and the tip angle are allowed to vary, and find that we can obtain slightly better balanced images.

We therefore adopt:

**Table 70. Adopted slit mask shape.**  
 Cylindrical radius -177.0 inches

Tip angle 0.841°

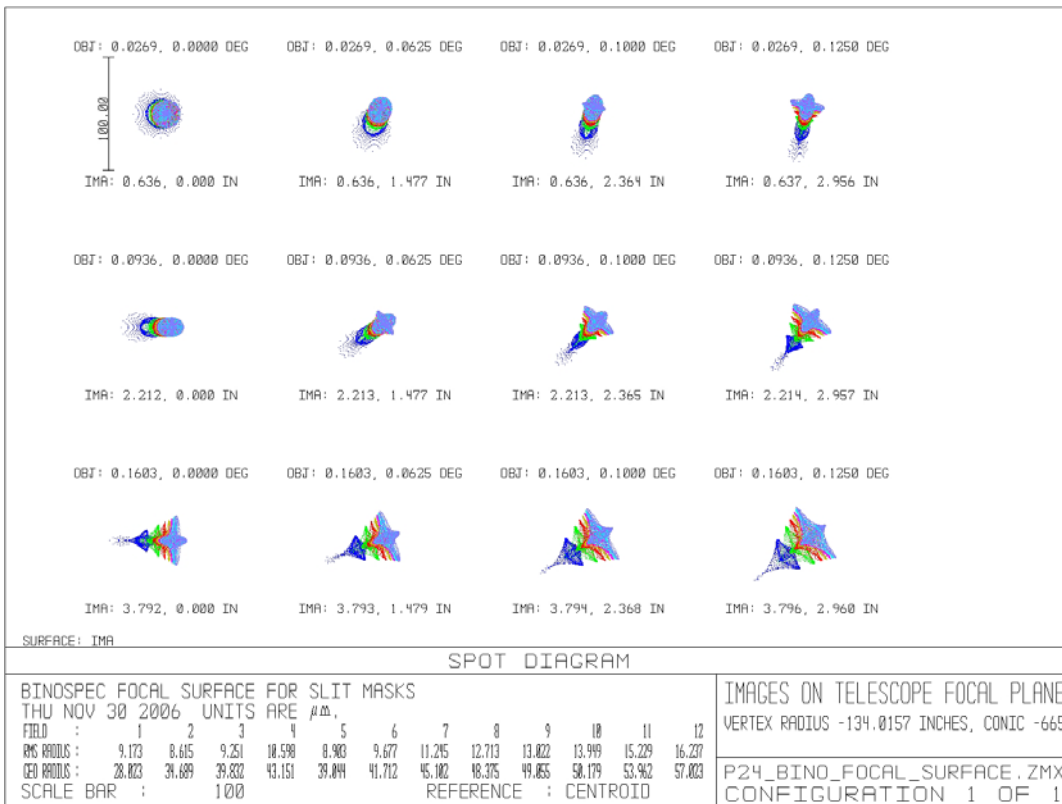


**Figure 192. The images on the telescope focal surface, an hyperboloid of revolution.**

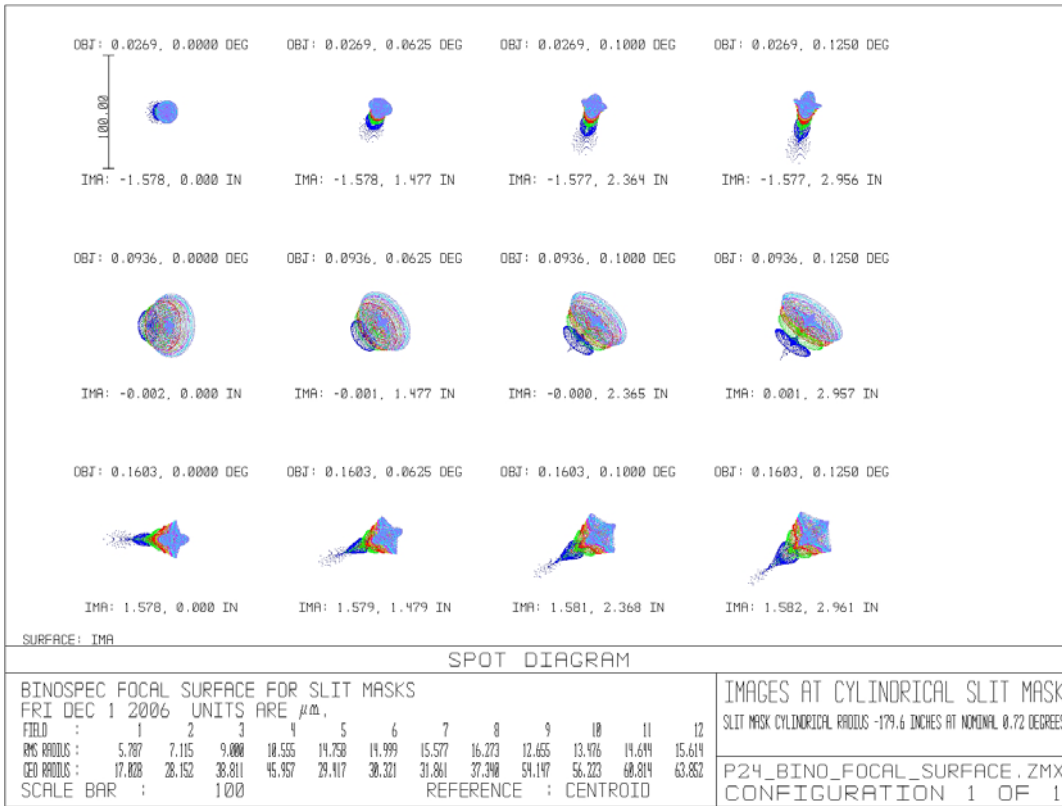


Figure 193. Images on a cylindrical focal surface with radius of -179.6 inches, tipped at 0.72°.

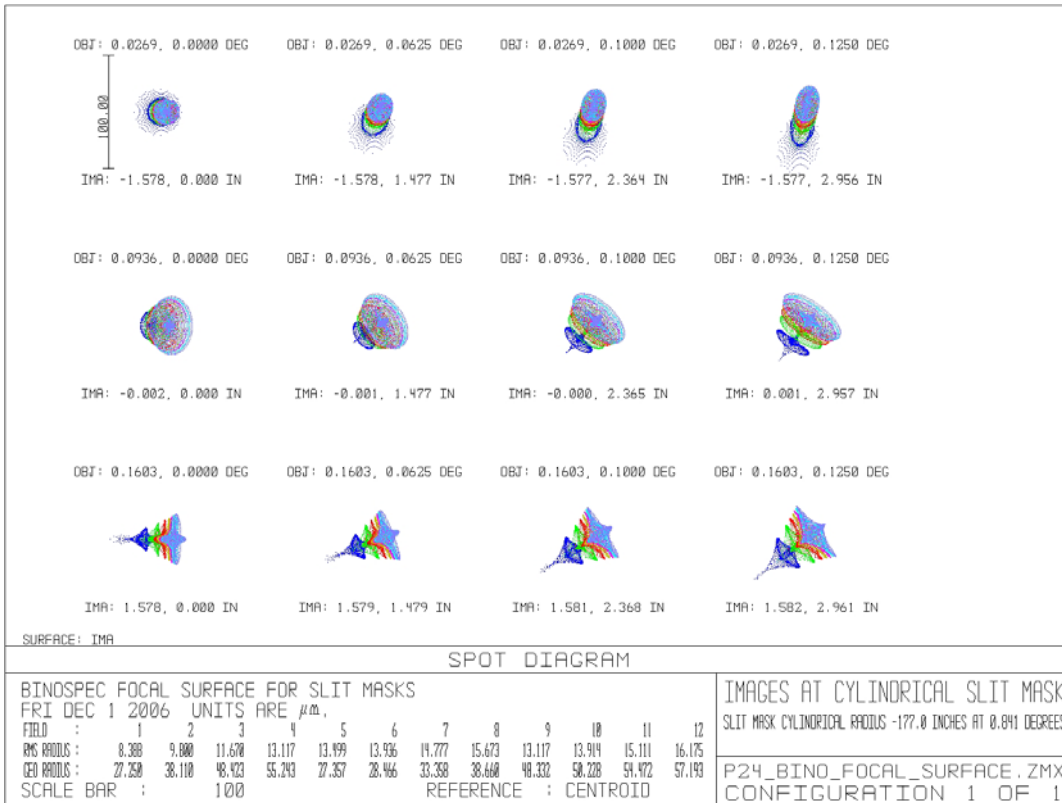


Figure 194. Images on a cylindrical slit mask with a radius of -177.0 inches tipped at 0.841°.

System/Prescription Data

File

C:\docs\Zemax\_Files\binospec\2006\_reopt\p24\_bino\_focal\_surface.ZMX

Title: Binospic focal surface for slit masks

Date : FRI DEC 1 2006

Surf	Type	Radius	Thickness	Glass	Diameter	Conic
OBJ	STANDARD	Infinity	Infinity		0	0
1	STANDARD	Infinity	245		257.6474	0
STO	STANDARD	-639.9724	-243.4901	MIRROR	256	-1
3	STANDARD	-202.7909	243.4901	MIRROR	63.62974	-2.6947
4	STANDARD	Infinity	1.156772		21.10908	0
5	STANDARD	23.80854	2.885354	SIL5C	32.73386	0
6	STANDARD	27.35535	3.152953		32.73386	0
7	STANDARD	39.86205	1.840197	SIL5C	31.37913	0
8	STANDARD	22.74866	6.742126		31.37913	0
9	STANDARD	-235.5551	1.933386	SIL5C	30.21299	0
10	STANDARD	-82.84606	2.119213		30.21299	0
11	STANDARD	Infinity	1	SFSL5Y_5C	29.48504	0
12	STANDARD	Infinity	0.005	CAF2P20	29.48504	0
13	STANDARD	Infinity	0.6	PBL6Y_5C	29.48504	0
14	STANDARD	Infinity	1.012008		29.47717	0
15	STANDARD	Infinity	0.6	PBL6Y_5C	29.48504	0
16	STANDARD	Infinity	0.005	CAF2P20	29.48504	0
17	STANDARD	Infinity	1	SFSL5Y_5C	29.48504	0
18	STANDARD	Infinity	27.54937		29.48504	0
19	STANDARD	Infinity	0.5	SIL5C	12.50874	0
20	STANDARD	Infinity	18.565		12.45614	0
21	STANDARD	-134.0157	-0.0175248		9.628889	-665
22	COORDBRK		0		-	-
IMA	TOROIDAL	-177			6.715406	0

SURFACE DATA DETAIL:

Surface OBJ : STANDARD  
 Surface 1 : STANDARD  
 Surface STO : STANDARD  
 Mirror Substrate : Curved, Thickness = 5.12000E+000  
 Surface 3 : STANDARD  
 Mirror Substrate : Curved, Thickness = 1.27259E+000  
 Surface 4 : STANDARD  
 Surface 5 : STANDARD  
 Aperture : Floating Aperture  
 Maximum Radius : 16.36693  
 Surface 6 : STANDARD  
 Aperture : Floating Aperture  
 Maximum Radius : 16.36693  
 Surface 7 : STANDARD  
 Aperture : Floating Aperture  
 Maximum Radius : 15.68957  
 Surface 8 : STANDARD  
 Aperture : Floating Aperture  
 Maximum Radius : 15.68957  
 Surface 9 : STANDARD  
 Aperture : Floating Aperture  
 Maximum Radius : 15.1065  
 Surface 10 : STANDARD  
 Aperture : Floating Aperture  
 Maximum Radius : 15.1065  
 Surface 11 : STANDARD  
 Aperture : Floating Aperture  
 Maximum Radius : 14.74252  
 Surface 12 : STANDARD  
 Aperture : Floating Aperture  
 Maximum Radius : 14.74252  
 Surface 13 : STANDARD  
 Aperture : Floating Aperture

```

Maximum Radius :      14.74252
Surface 14      : STANDARD
Aperture       : Floating Aperture
Maximum Radius :      14.73858
Surface 15      : STANDARD
Aperture       : Floating Aperture
Maximum Radius :      14.74252
Surface 16      : STANDARD
Aperture       : Floating Aperture
Maximum Radius :      14.74252
Surface 17      : STANDARD
Aperture       : Floating Aperture
Maximum Radius :      14.74252
Surface 18      : STANDARD
Aperture       : Floating Aperture
Maximum Radius :      14.74252
Surface 19      : STANDARD
Surface 20      : STANDARD
Surface 21      : STANDARD
Surface 22      : COORDBRK
Decenter X     :          2.214
Decenter Y     :          0
Tilt About X   :          0
Tilt About Y   :          0.841
Tilt About Z   :          0
Order          : Decenter then tilt
Surface IMA    : TOROIDAL
Rad of rev.    :          0
Coeff on y^2   :          0
Coeff on y^4   :          0
Coeff on y^6   :          0
Coeff on y^8   :          0
Coeff on y^10  :          0
Coeff on y^12  :          0
Coeff on y^14  :          0
Number of terms:          0
Maximum rad ap :          100
Aperture       : Rectangular Aperture
X Half Width   :          1.687
Y Half Width   :          4.250

```

GLOBAL VERTEX COORDINATES, ORIENTATIONS, AND ROTATION/OFFSET MATRICES:

Reference Surface: 2

Surf	R11	R12	R13	X
	R21	R22	R23	Y
	R31	R32	R33	Z
1	1.0000000000	0.0000000000	0.0000000000	0.000000000E+000
	0.0000000000	1.0000000000	0.0000000000	0.000000000E+000
	0.0000000000	0.0000000000	1.0000000000	-2.450000000E+002
2	1.0000000000	0.0000000000	0.0000000000	0.000000000E+000
	0.0000000000	1.0000000000	0.0000000000	0.000000000E+000
	0.0000000000	0.0000000000	1.0000000000	0.000000000E+000
3	1.0000000000	0.0000000000	0.0000000000	0.000000000E+000
	0.0000000000	1.0000000000	0.0000000000	0.000000000E+000
	0.0000000000	0.0000000000	1.0000000000	-2.434900543E+002
4	1.0000000000	0.0000000000	0.0000000000	0.000000000E+000
	0.0000000000	1.0000000000	0.0000000000	0.000000000E+000
	0.0000000000	0.0000000000	1.0000000000	0.000000000E+000
5	1.0000000000	0.0000000000	0.0000000000	0.000000000E+000
	0.0000000000	1.0000000000	0.0000000000	0.000000000E+000
	0.0000000000	0.0000000000	1.0000000000	1.156771654E+000
6	1.0000000000	0.0000000000	0.0000000000	0.000000000E+000
	0.0000000000	1.0000000000	0.0000000000	0.000000000E+000



## 11.2 Image Spot Diagrams from Raytracing

### 11.2.1 Spot Diagrams at +8 °C, On-axis Binospec Configuration

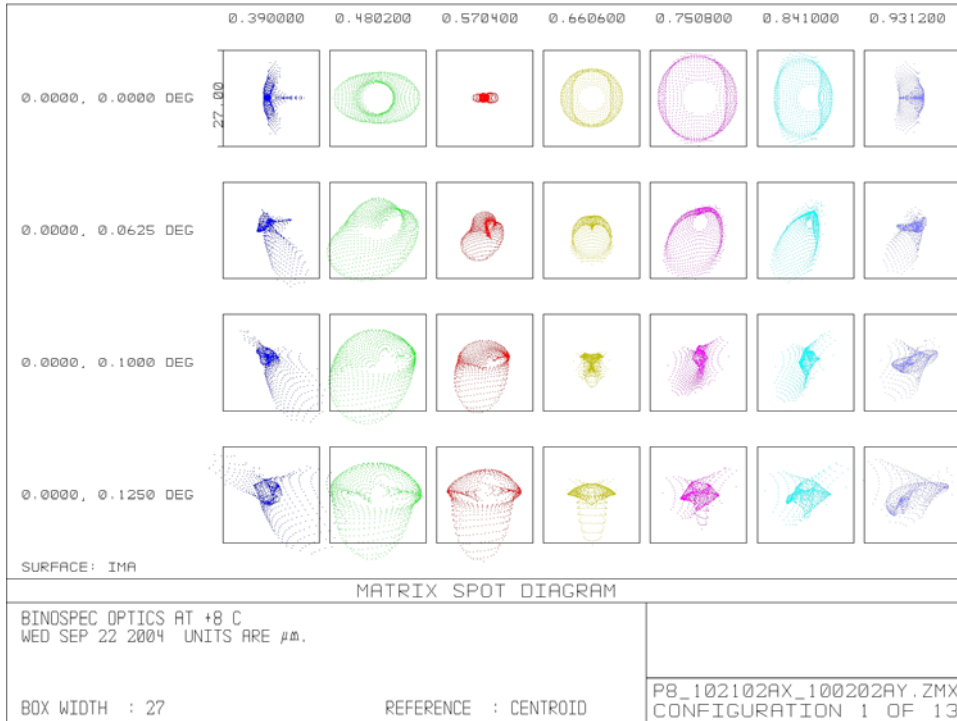
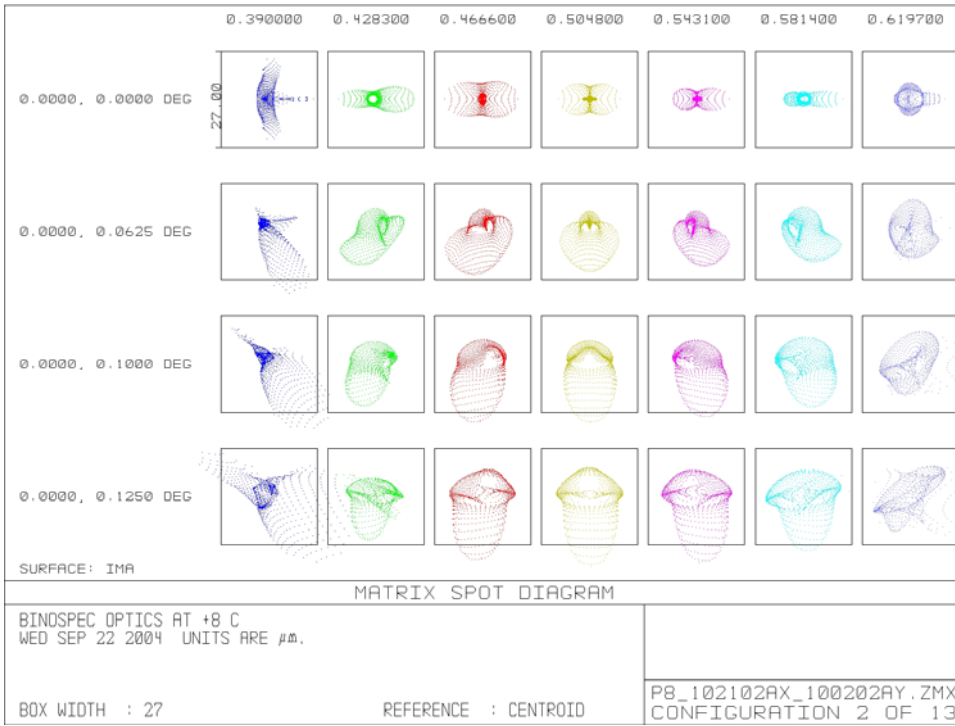
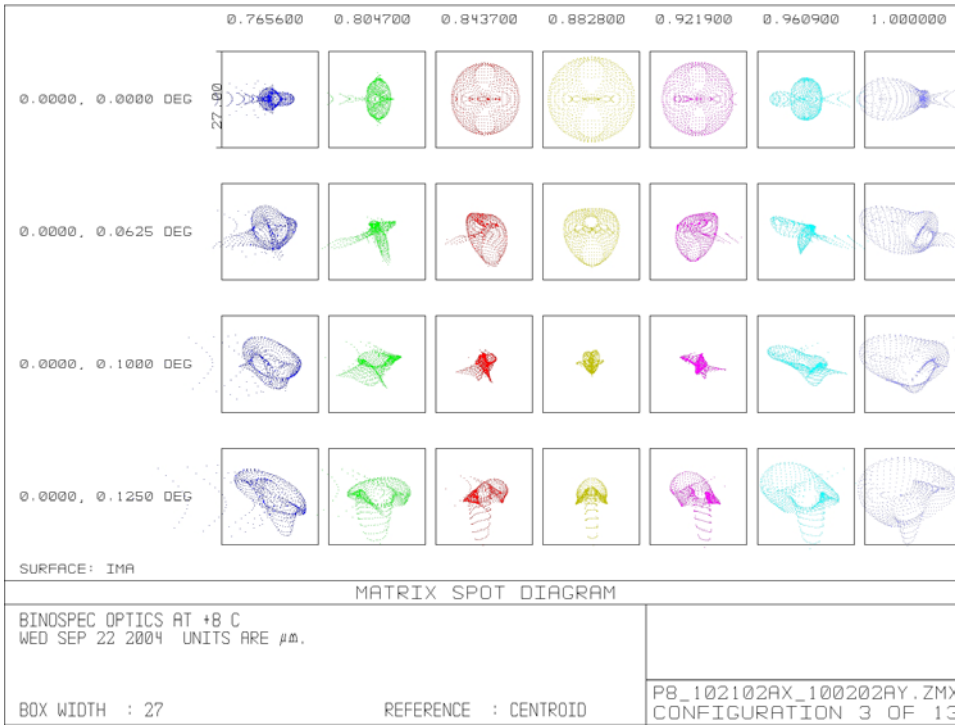


Figure 195. Configuration 1 (270 gpm grating) spots in a two pixel box.



**Figure 196. Configuration 2 (650 gpm grating) spots in a two pixel box.**



**Figure 197. Configuration 3 (650 gpm grating) spots in a two pixel box.**

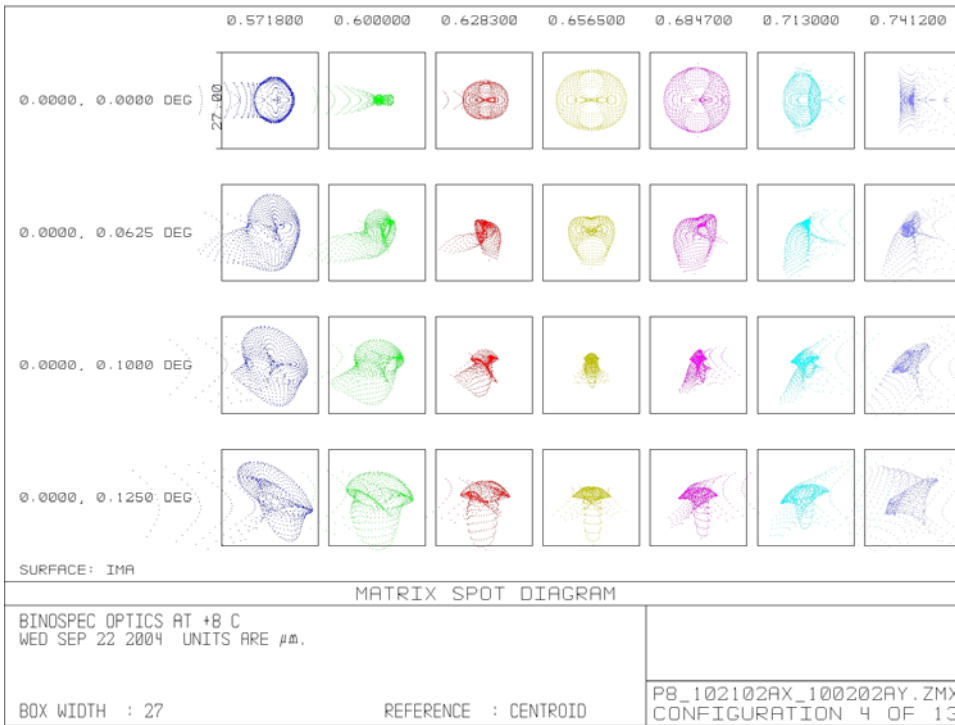


**Figure 198. Configuration 4 (900 gpm grating) spots in a two pixel box.**

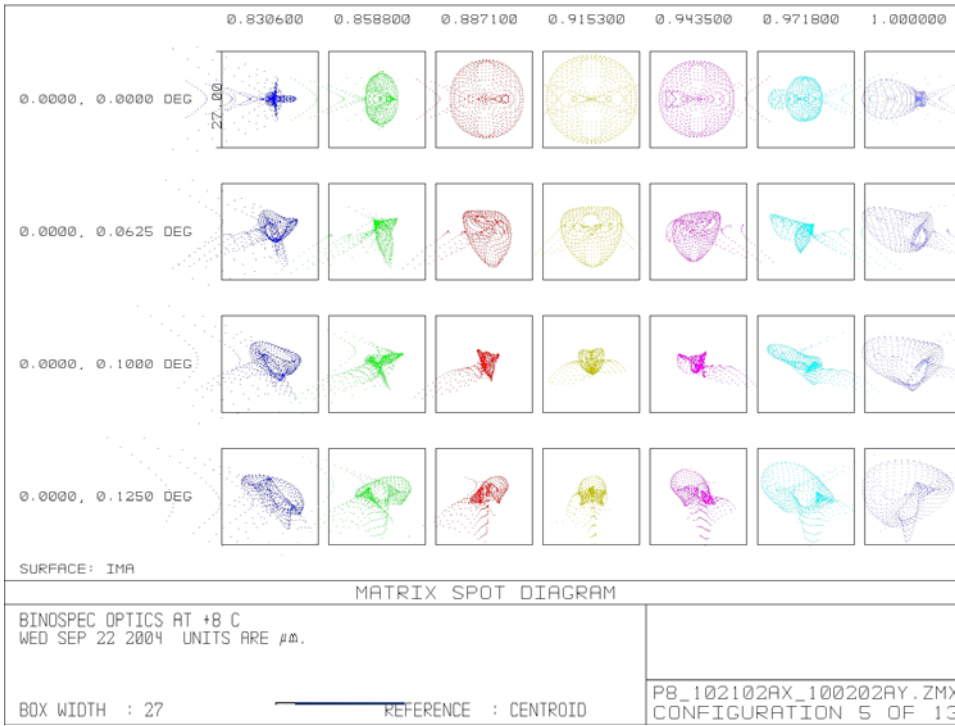


**Figure 199. Configuration 5 (900 gpm grating) spots in a two pixel box.**

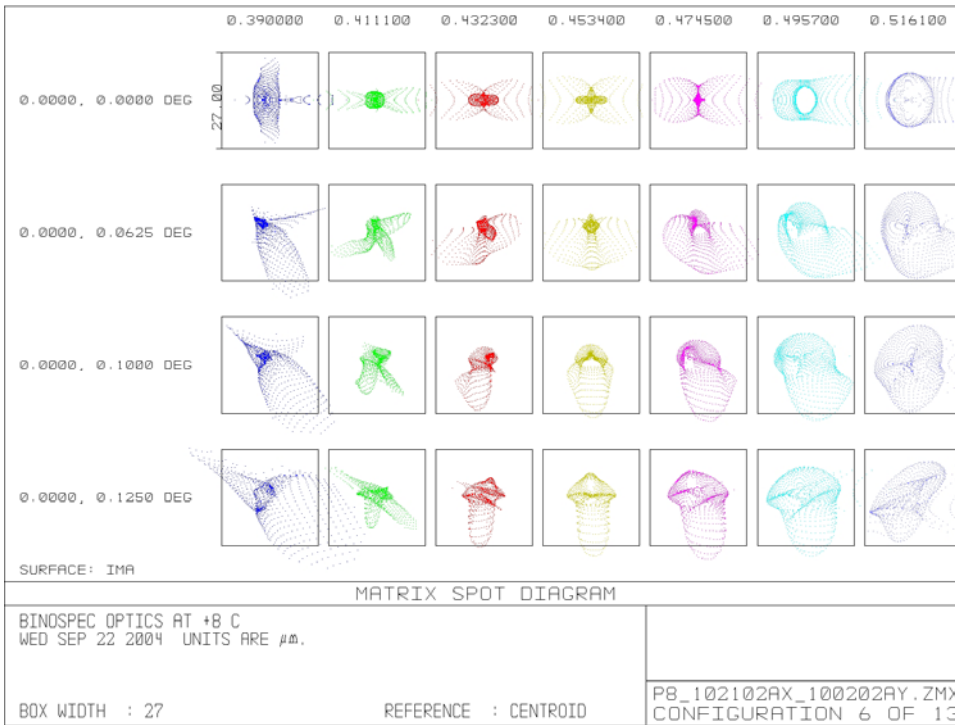


**Figure 200. Configuration 6 (1200 gpm grating) spots in a two pixel box.**

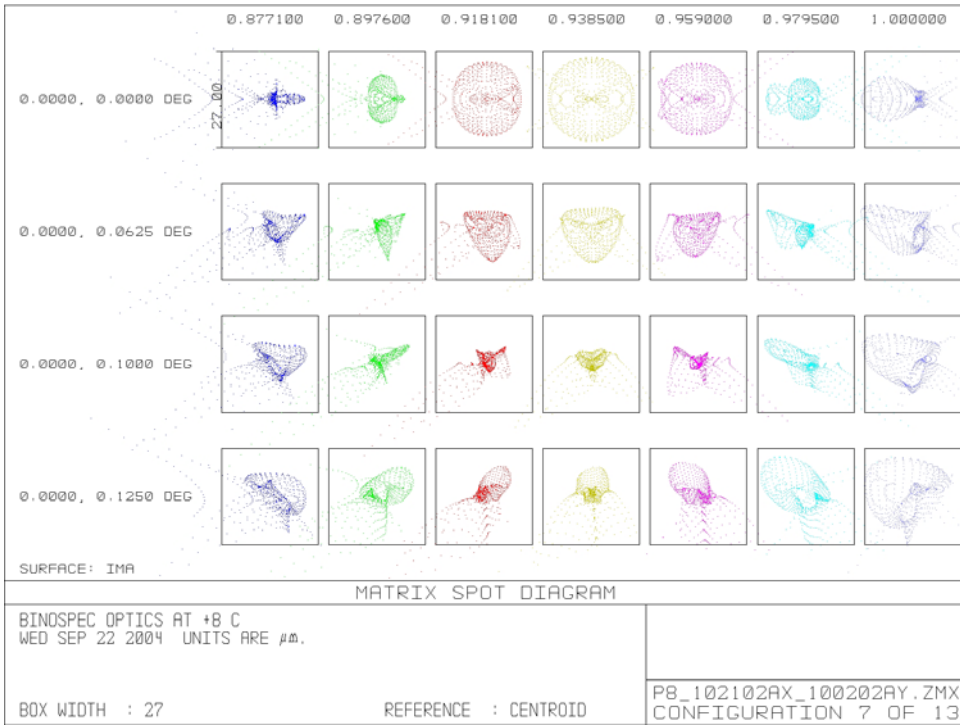


**Figure 201. Configuration 7 (1200 gpm grating) spots in a two pixel box.**

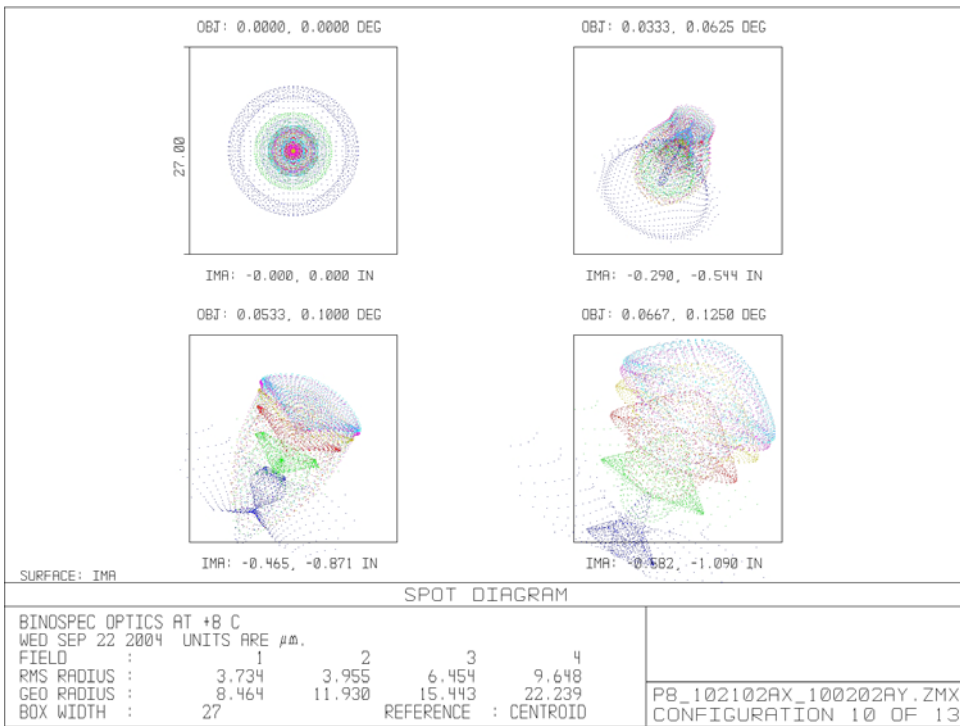


**Figure 202. Configuration 10, g' band (0.41-0.54 μm) polychromatic spots in a two pixel box.**

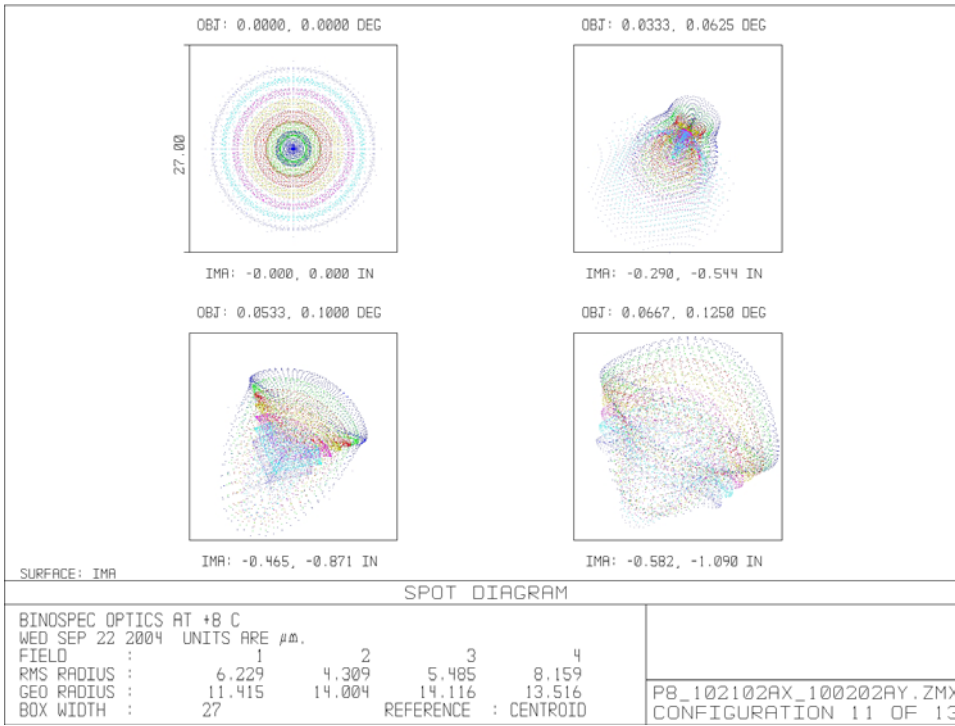


**Figure 203. Configuration 11, r' band (0.56-0.69  $\mu\text{m}$ ) polychromatic spots in a two pixel box.**

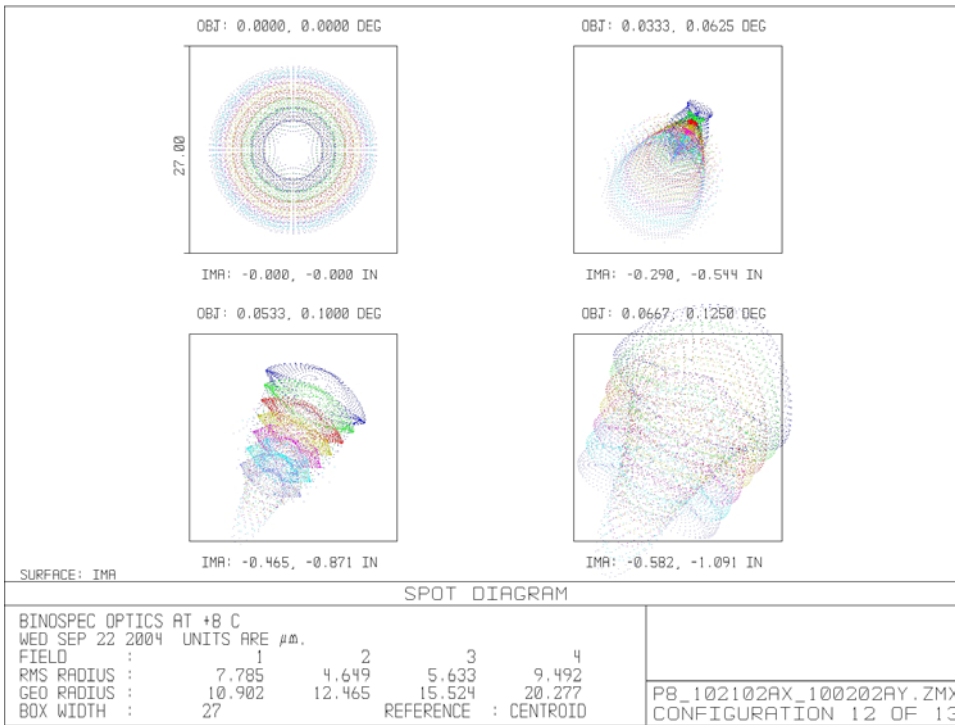


**Figure 204. Configuration 12, i' band (0.69-0.83  $\mu\text{m}$ ) polychromatic spots in a two pixel box.**

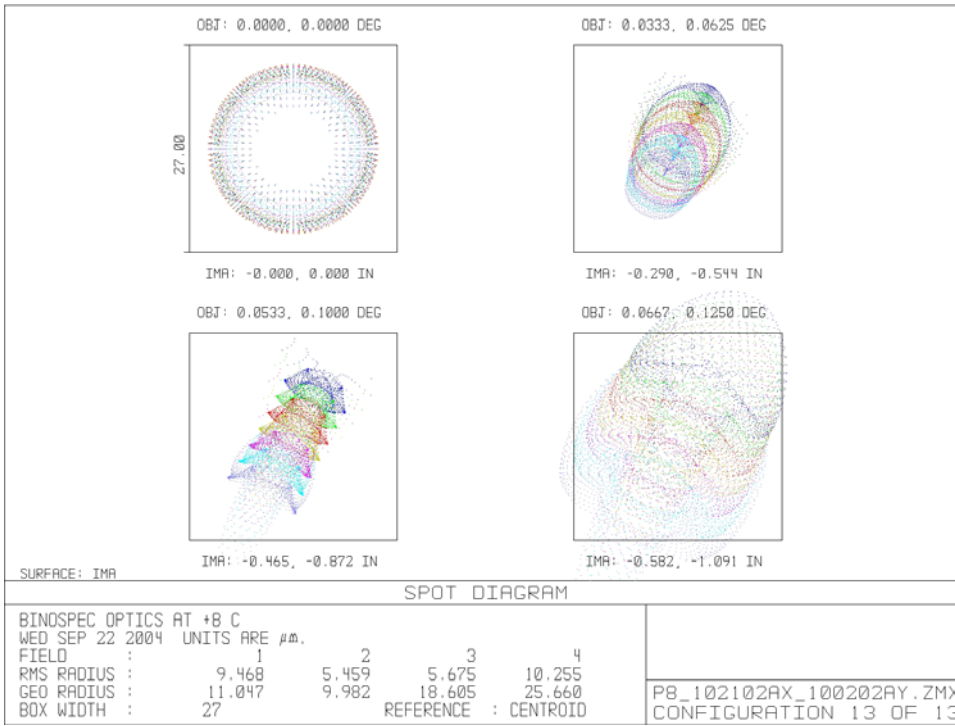


**Figure 205. Configuration 13, z' band (0.86-0.99  $\mu m$ ) polychromatic spots in a two pixel box.**

## 11.2.2 Spot Diagrams at +24 °C, Off-axis Binospec Configuration

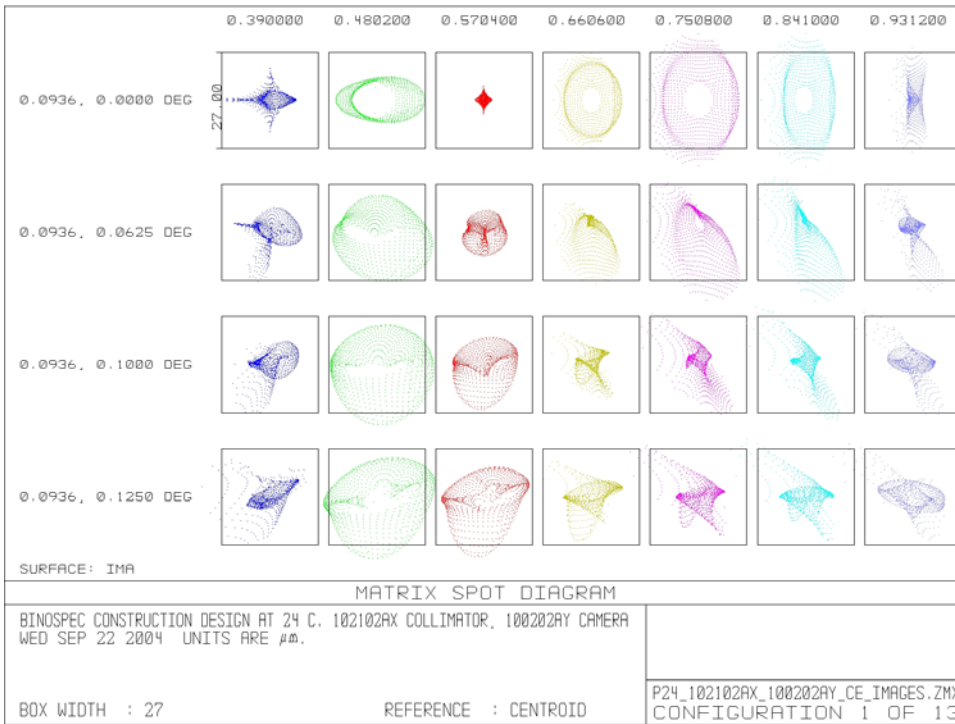


Figure 206. Configuration 1 (270 gpm grating) spots in a two pixel box.

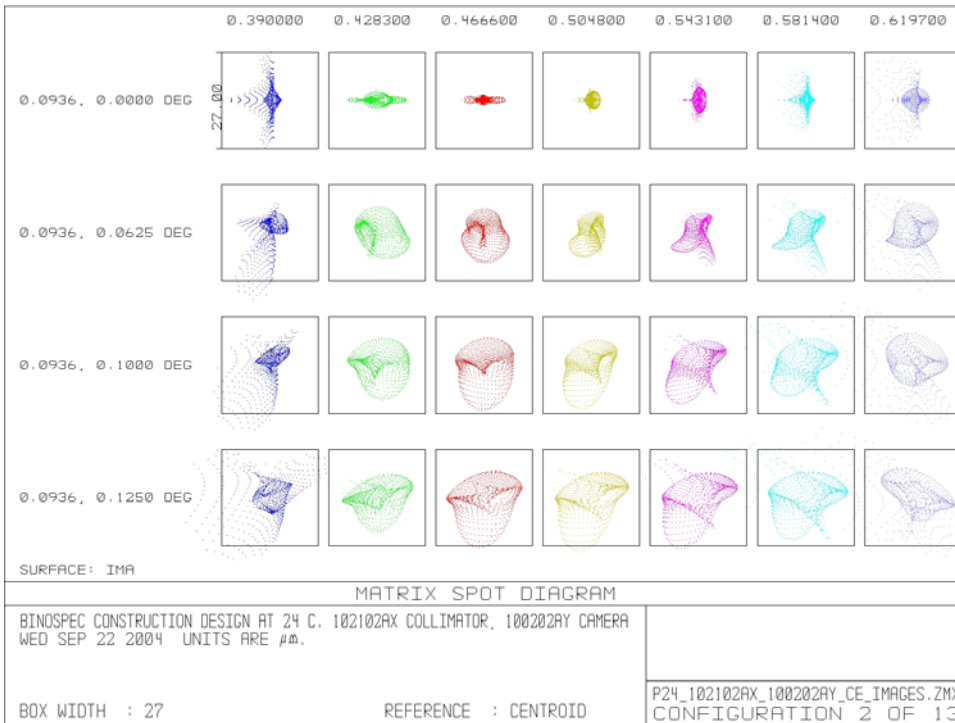
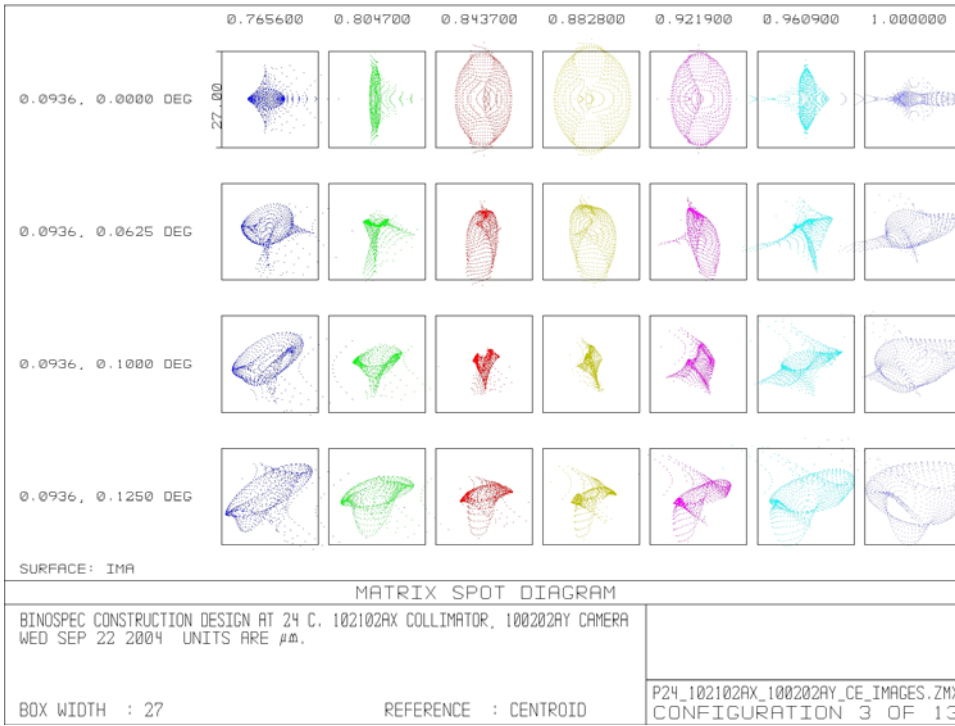
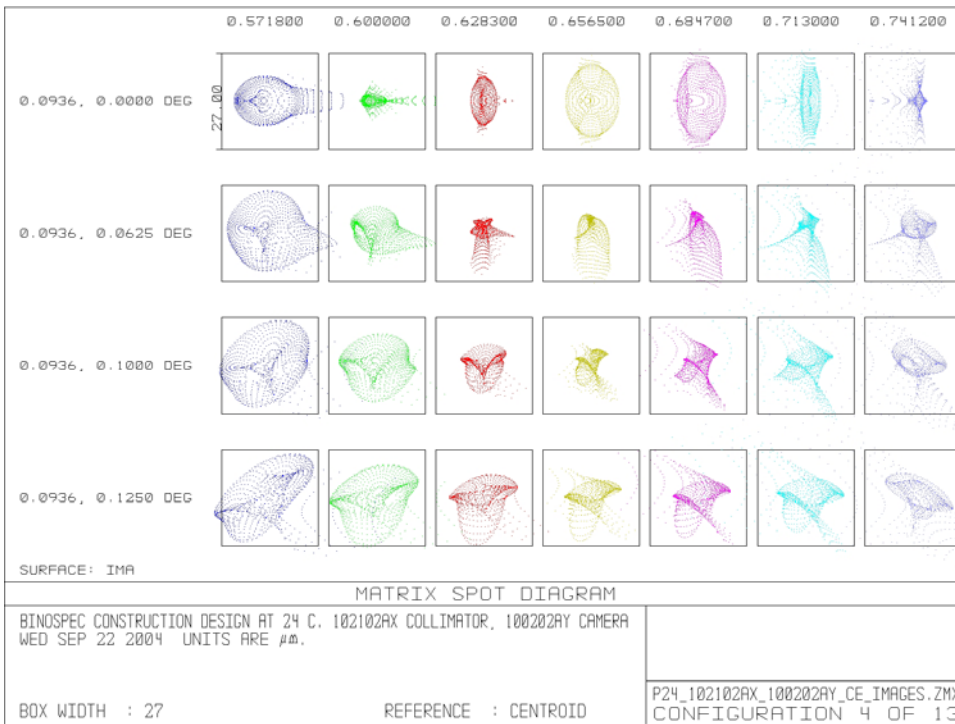


Figure 207. Configuration 2 (650 gpm grating) spots in a two pixel box.



**Figure 208. Configuration 3 (650 gpm grating) spots in a two pixel box.**



**Figure 209. Configuration 4 (900 gpm grating) spots in a two pixel box.**

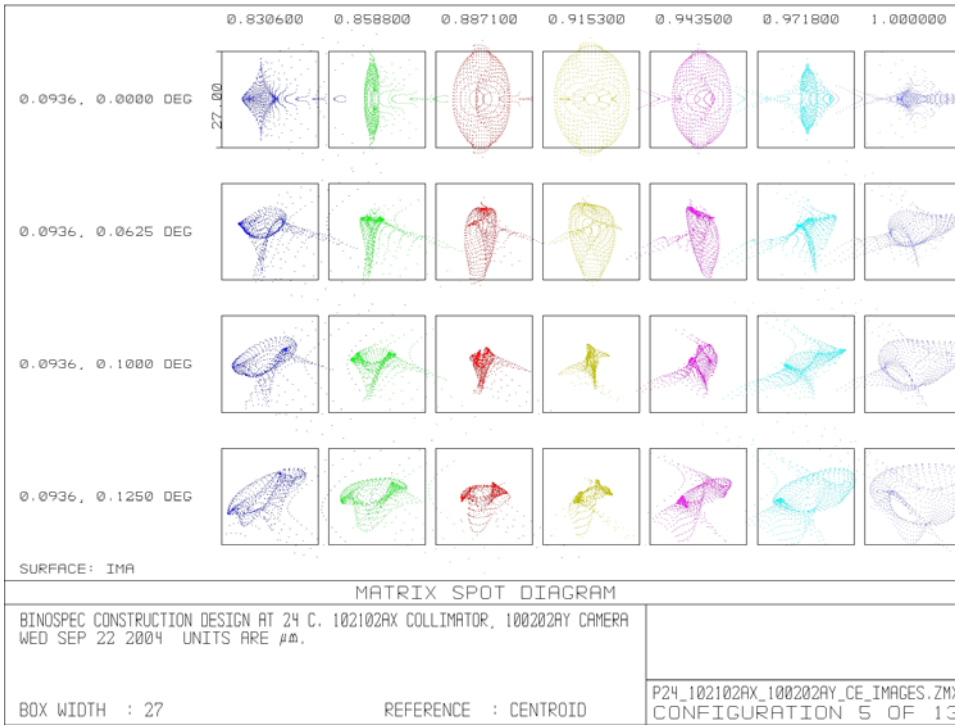


**Figure 210. Configuration 5 (900 gpm grating) spots in a two pixel box.**

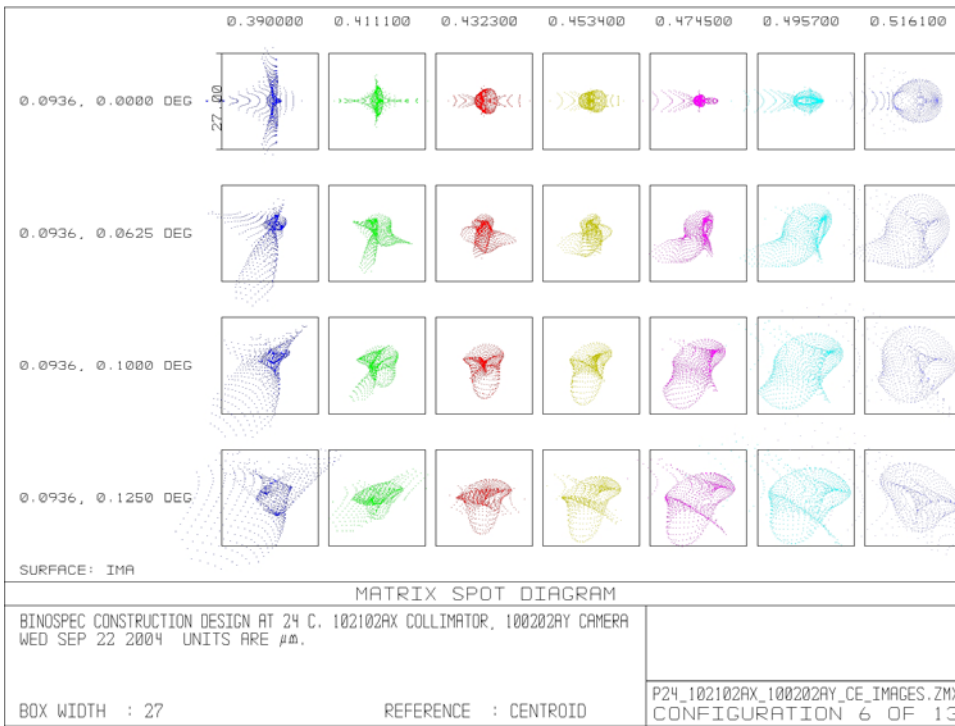


**Figure 211. Configuration 6 (1200 gpm grating) spots in a two pixel box.**

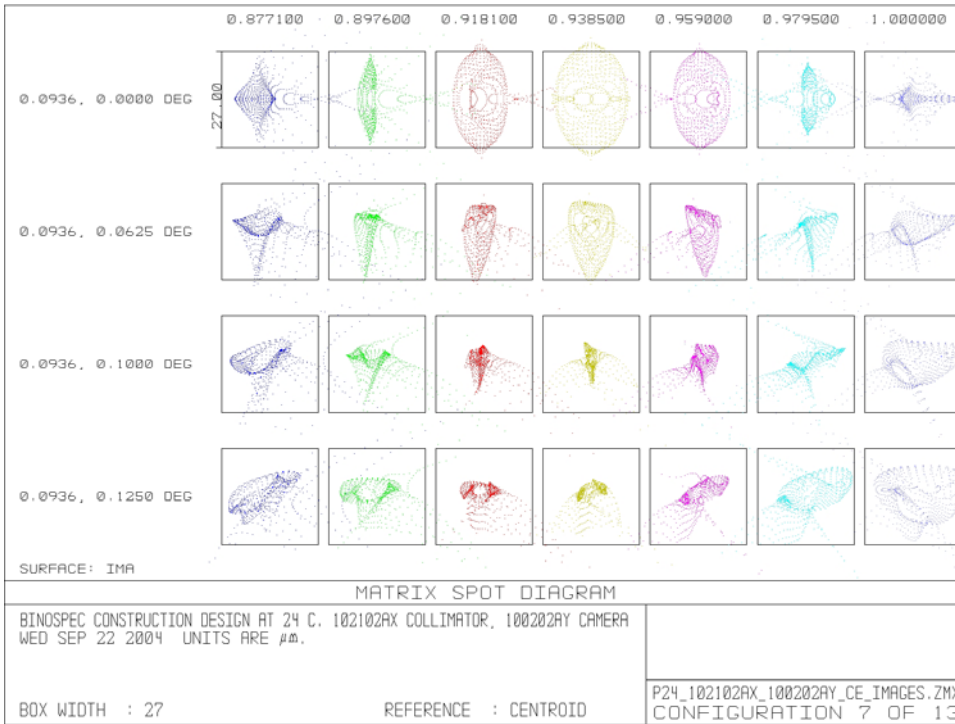


Figure 212. Configuration 7 (1200 gpm grating) spots in a two pixel box.

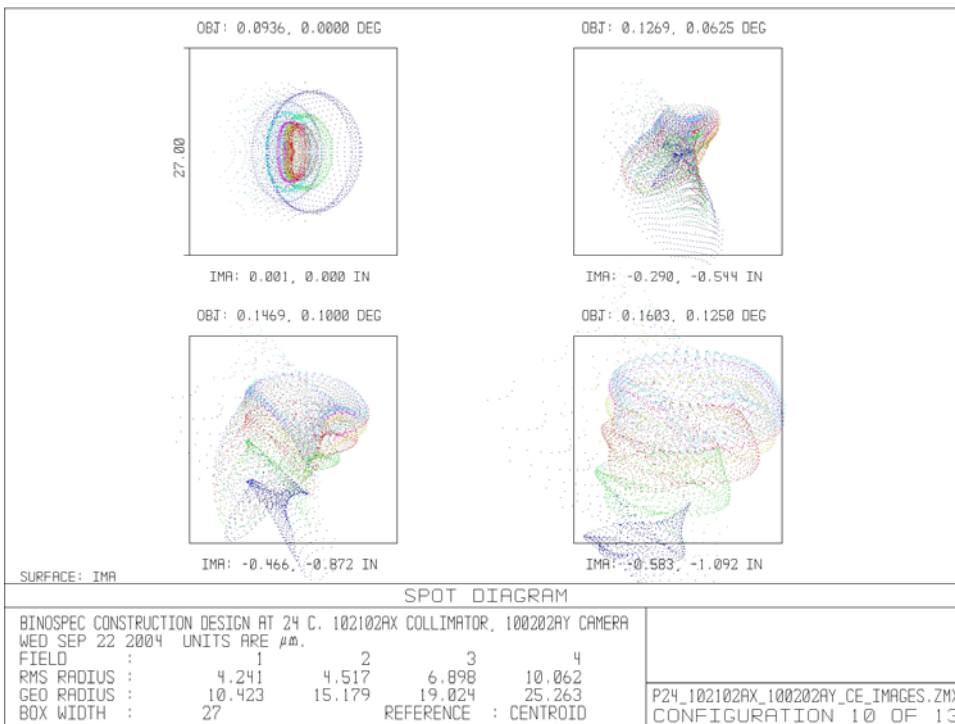
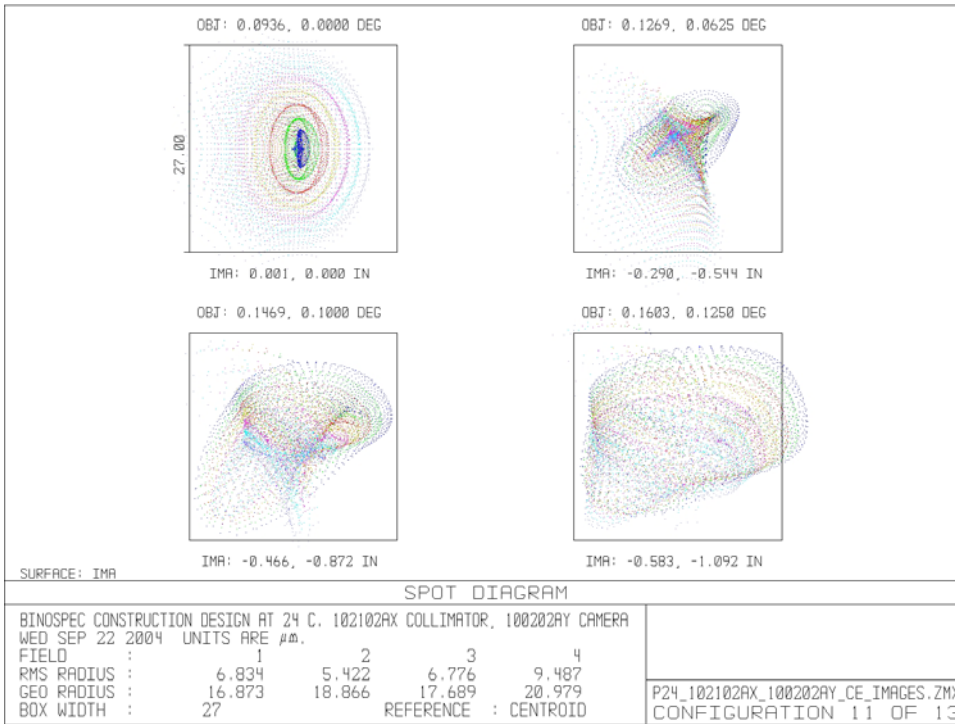
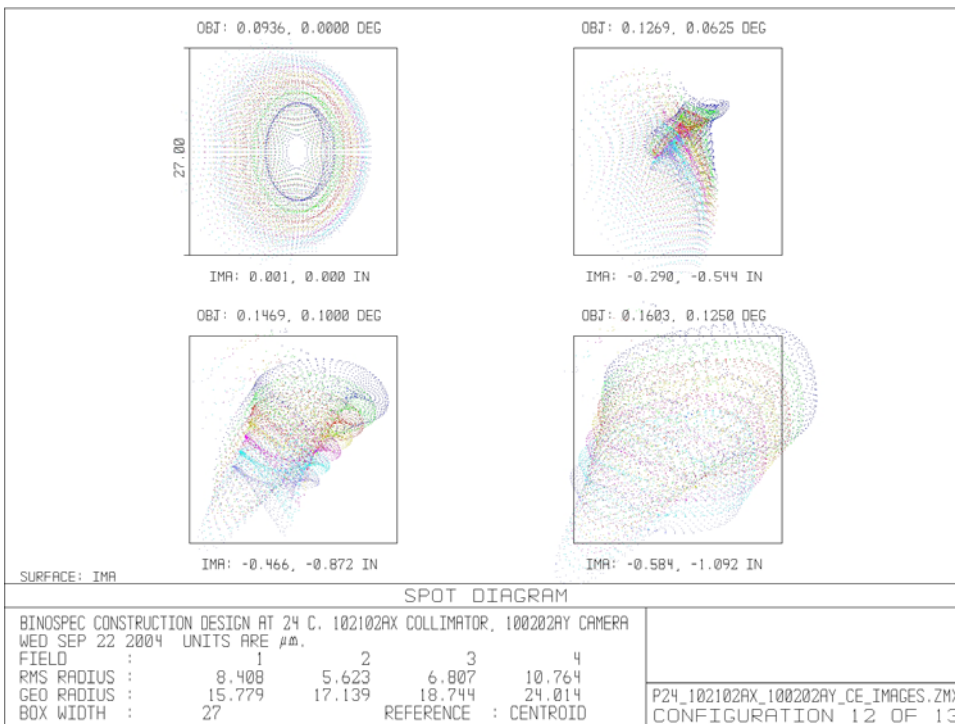


Figure 213. Configuration 10, g' band (0.41-0.54  $\mu\text{m}$ ) polychromatic spots in a two pixel box.



**Figure 214. Configuration 11, r' band (0.56-0.69  $\mu\text{m}$ ) polychromatic spots in a two pixel box.**



**Figure 215. Configuration 12, i' band (0.69-0.83  $\mu\text{m}$ ) polychromatic spots in a two pixel box.**

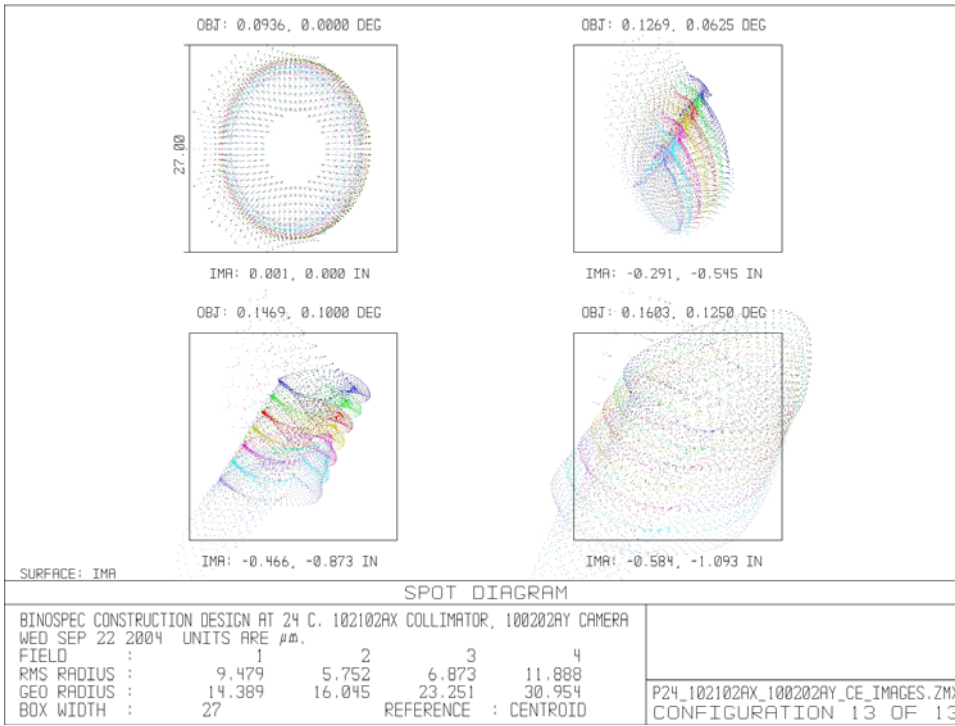


**Figure 216. z' band (0.86-0.99  $\mu m$ ) polychromatic spots in a two pixel box.**

### 11.3 Image Motion Sensitivity Matrix

Executing C:\DOCS\ZEMAX\_FILES\MACROS\FE.ZPL.

Zemax file is: p24\_102102ax\_100202ay\_CE\_inch\_FE.zmx Date:  
THU OCT 21 2004 Zemax Ver: 40722

Binospec Construction Design at 24 C. 102102ax collimator,  
100202ay camera

z move moves the entire element, the other movements affect only a  
single surface

Wavelength= 0.6606  
X-field= 0.093593  
Y-field= 0.000000

```
24 STANDARD MIRROR
  Radius of Curvature= 0.000 Zernike Norm Radius 4.700
                        dx      dy      focus  RMS image dia.
                        (all in microns)
x decenter  0.010  IN    0.000  0.000  0.000  2.247
y decenter  0.010  IN    0.000  0.000  0.000  2.247
z move      0.010  IN   -66.203  0.000 -57.292  2.243
rotate x    0.050  deg    0.039  64.137  0.000  2.280
rotate y    0.050  deg   -91.916  0.000  0.000  2.446
rotate z    0.050  deg    -0.000  -0.000  0.000  2.247
sph bend    100.000 microin  1.318  -0.000  4.592  1.864
```

```
27 STANDARD MIRROR
  Radius of Curvature= 0.000 Zernike Norm Radius 5.500
                        dx      dy      focus  RMS image dia.
                        (all in microns)
x decenter  0.010  IN    0.000  0.000  0.000  2.247
y decenter  0.010  IN    0.000  0.000  0.000  2.247
z move      0.010  IN    65.799  -0.000  57.452  2.261
rotate x    0.050  deg    0.081 -132.948  0.000  2.283
rotate y    0.050  deg   189.246  -0.000  0.000  2.184
rotate z    0.050  deg    0.000  -0.000  0.000  2.247
sph bend    100.000 microin -1.287  0.000 -13.225  3.663
```

```
30 STANDARD _FILTP24
  Radius of Curvature= 0.000 Zernike Norm Radius 5.400
                        dx      dy      focus  RMS image dia.
                        (all in microns)
x decenter  0.010  IN    0.000  0.000  0.000  2.247
y decenter  0.010  IN    0.000  0.000  0.000  2.247
z move      0.010  IN   -0.000  -0.000  0.000  2.247
rotate x    0.050  deg   -0.000  -79.873  0.000  2.477
rotate y    0.050  deg    79.878  -0.000  0.000  2.310
rotate z    0.050  deg   -0.000  0.000  0.000  2.247
sph bend    100.000 microin  0.105  -0.000  -8.021  2.245
```

31 STANDARD  
 Radius of Curvature= 0.000 Zernike Norm Radius 5.400  
 dx dy focus RMS image dia.  
 (all in microns)

x decenter	0.010	IN	0.000	0.000	0.000	2.247
y decenter	0.010	IN	0.000	-0.000	0.000	2.247
rotate x	0.050	deg	-0.000	80.442	0.000	2.490
rotate y	0.050	deg	-80.448	0.000	0.000	2.661
rotate z	0.050	deg	0.000	-0.000	0.000	2.247
sph bend	100.000	microin	-0.107	0.000	8.135	2.250

32 EVENASPH \_24COL01  
 Radius of Curvature= 19.403 Zernike Norm Radius 6.220  
 dx dy focus RMS image dia.  
 (all in microns)

x decenter	0.010	IN	61.545	-0.000	0.000	3.491
y decenter	0.010	IN	0.000	61.535	0.000	3.759
z move	0.010	IN	0.359	-0.000	-28.017	2.242
rotate x	0.050	deg	-0.000	-103.602	0.000	4.673
rotate y	0.050	deg	103.615	-0.000	0.000	4.397
rotate z	0.050	deg	0.000	-0.000	0.000	2.247
sph bend	100.000	microin	0.128	-0.000	-9.703	2.246

33 STANDARD \_COILP24  
 Radius of Curvature= 8.238 Zernike Norm Radius 5.984  
 dx dy focus RMS image dia.  
 (all in microns)

x decenter	0.010	IN	-15.590	0.000	0.000	2.864
y decenter	0.010	IN	-0.000	-15.585	0.000	2.659
rotate x	0.050	deg	-0.000	11.205	0.000	2.469
rotate y	0.050	deg	-11.208	0.000	0.000	2.626
rotate z	0.050	deg	-0.000	-0.000	0.000	2.247
sph bend	100.000	microin	-0.015	0.000	1.113	2.247

34 STANDARD \_24COL02  
 Radius of Curvature= 8.425 Zernike Norm Radius 6.122  
 dx dy focus RMS image dia.  
 (all in microns)

x decenter	0.010	IN	-2.849	0.000	0.000	2.306
y decenter	0.010	IN	-0.000	-2.848	0.000	2.263
z move	0.010	IN	0.041	0.000	-3.281	2.246
rotate x	0.050	deg	-0.000	2.094	0.000	2.256
rotate y	0.050	deg	-2.095	0.000	0.000	2.288
rotate z	0.050	deg	-0.000	-0.000	0.000	2.247
sph bend	100.000	microin	-0.003	0.000	0.198	2.247

35 STANDARD  
 Radius of Curvature= -44.233 Zernike Norm Radius 6.122  
 dx dy focus RMS image dia.  
 (all in microns)

x decenter	0.010	IN	24.812	-0.000	0.000	2.218
y decenter	0.010	IN	-0.000	24.811	0.000	2.256
rotate x	0.050	deg	-0.000	95.774	0.000	2.380
rotate y	0.050	deg	-95.779	0.000	0.000	2.522
rotate z	0.050	deg	-0.000	-0.000	0.000	2.247
sph bend	100.000	microin	-0.133	0.000	10.243	2.250

36 STANDARD \_24COL03  
 Radius of Curvature= 13.701 Zernike Norm Radius 5.945  
 dx dy focus RMS image dia.  
 (all in microns)

x decenter	0.010	IN	103.208	-0.000	0.000	3.679
y decenter	0.010	IN	-0.000	103.199	0.000	3.955
z move	0.010	IN	-0.280	0.000	19.812	2.258
rotate x	0.050	deg	-0.000	-123.389	0.000	4.494
rotate y	0.050	deg	123.400	-0.000	0.000	4.214
rotate z	0.050	deg	-0.000	-0.000	0.000	2.247
sph bend	100.000	microin	0.182	-0.000	-13.977	2.244

37 STANDARD \_COILP24  
 Radius of Curvature= -17.892 Zernike Norm Radius 5.945  
 dx dy focus RMS image dia.  
 (all in microns)

x decenter	0.010	IN	14.310	-0.000	0.000	2.238
y decenter	0.010	IN	0.000	14.308	0.000	2.344
rotate x	0.050	deg	0.000	22.340	0.000	2.476
rotate y	0.050	deg	-22.343	0.000	0.000	2.644
rotate z	0.050	deg	-0.000	0.000	0.000	2.247
sph bend	100.000	microin	-0.030	-0.000	2.302	2.247

38 STANDARD \_24COL04  
 Radius of Curvature= -16.901 Zernike Norm Radius 5.591  
 dx dy focus RMS image dia.  
 (all in microns)

x decenter	0.010	IN	-4.116	0.000	0.000	2.292
y decenter	0.010	IN	-0.000	-4.115	0.000	2.257
z move	0.010	IN	0.111	-0.000	-7.993	2.253
rotate x	0.050	deg	-0.000	-6.070	0.000	2.269
rotate y	0.050	deg	6.070	-0.000	0.000	2.216
rotate z	0.050	deg	0.000	-0.000	0.000	2.247
sph bend	100.000	microin	0.009	-0.000	-0.705	2.247

39 STANDARD \_COILP24  
 Radius of Curvature= 5.093 Zernike Norm Radius 4.528  
 dx dy focus RMS image dia.  
 (all in microns)

x decenter	0.010	IN	-14.052	0.000	0.000	2.965
y decenter	0.010	IN	-0.000	-14.047	0.000	2.743
rotate x	0.050	deg	-0.000	6.244	0.000	2.354
rotate y	0.050	deg	-6.246	0.000	0.000	2.468
rotate z	0.050	deg	0.000	-0.000	0.000	2.247
sph bend	100.000	microin	-0.013	-0.000	1.058	2.248

40 STANDARD \_24COL05  
 Radius of Curvature= 5.093 Zernike Norm Radius 4.547  
 dx dy focus RMS image dia.  
 (all in microns)

x decenter	0.010	IN	39.242	-0.000	0.000	4.474
y decenter	0.010	IN	0.001	39.229	0.000	4.743
z move	0.010	IN	-0.056	0.000	3.770	2.246
rotate x	0.050	deg	0.000	-17.436	0.000	2.915
rotate y	0.050	deg	17.442	-0.000	0.000	2.683
rotate z	0.050	deg	-0.000	0.000	0.000	2.247
sph bend	100.000	microin	0.037	0.000	-2.946	2.246

41 STANDARD \_COILP24  
 Radius of Curvature= 6.026 Zernike Norm Radius 4.350  
 dx dy focus RMS image dia.  
 (all in microns)

x decenter	0.010	IN	-30.463	0.000	0.000	3.087
y decenter	0.010	IN	-0.000	-30.457	0.000	2.855
rotate x	0.050	deg	-0.000	16.017	0.000	2.431
rotate y	0.050	deg	-16.020	0.000	0.000	2.573
rotate z	0.050	deg	0.000	-0.000	0.000	2.247
sph bend	100.000	microin	-0.036	-0.000	2.874	2.249

42 STANDARD NCAF2P24  
 Radius of Curvature= 5.717 Zernike Norm Radius 4.311  
 dx dy focus RMS image dia.  
 (all in microns)

x decenter	0.010	IN	-22.941	0.000	0.000	3.042
y decenter	0.010	IN	-0.000	-22.935	0.000	2.815
z move	0.010	IN	0.175	-0.000	-12.627	2.258
rotate x	0.050	deg	-0.000	11.442	0.000	2.401
rotate y	0.050	deg	-11.445	0.000	0.000	2.533
rotate z	0.050	deg	-0.000	-0.000	0.000	2.247
sph bend	100.000	microin	-0.026	0.000	2.059	2.248

43 STANDARD \_COILP24  
 Radius of Curvature= -8.448 Zernike Norm Radius 4.311  
 dx dy focus RMS image dia.  
 (all in microns)

x decenter	0.010	IN	-14.340	0.000	0.000	2.588
y decenter	0.010	IN	-0.000	-14.336	0.000	2.442
rotate x	0.050	deg	-0.000	-10.569	0.000	2.355
rotate y	0.050	deg	10.571	-0.000	0.000	2.239
rotate z	0.050	deg	-0.000	-0.000	0.000	2.247
sph bend	100.000	microin	0.023	0.000	-1.762	2.247

44 STANDARD \_24COL07  
 Radius of Curvature= -9.848 Zernike Norm Radius 4.213  
 dx dy focus RMS image dia.  
 (all in microns)

x decenter	0.010	IN	-6.131	0.000	0.000	2.317
y decenter	0.010	IN	-0.000	-6.130	0.000	2.268
z move	0.010	IN	-1.129	0.000	79.786	3.148
rotate x	0.050	deg	-0.000	-5.268	0.000	2.263
rotate y	0.050	deg	5.269	-0.000	0.000	2.218
rotate z	0.050	deg	0.000	-0.000	0.000	2.247
sph bend	100.000	microin	0.012	-0.000	-0.933	2.247

45 STANDARD  
 Radius of Curvature= 5.627 Zernike Norm Radius 3.701  
 dx dy focus RMS image dia.  
 (all in microns)

x decenter	0.010	IN	-183.627	0.000	0.000	23.825
y decenter	0.010	IN	-0.006	-183.543	0.000	23.007
rotate x	0.050	deg	-0.001	90.129	0.000	11.465
rotate y	0.050	deg	-90.165	0.000	0.000	12.027
rotate z	0.050	deg	-0.000	0.000	0.000	2.247
sph bend	100.000	microin	-0.248	0.000	19.174	2.252

47 STANDARD MIRROR  
 Radius of Curvature= 0.000 Zernike Norm Radius 6.800  
 dx dy focus RMS image dia.  
 (all in microns)

x decenter	0.010	IN	0.000	0.000	0.000	2.247
y decenter	0.010	IN	0.000	-0.000	0.000	2.247
z move	0.010	IN	2.062	-102.070	-145.597	14.772
rotate x	0.050	deg	-0.003	467.514	0.000	2.824
rotate y	0.050	deg	-330.590	0.181	0.000	2.774
rotate z	0.050	deg	-0.000	-0.000	0.000	2.247
sph bend	100.000	microin	-0.465	3.232	53.732	8.801

49 EVENASPH \_24COL08  
 Radius of Curvature= 25.449 Zernike Norm Radius 5.374  
 dx dy focus RMS image dia.  
 (all in microns)

x decenter	0.010	IN	-92.196	0.000	0.000	17.672
y decenter	0.010	IN	-0.001	-92.143	0.000	16.986
z move	0.010	IN	0.934	-0.000	-63.111	3.353
rotate x	0.050	deg	-0.000	187.519	0.000	7.047
rotate y	0.050	deg	-187.537	0.000	0.000	7.514
rotate z	0.050	deg	-0.000	-0.000	0.000	2.247
sph bend	100.000	microin	-0.541	0.000	41.547	2.253

50 STANDARD \_COILP24  
 Radius of Curvature= 87.533 Zernike Norm Radius 5.630  
 dx dy focus RMS image dia.  
 (all in microns)

x decenter	0.010	IN	4.439	-0.000	0.000	2.214
y decenter	0.010	IN	0.000	4.438	0.000	2.266
rotate x	0.050	deg	0.000	-33.900	0.000	3.171
rotate y	0.050	deg	33.906	-0.000	0.000	2.894
rotate z	0.050	deg	-0.000	-0.000	0.000	2.247
sph bend	100.000	microin	0.095	-0.000	-7.113	2.250

51 STANDARD NCAF2P24  
 Radius of Curvature= 98.235 Zernike Norm Radius 5.827  
 dx dy focus RMS image dia.  
 (all in microns)

x decenter	0.010	IN	2.432	-0.000	0.000	2.223
y decenter	0.010	IN	0.000	2.432	0.000	2.254
z move	0.010	IN	-2.142	0.000	148.368	5.204
rotate x	0.050	deg	0.000	-20.848	0.000	2.669
rotate y	0.050	deg	20.852	-0.000	0.000	2.450
rotate z	0.050	deg	-0.000	0.000	0.000	2.247
sph bend	100.000	microin	0.055	-0.000	-4.082	2.249

52 STANDARD  
 Radius of Curvature= 8.341 Zernike Norm Radius 5.827  
 dx dy focus RMS image dia.  
 (all in microns)

x decenter	0.010	IN	229.777	-0.000	0.000	36.449
y decenter	0.010	IN	0.005	229.661	0.000	36.167
rotate x	0.050	deg	0.003	-167.162	0.000	26.369
rotate y	0.050	deg	167.244	-0.000	0.000	26.458
rotate z	0.050	deg	0.000	0.000	0.000	2.247
sph bend	100.000	microin	0.388	0.000	-31.528	2.253

55 STANDARD MIRROR (Fold Mirror or Grating, rotate Z applies to grating only)  
 Radius of Curvature= 0.000 Zernike Norm Radius 7.200  
 dx dy focus RMS image dia.  
 (all in microns)

x decenter	0.010	IN	0.000	-0.000	0.000	2.247
y decenter	0.010	IN	0.000	0.000	0.000	2.247
z move	0.010	IN	0.016	-0.000	-0.000	2.236
rotate x	0.050	deg	704.511	-0.000	0.000	2.252
rotate y	0.050	deg	0.217	650.871	0.000	2.245
rotate z	0.050	deg	-0.000	-37.000	0.000	2.247
sph bend	100.000	microin	-0.004	-0.000	-97.036	4.780

58 EVENASPH \_24CAM01  
 Radius of Curvature= 21.509 Zernike Norm Radius 7.047  
 dx dy focus RMS image dia.  
 (all in microns)

x decenter	0.010	IN	105.343	0.000	0.000	8.898
y decenter	0.010	IN	0.000	105.337	0.000	8.428
z move	0.010	IN	-0.001	0.000	11.110	2.347
rotate x	0.050	deg	-0.000	-208.875	0.000	4.254
rotate y	0.050	deg	208.872	-0.000	0.000	3.822
rotate z	0.050	deg	0.000	0.000	0.000	2.247
sph bend	100.000	microin	-0.002	-0.000	-29.650	2.239

59 STANDARD \_COILP24  
 Radius of Curvature= 10.235 Zernike Norm Radius 6.811  
 dx dy focus RMS image dia.  
 (all in microns)

x decenter	0.010	IN	-37.217	0.000	0.000	4.547
y decenter	0.010	IN	0.000	-37.220	0.000	4.130
rotate x	0.050	deg	0.000	33.245	0.000	3.825
rotate y	0.050	deg	-33.243	0.000	0.000	4.227
rotate z	0.050	deg	-0.000	-0.000	0.000	2.247
sph bend	100.000	microin	0.000	-0.000	4.706	2.252

60 STANDARD NCAF2P24  
 Radius of Curvature= 10.450 Zernike Norm Radius 7.028  
 dx dy focus RMS image dia.  
 (all in microns)

x decenter	0.010	IN	-25.863	0.000	0.000	3.800
y decenter	0.010	IN	0.000	-25.865	0.000	3.424
z move	0.010	IN	-0.000	0.000	-0.443	2.280
rotate x	0.050	deg	0.000	23.588	0.000	3.256
rotate y	0.050	deg	-23.586	0.000	0.000	3.617
rotate z	0.050	deg	0.000	0.000	0.000	2.247
sph bend	100.000	microin	0.000	-0.000	3.125	2.250

61 STANDARD  
 Radius of Curvature= -126.109 Zernike Norm Radius 7.028  
 dx dy focus RMS image dia.  
 (all in microns)

x decenter	0.010	IN	13.347	-0.000	0.000	2.222
y decenter	0.010	IN	0.000	13.347	0.000	2.253
rotate x	0.050	deg	-0.000	146.887	0.000	2.838
rotate y	0.050	deg	-146.886	0.000	0.000	3.111
rotate z	0.050	deg	-0.000	-0.000	0.000	2.247
sph bend	100.000	microin	0.002	-0.000	20.376	2.250

62 STANDARD NCAF2P24  
 Radius of Curvature= 16.388 Zernike Norm Radius 7.323  
 dx dy focus RMS image dia.  
 (all in microns)

x decenter	0.010	IN	96.463	-0.000	0.000	3.277
y decenter	0.010	IN	-0.000	96.466	0.000	3.752
z move	0.010	IN	0.002	0.000	43.042	2.322
rotate x	0.050	deg	-0.000	-137.956	0.000	4.849
rotate y	0.050	deg	137.953	-0.000	0.000	4.327
rotate z	0.050	deg	0.000	0.000	0.000	2.247
sph bend	100.000	microin	-0.002	-0.000	-16.513	2.243

63 STANDARD \_COILP24  
 Radius of Curvature= -39.400 Zernike Norm Radius 7.323  
 dx dy focus RMS image dia.  
 (all in microns)

x decenter	0.010	IN	-5.474	0.000	0.000	2.385
y decenter	0.010	IN	0.000	-5.474	0.000	2.290
rotate x	0.050	deg	0.000	-18.823	0.000	2.707
rotate y	0.050	deg	18.821	-0.000	0.000	2.398
rotate z	0.050	deg	0.000	0.000	0.000	2.247
sph bend	100.000	microin	-0.000	0.000	-2.028	2.250

64 STANDARD \_24CAM04  
 Radius of Curvature= -31.907 Zernike Norm Radius 7.185  
 dx dy focus RMS image dia.  
 (all in microns)

x decenter	0.010	IN	-9.535	0.000	0.000	2.558
y decenter	0.010	IN	0.000	-9.536	0.000	2.390
z move	0.010	IN	-0.001	-0.000	-17.759	2.239
rotate x	0.050	deg	0.000	-26.551	0.000	3.193
rotate y	0.050	deg	26.549	-0.000	0.000	2.796
rotate z	0.050	deg	-0.000	0.000	0.000	2.247
sph bend	100.000	microin	-0.000	-0.000	-2.960	2.251

65 STANDARD \_COILP24  
 Radius of Curvature= 17.900 Zernike Norm Radius 6.949  
 dx dy focus RMS image dia.  
 (all in microns)

x decenter	0.010	IN	-16.314	0.000	0.000	2.514
y decenter	0.010	IN	0.000	-16.314	0.000	2.357
rotate x	0.050	deg	0.000	25.484	0.000	2.506
rotate y	0.050	deg	-25.483	0.000	0.000	2.733
rotate z	0.050	deg	-0.000	0.000	0.000	2.247
sph bend	100.000	microin	0.000	-0.000	3.057	2.247

66 STANDARD NCAF2P24  
 Radius of Curvature= 14.517 Zernike Norm Radius 6.909  
 dx dy focus RMS image dia.  
 (all in microns)

x decenter	0.010	IN	-14.290	0.000	0.000	2.526
y decenter	0.010	IN	0.000	-14.290	0.000	2.364
z move	0.010	IN	-0.001	-0.000	-10.922	2.239
rotate x	0.050	deg	0.000	18.103	0.000	2.432
rotate y	0.050	deg	-18.102	0.000	0.000	2.630
rotate z	0.050	deg	0.000	-0.000	0.000	2.247
sph bend	100.000	microin	0.000	-0.000	2.181	2.247

67 STANDARD \_COILP24  
 Radius of Curvature= -38.522 Zernike Norm Radius 6.909  
 dx dy focus RMS image dia.  
 (all in microns)

			dx	dy	focus	RMS image dia.
x decenter	0.010	IN	-4.979	0.000	0.000	2.379
y decenter	0.010	IN	0.000	-4.980	0.000	2.286
rotate x	0.050	deg	0.000	-16.740	0.000	2.654
rotate y	0.050	deg	16.739	-0.000	0.000	2.359
rotate z	0.050	deg	0.000	-0.000	0.000	2.247
sph bend	100.000	microin	-0.000	0.000	-1.844	2.250

68 STANDARD \_24CAM06  
 Radius of Curvature= -44.687 Zernike Norm Radius 6.831  
 dx dy focus RMS image dia.  
 (all in microns)

			dx	dy	focus	RMS image dia.
x decenter	0.010	IN	-7.946	0.000	0.000	2.469
y decenter	0.010	IN	-0.000	-7.946	0.000	2.334
z move	0.010	IN	0.008	-0.000	125.391	2.295
rotate x	0.050	deg	0.000	-30.987	0.000	3.331
rotate y	0.050	deg	30.986	-0.000	0.000	2.918
rotate z	0.050	deg	0.000	-0.000	0.000	2.247
sph bend	100.000	microin	-0.000	-0.000	-3.510	2.252

69 STANDARD  
 Radius of Curvature= -17.909 Zernike Norm Radius 6.909  
 dx dy focus RMS image dia.  
 (all in microns)

			dx	dy	focus	RMS image dia.
x decenter	0.010	IN	102.799	-0.000	0.000	14.522
y decenter	0.010	IN	-0.000	102.811	0.000	15.075
rotate x	0.050	deg	-0.000	160.680	0.000	23.406
rotate y	0.050	deg	-160.662	0.000	0.000	23.893
rotate z	0.050	deg	-0.000	-0.000	0.000	2.247
sph bend	100.000	microin	0.002	-0.000	16.189	2.238

70 STANDARD \_24CAM07  
 Radius of Curvature= 11.070 Zernike Norm Radius 5.453  
 dx dy focus RMS image dia.  
 (all in microns)

			dx	dy	focus	RMS image dia.
x decenter	0.010	IN	103.151	-0.000	0.000	2.541
y decenter	0.010	IN	0.000	103.152	0.000	2.892
z move	0.010	IN	0.012	-0.000	84.090	2.237
rotate x	0.050	deg	-0.000	-99.651	0.000	2.853
rotate y	0.050	deg	99.650	-0.000	0.000	2.510
rotate z	0.050	deg	-0.000	-0.000	0.000	2.247
sph bend	100.000	microin	-0.002	-0.000	-14.154	2.243

71 STANDARD \_COILP24  
 Radius of Curvature= -52.667 Zernike Norm Radius 5.453  
 dx dy focus RMS image dia.  
 (all in microns)

			dx	dy	focus	RMS image dia.
x decenter	0.010	IN	-0.032	0.000	0.000	2.248
y decenter	0.010	IN	0.000	-0.032	0.000	2.247
rotate x	0.050	deg	0.000	-0.145	0.000	2.247
rotate y	0.050	deg	0.145	-0.000	0.000	2.244
rotate z	0.050	deg	-0.000	-0.000	0.000	2.247
sph bend	100.000	microin	-0.000	-0.000	-0.015	2.247

72 STANDARD \_NACLP24  
 Radius of Curvature= -35.902 Zernike Norm Radius 5.197  
 dx dy focus RMS image dia.  
 (all in microns)

x decenter	0.010	IN	-2.383	0.000	0.000	2.330
y decenter	0.010	IN	0.000	-2.383	0.000	2.265
z move	0.010	IN	-0.003	0.000	-22.605	2.261
rotate x	0.050	deg	0.000	-7.466	0.000	2.419
rotate y	0.050	deg	7.465	-0.000	0.000	2.214
rotate z	0.050	deg	-0.000	-0.000	0.000	2.247
sph bend	100.000	microin	-0.000	-0.000	-0.842	2.249

73 STANDARD \_COILP24  
 Radius of Curvature= 6.266 Zernike Norm Radius 4.252  
 dx dy focus RMS image dia.  
 (all in microns)

x decenter	0.010	IN	-12.155	0.000	0.000	2.311
y decenter	0.010	IN	0.000	-12.155	0.000	2.257
rotate x	0.050	deg	0.000	6.647	0.000	2.250
rotate y	0.050	deg	-6.647	0.000	0.000	2.280
rotate z	0.050	deg	0.000	-0.000	0.000	2.247
sph bend	100.000	microin	0.000	-0.000	1.185	2.248

74 STANDARD NCAF2P24  
 Radius of Curvature= 6.266 Zernike Norm Radius 4.291  
 dx dy focus RMS image dia.  
 (all in microns)

x decenter	0.010	IN	-17.606	0.000	0.000	2.350
y decenter	0.010	IN	0.000	-17.606	0.000	2.271
z move	0.010	IN	0.005	-0.000	77.948	2.257
rotate x	0.050	deg	0.000	9.627	0.000	2.254
rotate y	0.050	deg	-9.627	0.000	0.000	2.298
rotate z	0.050	deg	-0.000	0.000	0.000	2.247
sph bend	100.000	microin	0.000	-0.000	1.685	2.248

75 STANDARD  
 Radius of Curvature= -167.316 Zernike Norm Radius 4.291  
 dx dy focus RMS image dia.  
 (all in microns)

x decenter	0.010	IN	3.286	-0.000	0.000	2.191
y decenter	0.010	IN	-0.000	3.286	0.000	2.278
rotate x	0.050	deg	-0.000	47.983	0.000	5.918
rotate y	0.050	deg	-47.978	0.000	0.000	6.384
rotate z	0.050	deg	-0.000	-0.000	0.000	2.247
sph bend	100.000	microin	0.001	-0.000	4.932	2.240

76 STANDARD \_24CAM10  
 Radius of Curvature= -10.778 Zernike Norm Radius 2.165  
 dx dy focus RMS image dia.  
 (all in microns)

x decenter	0.010	IN	-11.124	0.000	0.000	2.668
y decenter	0.010	IN	0.000	-11.125	0.000	2.467
z move	0.010	IN	-0.021	0.000	-35.423	2.339
rotate x	0.050	deg	0.000	-10.464	0.000	2.443
rotate y	0.050	deg	10.463	-0.000	0.000	2.229
rotate z	0.050	deg	-0.000	-0.000	0.000	2.247
sph bend	100.000	microin	-0.001	-0.000	0.476	2.247

77 STANDARD

Radius of Curvature=	13.290	Zernike Norm Radius	2.165			
		dx	dy	focus	RMS image dia.	
		(all in microns)				
x decenter	0.010	IN	-5.452	0.000	0.000	2.401
y decenter	0.010	IN	-0.000	-5.452	0.000	2.296
rotate x	0.050	deg	0.000	6.323	0.000	2.312
rotate y	0.050	deg	-6.323	0.000	0.000	2.434
rotate z	0.050	deg	-0.000	-0.000	0.000	2.247
sph bend	100.000	microin	0.000	0.000	-0.615	2.247

#### **11.4 Published Papers Concerning Binospec Thermal Design**

1. H. Epps and D. Fabricant, "Athermalizing Refractive Optics with Fluid Lenses", *PASP*, **114**, pp. 1252-1259, 2002.
2. W. Brown, D. Fabricant and D. Boyd, "A Detailed Thermal Analysis of the Binospec Spectrograph", *PASP*, **114**, pp. 1389-1400, 2002.
3. W. Brown, D. Fabricant and D. Boyd, "Thermal Considerations in Modern Spectrograph Design", *SPIE Proc.*, **4841**, pp. 1265-1272, 2003.